

# CARPET Version 3

Computer-Aided Radar Performance Evaluation Tool

## User's Manual

Version 1.0, 28th November 2024

Albert G. Huizing, Arne Theil

---

*Dedicated to Gerard A. van der Spek our former head of  
department who encouraged the publication of CARPET.*

## Change-log

Date	Version	Description
28-3-2018	0.9	First version, for review purposes.
6-4-2018	1	- Python code example added (Section 7.5). - URL to the Integrated Global Radiosonde Archive added (Section 2.10.3). - PPI diagram of received powers added in Section 4.2.1, the radar is on the Matterhorn.
12-4-2018	1	- Python code example slightly modified (Section 7.5). - Conversion from IGRA to M or N-profile explained (Section 2.10.3). - Date-stamp added on the title page. - MSYS added (Section 1.6).
19-4-2018	1	Contours added to the diagram layout dialogbox (Section 3.15).
30-4-2018	1	Figure 3.11 explaining quantities rain cloud range, azimuth angle and diameter added.
15-5-2018	1	Figure 6.25 showing rain reflectivity versus rainfall rate added, footnote on reflectivity factor according to the CCIR added.
18-5-2018	1	- Figure 6.11 showing rain attenuation versus rainfall rate for four different frequencies added. - Reference to Principles of Modern Radar, by Mark A. Richards <i>e.a.</i> added.
31-5-2018	1	Description of worksheet Azimuth Beamshape Loss (Section 5.15) added.
5-6-2018	1	- Example of a simple Python program (Section 7.5) has been added. - Python function GetDetectionRange has been added and is described.
2-7-2018	1	Python function GetTerrainProfile has been added and is described.
11-7-2018	1	Horizon Descent added to the Geometry Worksheet (Section 5.3).
12-9-2018	1	Description of four and five pulse cancelers added. Section 4.5 on KML file output added.
9-10-2018	1	Radar location name as well as minimum terrain height editbox added to the Siting dialogbox, see Figure 3.27.
24-10-2018	1	Fixed the erroneous reference to GIT sea clutter model description.
24-10-2018	1	Equations 6.264 and 6.265 augmented with 'backwards' equations.
25-10-2018	1	Demand Successiveness checkbox added to the Binary Integration Worksheet and to the Processing dialogbox, see for instance Figure 5.18. The description in this document is updated, see Section 6.9.10.
15-11-2018	1	Target dialogbox redesigned. The target altitude can be specified with respect to the mean sea level and with respect to the terrain height at the location of the sensor, see Figure 3.27.
16-11-2018	1	Colour pane of the Layout dialogbox is described, see Section 3.18.4.
29-11-2018	1	'Bob Hill explanation' of the radar equation added, Section 6.3.1.
20-12-2018	1	Descriptions of menu entries Site Name and Minimum Height added, see Section 3.17.
3-1-2019	1	Sea state wind speed conversion according to CARPET 2 has been re-introduced see Section 3.3.2.
4-1-2019	1	The number of combinations has been added to the binary integration worksheet.
4-2-2019	1	- The antenna pattern import functionality is described in more detail (Section 2.10.2). The meaning of dBi is explained in a footnote. - Reference to MSYS has been removed. - Section 6.9.5 on Doppler processing has been expanded.
13-2-2019	1	- Parameter Effective Clutter Height added, see the sections 3.5.1 and 6.1.8.8. - Antenna patterns can be exported to ASCII files, see Section 2.12.
15-2-2019	1	Equation 6.222 expanded.
20-2-2019	1	Additional parameter 'Maritime Surface Target' (Target dialogbox) is explained (Section 3.16).
1-3-2019	1	- Section 3.13.2 on time gating specification has been added. - Section 6.9.4 renamed and expanded.
7-3-2019	1	Section 6.9.9 on Detection somewhat expanded.
29-3-2019	1	Section 3.11 improved. The dialogboxes appeared to be erroneous. Field 'Height' is more explicitly explained.



Date	Version	Description
2-5-2019	1	Section 4.6 on GeoTIFF output added.
3-5-2019	1	- Helvetica font used rather than the default L <sup>A</sup> T <sub>E</sub> X Roman serif font. - Few so-called ‘typos’ corrected, Figure 3.1 added.
13-5-2019	1	Python program that saves a GeoTIFF PPI-view diagram added (Subsection 7.5). Again, some ‘typos’ were found and corrected.
3-6-2019	1	- Erroneous equation 6.147 has been repaired. - Fixed wrong TERPEM dialogboxes (Figure 3.7). - Erroneous equation 6.234 has been repaired.
5-6-2019	1	Reference to the publication of Christian Doppler (Section 6.9.1) has been added.
26-7-2019	1	- A footnote on Carl Friedrich Gauß added. - More explanation of the third pane of the Swerling Case worksheet (Section 5.5) added. - Optical horizon added to the geometry worksheet (Section 5.3).
18-9-2019	1	Format of saved plotdata is explained in more detail (Section 2.6).
3-10-2019	1	Figure 4.24 that explains how the line-of-sight condition is determined has been added. The so-called EULA (End-User License Agreement) has been modified (pages 2 and 3).
31-10-2019	1	Equation 6.63 which contained a curly bracket (}) too much has been corrected.
19-12-2019	1	Some re-phrasing of the section about pulse compression.
15-1-2020	1	- The Examples paragraph of Section 7 on the Python plug-in has been reorganized and one example has been added. - Three Python functions have been added: GetFirmTrackProbabilities, GetTrackLossProbabilities, GetTrackAcquisitionProbabilities (Section 7.3). - The Sensor Location dialogbox has been updated, parameters Height Scaling Factor and Water Height are clarified (Section 3.17).
16-1-2020	1	Function GetSCNR has been added to the Python plug-in (Section 7.3).
31-1-2020	1	Function GetReceivedPowersVersusRange has been added to the Python plug-in (Section 7.3).
4-2-2020	1	Correction in Section 7.5 (the received noise power is in column 2, not in column 1).
11-2-2020	1	Section 3.9.2 on sector blanking has been added.
12-2-2020	1	Section 3.10 describing the radar waveform has been added. A new parameter, $N_f$ , which is the number of Doppler filters is described as well. The symbol that is used for the number of fill-pulses is now $N_{p,f}$ (rather than $N_f$ ).
20-2-2020	1	- Variable $G_{pol}$ has been added to the explanation of volume clutter, Section 6.5.1. - Gnome desktop style (Linux) alertbox has been added, Section 2.4.
7-5-2020	1	Equation 6.162 was corrected, a + rather than a ×.
27-7-2020	1	Legend of Figure 3.38 was corrected.
12-11-2020	1	Several http’s were corrected to https’s.
13-11-2020	1	- Figure 3.1 has been replaced, it was way too complicated. - Figure 3.28 that illustrates the usage of the Maritime Surface Target checkbox has been inserted.
16-11-2020	1	New Python function GetPdSwerling is described, a seventh Python example program has been added (Figure 7.7).
17-11-2020	1	A reference to the paper of Neyman and Pearson has been added (Section 6.9.9).
10-12-2020	1	Even more Python functionality: GetTxAntennaGain. An example Python program has also been added (Section 7).
11-12-2020	1	A picture that illustrates the quantity ‘target horizon’ has been inserted, Figure 5.10.
9-1-2021	1	The EIRP has been added to the Transmitter dialogbox (Section 3.9.1).
28-1-2021	1	- A new version of TERPEM (7.3.2) has been inserted. This version ought to perform more stable in the case of a low antenna in mountainous terrain. - Parameter Number of Channels is described, see Section 3.9.
23-2-2021	1	Due to nostalgic reasons, author Arne Theil prefers the so-called ‘Eszett’ (ß) over two s’s. One correction has been made (Gaußian in stead of Gaussian).
25-3-2021	1	The ‘Bob Hill’ recipe has been enlarged with a footnote (Section 6.3.1).
15-6-2021	1	The description of the target line-of-sight diagram has been improved (Section 4.4.2).



---

Date	Version	Description
21-10-2021	1	Equation 6.4 has been expanded a bit.
12-1-2022	1	Section 2.3 expanded so that the installation procedure on MacOS is covered. - Section 2.12 expanded with the saving of the refractivity M-profile. - The (new) Refractivity Profile combobox in the Model dialogbox is discussed in Section 3.2. - The description of the Refractivity Profile dialogbox has been updated (Section 3.4). - The description of the Clutter dialogbox has been updated (Section 3.5).
13-1-2022	1	- Section 2.1 expanded; the MacOS version and Apple silicon is discussed. - A reference to QwtPolar has been removed since QwtPolar has become part of Qwt 6.2.0. - Rephrased OS-X to MacOS. - Updated Figure 1.10.
14-1-2022	1	- Section 4.3.7 on the ERA-15 diagram added. - Section 5.3 on the Conversions worksheet has been added.
24-1-2022	1	Section 6.6.1 somewhat expanded, 'burn through range' is explained.
30-3-2022	1	Section 6.9.2 on Hilbert filtering added.
4-5-2022	1	Equation 6.218 on the filter weights of a pulse canceler has been added.
24-5-2022	1	The modeling of STC (Sensitivity Time Control) has been added. There are three new sections: 2.10.6 and 2.11 on the import/cancel import STC functionality, and 6.11 on the calculation of gain and noise figure factors for different STC implementations.
2-6-2022	1	Font Size has been added to the Layout dialogbox. Section 3.18 has been expanded.
27-6-2022	1	Figure 6.7 which shows the magnitude of the complex reflection coefficient versus the grazing angle has been added.
16-9-2022	1	The Track Probabilities worksheet is explained (Section 5.14).
19-9-2022	1	An example that shows how the Python plug-in can be utilised to model 3D (range-azimuth-elevation) radar has been added, see Section 7.5.9.
28-9-2022	1	Two extra Python functions have been added: <code>GetPPF</code> and <code>GetPathLoss</code> .
29-9-2022	1	An extra download-site for 90 m SRTM data has been added.
9-12-2022	1	A blind speed versus unambiguous range diagram has been added in Section 6.9.
2-2-2023	1	The radar equation as a ratio of energies (in Section 6.7) and also a reference to the book of Budge and German has been inserted.
11-4-2023	1	The left pane of Figure 5.18 appeared to be erroneous, which has been repaired.
12-4-2023	1	Final Bearing added to the Lat-Long worksheet.
14-4-2023	1	Python example 9 has been expanded, graphical output is shown in Figure 7.9.
20-11-2024	1	Error handling when importing an elevation antenna pattern has been improved.

## Contents

<b>1</b>	<b>Introduction</b>	<b>11</b>
1.1	Main Characteristics . . . . .	11
1.2	Plug-ins . . . . .	12
1.2.1	TERPEM-light . . . . .	12
1.2.2	Multi-burst . . . . .	14
1.2.3	Multi-scatterer Target . . . . .	16
1.2.4	Python Interface . . . . .	17
1.3	New Features of the Base-version . . . . .	18
1.3.1	Backwards Compatible . . . . .	18
1.3.2	GUI, Graphics, Operating Systems . . . . .	19
1.3.3	Firm Track Probability . . . . .	19
1.3.4	PPI-view Diagrams . . . . .	20
1.3.5	Separate Transmit and Receive Antenna . . . . .	21
1.3.6	More Jammers . . . . .	21
1.3.7	Pulse Eclipsing . . . . .	22
1.3.8	Loss Factors . . . . .	22
1.3.9	Blake Chart . . . . .	23
1.4	Document Layout . . . . .	23
1.5	Future Developments . . . . .	23
1.6	Acknowledgment . . . . .	24
<b>2</b>	<b>How to Operate CARPET</b>	<b>25</b>
2.1	System Requirements . . . . .	25
2.2	Ordering . . . . .	25
2.3	Installation . . . . .	25
2.4	License File Procedure . . . . .	26
2.5	Making Hardcopies . . . . .	28
2.6	Saving Diagrams . . . . .	28
2.7	Loading Settings Files . . . . .	28
2.8	Saving Settings Files . . . . .	29
2.9	Select Directory . . . . .	29
2.10	Import . . . . .	30
2.10.1	CARPET 2 Settings . . . . .	30
2.10.2	Elevation Antenna Pattern . . . . .	31
2.10.3	Radiosonde Code . . . . .	32
2.10.4	TERMET Output . . . . .	33
2.10.5	Refractivity Data, N-profile, M-profile . . . . .	33

2.10.6	STC Characteristics . . . . .	33
2.11	Cancel Import . . . . .	36
2.12	Export . . . . .	36
<b>3</b>	<b>The Parameters</b>	<b>37</b>
3.1	Introduction . . . . .	37
3.2	Model . . . . .	38
3.3	Propagation . . . . .	40
3.3.1	Free Space . . . . .	40
3.3.2	EREPS-like . . . . .	40
3.3.3	TERPEM-light . . . . .	43
3.4	Refractivity Profile . . . . .	48
3.4.1	Water . . . . .	49
3.4.2	Upper Air . . . . .	49
3.4.3	Radiosonde . . . . .	51
3.4.4	Day, Month, Time . . . . .	51
3.5	Clutter . . . . .	52
3.5.1	Surface Clutter . . . . .	52
3.5.2	Rain . . . . .	53
3.5.3	Chaff . . . . .	54
3.6	Jamming . . . . .	55
3.7	Stand-off Jamming . . . . .	56
3.8	Self Screening Jamming . . . . .	57
3.9	Transmitter . . . . .	58
3.9.1	General . . . . .	58
3.9.2	Sector Blanking . . . . .	60
3.10	Waveform . . . . .	62
3.11	Antenna . . . . .	65
3.11.1	General . . . . .	65
3.11.2	Tx . . . . .	66
3.11.3	Rx . . . . .	66
3.12	Receiver . . . . .	68
3.13	Processing . . . . .	70
3.13.1	Sampling . . . . .	71
3.13.2	Time Gating . . . . .	72
3.13.3	Pulse Compression . . . . .	73
3.13.4	Doppler Filtering . . . . .	73
3.13.5	Detection . . . . .	74
3.14	Tracking . . . . .	77
3.15	Loss Factors . . . . .	78

3.16	Target . . . . .	80
3.16.1	General . . . . .	80
3.16.2	Scatterer . . . . .	84
3.17	Sensor Location . . . . .	85
3.18	Layout . . . . .	87
3.18.1	Limits . . . . .	88
3.18.2	Units . . . . .	89
3.18.3	Appearance . . . . .	90
3.18.4	Colours . . . . .	95
<b>4</b>	<b>Graphical Output</b>	<b>99</b>
4.1	Introduction . . . . .	99
4.2	Plot-1 . . . . .	99
4.2.1	Received Powers . . . . .	99
4.2.2	SCNR . . . . .	103
4.2.3	Detection Probability . . . . .	105
4.2.4	Firm Track Probability . . . . .	107
4.3	Plot-2 . . . . .	108
4.3.1	One-way Path Loss . . . . .	108
4.3.2	Two-way Path Loss . . . . .	109
4.3.3	One-way Pattern Propagation Factor . . . . .	109
4.3.4	Two-way Pattern Propagation Factor . . . . .	109
4.3.5	Refractivity Profiles . . . . .	109
4.3.6	Radiosonde Data . . . . .	110
4.3.7	ERA-15 Data . . . . .	110
4.4	Plot-3 . . . . .	111
4.4.1	Terrain . . . . .	111
4.4.2	Target Line of Sight . . . . .	115
4.4.3	Doppler Filters . . . . .	117
4.4.4	Doppler Filter Gains . . . . .	117
4.4.5	Synthesizer Spectrum . . . . .	118
4.4.6	Swerling Cases . . . . .	119
4.4.7	Antenna Pattern . . . . .	120
4.5	Keyhole Markup Language . . . . .	121
4.6	GeoTIFF . . . . .	121
<b>5</b>	<b>Worksheets</b>	<b>123</b>
5.1	Introduction . . . . .	123
5.2	Blake chart . . . . .	123
5.3	Geometry . . . . .	130



5.4	Conversions . . . . .	132
5.5	Swerling Cases . . . . .	133
5.6	Antenna . . . . .	134
5.7	Absorption . . . . .	135
5.8	Reflectivity . . . . .	136
5.9	Reflection . . . . .	137
5.10	Binary Integration . . . . .	138
5.11	False Alarm Probability . . . . .	139
5.12	Waveform Basics . . . . .	140
5.13	Doppler Filtering . . . . .	141
5.14	Track Probabilities . . . . .	142
5.15	Azimuth Beamshape Loss . . . . .	143
5.16	Latitude/Longitude . . . . .	144
<b>6</b>	<b>CARPET Models</b>	<b>145</b>
6.1	Radio Wave Propagation . . . . .	145
6.1.1	Introduction . . . . .	145
6.1.2	Refractive index . . . . .	145
6.1.3	Refractivity Profile . . . . .	149
6.1.4	ITU Recommendation P.835-6 Annex 2, Section 2 to 4 . . . . .	149
6.1.5	ITU Recommendation P.835-6 Annex 3 . . . . .	150
6.1.6	Free Space . . . . .	150
6.1.7	EREPS-like . . . . .	151
6.1.8	TERPEM-light . . . . .	161
6.1.9	Rain Attenuation . . . . .	170
6.2	System Noise . . . . .	175
6.2.1	Noise Power . . . . .	175
6.2.2	Doppler Spectrum . . . . .	176
6.2.3	Noise Temperature of the Sky . . . . .	176
6.3	Target . . . . .	179
6.3.1	Target Power . . . . .	179
6.3.2	Doppler Spectrum . . . . .	182
6.3.3	Swerling Cases . . . . .	182
6.3.4	Extended Target . . . . .	185
6.4	Surface Clutter . . . . .	189
6.4.1	Surface Clutter Power . . . . .	189
6.4.2	Surface Clutter Doppler Spectrum . . . . .	192
6.5	Volume Clutter . . . . .	195
6.5.1	Volume Clutter Power . . . . .	195
6.5.2	Volume Clutter Spectrum . . . . .	196

6.6	Jamming . . . . .	198
6.6.1	Jamming Power . . . . .	198
6.6.2	Jamming Doppler Spectrum . . . . .	199
6.7	Radar Equation . . . . .	200
6.8	Antenna Pattern . . . . .	201
6.9	Radar Signal Processing . . . . .	203
6.9.1	Basics . . . . .	203
6.9.2	Hilbert Filtering . . . . .	210
6.9.3	Pulse Compression . . . . .	211
6.9.4	Eclipsing . . . . .	212
6.9.5	Doppler Processing . . . . .	214
6.9.6	Antenna Rotation . . . . .	220
6.9.7	Phase and Amplitude Noise . . . . .	221
6.9.8	Timing Jitter . . . . .	222
6.9.9	Detection . . . . .	222
6.9.10	Post-detection Binary Integration . . . . .	229
6.9.11	Multi-scatterer Target . . . . .	232
6.10	Tracking . . . . .	233
6.11	Sensitivity Time Control . . . . .	234
<b>7</b>	<b>Python Plug-in</b>	<b>238</b>
7.1	Introduction . . . . .	238
7.2	Parameters . . . . .	238
7.3	Functions . . . . .	247
7.4	Diagrams . . . . .	248
7.5	Examples . . . . .	251
7.5.1	Example 1 . . . . .	251
7.5.2	Example 2 . . . . .	252
7.5.3	Example 3 . . . . .	253
7.5.4	Example 4 . . . . .	254
7.5.5	Example 5 . . . . .	255
7.5.6	Example 6 . . . . .	258
7.5.7	Example 7 . . . . .	259
7.5.8	Example 8 . . . . .	260
7.5.9	Example 9 . . . . .	261
<b>8</b>	<b>Abbreviations</b>	<b>265</b>
<b>A</b>	<b>Multipath in the Vertical Plane</b>	<b>271</b>

# 1 Introduction

## 1.1 Main Characteristics

The performance assessment of radar systems is a complicated task because of the interaction of many subsystems and the presence of a complex environment. Knowledge and experience gained from several disciplines are necessary to complete the task successfully. All aspects of the radar-environment-target chain, illustrated in Figure 1.1, must be studied in adequate detail.

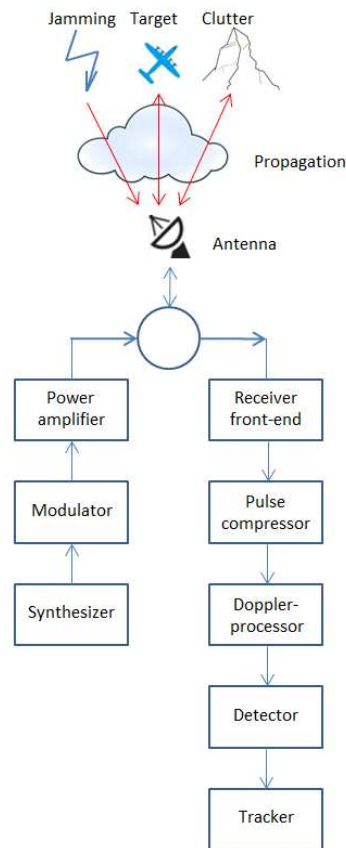


Figure 1.1: Radar-environment-target chain. The radar has been divided into several subsystems.

Because of the complexity of the task, computer support for radar system design and performance assessment is indispensable. Since its release date in 1993, the program CARPET (Computer Aided Radar Performance Evaluation Tool, [1]) provides such support. CARPET quickly became the most widely used radar performance assessment program. Its popularity

was unmistakably related to its attractive price. Also helpful was the fact that the use of CARPET was advised by IMO, the International Maritime Organization. A side-effect of the low price was, however, a lack of funds for further developments of CARPET.

TNO now comes with CARPET 3, a substantially more powerful radar performance assessment program compared to its precursors CARPET 1 (DOS) and CARPET 2 (Microsoft Windows, since 2003). While the so-called ‘base version’ of CARPET 3 is still very affordable, just like CARPET 1 and 2, CARPET 3 comes with a series of plug-ins, or extensions, which are more costly. Furthermore, the life-time of a CARPET license has been limited to a two-year period. This price strategy is intended to ‘strengthen the business case’ so that program maintenance and further developments will become more easy.

The sequel of this section provides a brief description of CARPET 3. The various plug-ins are discussed in Section 1.2 and new features of the base-version are considered in Section 1.3. The layout of this manual is discussed in Section 1.4.

## 1.2 Plug-ins

### 1.2.1 TERPEM-light

The specific plug-in that TNO considers to be most eminent is a product of Signals Science Ltd, UK: TERPEM-light. The plug-in provides a quantitative numerical model for calculating the effects of ducting and refraction in the atmosphere, which is a vast improvement compared to the EREPS-like propagation model which uses a qualitative/semi-empirical approach. Furthermore, the plug-in provides import capabilities of meteorological data, being either a refractivity N-profile, a modified refractivity profile (M-profile), WMO radiosonde code or TERMET-output. TERMET is a Signal Science product that makes available a global database of duct statistics, *i.e.*, ‘world-wide’ profiles that have been measured in different periods of the year. Thus, CARPET 3 is able to consider up-to-date meteorological conditions. Furthermore, the TERPEM-light plug-in provides ‘in situ’ radar performance assessment. CARPET 3 can be utilized to perform siting studies (Where should I place the radar? How tall must the radar be? What is the horizontal coverage against a target that follows the terrain profile at 25 m altitude?). Figure 1.2 shows an impression of this functionality. The DTED (Digital Terrain Elevation Data) information is NASA’s 3 arc second SRTM (Shuttle Radar Topography Mission) elevation data, that the user can download from [https://dds.cr.usgs.gov/srtm/version2\\_1/SRTM3](https://dds.cr.usgs.gov/srtm/version2_1/SRTM3). Since November 2021 CARPET 3 also supports 1 arc second SRTM (30 m) elevation data, which can conveniently be downloaded from <https://dwtkns.com/srtm30m/>. Please do not store SRTM1 (30 m) and SRTM3 (90 m) data in the same directory.

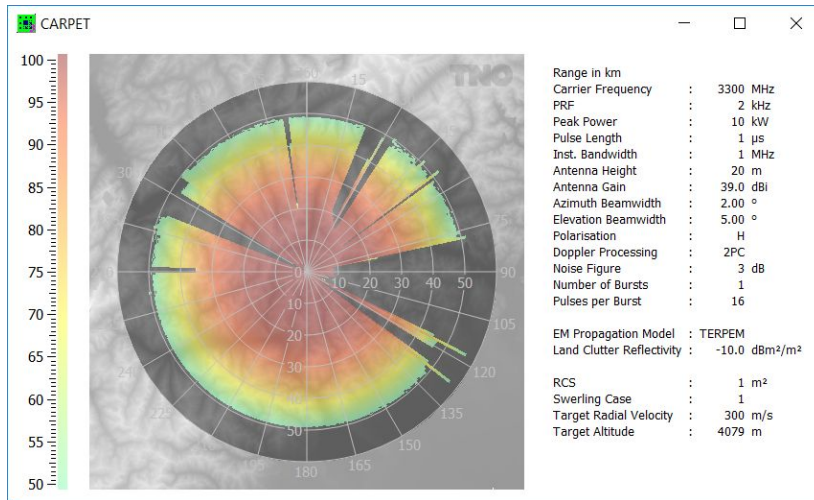


Figure 1.2: Example of the siting functionality of CARPET 3, which requires the TERPEM plug-in. The radar antenna is on a 20 m high tower, on top of Mount Matterhorn, Switzerland. The target travels at a constant altitude, 10 m above the top. The colour represents the single scan detection probability. The diagram reveals (not surprisingly) that it would be better to install the radar on top of the Monte Rosa massif, approximately 8 km east of the Matterhorn.

TERPEM is not as fast as EREPS-like, let alone free space propagation. Thus, PPI-view diagrams, such as the one presented above, take a while to calculate. To speed up the process, the processing load is distributed over the available CPU-cores. In case one wants to apply siting studies a fast multi-core CPU is therefore advised.

The suffix ‘light’ means that not all functionality of the original TERPEM program is available. The main limitations are that a single vertical refractivity profile and a single set of ground parameters (numerical, perfect conductor, wet ground, medium dry ground, very dry ground) can be specified for a path. The full TERPEM model allows these to vary with range. Also, some of the TERPEM sub-models that allow computational speed-ups for certain path geometries (such as high terminals) are not available.

The import capability of radiosonde code is illustrated in the figures 1.3 and 1.4. The top diagrams shows quantities measured by a weather balloon that was launched in the Gulf Region. These quantities appear in the so-called TTBB-part of the WMO radiosonde code. The effect that the meteorological conditions have on the detection performance of a non-coherent VTS radar is shown in the bottom-diagram. The specific meteorological conditions give rise to an elevated layer (surface duct). The ‘gap’ around 34 NM range is caused by the reception of seaclutter; since the PRF of the VTS radar is 2.4 kHz, a target beyond 33.7 NM is second-trace and its response competes with near-by sea clutter.

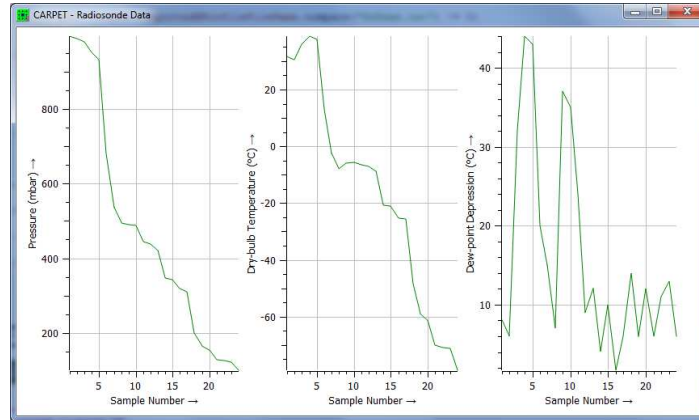


Figure 1.3: Radiosonde data, *i.e.*, pressure, dry-bulb temperature and dew-point depression, as gathered by a weather balloon.

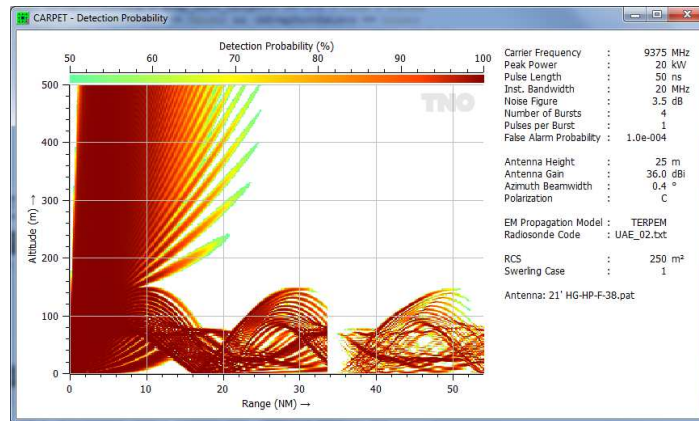


Figure 1.4: The effect of anomalous propagation to the detection performance of a non-coherent VTS radar. The gap at 34 NM is caused by near-by sea clutter.

### 1.2.2 Multi-burst

Modern radar systems apply the efficient coherent Doppler integration of multiple responses. Often, different bursts (or pulse trains) per dwell are applied, in order to eliminate blind velocities and sometimes also blind range spans; PRFs, RFs and also pulse lengths can vary (stagger) from burst to burst, long pulses are compressed on receive, short pulses are not. A widely applied processing scheme is that detection is done after Doppler integration, and that detections obtained from multiple bursts are combined using ‘post-detection  $M$ -out-of- $N$  integration’. CARPET 3 supports this scheme.

In case a modern VTS ‘solid state’ radar systems is involved or in case a radar that is designed to operate in a military domain is applied, the multi-burst plug-in is advised. Figure 1.5 shows the Transmitter dialogbox of CARPET 3. In case the multi-burst plug-in is not active, only a single line of the dialogbox can be edited. Figure 1.6 shows the received powers over range, in case two different bursts are applied.

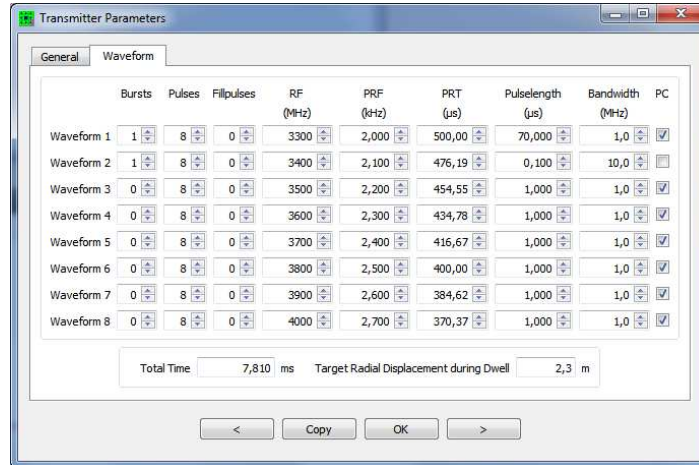


Figure 1.5: The Transmitter dialogbox in case the multi-burst plug-in is active.

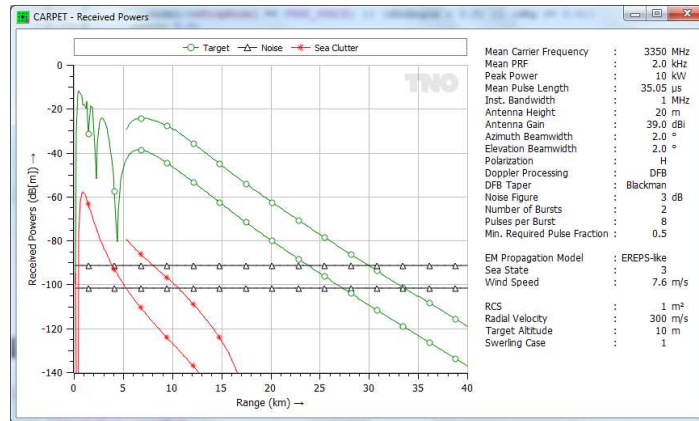


Figure 1.6: Received powers over range. There are two bursts within the dwell. A short pulse is for the detection at very short range. A long pulse (70 µs) is compressed and for the detection at long ranges.

### 1.2.3 Multi-scatterer Target

In CARPET 1 and 2 the target model was a single point target model, with the five Swerling cases. Consequently, deep multipath fades are predicted over sea with moderate sea states, which is not always realistic, *e.g.*, in case relatively large maritime surface targets (vessels) are observed. For such extended targets, CARPET 3 offers a point-cloud target model, see Figure 1.7.

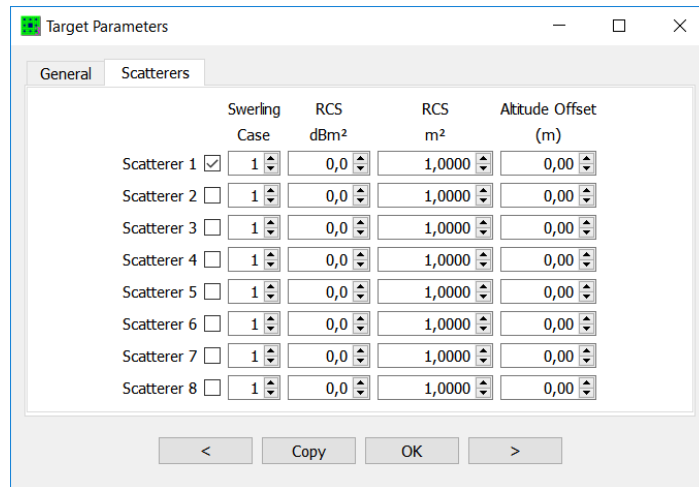


Figure 1.7: Target dialogbox in which a target made up of three point scatterers is defined. Note that for each individual point a Swerling case can be defined. In case the multi-scatterer target plug-in is not active, only this fields of the first line can be edited.

CARPET 3 contains two mechanisms to determine the detection probability of an extended target:

- Maximum detection probability  
The detection probability of each individual scatterer is determined, and subsequently the maximum of these detection probabilities is taken. Note that the Swerling case can differ from scatterer to scatterer.
- Power summation  
The powers of the individual scatterers are determined and subsequently summed, therefore assuming that the echoes from the individual scatterers are uncorrelated. The Swerling case of the dominant scatterer, *i.e.* the scatterer with highest radar cross section, is adopted for the extended target.

Results of the multi-scatterer model are shown in Figure 1.8. A more elaborate description of this features is given in Section 6.3.4.



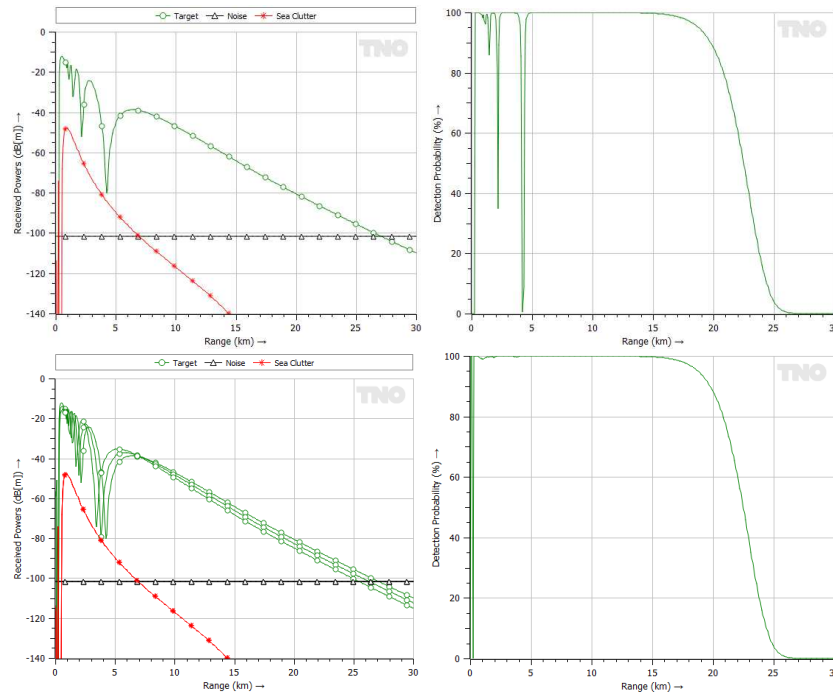


Figure 1.8: Top: Received powers and detection probability versus range, in case of a single point target. Bottom: Same diagrams, in case of a target made up of three point scatterers. The ‘Max Pd’ method has been applied.

### 1.2.4 Python Interface

Fourthly and finally, TNO offers a so-called Python plug-in that makes CARPET functionality available to Python programs. This feature serves users that wish to utilize CARPET to calculate and export numerical information that is not directly supported by the graphical user interface (GUI) of the program. Suppose you would like to have a diagram that shows firm track range (discussed in Section 3) versus sea state. The data can conveniently be gathered with the Python interface. CARPET 3 actually contains an editor in which Python programs can be developed, as shown in Figure 1.9.

Figure 1.9: The Python editor of CARPET 3.

The Python interface offers the following capabilities:

- All CARPET parameters can be set.
- All CARPET diagrams can be generated and saved.
- Numerical data of all diagrams can be saved.
- Numerical data of all diagrams can be imported in the Python program.
- CARPET settings can be read from file.
- CARPET settings can be saved to file.

### 1.3 New Features of the Base-version

#### 1.3.1 Backwards Compatible

CARPET 3 can read CARPET 2 settings files. CARPET 3 writes settings files in an encrypted format.

### 1.3.2 GUI, Graphics, Operating Systems

The GUI (Graphical User Interface) and the graphics have been modified. By utilizing Qt and Qwt<sup>1</sup>, the program is now also available for non-Microsoft Windows platforms, like Linux and MacOS. Furthermore, CARPET 3 is much more convenient to operate than the previous versions and extra features are offered, such as polar antenna diagrams and zoom-in capability.

### 1.3.3 Firm Track Probability

TNO has replaced the cumulative detection diagram of CARPET 1 and 2 by firm track probability,  $P_{ft}$ , diagrams. Having  $P_{ft}$  diagrams is important, since many modern radar systems provide plots (target reports) that associate with local tracks. TNO has implemented Richard Worsham's procedure to determine firm track probability, [2]. A Tracking dialogbox has been added to the GUI, as shown in Figure 1.10. Figure 1.11 shows firm track probability over target range. The single dwell detection probability is depicted in the diagram as well.

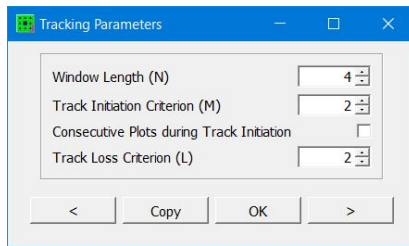


Figure 1.10: The Tracking dialogbox of CARPET 3.

<sup>1</sup>See <https://www.qt.io>, <https://qwt.sourceforge.net/>

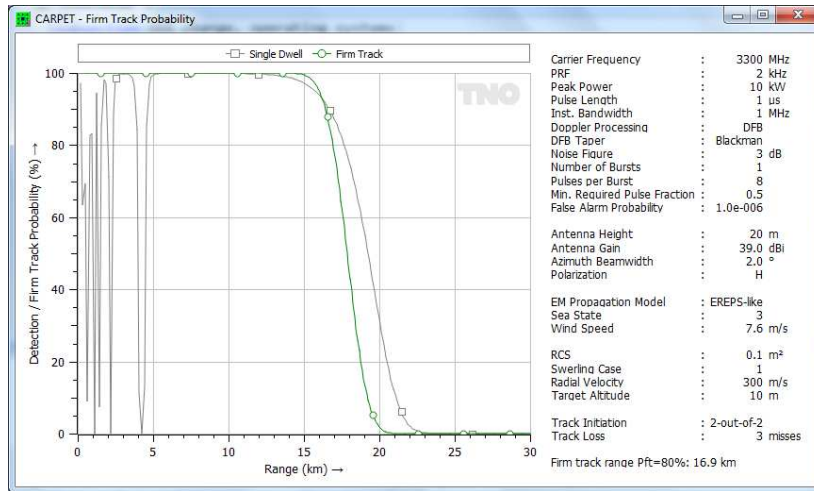


Figure 1.11: Firm Track Probability diagram.

### 1.3.4 PPI-view Diagrams

Figure 1.2 is an example of a PPI-view diagram. It is a polar diagram, the target altitude behaviour is either ‘terrain following’ or ‘fixed altitude’. This addition led to the necessity to specify the shape of volume clutter (rain or chaff) more precisely. Rather than specifying a start and stop range (in CARPET 2), the user now has the ability to specify the range to the center of the volume clutter, its diameter and its azimuth angle. Figure 1.12 shows how rain affects the radar coverage of an X-band radar, in a PPI-view diagram.

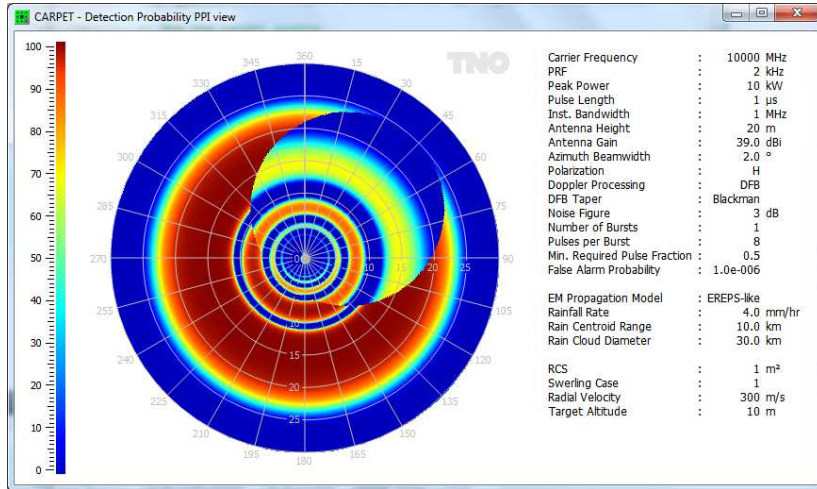


Figure 1.12: The influence of a rain cloud to the detection performance of an X-band radar is shown. The diameter of the rain cloud is 24 km.

### 1.3.5 Separate Transmit and Receive Antenna

These two antennas do not have to be identical. Apart from built-in antenna elevation patterns, one can also import antenna patterns.

### 1.3.6 More Jammers

The number of jammers has been increased to four, the bearing angles, ranges and altitudes of the jammers need to be specified, see Figure 1.13 and Figure 1.14.

The screenshot shows the 'Jamming Parameters' dialog box. It contains a table with columns for Mode, Power (dBW and kW), Ant. Gain (dBi), Bbarrage (MHz), Responsive (MHz), Range (km), Altitude (m), Bearing ( $^{\circ}$ ), and Free Space. There are four rows for Jammer 1 through Jammer 4. Each jammer is currently set to 'Off' mode. The parameters for each jammer are: Power (40.0 dBW, 10,000 kW), Ant. Gain (12.0 dBi), Bbarrage (600 MHz), Responsive (10.0 MHz), Range (200 km), Altitude (3000 m), and Bearing (0, 10, 20, and 30 degrees respectively). There are checkboxes for 'Free Space' which are all checked. Navigation buttons '<', 'Copy', 'OK', and '>' are at the bottom.

	Mode	Power dBW	Power kW	Ant. Gain dBi	Bbarrage MHz	Responsive MHz	Range km	Altitude m	Bearing $^{\circ}$	Free Space
Jammer 1	Off	40,0	10,000	12,0	600	10,0	200	3000	0	<input checked="" type="checkbox"/>
Jammer 2	Off	40,0	10,000	12,0	600	10,0	200	3000	10	<input checked="" type="checkbox"/>
Jammer 3	Off	40,0	10,000	12,0	600	10,0	200	3000	20	<input checked="" type="checkbox"/>
Jammer 4	Off	40,0	10,000	12,0	600	10,0	200	3000	30	<input checked="" type="checkbox"/>

Figure 1.13: Jamming dialogbox of CARPET 3.

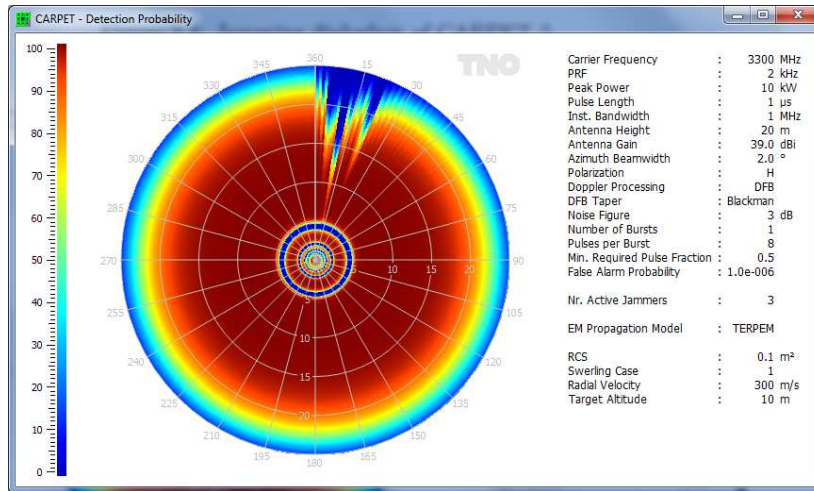


Figure 1.14: The effect of three stand-off jammers (at bearings 5, 10 and 20°) on a radar's horizontal coverage.

### 1.3.7 Pulse Eclipsing

A radar receiver is protected during the time intervals that pulses are transmitted. Modern radar systems are often able to process partially eclipsed pulses. CARPET 3 models pulse eclipsing, the user has to specify a minimum required pulse fraction.

### 1.3.8 Loss Factors

Whereas CARPET 1 and 2 came with limited number of loss factors, CARPET 3 offers a more detailed specification, as shown in Figure 1.15.

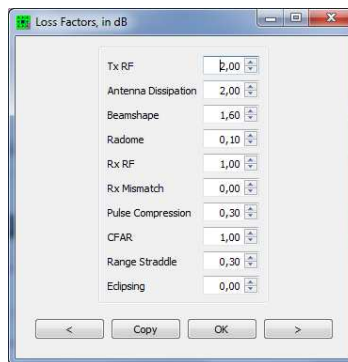


Figure 1.15: The Loss Factors dialogbox of CARPET 3.

### 1.3.9 Blake Chart

The classical Blake chart has been added, as a worksheet, see Figure 1.16.

	1. Detectability	2. System Noise	3. Propagation	4. Losses	5. Range Factors
Power	10,0 kW		40,0 dBW		40,0 dBW
Pulse Length (uncompressed)	1,0 μs				-60,0 dBs
Gain Transmit Antenna	39,0 dBi				39,0 dBi
Gain Receive Antenna	39,0 dBi				39,0 dBi
Target RCS	1,000 m <sup>2</sup>		0,0 dBm <sup>2</sup>		0,0 dBm <sup>2</sup>
Wavelength Squared	0,0083 m <sup>2</sup>				-20,8 dBm <sup>2</sup>
1: Required Single Pulse SNR					-17,9 dB
2: System Noise Temperature	634,0 K				-28,0 dBK
4: Losses					-5,5 dB
Range Equation Constant					195,6 dB/K
Column Total					192,4 dB
Free Space Range			34,8 NM		64,5 km
Free Space Range times PPF			34,8 NM		64,5 km
Range, First Approximation			33,9 NM		62,7 km
Range, Second Approximation			33,9 NM		62,7 km

Figure 1.16: Blake chart worksheet of CARPET 3.

## 1.4 Document Layout

This manual is ‘new’ it doesn’t require the manual of CARPET 2, [1]. There is, however, a substantial overlap with the CARPET 2 manual. In Chapter 2 the computer system requirements and matters related to the installation and use of CARPET are discussed. In Chapter 3 the meaning of the ‘settings’, *i.e.*, the many model parameters is explained. In Chapter 4 the so-called Worksheets are discussed, and in Section 5 the graphical output. The various models that CARPET uses are described in Section 6. Abbreviations are clarified in Chapter 7 and finally the references are given.

## 1.5 Future Developments

The release of CARPET 3 represents a significant upgrade. Equipped with the multi-burst plug-in, CARPET 3 is fit to model modern solid-state radar systems. The inclusion of TERPEM brought together expertise areas of two different groups (Signal Science’s EM propagation modeling, TNO’s radar system modeling). As a result, the EM propagation modeling has improved significantly, in-situ radar performance assessment is offered and

CARPET 3 can consider imported radiosonde data. In case the capabilities that the GUI offers are considered to be insufficient, the Python plug-in offers additional flexibility.

The developers of CARPET 3 are aware of items still on the wish-list, such as modeling of STC (sensitivity time control), multi-beam radar, FMCW waveforms, multi-radar coverage, additional DTED formats, TERPEM-‘heavy’ and importable Doppler filter coefficients. TNO has changed the pricing strategy to ease the implementation of future upgrades. Requests to customize the program are more than welcome; please send your comments and suggestions to [carpet@tno.nl](mailto:carpet@tno.nl).

## 1.6 Acknowledgment

The authors of CARPET and of this manual are grateful to the TNO management that supplied funds to develop CARPET 3. Furthermore, we thank the developers of Qt, Qwt, QwtPolar, QtCreator, CMake, CPack, NSIS, of freeware C++ compilers (MinGW, g++) and of L<sup>A</sup>T<sub>E</sub>X. We are obviously also grateful to the many authors of excellent ‘radar literature’ see Figure 1.17. Special thanks goes to our colleague and IT-expert Johan van de Pol and to Ken Craig of Signal Science. Paul Kimmel and Frans Annema also deserve to be mentioned, these gentlemen contributed to CARPET 1 and 2, respectively. And of course Michael Polushkin who set-up the CI/CD pipeline. And of course Jeroen Boschma, who implemented the unit-test-bed. And of course many others who gave valuable suggestions.



Figure 1.17: Radar literature.



## 2 How to Operate CARPET

### 2.1 System Requirements

CARPET runs on x86 and x64 Intel architectures, under Microsoft Windows 7, 8, 10. At least 4 Gbytes of RAM is advised. Since January 2022 a MacOS version is also obtainable. A native Apple M1-version of CARPET 3 is, however, not yet available so that the so-called Rosetta2 layer is required to run CARPET 3 on Apple silicon. TNO intends to support an M1-version when M1-versions of Python and Qt-libraries become available. In case you want CARPET 3 under MacOS or under Linux, please email this request to [carpet@tno.nl](mailto:carpet@tno.nl). Having multiple processor cores will especially be useful when the TERPEM plug-in is used, since CARPET distributes TERPEM calculations over processor cores.

### 2.2 Ordering

Open an Internet browser, go to <https://www.tno.nl/carpnet> and fill in the CARPET 3 order form. Here you can indicate the plug-ins that you want. Submit the order form. Installation instructions, the invoice and payment instructions will be e-mailed to you.

### 2.3 Installation

On the Microsoft Windows operating system, an NSIS (Nullsoft Scriptable Install System) install script will install CARPET 3. The Windows program CARPET3.exe is a 64-bit executable that requires a series of DLLs, as shown in Figure 2.1. Several 3 arc second SRTM (90 m) files and the ERA-15 data files will also be installed.

File Name	Date/Time	Type	Size
platforms	5-10-2016 9:20	File folder	
CARPET3.exe	5-10-2016 9:16	Application	5.290 KB
libgcc_s_dw2-1.dll	21-12-2014 17:07	Application extension	118 KB
libstdc++-6.dll	21-12-2014 17:07	Application extension	1.003 KB
libwinpthread-1.dll	21-12-2014 17:07	Application extension	48 KB
python3.dll	6-12-2015 0:39	Application extension	51 KB
python35.dll	6-12-2015 0:39	Application extension	3.050 KB
python35.zip	1-8-2016 11:35	Compressed (zipped) Folder	34.074 KB
Qt5Core.dll	29-3-2016 13:01	Application extension	5.265 KB
Qt5Gui.dll	12-10-2015 21:31	Application extension	5.210 KB
Qt5Network.dll	12-10-2015 21:26	Application extension	1.493 KB
Qt5OpenGL.dll	12-10-2015 21:42	Application extension	327 KB
Qt5PrintSupport.dll	12-10-2015 21:42	Application extension	350 KB
Qt5Svg.dll	12-10-2015 21:48	Application extension	324 KB
Qt5Widgets.dll	12-10-2015 21:37	Application extension	6.389 KB
vcruntime140.dll	25-6-2015 23:34	Application extension	84 KB
N44E005.hgt	29-3-2016 13:23	HGT File	2.818 KB
N44E006.hgt	29-3-2016 13:23	HGT File	2.818 KB
N44E007.hgt	29-3-2016 13:23	HGT File	2.818 KB
N44E008.hgt	29-3-2016 13:23	HGT File	2.818 KB
N44E009.hgt	29-3-2016 13:23	HGT File	2.818 KB
N45E005.hgt	29-3-2016 13:23	HGT File	2.818 KB
N45E006.hgt	29-3-2016 13:23	HGT File	2.818 KB
N45E007.hgt	29-3-2016 13:23	HGT File	2.818 KB
N45E008.hgt	29-3-2016 13:23	HGT File	2.818 KB
N45E009.hgt	29-3-2016 13:23	HGT File	2.818 KB
N46E005.hgt	29-3-2016 13:23	HGT File	2.818 KB

Figure 2.1: Program and a part of the SRTM3 (90 m) files.

On the MacOS operating system, a so-called DRM file must be executed. This results in the CARPET 3 application and a few directories, as shown in Figure 2.1. It is advised that the user moves the srtm3 and era-15 directories, which are in fact only relevant if you

have a TERPEM license. *E.g.* create a sub-directory ‘data’ or ‘carpet/data’ under the home directory ( $\$(user)$ ) and move them there. CARPET needs to know, however, where these directories are, which you can specify under File – Select Directory. The lib directory can be removed. The CARPET 3 executable can be moved to the Applications directory.

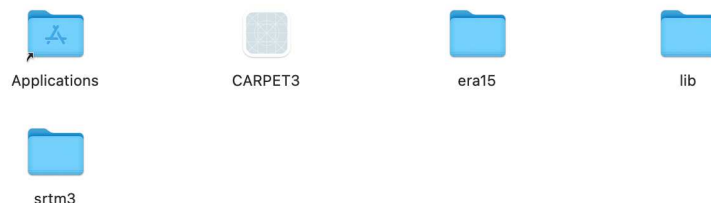


Figure 2.2: File and directories after execution of the DRM program.

The main window of CARPET 3 is shown in Figure 2.3. Operating the program is straightforward. Dialogboxes are available under ‘Parameters’ and also under a series of buttons.

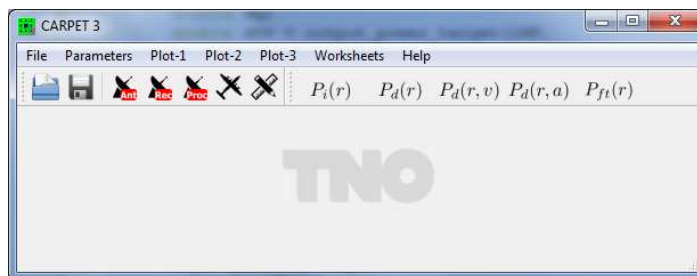


Figure 2.3: The main window of CARPET 3 (Windows version).

## 2.4 License File Procedure

When you run CARPET for the first time, a license file is created named `carpet3.lcs`, see Figure 2.4. E-mail this file to `carpet@tno.nl` and we will return a valid file. Please copy the returned file to your hard disk, overwriting the old one. CARPET should then behave as you wish. If not: communicate this to `carpet@tno.nl`. Please do not forget that licenses are time-limited. The expiry dates can be viewed in the Help - About CARPET box, see Figure 2.5.

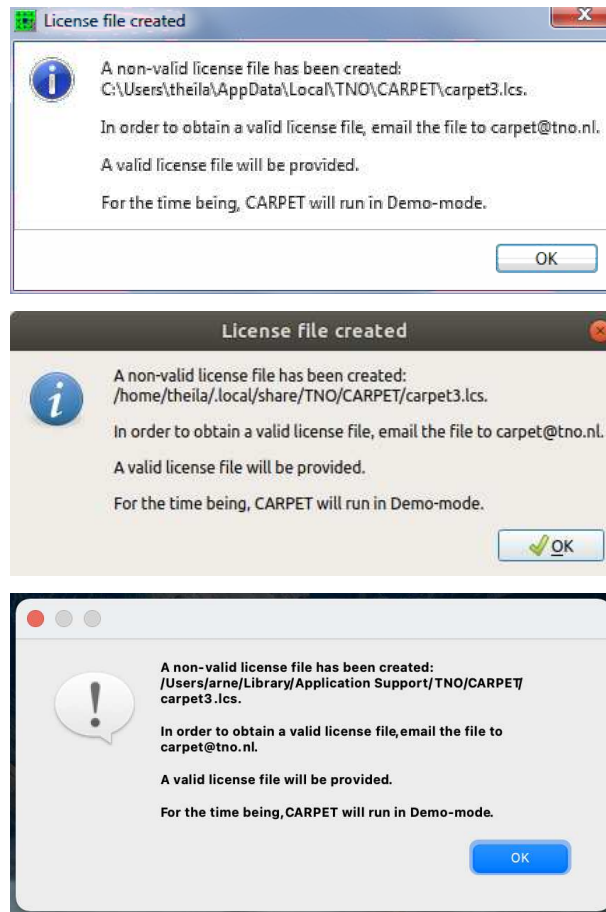


Figure 2.4: Alertboxes notifying that a license file has been created. Top: Microsoft Windows. Middle: Gnome desktop, Linux. Bottom: MacOS.

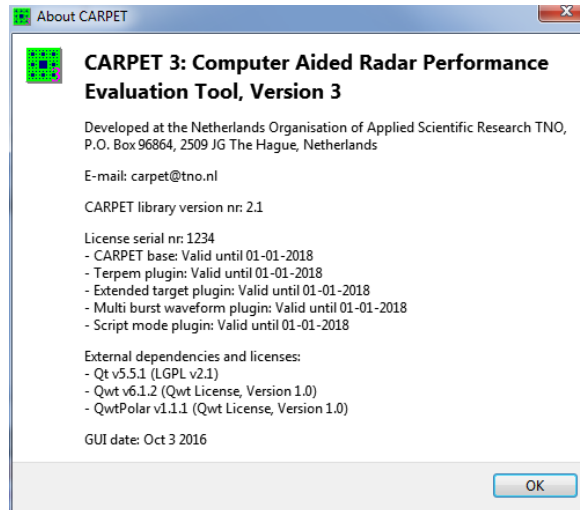


Figure 2.5: The Help - About CARPET info-box, showing expiry dates.

## 2.5 Making Hardcopies

Diagrams can directly be printed by right-clicking (on) a diagram and selecting Print Image...

## 2.6 Saving Diagrams

Diagrams can be saved by right-clicking a diagram and selecting Export Image. Note that CARPET proposes a specific file name, that contains the date and time, as shown in Figure 2.6. In case of a so-called spectrogram plot, the first line in the output file contains the values along the horizontal axis. Subsequently, the values along horizontal lines are written, preceded by the value along the vertical axis.

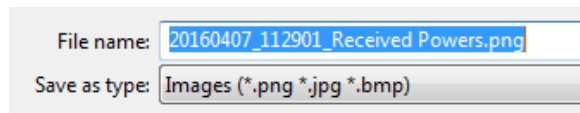


Figure 2.6: Proposed file name when saving a graph.

## 2.7 Loading Settings Files

Select one of the following:

- CARPET 3 Settings: Select File - Load
- CARPET 2 Settings: Select File - Import - Load CARPET 2 Settings

## 2.8 Saving Settings Files

Select either File - Save or File - Save As. Settings of CARPET 3 are not in readable format.

Relatively young CARPET users may not recognize the File - Save icon, depicted in Figure 2.7. It is an image of a 3.5 inch (micro) diskette, a computer storage device that could hold up to 1.44 Mbyte. Incidentally, in the old days we also had so-called floppy disks, which were (physically) larger. A picture of an 8 inch floppy disk is shown in Figure 2.7 as well.

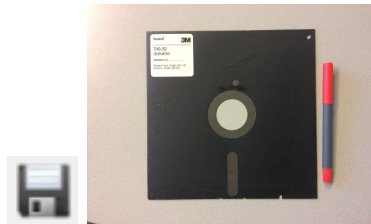


Figure 2.7: Left: File - Save icon, *i.e.*, a drawing of a 3.5 inch diskette. Right: An 8 inch floppy disk.

## 2.9 Select Directory

In case you have the TERPEM plug-in, you can position a radar in a landscape and you can investigate (for instance) if the radar coverage is affected by the terrain profile, as shown in Figure 1.2. For this to work, CARPET needs to know where it can locate the terrain altitude data (DEM data), which is either in the 1 arc second SRTM format (30 m) or in the 3 arc second SRTM format (90 m). The filename extension of these files is `.hgt`. The size of an 1 arc second SRTM file is 25,934,402 byte (24.7 Mbyte). The size of a 3 arc second SRTM file is 2,884,802 bytes byte (2.75 Mbyte).<sup>2</sup>

From January 2022 on, CARPET supports refractivity profiles that are derived from the so-called ERA-15 meteorological dataset. This functionality is, again, only supported in case of a valid TERPEM license. CARPET needs to know where it can locate the ERA-15 data.

Figure 2.8 shows the sub-pulldown menu with which the directories (or folder) can be selected.

<sup>2</sup>SRTM3 (90 m) ‘tiles’ can be downloaded from [https://dds.cr.usgs.gov/srtm/version2\\_1/SRTM3/](https://dds.cr.usgs.gov/srtm/version2_1/SRTM3/) , from <http://firmware.ardupilot.org/SRTM/> and from <https://bailu.ch> (*e.g.* <https://bailu/dem3/N48>). SRTM1 (30 m) elevation data can for instance be downloaded from <https://dwtkns.com/srtm30m/>, which requires, however, registration at NASA EARTHDATA, <https://urs.earthdata.nasa.gov>. Alternatively, <https://e4ftl01.cr.usgs.gov/> might be consulted.

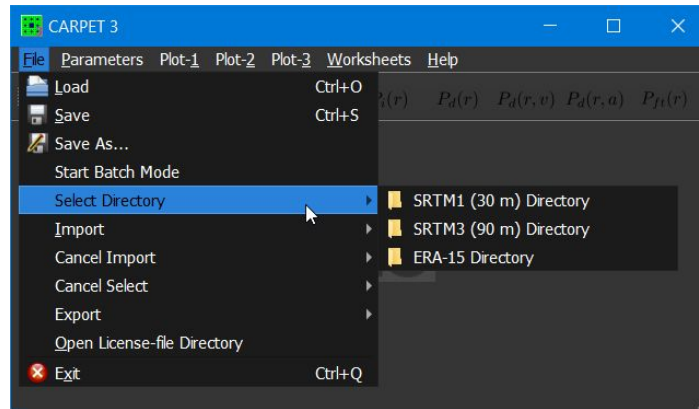


Figure 2.8: Sub-pull-down menu to specify the locations of certain directories.

## 2.10 Import

The Import sub-pull-down-list is depicted in Figure 2.9. The entries ‘Radiosonde Code’, ‘TERMET Data’, ‘Refractivity N Profile’ and ‘Refractivity M Profile’ are enabled if the TERPEM plug-in is active.

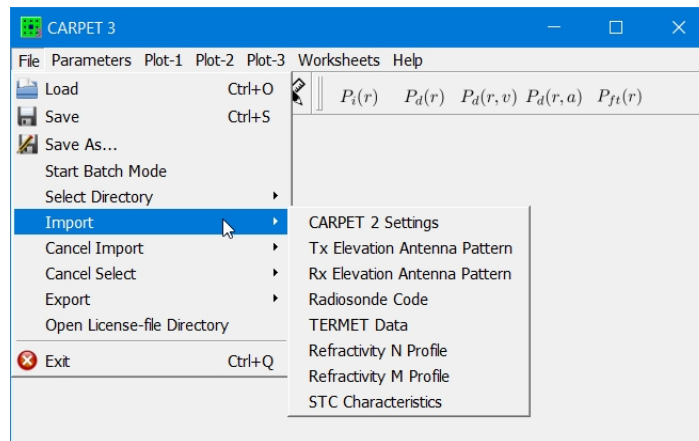


Figure 2.9: The Import sub-pull-down-list.

### 2.10.1 CARPET 2 Settings

CARPET version 3 can import settings that have been saved with CARPET version 2. CARPET 3 can not save settings in CARPET 2 format.

### 2.10.2 Elevation Antenna Pattern

CARPET 3 can import antenna elevation patterns on transmit as well as on receive via File - Import - Tx Antenna Pattern and File - Import - Rx Antenna Pattern. The program expects an ASCII file containing a series of lines. Each line has two numbers. The first number represents an elevation angle in degrees. The second number represents the antenna's power gain in dB at the aforementioned elevation angle. This gain factor can represent the gain relative to the gain of an isotropic radiator, in dBi, but an other reference level (*e.g.*, 0 dB gain at antenna boresight) is also possible.<sup>3</sup> The CARPET user must realize that the antenna power gain at boresight is specified in the Antenna dialogbox of the GUI, see Section 3.11.

A second topic of caution is the so-called elevation tilt angle. Radar antennas may have a facility to adjust the mechanical tilt angle and a tilting indicator that shows this angle, see Figure 2.10. The user can specify the tilt angle in the Antenna dialogbox. It is, however, also possible that the imported antenna pattern is 'tilt adjusted', in which case the tilt angle in the Antenna dialogbox must be set to zero degrees.



Figure 2.10: A tilting indicator on the antenna of an ATC radar.

An example of a two-column antenna-file is as follows:

<sup>3</sup>An antenna gain of 12 dBi in a specific direction means that the antenna radiates 12 dB more in that specific direction when compared to an isotropic radiator, *i.e.*, a source that radiates equally in all spatial directions, like the sun. 12 dB is equal to a factor of 15.8 ( $10^{12/10}$ ).

```

-18 -9.8
-16 -8.0
-14 -7.2
-12 -7.3
-10 -7.2
-8 -5.6
-6 -3.4
-4 -1.6
-2 -0.7
0 -0.1
2 0.0
4 -0.4
6 -0.9
8 -2.2
10 -4.0
12 -6.0
14 -8.2
16 -10.0
18 -11.3
20 -12.7
22 -14.9
24 -17.4
26 -19.6
28 -21.5
30 -23.4

```

The shape of the imported antenna pattern can be verified via Plot-3 - Antenna Pattern.

### 2.10.3 Radiosonde Code

In case the TERPEM plug-in has been purchased, CARPET 3 enables the import of upper-air meteorological data that have been measured by a weather balloon. This so called radiosonde code comes in a specific format, see for instance [3]. An example of file containing radiosonde code is as follows:

```

TTAA 73001 41217 99995 31858 02009 00515 // // 92693 37493 09515 85457
31686 07516 70147 15472 07011 50588 07358 35521 40762 11960 12013 30975 27547
12018 25103 37559 12022 20254 48364 12530 15437 62762 13554 10676 78956 09048
88999 77136 13559 42435 31313 44108 82304
TTBB 73008 41217 00995 31858 11989 30656 22979 36082 33952 38894 44932 37893
55680 13270 66535 02565 77494 07957 88489 05987 99487 05785 11444 06574 22438
07159 33420 08762 44346 20941 55342 21160 66318 25317 77310 25756 88199 48364
99166 58956 11154 61362 22129 70156 33125 70961 44121 71363 55100 78956 21212
00995 02009 11977 04019 22931 09514 33831 06515 44742 05515 55695 07010 66663
04509 77617 03016 88575 03023 99557 03023 11511 35521 22462 02512 33425 11010
44381 14016 55353 10511 66342 07510 77326 10506 88318 12510 99289 11519 11255
12017 22225 12539 33192 12023 44184 11025 55167 12527 66150 13554 77136 13559
88126 13554 99112 09534 11109 08536 22100 09048 31313 44108 82304 41414 00900

```

The CARPET user can inspect the content of an imported radiosonde file via Plot-Prop - Radiosonde Data, as shown in Figure 1.3. Please be aware that a weather balloon launch height needs to be specified, which can be done in the TERPEM Propagation dialogbox, shown in Section 3.3.3.

For the retrieval of radiosonde data, one may consult the Integrated Global Radiosonde Archive (IGRA).<sup>4</sup> CARPET 3 cannot (yet) import IGRA data files so that the user has to

<sup>4</sup><https://www.ncdc.noaa.gov/data-access/weather-balloon/integrated-global-radiosonde-archive>



convert the content of an IGRA data file to either an N or an M-profile, making use of the equations 6.2 and 6.4.

#### 2.10.4 TERMET Output

TERMET is a Signal Science product that accesses a global database of duct statistics and that constructs refractivity profile from meteo balloon ascents, see [4]. TERMET output can directly be imported in CARPET 3 (provided the TERPEM plug-in is active).

#### 2.10.5 Refractivity Data, N-profile, M-profile

In case the TERPEM plug-in has been purchased, CARPET enables the import of a refractivity profile (N-profile), a modified refractivity profile (M-profile) and a TERMET output file, which contains an M-profile. The (modified) refractivity profile characterises the way EM radiation propagates through the atmosphere. The relationship between  $M$  (M-unit) and  $N$  (N-unit) is given by equation 6.4.

The data files containing an N- or an M-profile must be in a two-column format, like:

0.001	459.297
0.002	455.057
0.005	449.457
0.01	445.237
0.02	441.037
0.05	435.577
0.1	431.587
0.21	427.587
0.46	423.827
1	420.777
1.5	419.497
2.1	418.597
3.2	417.687
4.6	417.087
6.8	416.657
10	416.457
16.935	416.613
23	415.731
234.7	384.931
443.9	400.471
644.29	416.471
761.8	400.471
1023	422.811
1523	468.961
2023	519.101
2523	572.741
3023	629.451
4000	757.713
7000	1169.932
10000	1602.323
20000	3116.627
50000	7808.696

#### 2.10.6 STC Characteristics

Sensitivity Time Control (STC) is commonly applied in radar systems in order to compress the dynamic range of the received signal, the number of bits required for AD-conversion. Since May 2022, CARPET 3 supports STC. Since there are numerous ways to implement STC, a

generic approach has been followed, in which STC characteristics are passed to CARPET 3 using a file interface. An ‘STC-file’ contains the receiver gain as well as the receiver noise figure for a series of time instances. If a CARPET 3 user imports a specific STC-file (via option File - Import - STC Characteristics), the noise figure that is specified in the Receiver Dialogbox is not used in the calculations.

CARPET 3 expects STC-files to be in ASCII format. Each line must contain three numbers, spacing separated, which are interpreted as ‘real’ (or floating point) numbers. The first numeral denotes a time instance since the moment that beginning of the pulse leaves the antenna, in s. The second and the third numerals denote receiver gain and noise figure respectively, in linear notation. Thus, a suppression of 20 dB should be specified as 0.01. An example of an STC-file for a stepped-gain STC is as follows:

```
0.0 0.001 8.45098
1.3343e-5 0.001 8.45098
1.3343e-5 0.01 3.1428
4.0028e-5 0.01 3.1428
4.0028e-5 0.1 2.23872
5.5e-005 0.1 2.23872
5.5e-005 1.0 1.99526
```

The corresponding STC response is depicted in Figure 2.11. (Note that such diagrams can be made with CARPET 3, via Plot 3 - STC Characteristics.) The effect of this STC on the Received Powers and Vertical Coverage diagrams is illustrated in Figure 2.12.

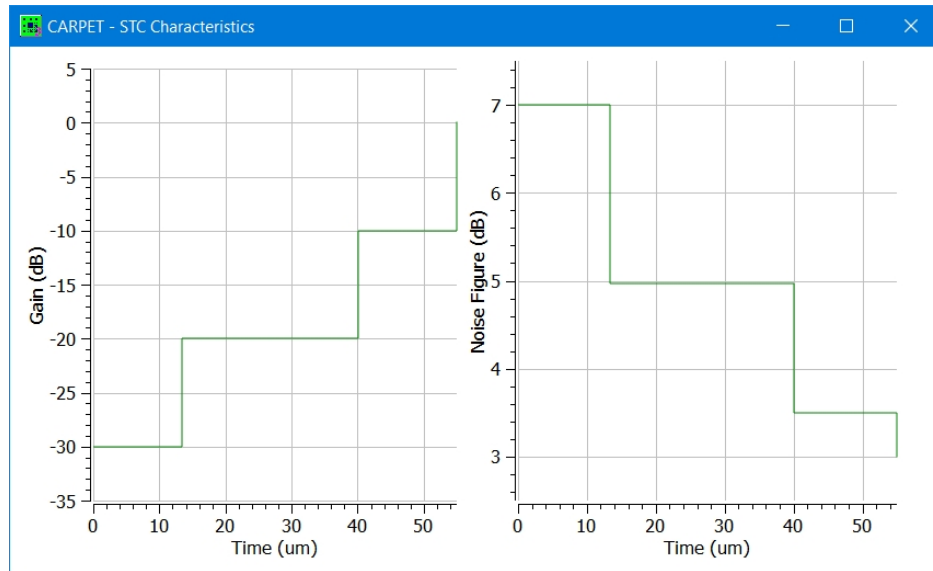


Figure 2.11: Example of STC characteristics; gain and noise figure over time.

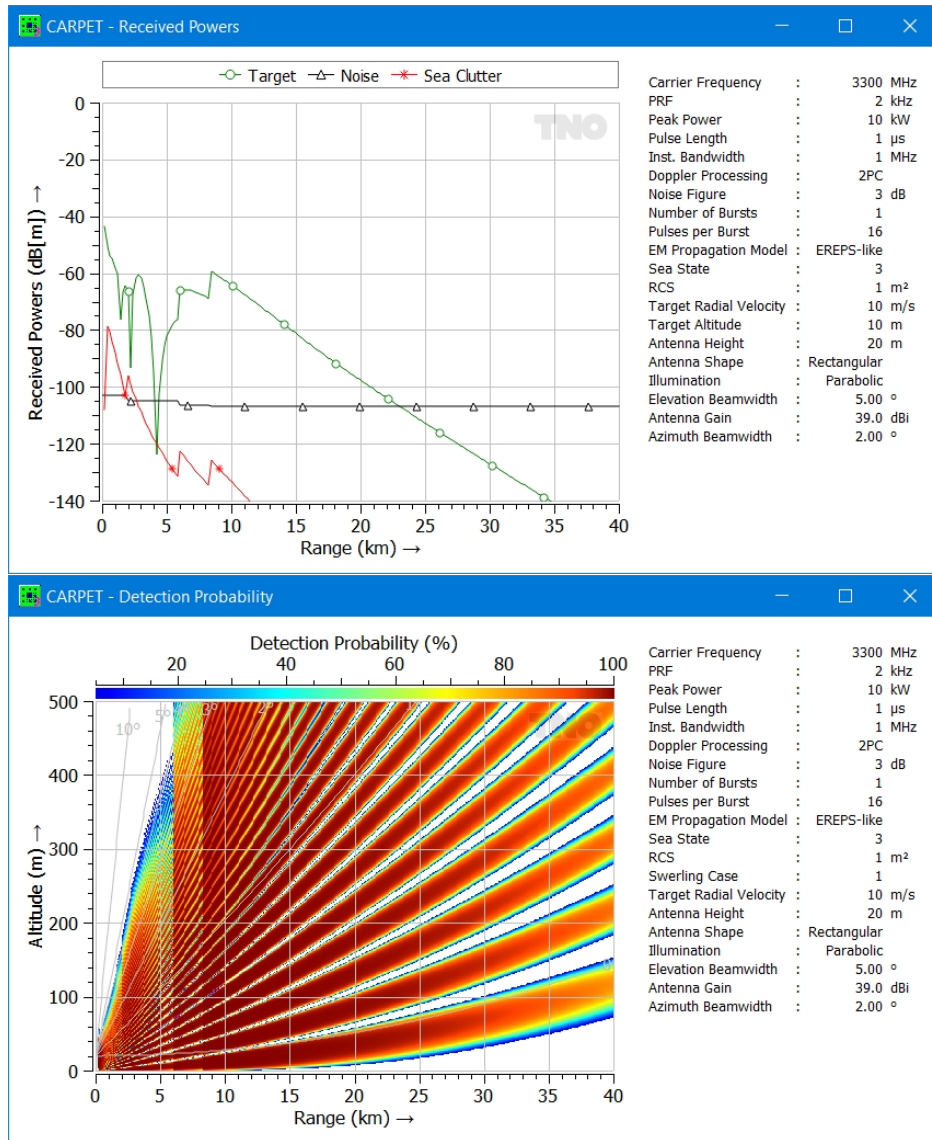


Figure 2.12: Illustration of the effect of STC.

CARPET also supports swept-gain STC in which case no identical time-instances occur in the STC-file. Linear interpolation is applied to obtain gain and noise figure values in between two specified time-instances.

Expressions for overall gain and noise figure for several architectures are presented in Section 6.11.

## 2.11 Cancel Import

Imported quantities (antenna pattern(s), radiosonde code, refractivity profile, STC characteristics) can be canceled (or ‘unimported’), see Figure 2.13.

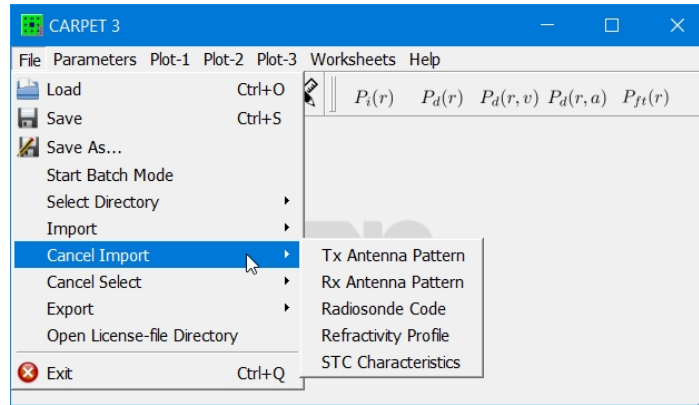


Figure 2.13: The Cancel Import sub-pull-down-list.

## 2.12 Export

The Export sub-pull-down-list is depicted in Figure 2.14. Antenna pattern files can be exported, the output is a two-column ASCII file of gain versus elevation angle. Since January 2022 the refractivity M-profile can also be exported (provided that one has a TERPEM license).

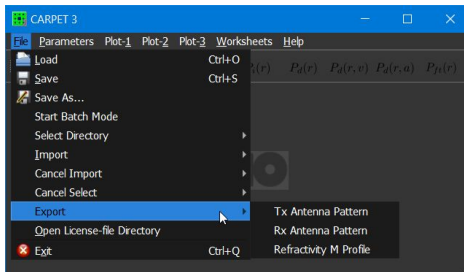


Figure 2.14: The Export sub-pull-down-list.

## 3 The Parameters

### 3.1 Introduction

This section contains a catalogue of the parameters. The parameters come with a brief explanatory note to expand the terse descriptions that appear in the dialogboxes. For each parameter, a reference is made to one or several paragraphs in section 6, where the role of the parameters in the various models is discussed. The corresponding symbol in the equations is presented as well. Figure 3.1 shows how the subsystems of a radar system, the target and ‘external’ phenomena (propagation, jamming, clutter) are described in CARPET dialogboxes.

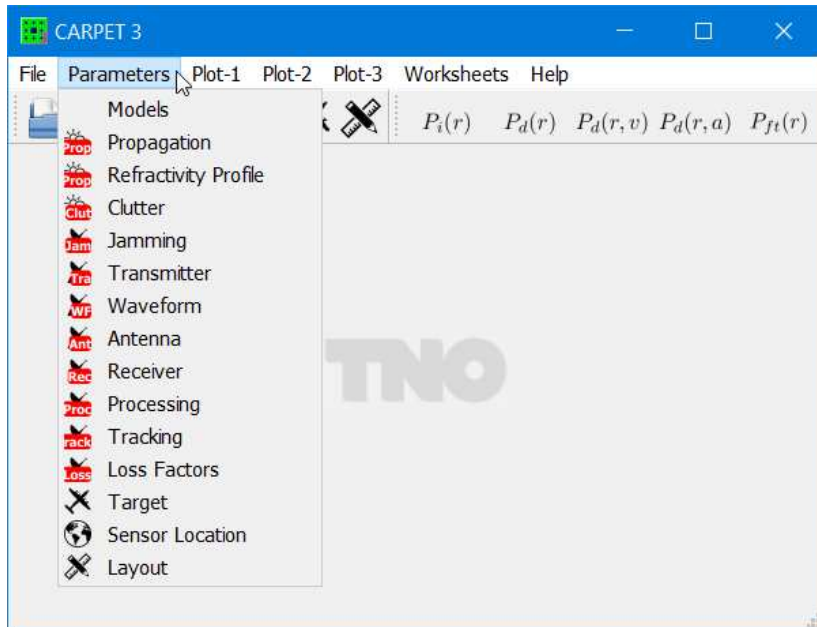


Figure 3.1: Overview of the CARPET dialogboxes.

### 3.2 Model

The Model dialogbox, shown in Figure 3.2, contains four entries.

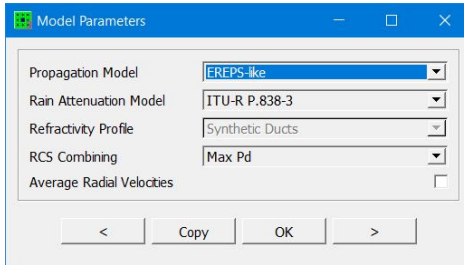


Figure 3.2: The Model dialogbox of CARPET 3.

#### **Propagation Model** — Section 6.1.1

In case the TERPEM plug-in is active, the user can switch between free space, EREPS-like and TERPEM-light. In case the TERPEM plug-in is not active, the user can switch between free space and EREPS-like.

#### **Rain Attenuation Model** — Section 6.1.9

Either the old CCIR model or the modern ITU-R model can be chosen.

#### **Refractivity Profile** — Section 6.1.1

In case the TERPEM plug-in is active, the user can switch between Synthetic Duct, ITU-R P.835 Annex 2 Section 2-4, and ITU-R P.835 Annex 3.

#### **RCS Combining** — Sections 1.2.3 and 6.3.4

In case the multi-scatterer target plug-in is active, one can choose between Maximum Detection Probability ('Max Pd') and Power Summation.

#### **Average Radial Velocities**

In case this checkbox is enabled, CARPET calculates detection probabilities for a series of radial velocities. which are subsequently averaged. The velocity interval and the number of steps can be specified in the Layout dialogbox. The relevance of this option is shown in Figure 3.3.

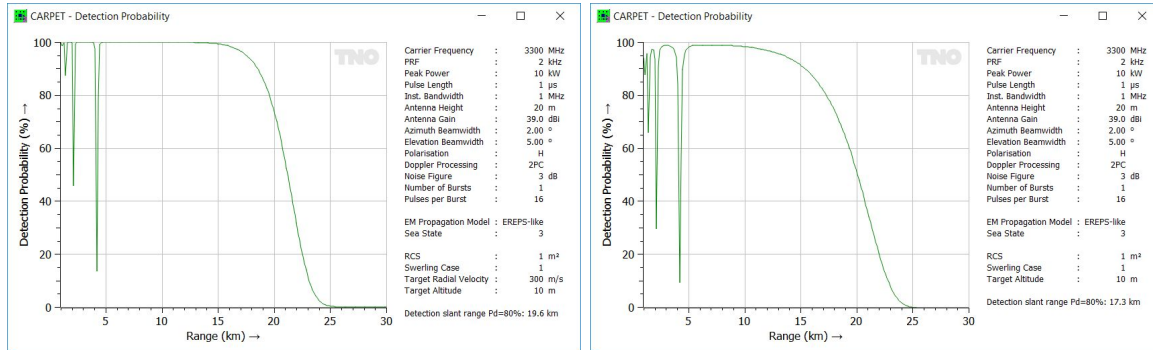


Figure 3.3: The effect of velocity averaging on  $P_d$  over range diagrams. In this case the Doppler filtering consists of a two-pulse canceler. Left: no velocity averaging. Right: radial speed is averaged from 0 to 300 m/s.

### 3.3 Propagation

CARPET 3 has different Propagation dialogboxes; one for the free space propagation model, one for the EREPS-like propagation model and one for the TERPEM-light propagation model. In case TERPEM-light has been selected, a Refractivity Profile dialogbox is also available. In CARPET 3, the modeling of anomalous (ducting) propagation phenomena requires the TERPEM-light plug-in, ducting functionality has been removed from the EREPS-like model.

#### 3.3.1 Free Space

The propagation dialogbox in case free space propagation has been selected is shown in Figure 3.4.

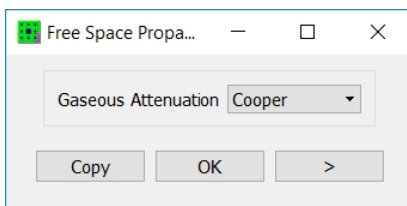


Figure 3.4: The propagation dialogbox when free space propagation has been selected.

#### **Gaseous Attenuation** — Section 6.1.6

When activated the absorption of the EM-wave in the atmosphere, by oxygen and water vapour molecules, is being considered. CARPET 3 uses either the Cooper-model or the ITU-R P.676 model for this purpose, see [5], [50]. The Cooper model is valid for frequencies from 1 to 10 GHz. If the RF is higher than 10 GHz, atmospheric absorption is calculated for 10 GHz, which can be too optimistic. If the RF is less than 1 GHz, atmospheric absorption is neglected. It is advised that the ITU-R P.676 model is used for these higher and lower frequencies.

Default value: Cooper model. Other values: Off, ITU-R P.676.

#### 3.3.2 EREPS-like

The EREPS-like dialogbox is shown in Figure 3.5.



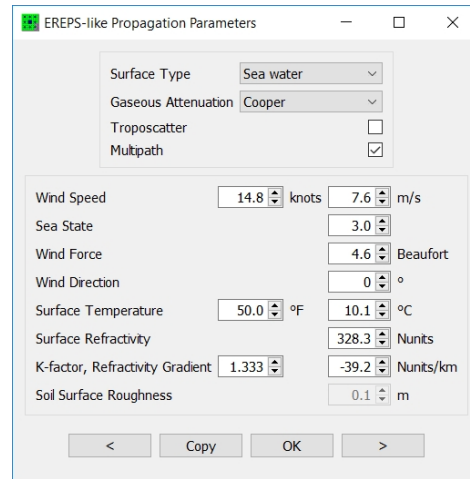


Figure 3.5: The EREPS-like dialogbox of CARPET 3.

### Surface Type

Either sea water, fresh water, very dry ground, medium dry ground or wet ground can be selected. The electrical properties of these surfaces differ. For sea water, 3.5% dissolved salt by weight is assumed. For fresh water, 0.2% dissolved salt by weight is assumed. Default value: Sea water. Other values: Fresh water, Very dry ground, Medium dry ground, Wet ground.

### Troposcatter — Section 6.1.7.5

Scattering from irregularities in the troposphere may become significant at ranges sufficiently greater than the horizon. The activation of the Troposcatter checkbox results in the inclusion of this effect in the calculation of the pattern propagation factor. Default value: off. Other value: on.

### Absorption — Section 6.1.6

See the explanation that is offered in Section 3.3.1.

### Multipath — Section 6.1.7.1

This checkbox activates multipath in the optical interference zone. Default value: on. Other value: off.

### Wind Speed (knots, m/s) — $v_w$ , Sections 6.4.1, 6.1.8.3

### Sea State — $s_s$ , Section 6.4.1

### Wind Force (Beaufort) — $B$

In a maritime scenario the roughness of the sea surface influences its reflectivity and also the value of the reflection coefficient; as the sea state increases, sea surface backscatter (sea

clutter) increases and forward scatter (multipath) decreases. CARPET's Beaufort wind force scale goes from 0 to 12, in agreement with the 2012 edition of the WMO Manual on Marine Meteorological Services, [7], Appendix 1.5. Once a specific wind force,  $B$ , has been selected, CARPET will derive a wind speed,  $v_w$  (m/s), from the equation (see [8])

$$v_w = 0.836 \cdot B^{3/2}. \quad (3.1)$$

The sea state scale in CARPET 3 goes from 0 to 9 and the wind speed is determined according to

$$v_w = 3.16 \cdot s_s^{0.8}. \quad (3.2)$$

A comparison of the wind speed according to this equation and the so-called Douglas sea state scale is provided in Table 3.1.

Table 3.1: Wind speed according to the model and wind speed according to the Douglas sea state scale compared.

Sea state	Model wind speed m/s	Douglas wind speed m/s	Description
0	0.0		Glassy
1	3.2	0 - 3.6	Rippled
2	5.5	3.6 - 6.2	Smooth
3	7.6	6.2 - 8.2	Slight
4	9.6	8.2 - 9.8	Moderate
5	11.5	9.8 - 11.8	Rough
6	13.2		Very rough
7	15.0		High
8	16.7		Very high
9	18.3		Phenomenal

Figure 3.6 shows the wind speed in m/s for the two scales.

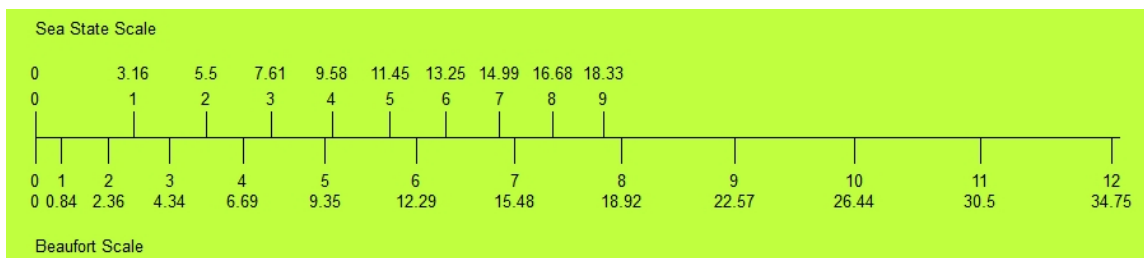


Figure 3.6: Wind speed in m/s for the sea state and Beaufort scales.

Default value wind speed: 7.6 m/s. Minimum value: 9 m/s. Maximum value: 40 m/s.

Default value sea state: 3. Minimum value: 0. Maximum value: 9.

Default value wind force: 4. Minimum value: 0. Maximum value: 12.

**Wind Direction** ( $^{\circ}$ ) —  $\phi_w$ , Section 6.4.1

The wind direction is used in the calculations of the sea clutter reflectivity and the Doppler spectrum of both surface and volume clutter in maritime and land-based scenarios.  $0^{\circ}$  corresponds with wind coming from the North direction.

Default value:  $0^{\circ}$ . Minimum value:  $0^{\circ}$ . Maximum value:  $360^{\circ}$ .

**Surface Temperature** ( $^{\circ}\text{F}$ ,  $^{\circ}\text{C}$ ) —  $T_s$ , Section 6.1.7.4

The temperature of the earth's surface determines its reflective properties.

Default value:  $10^{\circ}\text{C}$ . Minimum value:  $-10^{\circ}\text{C}$ . Maximum value:  $30^{\circ}\text{C}$ .

**Surface Roughness** (m) —  $h_{sd}$ , Section 6.1.7.4

The standard deviation of the surface height affects the magnitude of the reflection coefficient in a land-based scenario.

Default value: 0.1 m. Minimum value: 0 m. Maximum value: 99 m.

**Surface Refractivity** (N-units) —  $N_0$ , Section 6.1.2

The refractivity at the surface is used in the calculations of the natural units of range and height and affects the propagation factor in the diffraction region of the EREPS-like model. The surface refractivity may be determined from the atmospheric pressure, the relative humidity, and the air temperature by changing the value of these parameters. However, the user may overrule the value determined from the meteorological parameters by entering a new value. The value displayed in the dialog box is the value used in the calculation of the propagation factor.

Default value: 328. Minimum value: 200. Maximum value: 500.

**k-factor, Refractivity Gradient** —  $k$ , Section 6.1.2

The effective earth radius factor,  $k$ , is defined as the ratio between the effective earth radius and the actual earth radius (6371 km). The effective earth radius factor influences the reflectivity of surface clutter and the propagation factor in the interference region in both maritime and land-based scenarios.

Default value: 1.33. Minimum value: 1. Maximum value: 10.

**3.3.3 TERPEM-light**

The TERPEM-light plug-in assumes that the meteorology and electrical properties of the earth's surface are the same at all points along the propagation path. In most cases, this limitation will only have a minor effect on the propagation results. Exceptions include modeling of the recovery effect seen at land-sea boundaries at frequencies below 10 MHz.

Contrast to the free space and the EREPS-like models, TERPEM determines path loss values for a series of range-height grid points. The path loss value at a specific range-height

(or altitude) position is determined by means of interpolation. The pattern propagation power factor ( $F^2$ ), that is used in the radar equation, is derived from the interpolated path loss value.

The TERPEM-light dialogbox contains three panes and is shown in Figure 3.7.

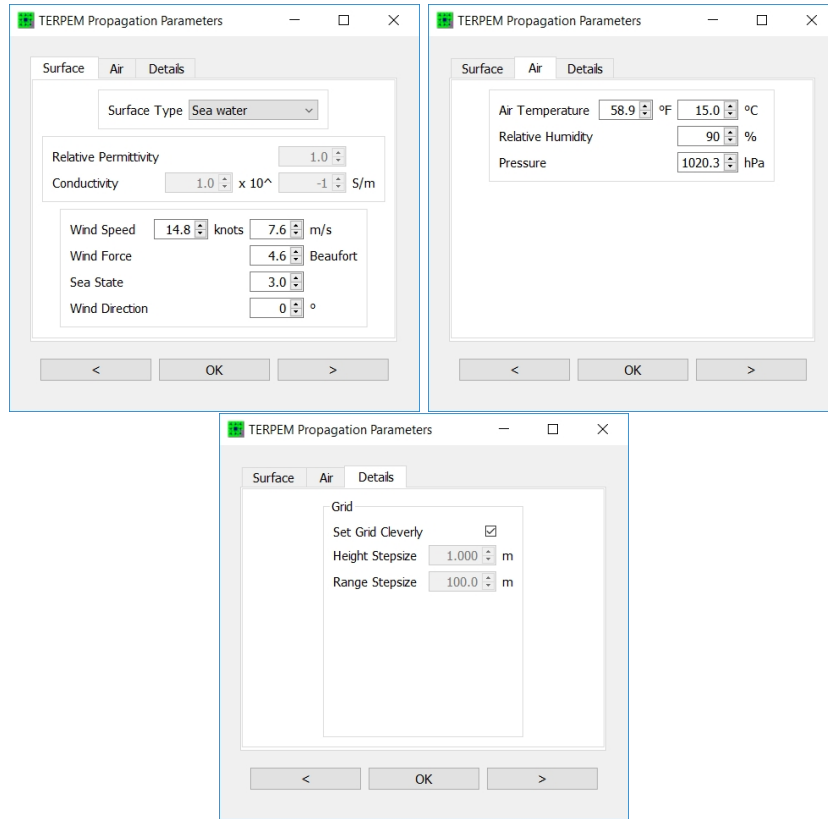


Figure 3.7: The three panes of the TERPEM-light dialogbox of CARPET 3.

### 3.3.3.1 Surface

The roughness of the sea surface affects the reflection of electromagnetic waves, and can have a significant effect on radar coverage in the presence of ducting. In TERPEM, the roughness is incorporated by reducing the smooth Fresnel reflection coefficient by an amount that depends on the RMS waveheight via the Miller-Brown model, [9]. The RMS waveheight is derived from the wind speed. The roughness can be specified by wind speed, wind force or sea state, see the discussion in Section 3.3.2 for more details.

Over land, the varying terrain surface generally dominates over any small scale roughness effects in determining the appearance of the coverage diagram. Nevertheless, in TERPEM,

surface roughness is still applied over land using the RMS roughness derived from the specified windspeed (although of course the wind model is not appropriate for overland propagation). The roughness model should not be used at low frequencies (say, below 1 GHz). The small scale surface roughness can be disabled by setting the wind speed to 0.

### Surface Type

Either Sea Water, Fresh Water, Very Dry Ground, Medium Dry Ground, Wet Ground or User Defined can be selected, also see the explanation in Section 3.3.2. In case User Defined is selected, the relative permittivity and the conductivity of the surface can be specified.

Default value: Sea water

### Relative Permittivity — $\epsilon_r$

Determines the electrical characteristics of the earth's surface, see ITU publication 229-6, [10]. Formerly known as dielectric constant.

Default value: 1. Minimum value: 0.3. Maximum value: 100.

### Conductivity (S/m) — $\sigma_g$

Determines the electrical characteristics of ground, see ITU publication 229-6, [10].

Default value: 5 S/m. Minimum value:  $1 \times 10^{-6}$  S/m. Maximum value: 1000 S/m.

### Wind Speed (knots, m/s) — $v_w$ , Sections 6.4.1, 6.1.8.3

### Sea State — $s_s$ , Section 6.4.1

### Wind Force (Beaufort) — $B$

We refer to the explanation given in Section 3.3.2.

#### 3.3.3.2 Air

### Absorption

See the explanation that is given in Section 6.1.6. TERPEM-light contains Liebe's MPM (mm-wave propagation model) to compute atmospheric absorption, [6].

Default value: on. Other value: off.

### Air Temperature (°F, °C) — $T_a$

Air temperature used in the MPM.

Default value: 15°C. Minimum value: -30°C. Maximum value: 50°C.

### Relative Humidity (%)

Relative humidity, used in the MPM.

Default value: 90%. Minimum value: 1%. Maximum value: 100%.

**Pressure (hPa)**

Barometric pressure, used in the MPM. Note: 1 mbar = 100 Pa = 1 hPa.

Default value: 1020.3 hPa. Minimum value: 900 hPa. Maximum value: 1100 hPa.

**3.3.3.3 Details****Set Grid Cleverly**

In the on-position, CARPET 3 attempts to determine proper grid height and range stepsizes, given the requested graphical output. However for special purposes it is possible to override the automatic selection, an example is provided in Figure 3.8. It is advised to check the pathloss diagrams for anomalies.

Default value: on. Other value: off.

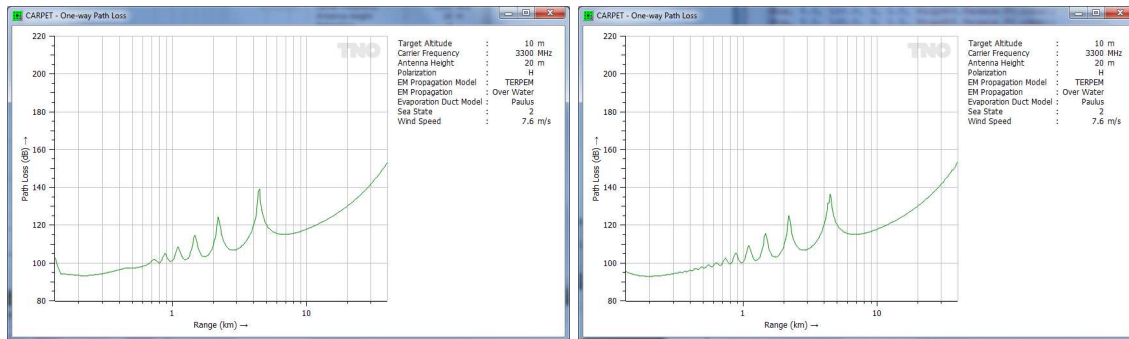


Figure 3.8: One-way path loss according to TERPEM. Since the range axis is displayed logarithmically, quantisation of path-loss appears in the left diagram, at ranges less than 1 km. Right diagram: Set Grid Cleverly is off, a 10 m range step has been taken.

**Height Stepsize (m)**

Height stepsize of the TERPEM output grid in case set grid cleverly is switched off.

Default value: 1 m. Minimum value: 1 mm. Maximum value: 100 m.

**Range Stepsize (m)**

Range stepsize of the TERPEM output grid in case set grid cleverly is switched off.

Default value: 100 m. Minimum value: 1 m. Maximum value: 1000 m.

**Automatic Mode**

Default value: on. Other value: off.

**Hybrid Model**

Default value: on. Other value: off.

**Mixed Transform**

Default value: on. Other value: off.

**Fast HPE Model**

Default value: off. Other value: on.

**Output Interpolation**

Default value: on. Other value: off.

**Diffraction Angle Selection**

Default value: off. Other value: on.

**Maximum Diffraction Angle**

Default value: 1°. Minimum value: 0.1°. Maximum value: 30°.

### 3.4 Refractivity Profile

This specific dialogbox can only be accessed when a TERPEM license is available. Furthermore, in case an N-profile, M-profile or in case TERMET output has been imported, all entries in the dialogbox are disabled. ‘Un-importing’ the imported profile is required to enable the entries.

The dialogbox contains four panes, as shown in Figure 3.9.

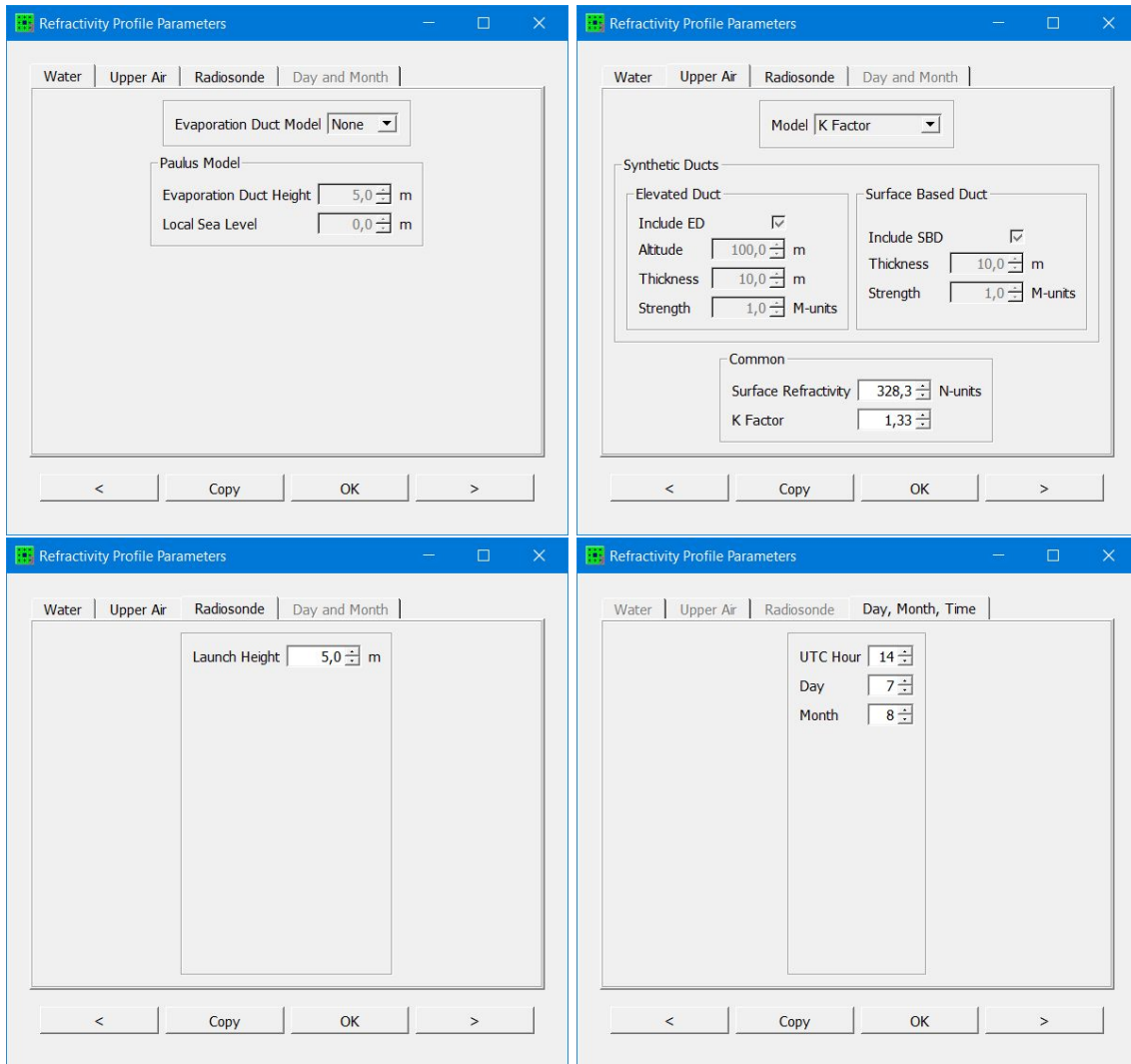


Figure 3.9: The four panes of the refractivity profile dialogbox of CARPET 3.



### 3.4.1 Water

The Water pane is used to specify the height and shape of the evaporation duct which occurs over large bodies of water. It is caused by transport processes in the boundary layer between the water and the air, which result in a strong humidity gradient near the surface. It is always present, although the height of the duct varies with location and time. The evaporation duct lies mostly in the first 40 m or so above the sea surface, and has considerable influence on shipborne radar and communications systems.

It is extremely difficult, particularly in operational environments, to obtain vertical profiles of temperature and humidity at the very low heights which characterise the evaporation duct. Measured profiles have to be replaced with models defined by a few simple bulk parameters. These models are based on the Monin-Obukhov similarity theory of turbulence in the boundary layer above the sea surface. The main inputs required are water temperature and the air temperature, humidity and wind speed at some fixed height above the sea surface. When the air and sea temperatures are almost equal, the boundary layer is neutrally buoyant and the models simplify. In that case duct, height is sufficient to parametrise the evaporation duct profile.

CARPET 3 only contains the relatively straightforward ‘Paulus-recipe’ to characterise the refractivity profile at low altitudes (above water), [11]. In case the CARPET user wishes to utilize more advanced models, such as the model described by M.R. Battaglia, [13], or TNO’s TARMOS model, [14], the advice is to use the import profile functionality.

#### Evaporation Duct Model

Either ‘none’ or ‘Paulus’ can be selected. In case of ‘none’ the upper air profile is extrapolated towards the surface level. The Paulus model is described in Section 6.1.8.7.

Default value: Paulus. Other value: none.

#### Evaporation Duct Height (m) — $d$ (m), Section 6.1.8.7

The height where the M-profile according to the Paulus model has its minimum. This is the only parameter required by the Paulus model.

Default value: 5 m. Minimum value: 1 m. Maximum value: 40 m.

### 3.4.2 Upper Air

The Upper Air pane is used to specify the vertical refractivity profiles at all heights above the low-lying evaporation duct. Normally, the upper air data are obtained from radiosonde ascents, and CARPET provides various import options for such data (see Section 2.10). However, the Upper Air pane provides several options for simulating the impact of specific anomalous atmospheric structures such as surface and elevated ducts. In the absence of measured upper air data, simple analytical models are available. These could be appropriate

even in operational circumstances where the evaporation duct dominates.

### Model

There are two options: K Factor and Synthetic Ducts. The following two parameters are common to both the K Factor and Synthetic Ducts models:

#### Surface Refractivity (N-units)

This denotes the refractivity at the earth's surface. Refraction in the atmosphere is only affected by the refractive index *gradient*, not by the absolute value of the refractive index. However, the value entered here is used to give realistic values to the profiles created.

Default value: 320 N-units. Minimum value: 200 N-units. Maximum value: 500 N-units.

#### K Factor

The effective earth radius factor,  $k$ , is defined as the ratio between the effective earth radius and the actual earth radius. The effective earth radius factor influences the distance to the radio horizon in both maritime and land-based scenarios.

Default value: 1.33, minimum value: 0.5, maximum value: 5.

The Synthetic Ducts model allows the user to superimpose simple elevated and surface duct effects onto an atmosphere defined by the Standard or K Factor models.

#### Include ED

Selecting the Include option for an Elevated Duct will create a simple elevated duct. An elevated duct is caused by an atmospheric layer which produces a negative slope in the modified refractivity-height curve. The duct extends from the top of the ducting layer down to the height at which the modified refractivity returns to the same value as at the top of the layer. Elevated ducts can be caused by temperature inversions in the atmosphere. The simple model duct shape is specified by three parameters.

#### Altitude (m)

The height of the top of the duct.

Default value: 100 m. Minimum value: 10 m. Maximum value: 5000 m.

#### Thickness (m)

The thickness of the duct. It is important to distinguish between the ducting layer and the duct itself. The top of both of these lies at the altitude specified above. The extent of the ducting layer is identified by the negative slope of the modified refractivity-height curve. Radio or radar waves trapped in an elevated duct will propagate with significant energy spread over the height of the duct, not just the ducting layer. It is for this reason that the duct thickness is specified, rather than the meteorologically determined ducting layer.

Default value: 10 m. Minimum value: 500 m. Maximum value: 10 m.

**Strength** (N-units)

The strength of the ducting layer. Note that for a given duct thickness, a stronger ducting layer will produce a thinner ducting layer.

Default value: 1 N-units. Minimum value: 1 N-units. Maximum value: 300 N-units.

**Include SBD**

Selecting the Include option for a Surface Based Duct will create a simple surface duct. A surface duct is caused by an atmospheric layer which produces a negative slope in the modified refractivity-height curve. The duct extends from the top of the duct down to the surface. Surface ducts can be caused by a rapid decrease of humidity or temperature inversions near the ground. A common cause is advection in coastal areas. The simple model duct shape is specified by two parameters.

**Thickness** (m)

The thickness of the ducting layer. For a surface duct the duct height and thickness are the same.

Default value: 10 m. Minimum value: 10 m. Maximum value: 1000 m.

**Strength** (N-units)

The strength of the ducting layer.

Default value: 1 N-units. Minimum value: 1 N-units. Maximum value: 300 N-units.

**3.4.3 Radiosonde**

In case the CARPET user imports radiosonde code, the height at which the weather balloon is launched must be known. This height can be specified in this pane.

**Radiosonde Launch Height** (m)

Default value: 5 m. Minimum value: 0 m. Maximum value: 3000 m.

**3.4.4 Day, Month, Time**

In case one of the two ITU-R P.835 models has been selected (see Section 3.2) the month, day and UTC (Universal Time Coordinated) can be specified.

### 3.5 Clutter

Clutter is an important factor in the design of radar systems. Surface clutter (*i.e.*, clutter from land or sea) can severely hamper the detection capability. Scattering from rainclouds is even more important, especially when assessing the performance of millimeter wave radars. CARPET assumes a cylindrical column of rain or chaff, infinitely high. The backscatter of clutter depends upon several radar system parameters like frequency, polarisation, and beamwidth. The Clutter dialogbox is shown in Figure 3.10.

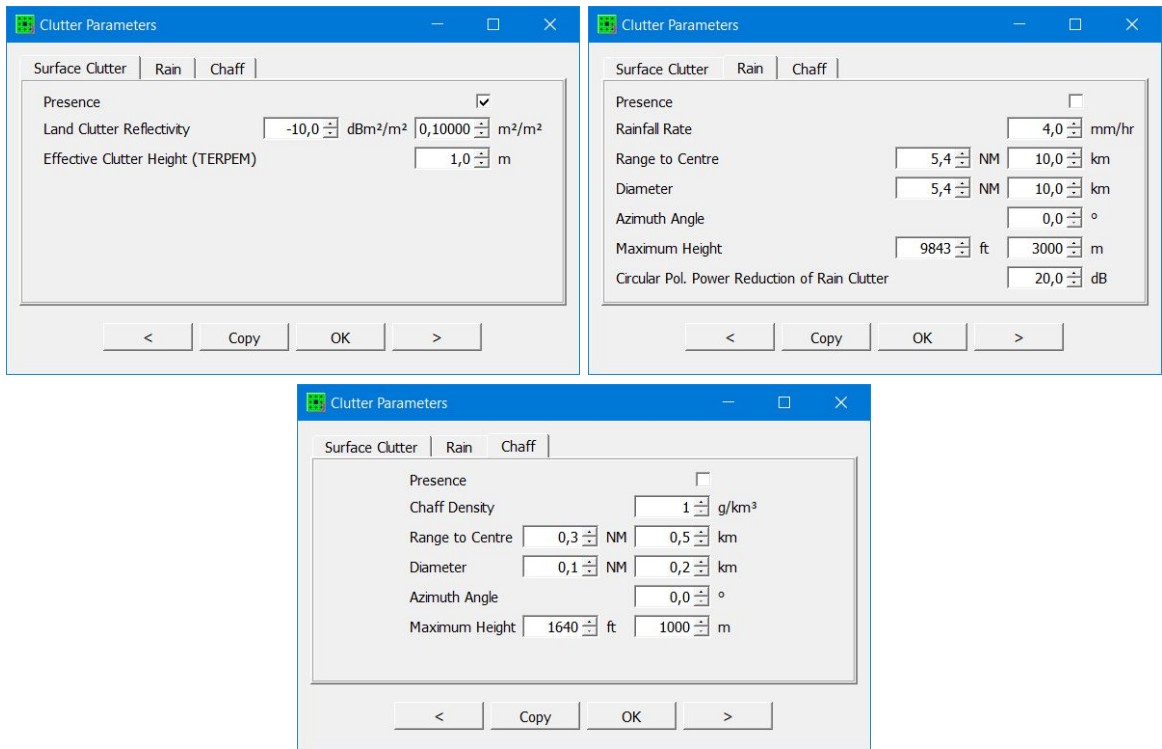


Figure 3.10: The three panes of the Clutter dialogbox of CARPET 3.

#### 3.5.1 Surface Clutter

##### Presence

The presence of surface clutter can be switched off.

Default value: on (surface clutter present). Other value: off.

##### Land Clutter Reflectivity (dBm<sup>2</sup>/m<sup>2</sup>) — $\sigma^0$ , Section 6.4.1

The strength of the surface clutter in a land-based scenario is characterized by the reflectivity

of the land clutter.

Default value:  $-10 \text{ dBm}^2/\text{m}^2$ . Minimum value:  $-100 \text{ dBm}^2/\text{m}^2$ . Maximum value:  $0 \text{ dBm}^2/\text{m}^2$ .

**Effective Clutter Height (TERPEM) (m)**

The height above the land or sea surface at which the pattern propagation factor or the path loss for the surface clutter response is assessed.

Default value: 1 m. Minimum value: 0.1 m. Maximum value: 1 m.

### 3.5.2 Rain

**Presence**

The presence of rain clutter can be switched on.

Default value: off (rain clutter absent). Other value: on.

**Rainfall Rate (mm/hr) —  $r_r$ , Section 6.5.1**

The rainfall rate determines the reflectivity of rain clutter and the attenuation of radio waves.

Default value: 4 mm/hr. Minimum value: 0 mm/hr. Maximum value: 100 mm/hr.

**Range to Centre (NM and km) —  $R_c$**

The ground range (distance) to the center of the rain column, see Figure 3.11.

Default value: 10 km. Minimum value: 0 km. Maximum value: 1000 km.

**Diameter (NM and km) —  $D_c$**

The diameter of the raincloud, see Figure 3.11.

Default value: 10 km. Minimum value: 0 km. Maximum value: 100 km.

**Azimuth Angle ( $^\circ$ ) —  $\phi_c$**

The azimuth angle (or bearing) to the center of the raincloud (0  $^\circ$  is North), see Figure 3.11.

Default value:  $0^\circ$ . Minimum value:  $0^\circ$ . Maximum value:  $360^\circ$ .

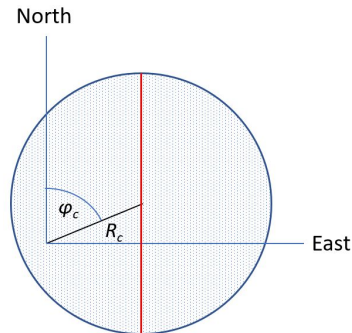


Figure 3.11:  $R_c$  is the range to the centre of the raincloud,  $\phi_c$  is the azimuth angle (from North) to the centre of the raincloud. The red line denotes the diameter of the raincloud.

### 3.5.3 Chaff

#### Presence

The presence of chaff can be switched on.

Default value: off (chaff absent). Other value: on.

#### Chaff Density ( $\text{g}/\text{km}^3$ ) — $W$ , Section 6.5.1

The chaff density determines the reflectivity of chaff.

Default value:  $30 \text{ g}/\text{km}^3$ . Minimum value:  $0 \text{ g}/\text{km}^3$ . Maximum value:  $1000 \text{ g}/\text{km}^3$ .

#### Range to Centre (NM and km) — $R_c$

The ground range (distance) to the center of the chaffcloud, see Figure 3.11.

Default value: 10 km. Minimum value: 0 km. Maximum value: 1000 km.

#### Diameter (NM and km) — $D_c$

The diameter of the chaffcloud, see Figure 3.11.

Default value: 10 km. Minimum value: 0 km. Maximum value: 100 km.

#### Azimuth Angle ( $^\circ$ ) — $\phi_c$

The azimuth angle (or bearing) to the center of the chaffcloud ( $0^\circ$  is North), see Figure 3.11.

Default value:  $0^\circ$ . Minimum value:  $0^\circ$ . Maximum value:  $360^\circ$ .

### 3.6 Jamming

Since February 2022 CARPET can take into account both stand-off jamming and self-screening jamming, *i.e.*, the jammer is mounted on the target. (Before February 2022 only stand-off jamming was available.) For both configurations two types of noise jamming are available: barrage and responsive jamming. Barrage jamming means that the jammer is always transmitting. Responsive means that the jammer ‘listens’, and comes into action by emitting white noise when a radar pulse is received. The jamming signal is received via the (constant) azimuthal sidelobes of the radar antenna or via the mainlobe. The Jamming dialogbox is depicted in Figure 3.12. Note that CARPET 3 can consider up to four stand-off jammers, at different bearings (azimuth angles).

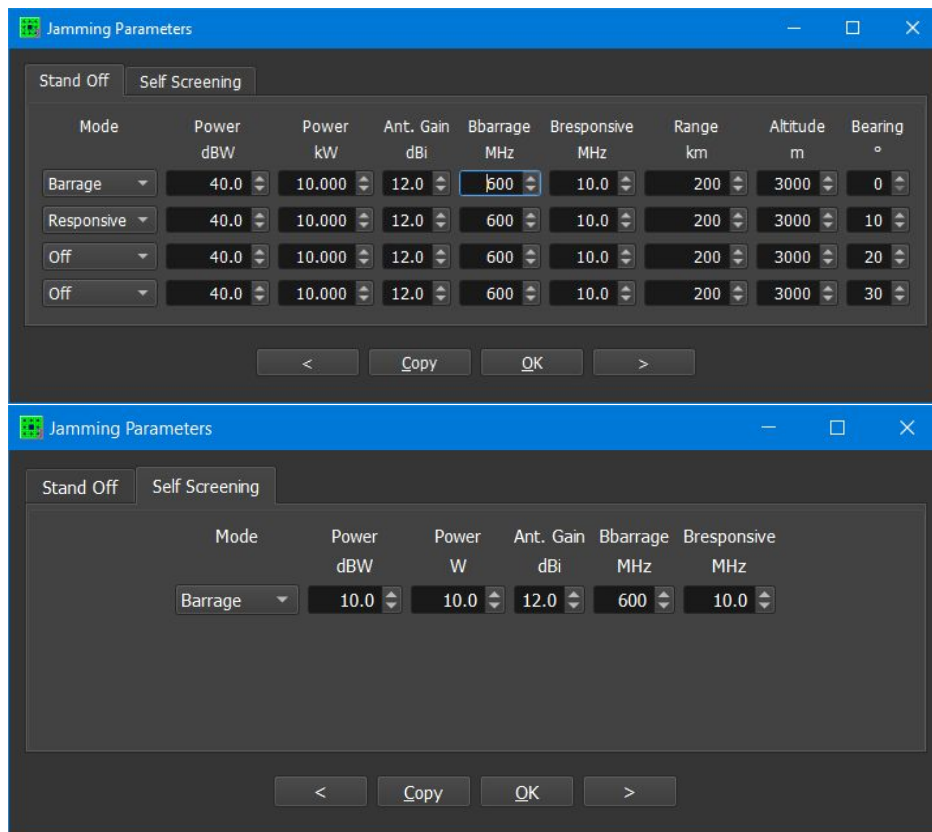


Figure 3.12: The Jamming dialogbox of CARPET 3.

### 3.7 Stand-off Jamming

**Mode**, Section 6.6.1

Either Off, Barrage and Spot can be selected. In the barrage mode, a jammer radiates white noise with a specified bandwidth normally chosen not less than the agility bandwidth of the radar. A responsive jammer emits noise with a bandwidth that is slightly larger than the instantaneous bandwidth of the radar in order to achieve a higher spectral density (W/Hz). A jammer of this kind has to measure the frequency of the radar emission before jamming is possible. This results in a delay (dependent on the jammer range) before jamming is received in the radar. Short coherent integration times in the radar, or pulse to pulse RF staggering may therefore defeat responsive jammers.

**Jammer Power** (dBW, kW) —  $P_{pj}$ , Section 6.6.1

The average power of the jammer available for noise jamming.

Default value: 10 kW. Minimum value: 0.001 kW. Maximum value: 100 kW.

**Antenna Gain** (dBi) —  $G_j$ , Section 6.6.1

The gain of the jammer antenna with respect to an isotropic radiator in the direction of the radar.

Default value: 12 dBi. Minimum value: 0 dBi. Maximum value: 50 dBi.

**Bandwidth Barrage Mode** (MHz) —  $B_j$ , Section 6.6.1

The bandwidth of the noise jamming signal that is emitted in the barrage (wide band) mode.

Default value: 600 MHz. Minimum value: 10 MHz. Maximum value: 10,000 MHz.

**Bandwidth Responsive Mode** (MHz) —  $B_j$ , Section 6.6.1

The bandwidth of the noise jamming signal that is emitted in the responsive (narrow band) mode.

Default value: 10 MHz. Minimum value: 1 MHz. Maximum value: 100 MHz.

**Range** (km) — Section 6.6.1

The ground range of the jammer to the radar.

Default value: 200 km. Minimum value: 1 km. Maximum value: 500 km.

**Altitude** (m) — Section 6.6.1

The altitude of the jammer is used to determine the slant range to the radar.

Default value: 3 km. Minimum value: 0.1 km. Maximum value: 30 km.

**Bearing** (°)

The bearing (azimuth angle) of the jammer.

Default values: 0°, 10°, 20°, 30°. Minimum value: 0°. Maximum value: 360°.



### 3.8 Self Screening Jamming

**Mode**, Section 6.6.1

Either Off, Barrage and Spot can be selected, see the description given above.

**Jammer Power** (dBW, kW) —  $P_{pj}$ , Section 6.6.1

The average power of the jammer available for noise jamming.

Default value: 10 kW. Minimum value: 0.001 kW. Maximum value: 100 kW.

**Antenna Gain** (dBi) —  $G_j$ , Section 6.6.1

The gain of the jammer antenna with respect to an isotropic radiator in the direction of the radar.

Default value: 12 dBi. Minimum value: 0 dBi. Maximum value: 50 dBi.

**Bandwidth Barrage Mode** (MHz) —  $B_j$ , Section 6.6.1

The bandwidth of the noise jamming signal that is emitted in the barrage (wide band) mode.

Default value: 600 MHz. Minimum value: 10 MHz. Maximum value: 10,000 MHz.

**Bandwidth Responsive Mode** (MHz) —  $B_j$ , Section 6.6.1

The bandwidth of the noise jamming signal that is emitted in the responsive (narrow band) mode.

Default value: 10 MHz. Minimum value: 1 MHz. Maximum value: 100 MHz.

### 3.9 Transmitter

The Transmitter dialogbox in the case of a pulsed radar system is shown in Figure 3.13.

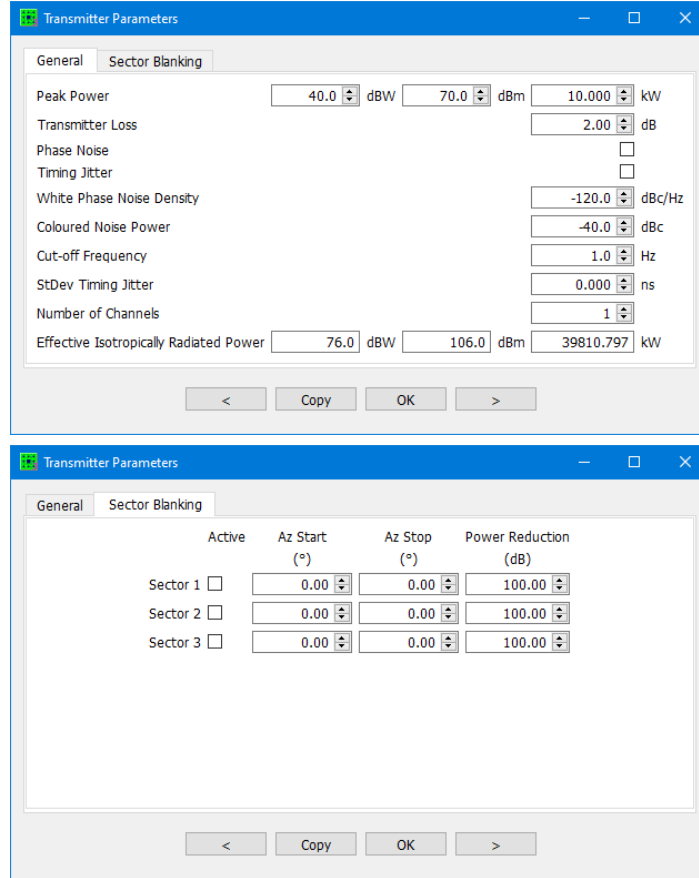


Figure 3.13: The two panes of the Transmitter dialogbox of CARPET 3, in the case of a pulse radar system.

#### 3.9.1 General

**Peak Power (kW)** —  $P_p$ , Sections 6.3.1, 6.4.1, 6.5.1

The received target and clutter power is proportional to the peak power of the transmitted pulses.

Default value: 10 kW. Minimum value: 0.001 kW. Maximum value: 1000 kW.

**Transmitter Loss** —  $L_t$ , Sections 6.3.1, 6.4.1, 6.5.1

This quantity represents the RF losses between the final power amplifier stage of the transmitter and the antenna. These losses affect the signal component of the target, of surface clutter and of volume clutter.

Default value: 2 dB. Minimum value: 0 dB. Maximum value: 30 dB.

**Phase Noise**, Section 6.9.7

If the Phase Noise checkbox is switched on, an increase in clutter residue at the output of a Doppler filter due to phase instabilities of the synthesizer is taken into account.

Default value: off. Other value: on.

**Timing Jitter**, Sections 6.9.7, 6.9.8

The clutter cancellation is limited by the timing uncertainty or jitter in the clock signals that drive the transmitter and the receiver. The Timing Jitter checkbox allows this effect to be included in the calculation of the clutter power at the output of the Doppler processor.

Default value: off. Other value: on.

**White Phase Noise Density** (dBc/Hz) —  $Q_{wn}$ , Section 6.9.7

The white phase noise density (single sideband) of the synthesizer at a large distance from the carrier affects the clutter residue at the output of a Doppler filter if the Phase Noise and Doppler Processing checkboxes are switched on.

Default value: -120 dBc/Hz. Minimum value: -150 dBc/Hz. Maximum value: 50 dBc/Hz.

**Coloured Phase Noise Power** (dBc) —  $P_{cn}$ , Section 6.9.7

The coloured phase noise power of the synthesizer affects the clutter residue at the output of a Doppler filter if the Phase Noise and Doppler Processing checkboxes are switched on.

Default value: -40 dBc. Minimum value: -100 dBc. Maximum value: 0 dBc.

**Cut-off Frequency** (Hz) —  $f_{co}$ , Section 6.9.7

The cut-off frequency of the colored noise of the synthesizer has an effect on the clutter residue at the output of a Doppler filter if the Phase Noise and Doppler Processing checkboxes are switched on.

Default value: 1 Hz. Minimum value: 0 Hz. Maximum value: 10,000 Hz.

**Standard Deviation Timing Jitter** (ns) —  $\sigma_j$ , Section 6.9.7

The standard deviation of the timing uncertainty in the clock signals driving the transmission of the pulses. The timing jitter results in an increased clutter residue if the checkboxes Timing Jitter and Doppler Processing are switched on.

Default value: 0.1 ns. Minimum value: 0.001 ns. Maximum value: 1000 ns.

**Number of Channels** —  $N_c$ , Section 6.9.10

Certain radar systems have multiple transmit channels, the terminology master and slave channel may be used in two-channel systems. The transmit frequencies in the channels differ. The number of receive channels is identical to the number of transmit channels. Multiple frequencies may be transmitted simultaneously. More common, however, seems to be the scheme that pulses with different (centre) frequencies are transmitted one after the other. Frequency diversity is beneficial for the detection capability since RCS is aspect angle and also frequency dependent.

**Effective Isotropically Radiated Power**

Effective isotropically radiated power (EIRP) is the hypothetical power that would have to be radiated by an isotropic antenna in order to give the same signal strength as the actual antenna gives in the boresight direction, *i.e.*, the direction where the antenna delivers maximum gain. The EIRP is therefore larger than the power that is delivered by the transmitter, the relation is given by

$$\text{EIRP} = \frac{P_p G_{Tx}}{L} \quad (3.3)$$

in which  $G_{Tx}$  is the boresight antenna gain on transmit and  $L$  denotes losses, *e.g.*, dissipative losses within the antenna and losses in the transmit path.

The EIRP is shown for information only, the CARPET user cannot modify the values (in dBW, dBm and in kW) that are shown. Changing the peak power, antenna gain and certain loss factors will affect the reported values.

**3.9.2 Sector Blanking**

A radar system may have the feature to reduce the transmit power in specific azimuth sectors, or even to cease transmission in azimuth sectors, *e.g.* in order to meet ‘RadHaz’ (radiation hazard) regulations. The start and stop azimuth angles and the transmit power reduction of three sectors can be defined. The effect is shown in Figure 3.14.

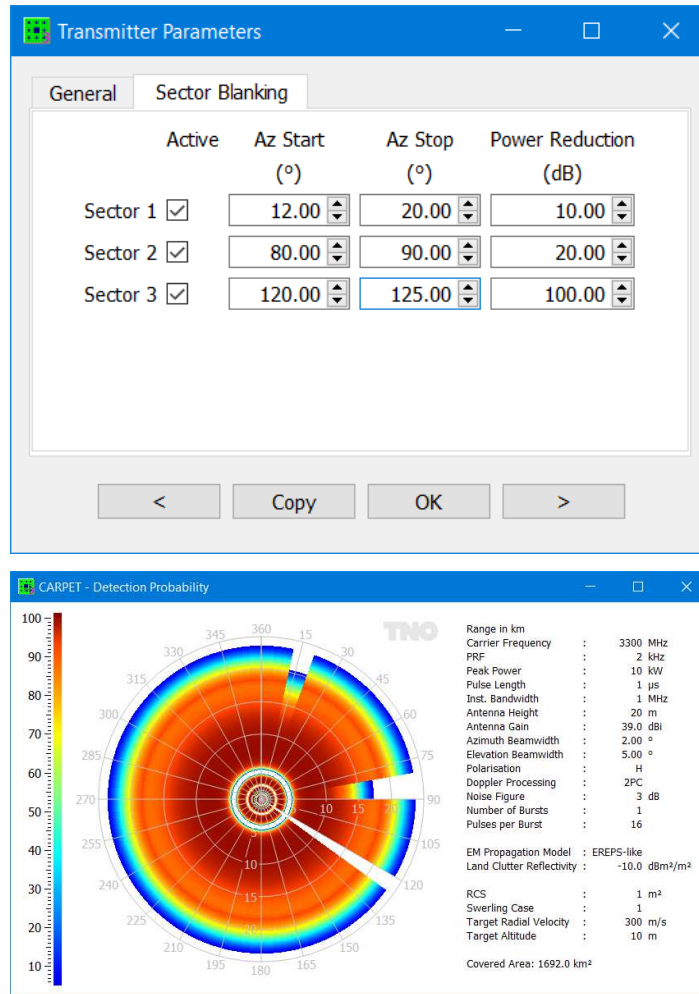


Figure 3.14: The effect of sector blanking on the PPI-view detection probability diagram.

### 3.10 Waveform

The waveform dialogbox is shown in Figure 3.15. Note: if the multi-burst plug-in is active, none of the edit boxes are greyed out.

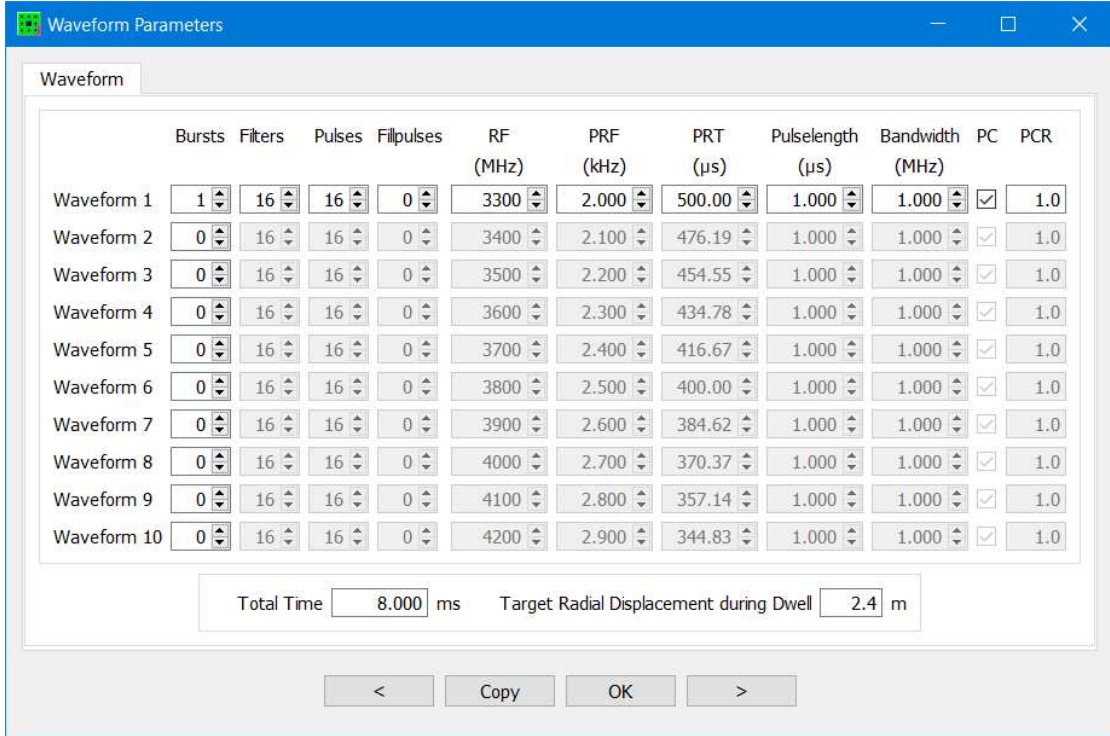


Figure 3.15: The waveform dialogbox in case of a pulsed radar system.

**Bursts** —  $N_b$ , Section 6.9.5

**Filters** —  $N_f$ , Section 6.9.5

**Pulses** —  $N_p$ , Section 6.9.5

**Fill-pulses** —  $N_{p,f}$ , Section 6.9.5

A burst is a series of pulses with identical RF, which allows coherent integration of multiple pulse responses. The number of filters refers to the number of Doppler filters, which does not necessarily have to be identical to the number of pulses within a burst. Fill-pulses are transmissions to make the Doppler integration for multi-trace targets more efficient, which is relevant for radar systems that apply a medium or high PRF.

Examples of radar waveforms are the following:

- A single waveform having 1 burst and  $N_p$  pulses:  $N_p$  pulses are coherently integrated,

while there are  $N_f$  Doppler filters.

- Multiple waveforms, each waveform having 1 burst and  $N_p$  pulses. The number of pulses per burst as well as the number of Doppler filters may vary from waveform to waveform: Pulses are coherently integrated. Responses from multiple waveforms are integrated using  $M$ -out-of- $N$  post-detection binary integration.
- A single waveform having  $N_b$  single-pulse bursts ( $N_p = 1$ ): The  $N_b$  pulse responses are non-coherently integrated.
- Multiple waveforms, each waveform having  $N_b$  single-pulse bursts ( $N_p = 1$ ),  $N_b$  may vary from waveform to waveform: Pulses are first non-coherently integrated. Subsequently, waveforms are integrated using  $M$ -out-of- $N$  post-detection binary integration. The RF may vary from pulse to pulse in order to mislead intentional jamming.

The number of pulses that is coherently integrated is equal to the number of transmitted pulses ( $N_p$ ) minus the number of fill-pulses, ( $N_{p,f}$ ). In radars with a medium or high PRF regime, fill-pulses are transmitted to avoid problems with suppression of multiple-time-around clutter in the Doppler processor. The number of fill-pulses must be smaller than the number of pulses transmitted per burst.

**RF, Carrier Frequency** (MHz) —  $f$ , numerous sections

The carrier frequency which assumed to be constant during a pulse burst. The transmit and receive antenna gain must be specified at the mean carrier frequency. Pulse integration demands that the RF is constant within a burst.

Default value: 3300 MHz. Minimum value: 10 MHz. Maximum value: 100,000 MHz.

**PRF (Pulse Repetition Frequency)** (Hz) —  $PRF$ , Sections 6.9.1, 6.9.5

**PRT (Pulse Repetition Time)** (ms) —  $PRT = 1/PRF$ , Sections 6.9.1, 6.9.5

Obviously, integration gain benefits as the number of pulses that is integrated goes up, which can be achieved by increasing the PRF (assuming the target does not decorrelate within the integration time). An improved clutter suppression capability is a side-effect. Medium or high PRFs can, however, result in multiple-time-around clutter and in ‘dead’ zones. To counter this phenomenon multiple bursts per dwell are often applied, with a different PRF from burst to burst. This waveform strategy cannot (easily) be investigated if the multi-burst plug-in is not active.

Default value: 2 kHz. Minimum value: 0.1 kHz. Maximum value: 100 kHz or 50% of the reciprocal of the pulse length.

**Pulselength** ( $\mu$ s) —  $\tau$ , Section 6.9.1

The length of the transmitted (uncompressed) pulse. When the Pulse Compression checkbox

is on, the pulse is compressed on receive to a length equal to the reciprocal of the instantaneous bandwidth. Large pulse lengths result in deep dead zones.

Default value: 1  $\mu\text{s}$ . Minimum value: 0.05  $\mu\text{s}$  (50 ns). Maximum value: 10,000  $\mu\text{s}$  (10 ms) or 50% of the pulse repetition interval.

**Instantaneous Bandwidth** (MHz) —  $B$ , Section 6.9.1

The instantaneous bandwidth of the transmitted pulses. A short (compressed) pulse demands a large instantaneous bandwidth.

Default value: 1 MHz. Minimum value: 0.1 kHz. Maximum value: 200 MHz.



### 3.11 Antenna

The dialogbox depicted in Figure 3.16 can be used to change antenna parameters.

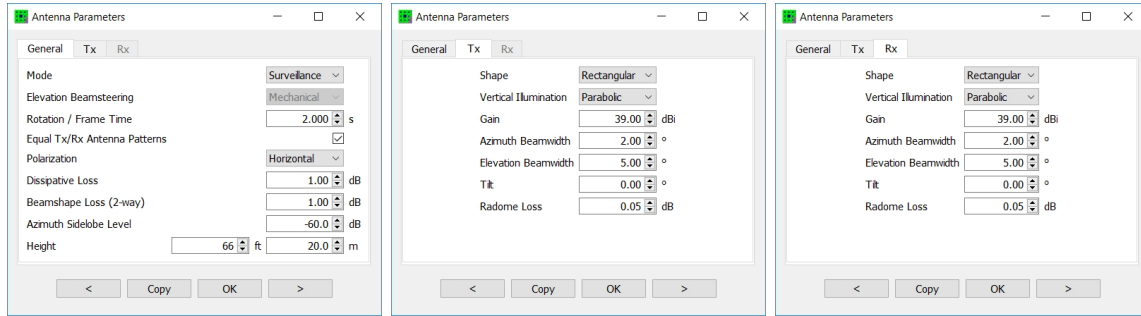


Figure 3.16: The three panes of the Antenna dialogbox of CARPET 3.

#### 3.11.1 General

##### Mode

Either ‘Surveillance’ or ‘Tracking’ can be selected. A tracking radar points the maximum of the antenna pattern in the direction of the target, which can be achieved by electronic or mechanical means. The Tracking mode cannot be combined with TERPEM. Default value: Surveillance. Other value: Tracking.

##### Elevation Beamsteering

Either ‘Mechanical’ or ‘Electronic’ can be selected. If electronic tracking is selected, the gain and beamwidth of the elevation pattern are adjusted for the off-boresight pointing angle. Default value: Mechanical. Other value: Electronic.

##### Rotation / Frame Time (s) — $T_{frame}$ , Section 6.10

The time between successive scans. For a rotating antenna the frame time is the reciprocal of the rotation rate. The frame time affects the shape of the Doppler spectrum of clutter. The frame time is also used in the calculations of the firm track probability. Default value: 2 s. Minimum value: 0 s. Maximum value: 100 s.

##### Number of Apertures

Either ‘Single’ ( $T_x = R_x$ ) or ‘Dual’ ( $T_x \neq R_x$ ) can be selected. Default value: Single. Other value: Dual.

**Polarisation**, Sections 6.1.8.4, 6.1.9, 6.3.3

The polarisation of the radar waves influences the received target power, the power of sea and rain clutter and the value of the reflection coefficient.

Default value: Horizontal. Other values: Vertical, Circular.

**Dissipative Loss** (dB) —  $L_a$ , Section 6.2.1

A dissipative loss results in transmit and receive power loss caused by impedance mismatch.

Default value: 1 dB. Minimum value: 0 dB. Maximum value: 10 dB.

**Beamshape Loss** (dB) —  $L_{bs}$ , Sections 6.3.1, 6.6.1

The losses resulting from the nonuniform gain within the 3-dB beamwidth. These losses affect the signal component of the target and of jamming. For low-PRF surveillance radars 1.6 dB is often used.

Default value: 1 dB. Minimum value: 0 dB. Maximum value: 10 dB

**Azimuth Sidelobe Level** (dB) —  $G_{az}$ , Section 6.8

The root mean square (RMS) sidelobe level of the radar receive antenna in azimuth with respect to the main beam. The azimuth sidelobe level influences the received jamming power.

Default value: -40 dB. Minimum value: -80 dB. Maximum value: -10 dB.

**Height** (ft and m) —  $h_a$ , Section 6.4.1

The height (altitude) of the radar antenna influences the received surface clutter power and the pattern propagation factor. Note: the height must be specified with respect to the terrain (or water) level at the sensor.

Default value: 20 m. Minimum value: 0 m. Maximum value: 20,000 m.

**3.11.2 Tx****3.11.3 Rx****Shape**, Section 6.8

Two different aperture shapes are supported by CARPET: an antenna with a circular or rectangular aperture.

Default value: Rectangular. Other values: Circular.

This item is disabled if a user specified antenna patterns has been loaded.

**Vertical Illumination**, Section 6.8

The illumination function in the vertical plane of the circular or rectangular aperture which influences the pattern propagation factor and the surface clutter power. Default value: Parabolic. Other values: Uniform, Parabolic<sup>2</sup> and — only for the rectangular aperture — Cosec<sup>2</sup>,

Inverse cosec<sup>2</sup>.

This item is disabled if a user specified antenna patterns has been loaded.

**Boresight Gain** (dBi) —  $G_{Tx}$ ,  $G_{Rx}$ , Section 6.8

The gain of the antenna with respect to an isotropic radiator at the mean carrier frequency. If electronic tracking is selected, the gain is multiplied by the cosine of the off-boresight angle (tilt minus target elevation).

Default value: 39 dB. Minimum value: 0 dB. Maximum value: 50 dB.

**Azimuth Beamwidth** (°) —  $\phi_{az}$ , Section 6.4.1

The one-way 3-dB beamwidth in azimuth at the mean carrier frequency. The azimuthal beamwidth influences the received volume and surface clutter power.

Default value: 2°. Minimum value: 0.1°. Maximum value: 100°.

**Elevation Beamwidth** (°) —  $\theta_{el}$ , Section 6.8

The one-way 3-dB beamwidth in elevation at the mean carrier frequency. If electronic tracking is selected, the beamwidth is divided by the cosine of the off-boresight angle (tilt minus target elevation).

Default value: 2°. Minimum value: 0.1°. Maximum value: 100°.

**Tilt** (°) —  $\theta_t$ , Section 6.8

For the non-tracking and the electronic tracking antennas: the tilt angle of the radar antenna with respect to the horizontal plane. The received target power, surface clutter power, and the pattern propagation factor are affected by the tilt angle.

Default value: 0°. Minimum value: -10°. Maximum value: 90°.

**Radome Loss** (dB) —  $L_{r,Tx}$ ,  $L_{r,Rx}$ , Sections 6.3.1, 6.4.1, 6.5.1,

This losses is caused by dissipation within a radome.

Default value: 0.1 dB. Minimum value: 0 dB. Maximum value: 3 dB.

### 3.12 Receiver

The dialogbox illustrated in Figure 3.17 can be used to change the receiver parameters.

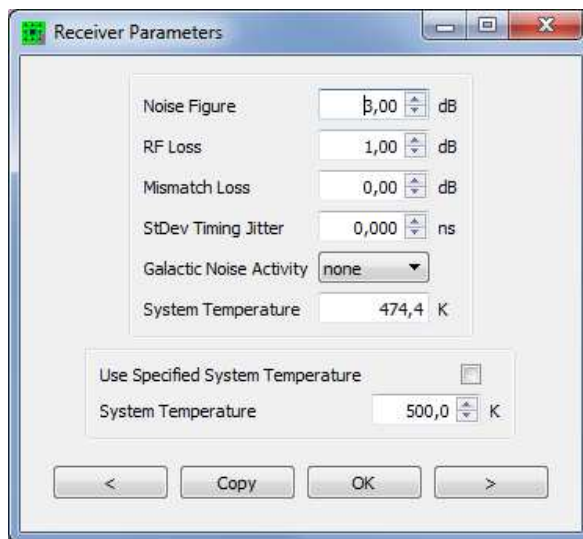


Figure 3.17: The Receiver dialogbox of CARPET 3.

#### Noise Figure (dB) — $F_n$ , Section 6.2.1

The noise figure (the noise factor expressed in dB) of the radar receiver. This quantity affects the receiver noise floor.

Default value: 3 dB. Minimum value: 0 dB. Maximum value: 20 dB.

#### RF Loss (dB) — $L_r$ , Section 6.2.1

The attenuation from the antenna output flange to the receiver, caused by microwave components. This loss affects the noise power.

Default value: 1 dB. Minimum value: 0 dB. Maximum value: 20 dB.

#### Mismatch Loss (dB) — $L_{r,m}$ , Sections 6.3.1, 6.4.1, 6.5.1,

A loss that is associated with impedance mismatch (in the receive channel). This loss affects all signal components.

Default value: 0 dB. Minimum value: 0 dB. Maximum value: 3 dB.

#### Standard Deviation Timing Jitter (ns) — $d_{Rx}$ , Section 6.9.8

The standard deviation of the timing uncertainty in the clock signals driving the receiver, *e.g.*, the analog-to-digital (A/D) converter. The timing jitter results in an increased clutter residue if the checkbox Timing Jitter and Doppler Processing are switched on.

Default value: 0.1 ns. Minimum value: 0.001 ns. Maximum value: 1000 ns.

**Galactic Noise Activity**, Section 6.2.3

The activity of the galaxy (solar and galactic sources) affects the system noise temperature. When switched off, it is assumed that the antenna is pointing at an absorbing surface with temperature 290 K.

Default value: None. Other values: Average, Minimum, Maximum.

**Use Specified System Temperature**

When switched on, the specified system temperature is taken.

Default value: off. Other value: on.

**Specified System Temperature (K)** —  $T_s$ , Section 6.2.1

The system temperature in case the checkbox is switched on.

### 3.13 Processing

The five panes of the Processing dialogbox are illustrated in Figure 3.18. Features of the tracking algorithm are specified in a separate dialogbox, see Section 3.14.

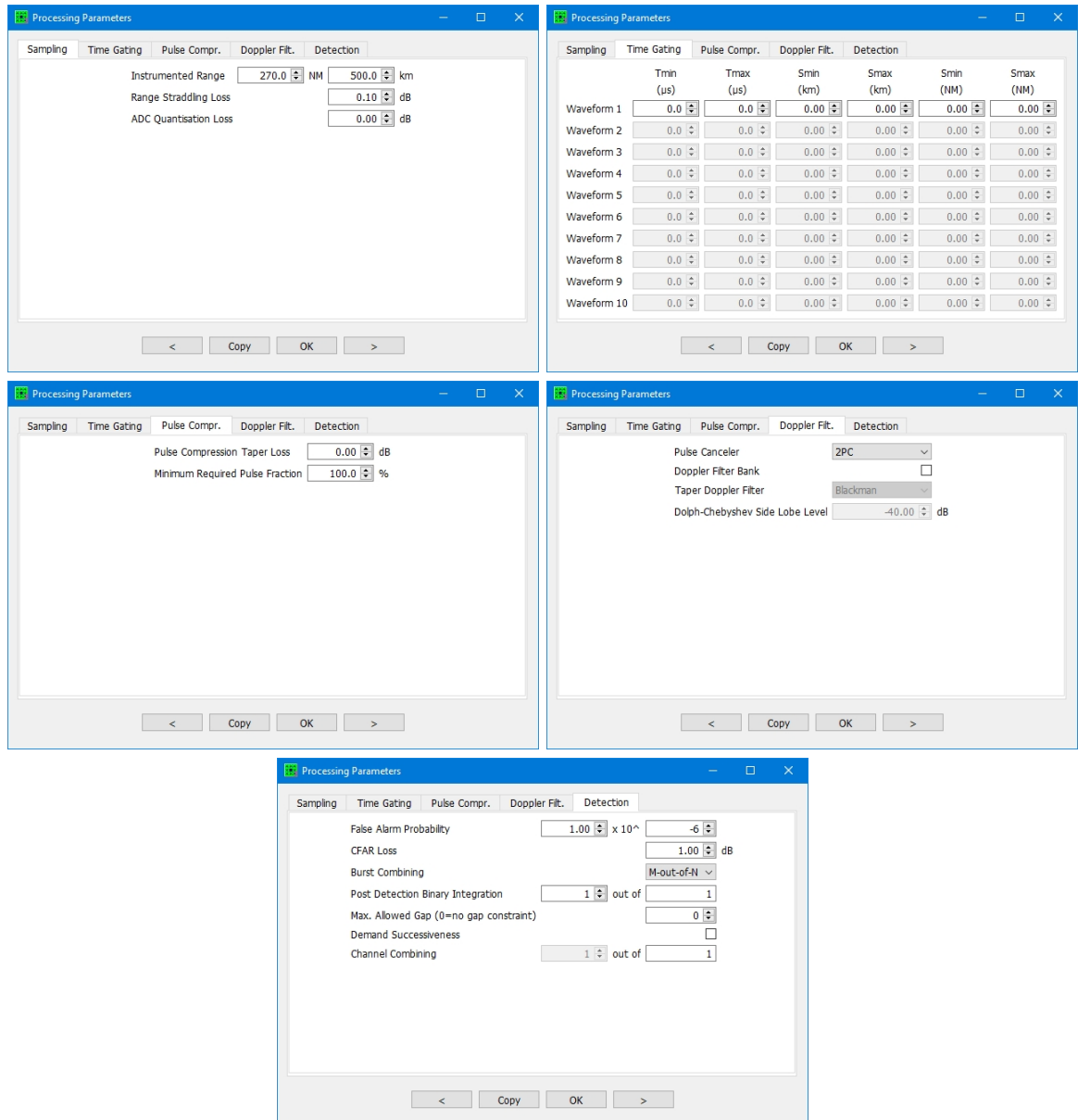


Figure 3.18: The five panes of the Processing dialogbox of CARPET 3.

### 3.13.1 Sampling

#### Instrumented Range (NM, km) — $R_{inst}$

The maximum slant range that is supported by the signal processor of the radar; a target with slant range that is outside the specified slant range interval will not be reported. Figure 3.19 illustrates target eclipsing by the instrumented range.

Default value: 500 km. Minimum value: 0 km. Maximum value: 10000 km.

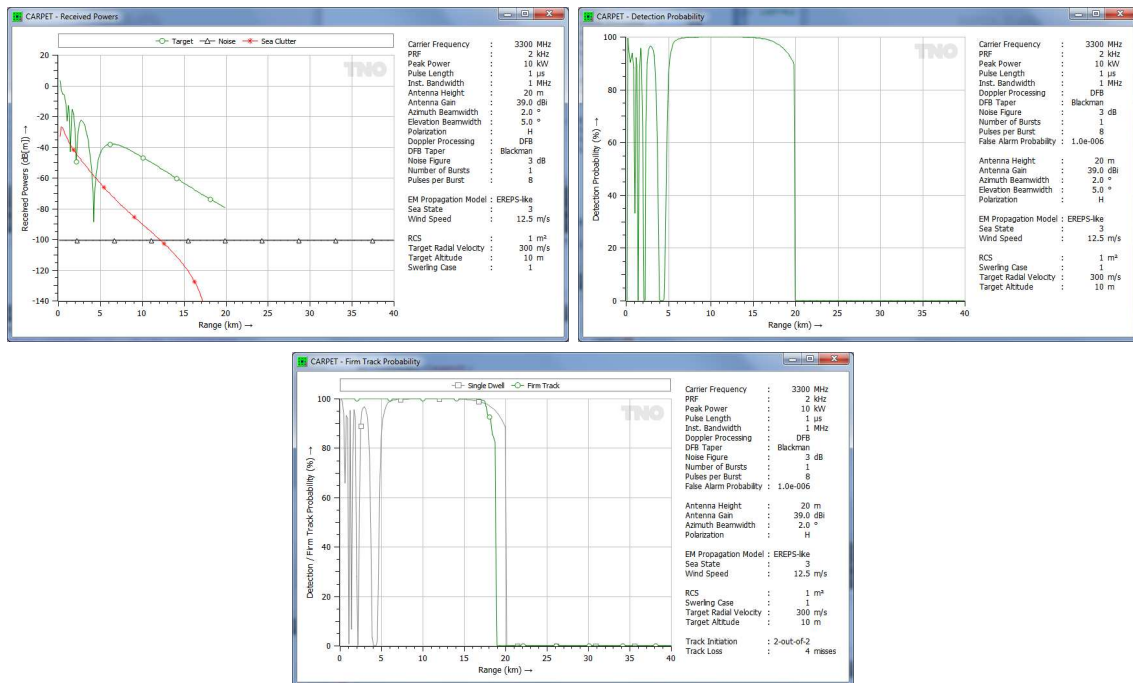


Figure 3.19: Received powers (top-left), single-scan detection probability (top-right) and firm track probability (bottom) in case the instrumented range, set at 20 km, eclipses the target.

#### Range Straddling Loss (dB) — $L_{rs}$ , Section 6.3.1

This loss relates to the phenomenon that a target's position will generally not coincide with the ranges that correspond with the sampling moments. Range straddling loss only applies to the target response.

Default value: 0.1 dB. Minimum value: 0 dB. Maximum value: 3 dB.

#### ADC Quantisation Loss (dB) — $L_q$ , Section 6.3.1

This loss relates to the finite number of bits of the analogue to digital convertor (ADC). CARPET 3 applies the pulse compression taper loss only to the target response.

Default value: 0.0 dB. Minimum value: 0 dB. Maximum value: 3 dB.

### 3.13.2 Time Gating

Since the adaptation of CARPET 3 in March 2019, time gating of each waveform can be applied. Figure 3.20 presents an example of this option.

**Minimum Time** ( $\mu\text{s}$ ) —  $T_{min}$ , Section 6.9.4

**Maximum Time** ( $\mu\text{s}$ ) —  $T_{max}$

The minimum and maximum arrival time of the radar response that is supported by the signal processor of the radar.

**Minimum Slant Range** (km) —  $S_{min}$ , Section 6.9.4

**Maximum Slant Range** (km) —  $S_{max}$

The minimum and maximum slant range that is supported by the signal processor of the radar; a target with slant range that is outside the specified slant range interval will not be reported. The relationship between time of arrival,  $t$  (s), and slant range,  $S$  (m), is simply given by  $S = c \cdot t/2$  with  $c$  (m/s) the speed of light.

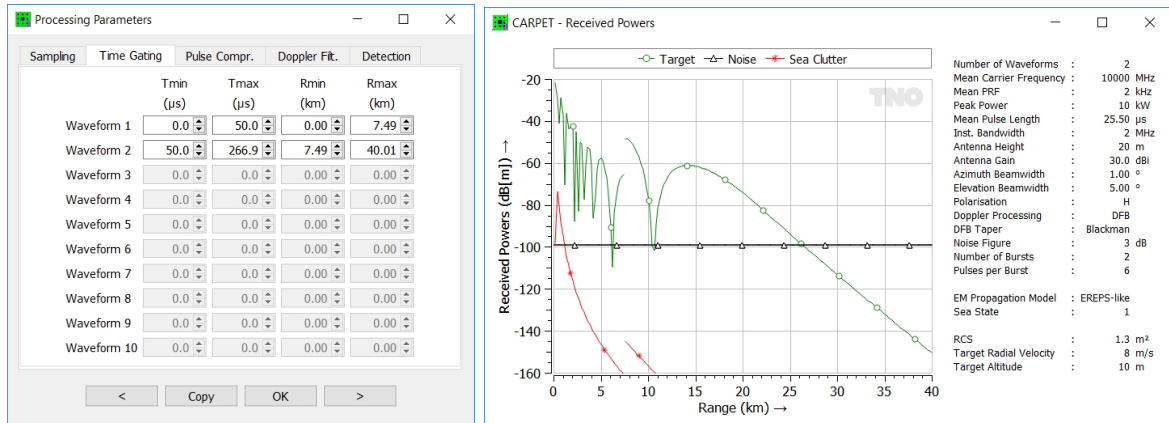


Figure 3.20: Simulation of a radar with two waveforms. A short pulse waveform is applied to provide coverage from 0 to 7.5 km, a long pulse waveform is applied to provide coverage beyond 7.5 km. Post-detection binary integration is (obviously) 1-out-of-2.



### 3.13.3 Pulse Compression

#### Pulse Compression Taper Loss, $L_{PC}$ , Section 6.3.1

Pulse compression is a means to combine good range resolution with relatively long pulses (which implies a relatively deep dead zone). The technique demands that a modulated pulse is transmitted which is compressed on receive. Often, frequency modulation is applied (chirp waveform, like non-linear FM). CARPET 3 applies the pulse compression taper loss only to the target response.

Default value: 0 dB. Minimum value: 0 dB. Maximum value: 3 dB.

#### Minimum Required Pulse Fraction, Section 6.9.4

To counter the dead zone that is inherent to pulse compression processing, partially eclipsed pulses may be applied. This means that pulse compression is applied on the back-end of the received pulse; the initial part of the reflected pulse goes lost as the receiver is protected. The effect is illustrated in Figure 3.21.

Default value: 100%, which means that only un-eclipsed pulses are processed. Minimum value: 20%. Maximum value: 100%.

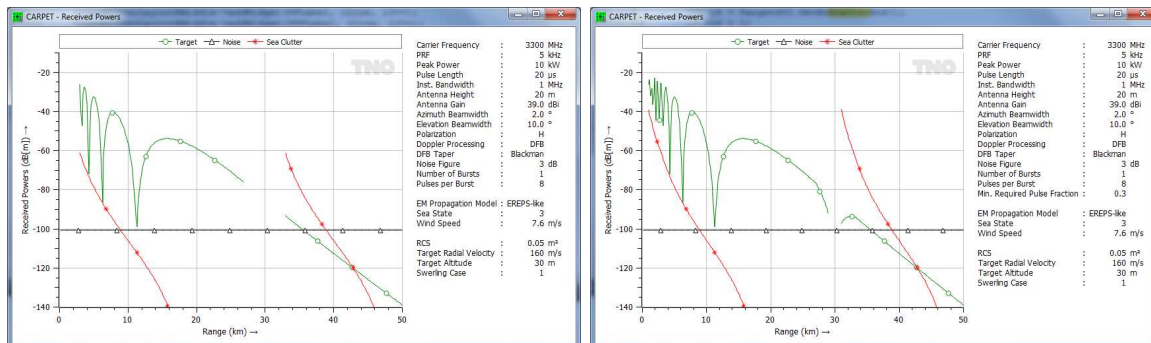


Figure 3.21: Received powers as a function of target ground range. Left: pulse compression is applied on whole pulses only. Right: 70% of the received pulse may go lost, due to eclipsing.

### 3.13.4 Doppler Filtering

#### Pulse Canceler, Section 6.9.5

A pulse canceler is a bandstop filter in the Doppler domain to suppress echoes of stationary objects. Radial speed estimation is not possible with a pulse canceler.

Default value: None. Other values: Two-pulse canceler, Three-pulse canceler, Four-pulse canceler, Five-pulse canceler.

**Doppler Filter Bank**, Section 6.9.5

The Doppler filter bank is a set of contiguous filters in the Doppler domain intended to provide clutter suppression (as the Doppler-integrated target response emerges in a different Doppler filter as the Doppler-integrated clutter response) and estimation of the radial speed of a target. CARPET assumes the filters to be uniformly distributed over the Doppler frequency band, as shown in Figure 3.22.

Default value: on. Other value: off.

**Taper Doppler Filter** —  $t(n)$ , Section 6.9.5

A taper reduces the sidelobe level of a Doppler filter and therefore improves the suppression of clutter through ‘leakage’. However, the taper introduces a loss and increases the width of the pass-band of the filter. Five different tapers are available.

Default value: Blackman. Other values: Uniform, Hamming, Hanning, Dolph-Chebyshev.

**Dolph-Chebyshev Side Lobe Level**, Section 6.9.5

The side lobe level of a Dolph-Chebyshev Doppler taper (weighting function).

Default value: -40 dB. Minimum value: -80 dB. Maximum value: 15 dB

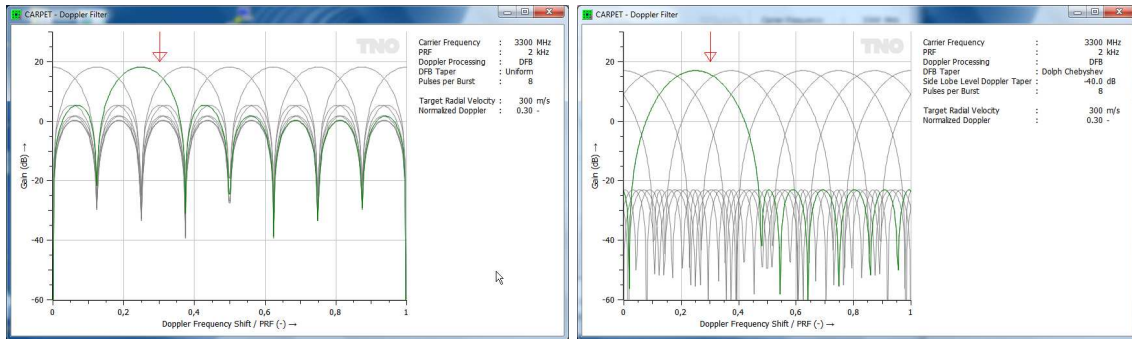


Figure 3.22: Doppler filter responses. Left: responses are not tapered (‘uniform taper’). Right: responses are Dolph-Chebyshev tapered with -40 dB side lobe level.

**3.13.5 Detection****False Alarm Probability** —  $P_{fa}$ , Section 6.9.9

Given a specific SCNR (signal to clutter plus noise ratio), the detection probability depends on the fluctuation characteristics of the target response (Swerling case), the number of pulses that is non-coherently integrated and on the false alarm probability,  $P_{fa}$ . Defining the proper value for  $P_{fa}$  is by no means trivial. Two aspects are relevant:

- The point in the radar’s signal processing chain where the specified  $P_{fa}$  is applicable.

- The effect of post-detection processing, such as  $M$ -out-of- $N$  post-detection binary integration, multi-scan correlation and tracking.

With respect to the first aspect: the specified  $P_{fa}$  is applicable for the point in the signal processing chain where detection is done. To illustrate this with an example: suppose  $1 \times 10^{-6}$  is demanded at the end of the signal processing chain. The chain has no tracker and also no multi-scan correlator. Detections of four subsequent bursts are combined according to 2-out-of-4 binary integration. Prior to this process, the  $P_{fa}$  is  $4.09 \times 10^{-4}$ , as explained in Section 6.9.10, so the allowed false alarm probability at this point (before the  $M$ -out-of- $N$  integrator) is higher than the false alarm probability at the end of the processing chain. The CARPET user can also figure out this number with the Binary Integration worksheet, discussed in Section 5.10.

Note that a multi-target tracker is an efficient method to suppress false alarms.  $P_{fa}$  prior to the tracker that is a factor 100 higher (poorer) than  $P_{fa}$  at the output of the tracker is no exception.

Default value:  $1 \times 10^{-6}$ . Minimum value:  $1 \times 10^{-12}$ . Maximum value: 0.1.

#### **CFAR Loss** — $L_{CFAR}$ , Section 6.3.1

Target detection is generally done with a CFAR (constant false alarm rate) filter. This filter estimates the ‘background’ signal (noise plus potentially also clutter) from data that surround the cell-under-test (CUT). Since, for practical reasons, the number of cells that are used to estimate the background is limited, the estimated background level may deviate from the true background level. A loss is therefore associated with a specific CFAR implementation. This loss only affects the target response.

Default value: 1 dB. Minimum value: 0 dB. Maximum value: 6 dB.

#### **Post-Detection Binary Integration** — $M$ , Section 6.9.10

Detections (or misses) obtained from multiple bursts (or pulse trains) are generally combined with  $M$ -out-of- $N$  post-detection binary integration logic. The value for  $M$  can be specified here, the value for  $N$  is derived from the specified waveform. *E.g.*, in case a single burst is being transmitted,  $N$  equals 1 so that  $M$  cannot be specified (is 1 as well). The worksheet Binary Integration provides a means to investigate how a certain  $M$ -out-of- $N$  logic affects the false alarm and the detection probability, see Section 5.10.

Default value: 1-out-of- $N$ . Minimum value: 1-out-of- $N$ . Maximum value:  $N$ -out-of- $N$

#### **Maximum Allowed Gap** — $G$ , Section 6.9.10

The ‘gap’ parameter, see Section 6.9.10 for a discussion.

Default value: 0 (no gap).

**Demand Successiveness**, Section 6.9.10

See Section 6.9.10 for a discussion.

Default value: off. Other value: on.

**Channel Combining** —  $M_c$ , Section 6.9.10

In case the radar has multiple channels,  $M_c$ -out-of- $N_c$  integration is applied prior to the integration of multiple bursts,  $N_c$  being the number of channels. This option is only available if the multi-burst license is available.

Default value: 1. Other value: 2 up to and including  $N_c$ .

### 3.14 Tracking

The tracking dialogbox is shown in Figure 3.23.

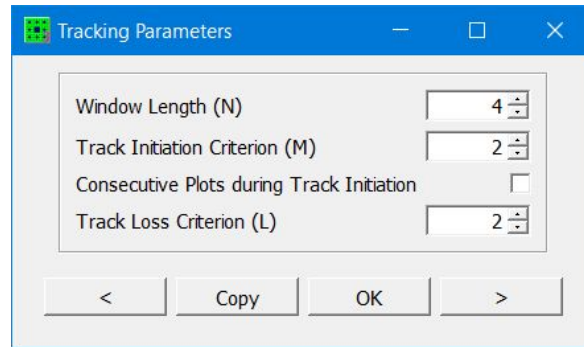


Figure 3.23: The Tracking dialogbox of CARPET 3.

#### **Track Initiation Logic** — $M$ and $N$ , Section 6.10

A track is initiated in case a  $M$ -out-of- $N$  criterion is met, the values of  $M$  and  $N$  ( $M \leq N$ ) need to be specified. These parameters determine the shape of the firm track probability diagram.

Default value: 2-out-of-2

#### **Consecutive Plots during Track Initiation**, Section 6.10

When switch on, tracks are initiated when the ‘hits’ are consecutive.

Default value: off. Other value: on

#### **Track Loss** — $L$ , Section 6.10

A track is declared lost (or dropped, or broken) in case of a number of subsequent misses,  $L$ . This parameters also determines the shape of the firm track probability diagram.

Default value: 4

### 3.15 Loss Factors

The loss factors dialogbox is shown in Figure 3.24.

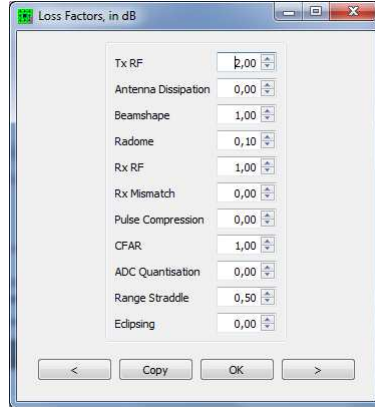


Figure 3.24: The Loss Factors dialogbox of CARPET 3.

The various loss factors are summarised in this dialogbox. One factor has not yet been discussed:

#### **Eclipsing Loss (dB)** — $L_e$ , Section 6.3.1

In case of medium PRF, pulse compression radar systems, measures are needed to reduce range eclipsing (or masking) effects. The strategy that is commonly applied is to stagger the PRF, so that dead zones are at different range intervals from burst to burst. The effect under free space conditions is illustrated in the left diagram of Figure 3.25. In this case there are three different waveforms and 1-out-of-3 post-detection binary integration is applied. When an eclipsing loss of 5 dB is specified, the diagram shown at the right is obtained. The target response is reduced with 5 dB and range eclipsing is not modelled. The rationale of this adaptation of the modelling is that the PRF stagger scheme differs from dwell to dwell. Figure 3.26 shows similar diagram when the EREPS-like mode is applied.

Default value: 0 dB (off). Minimum value: 0 dB. Maximum value: 10 dB.

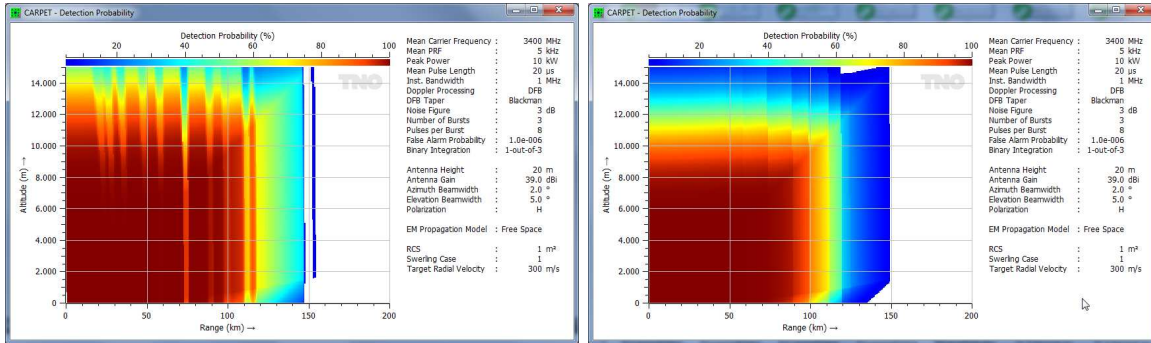


Figure 3.25: Vertical coverage diagrams in the case of three bursts with different PRFs to spread dead zones. Propagation in free space is assumed. Left: Eclipsing loss is not applied. Right: Eclipsing loss is set at 5 dB.

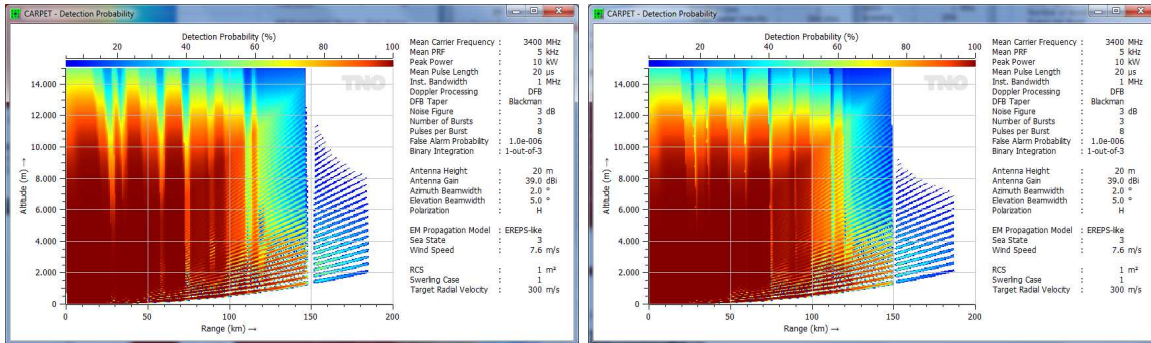


Figure 3.26: Similar diagrams while the EREPS-like propagation model is used.

### 3.16 Target

The two panes of the target dialogbox are shown in Figure 3.27.

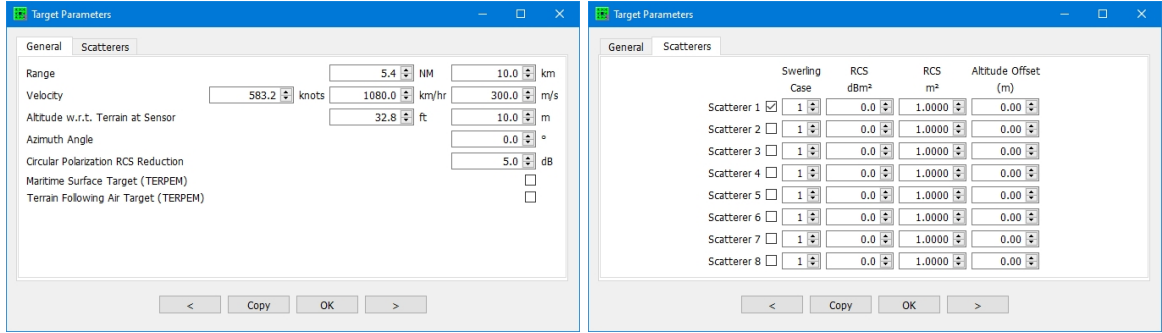


Figure 3.27: The two panes of the Target dialogbox of CARPET 3.

#### 3.16.1 General

##### Target Range (NM and km) — $R_t$ , Section 6.3.1

The range of the target is used in calculations in which either the velocity or the height of the target is varied. The user is warned if the target is eclipsed by the transmission of a radar pulse.

Default value: 10 km. Minimum value: 1 km. Maximum value: 1000 km.

##### Target Velocity (knots and m/s) — $v_r$ , Sections 6.9.1

The velocity of the target is used in calculations in which either the height or the range of the target is varied. If the Doppler Processing consists of a pulse canceler or Doppler filter bank, the target response may be suppressed if the target speed is equal or close to a blind speed, *i.e.*, a target Doppler frequency shift that is equal to a multiple of the PRF.

Default value: 300 m/s. Minimum value: 0 m/s. Maximum value: 1500 m/s.

##### Target Altitude w.r.t. Terrain at Sensor (ft and m) — $h_t$ , Section 6.1.7.3

The altitude of the target is used in calculations in which either the velocity or range of the target is varied. The altitude is with respect to the height of the terrain at the location of the radar sensor.

Default value: 10 m. Minimum value: -4000 m. Maximum value: 40,000 m.

##### Target Altitude w.r.t. Mean Sea Level (ft and m) — $h_t$ , Section 6.1.7.3

The altitude of the target is used in calculations in which either the velocity or range of the target is varied. The altitude is with respect to the mean sea level, *i.e.*, level 0 m in the SRTM terrain height data. In case a TERPEM license is absent, this altitude is identical to



altitude with respect to the terrain at the sensor.

Default value: 10 m. Minimum value: -430 m. Maximum value: 40,000 m.

**Azimuth Angle (°)**

The azimuth angle (or bearing) of the target.

Default value: 0°. Minimum value: 0°. Maximum value: 360°.

**Circular Polarisation RCS Reduction, Section 6.3.1**

The reduction in RCS in case circular polarisation is applied.

Default value: 5 dB. Minimum value: 0 dB. Maximum value: 10 dB.

**Maritime Surface Target (TERPEM)**

When enabled range-azimuth cells above landmasses are not being considered. This checkbox is enabled if the TERPEM propagation model has been chosen. Figure 3.28 reveals the use of this parameter.

Default value: off. Other value: on.

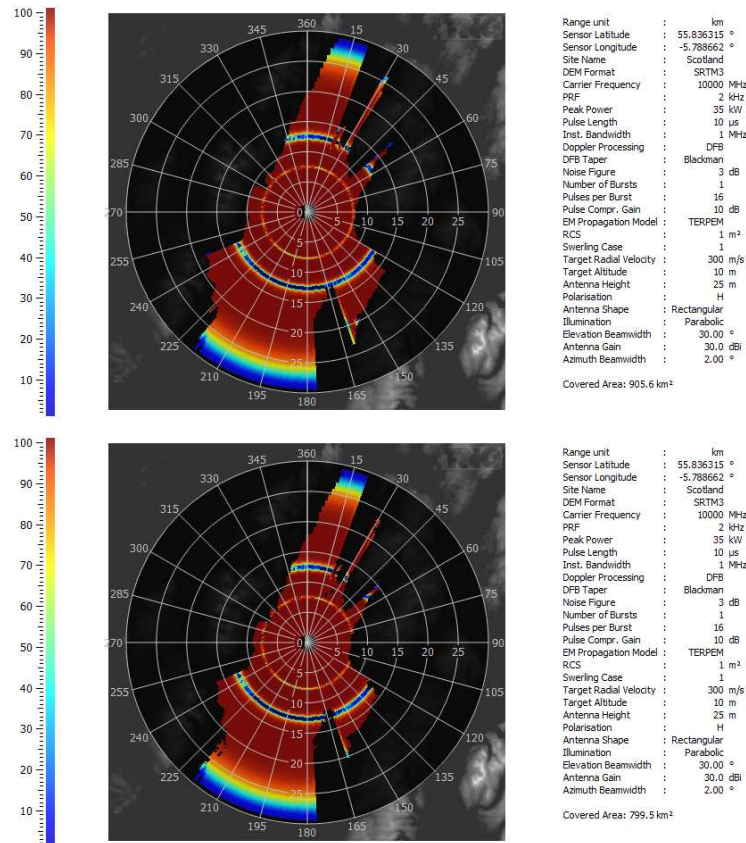


Figure 3.28: Top: Detection probability for a target at 10 m altitude. Bottom: Detection probability for a maritime surface target at 10 m altitude. Note that the covered area in the lower diagram is less than the covered area in the top diagram.

### Terrain Following Air Target (TERPEM)

When enabled the altitude profile of the target is terrain following. This checkbox is enabled if the TERPEM propagation model has been chosen. Examples for a terrain following and a fixed altitude target are provided in Figure 3.29.

Default value: off. Other value: on.

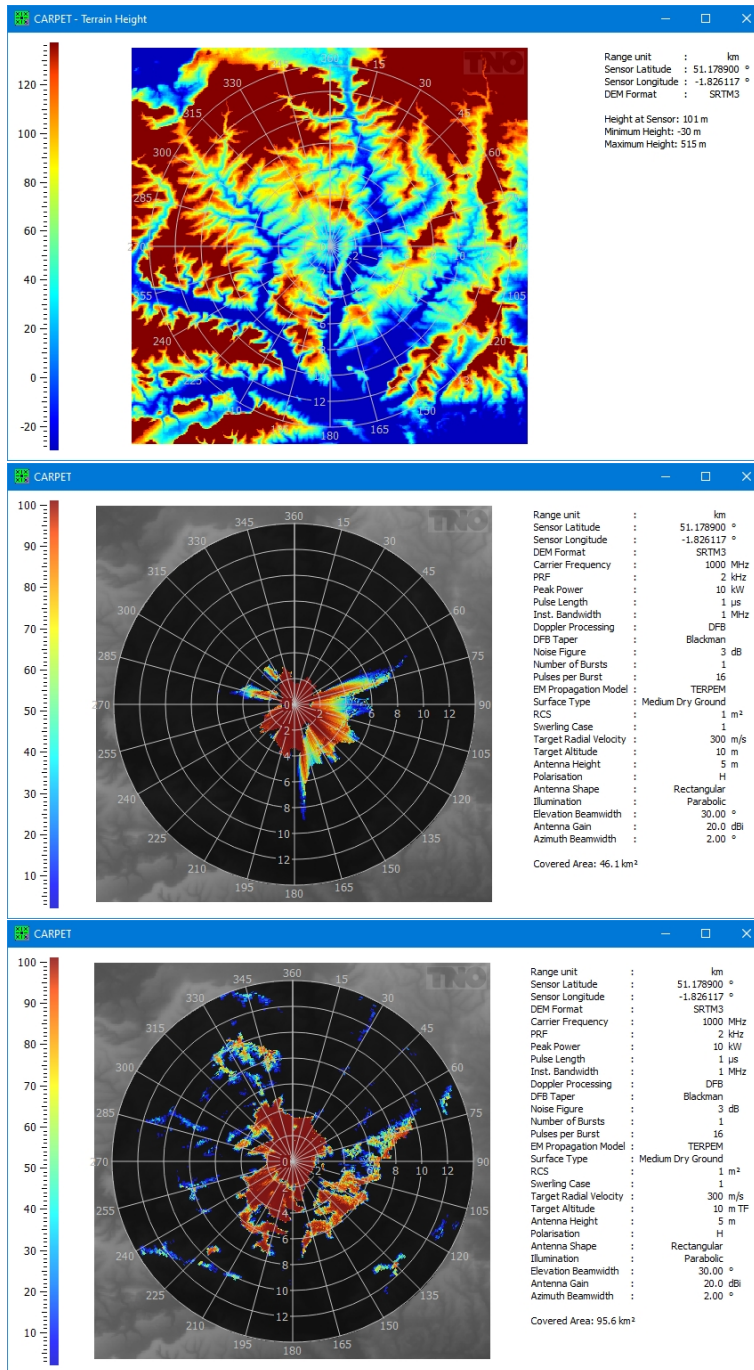


Figure 3.29: Top: terrain height diagram. Middle: Detection probability for a target that travels at a fixed altitude, *i.e.*, 10 m above the terrain at the location of the sensor. Bottom: Detection probability for a target that travels 10 m above the terrain ('terrain following'). Note the 'TF' suffix in the legend at Target Altitude.



### 3.16.2 Scatterer

In case the multi-scatterer target plug-in has been purchased, a ‘point-cloud’ model of the target is supported. Per scatterer, an RCS and Swerling case can be specified. Also, the position of the point in a vertical plane can be specified. In case the multi-scatterer target plug-in is not active, only the values on the first line can be changed.

#### **Radar Cross Section** (dBm<sup>2</sup> and m<sup>2</sup>) — $\sigma_t$ , Section 6.3.1

The received target power is proportional to the radar cross section of the target.

Default value: 1 m<sup>2</sup>. Minimum value: 0.001 m<sup>2</sup>. Maximum value: 20,000 m<sup>2</sup>.

#### **Swerling Case**, Section 6.9.9

The Swerling case describes the target fluctuation model that is used in the calculation of the detection probability as shown in Table 3.2.

Table 3.2: The four Swerling cases.

Fluctuation speed	No dominant scatterer	One dominant scatterer
Scan-to-scan	1	3
Pulse-to-pulse	2	4

The Swerling cases 1 and 2 are applicable for relatively complex targets like aircraft. The fluctuations of missile-like targets can be represented by cases 3 and 4. Swerling 0 is the nonfluctuating case that may be used to model a sphere.

Default value: 1. Other values: 0, 2, 3, 4.

#### **Altitude Offset** (m)

The offset in altitude with respect to the altitude specified in the General pane.

Default value: 0 m. Minimum value: -50 m. Maximum value: 50 m.

### 3.17 Sensor Location

The Sensor Location dialogbox is shown in Figure 3.30.

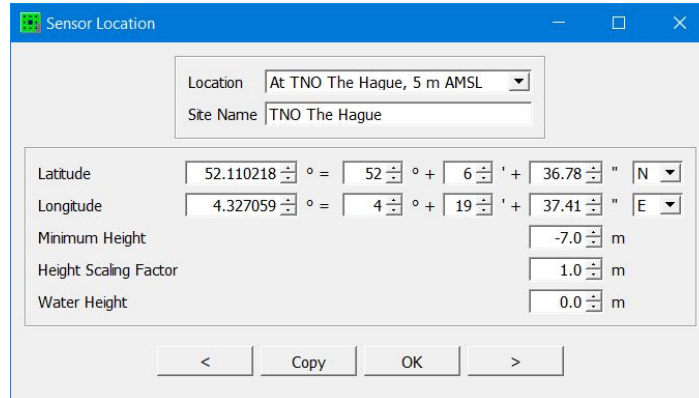


Figure 3.30: The Sensor Location dialogbox of CARPET 3.

The dialogbox is disabled in case the TERPEM plug-in is not active. Otherwise, the following can be set:

#### Location

Three predefined locations are available: ‘At TNO The Hague’, ‘On the Matterhorn’ (which is in Switzerland) and ‘At Stonehenge’ (in the United Kingdom). Location ‘At Sea/On Flat Ground’ means that CARPET 3 does not require terrain altitude data. In case the user enters latitude/longitude data the combobox will show ‘Somewhere’.

#### Site Name

A name can be specified, which is annotated in the legend, at the right of the diagram.

#### Latitude

The latitude of the sensor location, see Figure 3.31.

Minimum value:  $-90^\circ$ . Maximum value:  $90^\circ$ .

#### Longitude

The longitude of the sensor location, see Figure 3.31.

Minimum value:  $-180^\circ$ . Maximum value:  $180^\circ$ .

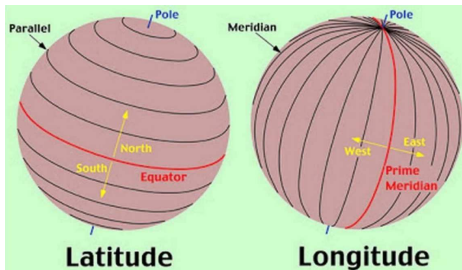


Figure 3.31: Latitude and Longitude clarified.

#### **Minimum Height (m)**

SRTM data may contain so-called ‘voids’, *i.e.*, terrain cells with an unrealistic height, -32767 m or -32768 m. The height data are clipped to the value that is specified here, in order to eliminate void values.

#### **Height Scaling Factor**

In case GeoTIFF terrain height data is used, the height-resolution can be different from unity, *e.g.*, a value of 123 means 12.3 m. The height scaling factor in this case is 0.1 m.

#### **Water Height (m)**

Certain bodies of water are not at sea level, *e.g.*, the Caspian sea is at approximately 27.5 m (90 feet) below sea level, Lake Erie is at 174 m (571 feet) above sea level. The Maritime Surface Target feature (see Section 3.16) requires the height of the body of water to be known, which can be specified here.

### 3.18 Layout

The Layout dialogboxes shown in Figure 3.32 allows the user to modify the layout of the diagrams produced by CARPET.

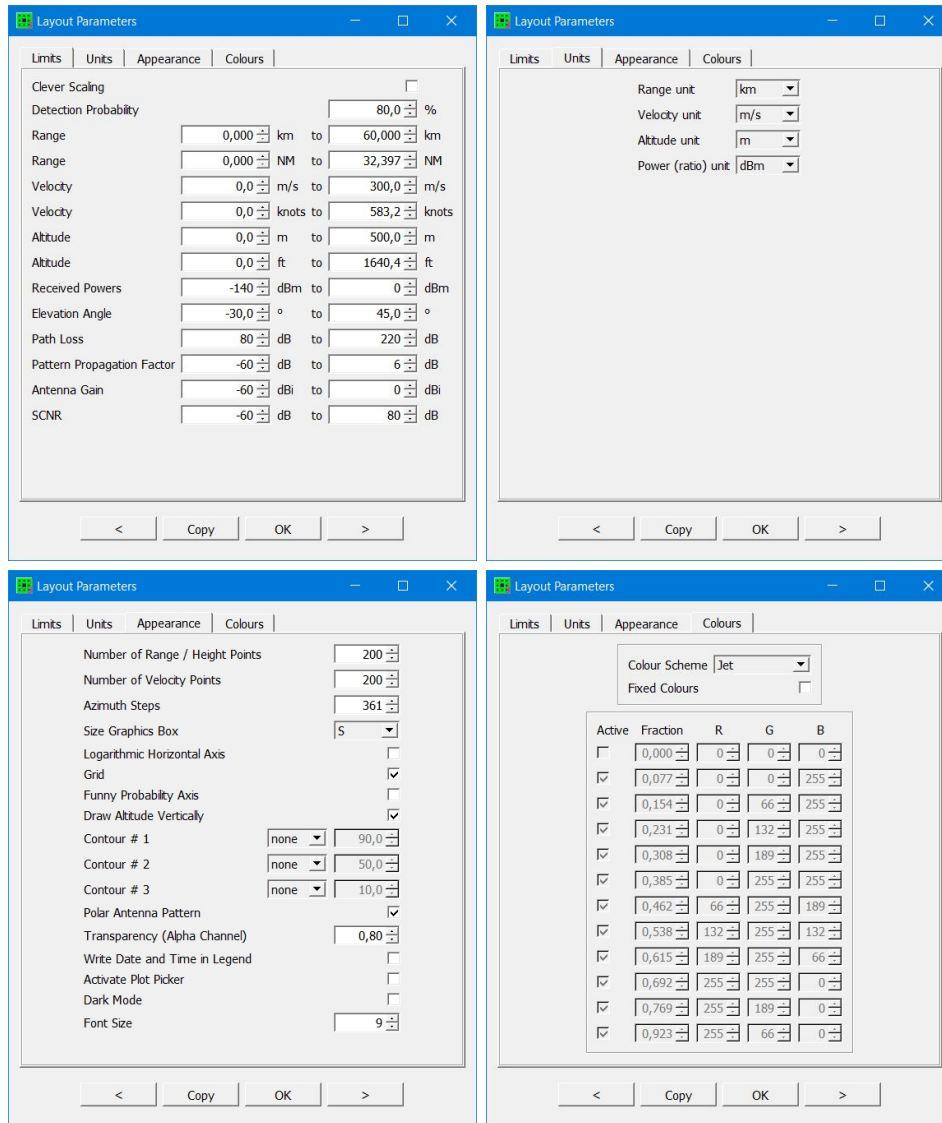


Figure 3.32: The four panes of the Layout dialogbox of CARPET 3.

### 3.18.1 Limits

#### Detection Probability

The so-called detection probability spectrogram plots, like detection  $P_d$  versus range and altitude and  $P_d$  versus range and velocity reveal only detection probabilities that are larger than the value that is set here, see Figure 3.33.

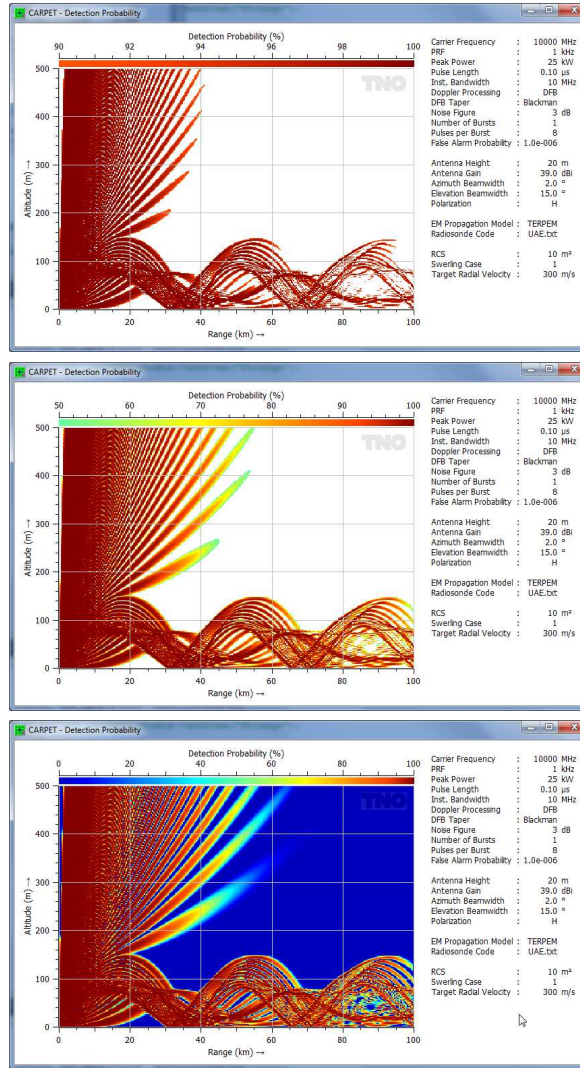


Figure 3.33: Detection probability versus range and altitude for three different values of the threshold: 90% (top), 50% (middle) and 0% (bottom).



**Maximum Range (NM and km)**

The maximum range (distance) in diagrams that have range on the horizontal axis.

**Velocity (m/s and knots)**

The minimum and maximum radial speed of diagrams that have velocity on the horizontal axis.

**Minimum Altitude (m and ft)**

The minimum altitude in diagrams that have altitude on one of the axes. In case a TERPEM license is not present, the minimum value is 0 m and cannot be modified.

**Maximum Altitude (m and ft)**

The maximum altitude in diagrams that have altitude on one of the axes.

**Received Powers (dB)**

The span of the received powers diagram (along the vertical axis (unless target altitude is displayed vertically)).

**Elevation Angle (°)**

The span of the elevation angle in the antenna pattern diagrams.

**Path Loss (dB)**

The span of the path loss in the path loss diagrams.

**Pattern Propagation Power Factor (dB)**

The span of the pattern propagation power factor ( $F^2$ ) in pattern propagation power factor diagrams.

**Antenna Gain (dBi)**

The span of the antenna gain in transmit (Tx) or receive (Rx) antenna pattern diagrams.

**SCNR (dB)**

The span of the SCNR diagrams.

**3.18.2 Units****Range Unit**

Default value: km. Other value: NM.

**Velocity Unit**

Default value: m/s. Other value: knots.

### Altitude Unit

Default value: m. Other values: ft, kft.

### Power Ratio Unit

Default value: dBm. Other value: dBW.

### 3.18.3 Appearance

#### Number of Points

The number of points along the horizontal and vertical axes. Obviously, the number of steps affects the time to complete a diagram, especially the blind-zone and coverage diagrams.

Default value: 200. Minimum value: 10. Maximum value: 500.

#### Azimuth Steps

The number of azimuth points in the PPI-view diagrams. This number affects the time to complete a diagram.

Default value: 360. Minimum value: 30. Maximum value: 7200.

#### Size Graphics Box

One can select either 'S', 'M' or 'L' (small, medium or large). Obviously, diagrams can be stretched, using the mouse (left button), see Figure 3.34.

Default value: M. Other values: S and L.

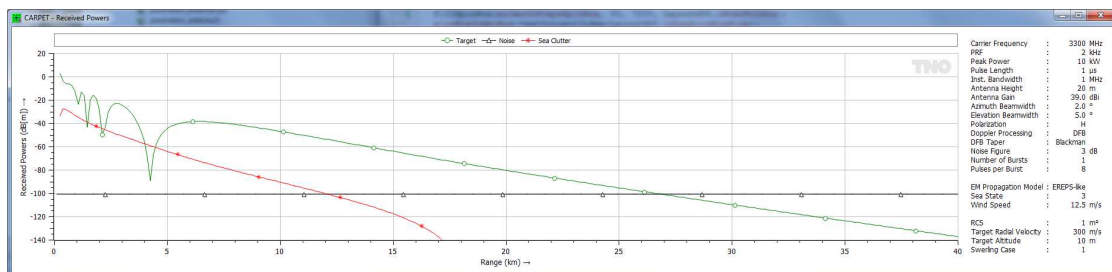


Figure 3.34: Stretched version of a received powers diagram.

#### Logarithmic Range Axis

The Logarithmic Range Axis checkbox determines whether the received powers, detection probabilities, blind zone and coverage diagrams, and the propagation factor are using a linear or logarithmic range axis, see Figure 3.35.

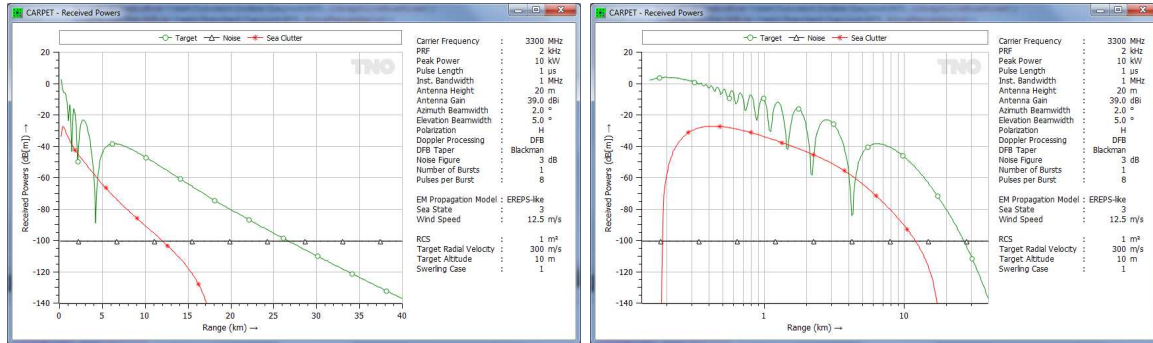


Figure 3.35: Left: linear range axis. Right: logarithmic range axis.

**Grid**

If the Grid checkbox is switched off, no grid appears in the diagrams, see Figure 3.36.

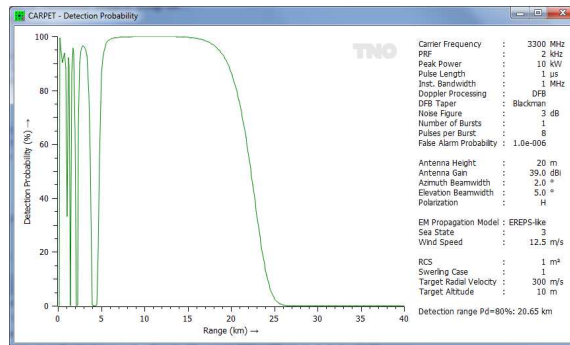


Figure 3.36: A diagram without grid lines.

**Funny Probability Axis**

If this checkbox is switched on, the scaling of the probability axis is done according to the error function centered at 50%, which stretches low and high probability values, see Figure 3.37. This type of scaling is applied in the Meyer and Mayer textbook, [16].

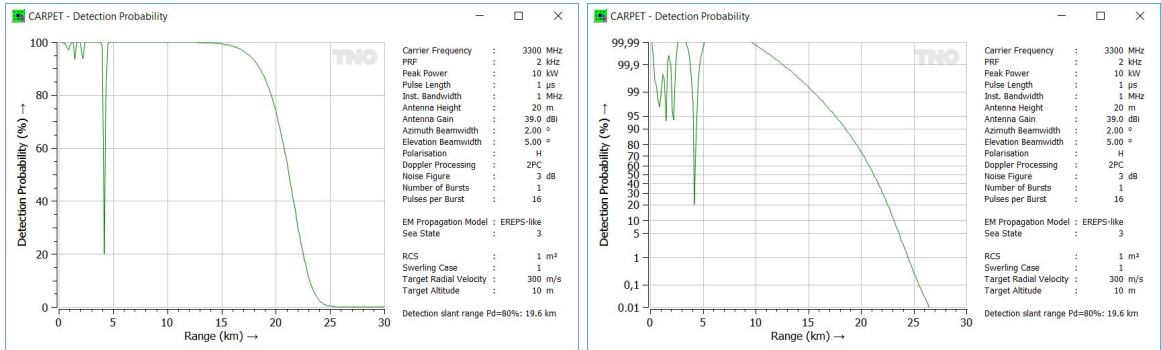


Figure 3.37:  $P_d$  over range diagrams. Left: no funny scaling of the vertical axis. Right: funny scaling.

### Draw Altitude Vertically

When switched on, target altitude is displayed along the vertical axis in diagrams where target altitude is varied, see Figure 3.38.

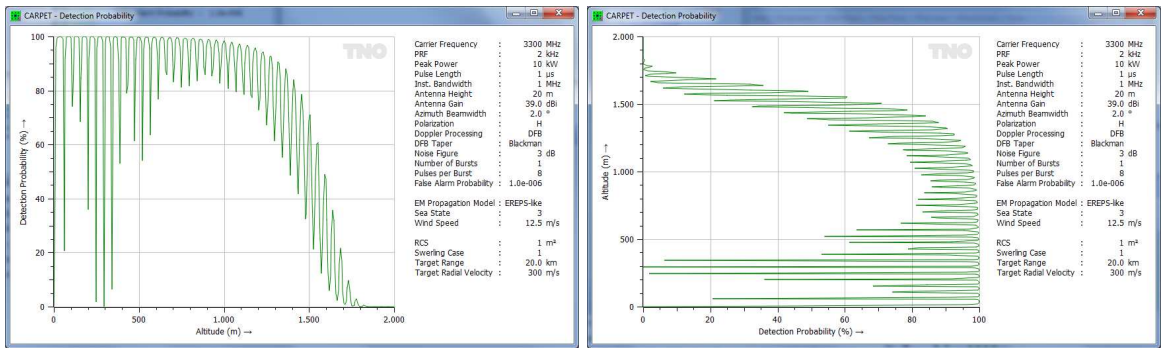


Figure 3.38: Altitude along the horizontal axis (left) and along the vertical axis (right).

### Contour # 1, Contour # 2, Contour # 3

When one or multiple of these checkboxes are marked, contours are drawn rather than a (colourful) spectrogram diagram, for instance in the  $P_d$  versus range and altitude diagram, see Figure 3.39. Up to three contours can be penciled. The contour values can be specified at the right of the checkboxes. led. The contour values can be specified at the right of the checkboxes.

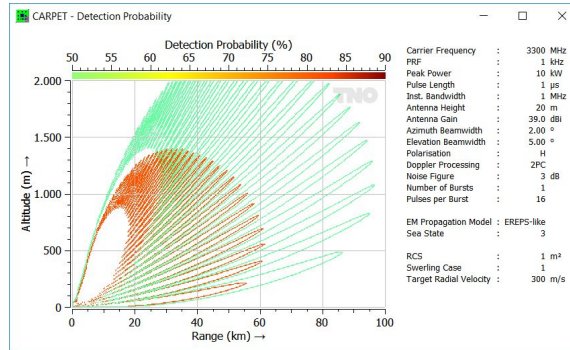


Figure 3.39: Vertical coverage diagrams. The detection probabilities 50% (green) and 90% (red) are drawn as contours.

### Polar Antenna Pattern

When switched on, antenna pattern diagrams are displayed in polar format, see Figure 3.40.

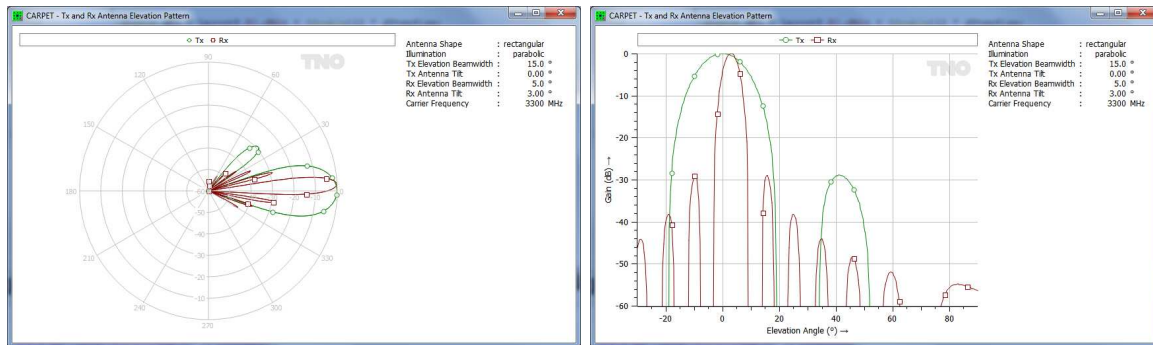


Figure 3.40: Left: Antenna patterns depicted in polar format. Right: Cartesian format.

### Transparency

This quantity is only relevant if the TERPEM plug-in is present. In case of a PPI-view diagram (*e.g.*, detection probability or firm track probability over land, line of sight diagram), the transparency of the colour can be defined, see Figure 3.41.

Default value: 0.4. Minimum value: 0.1. Maximum value: 1.0.

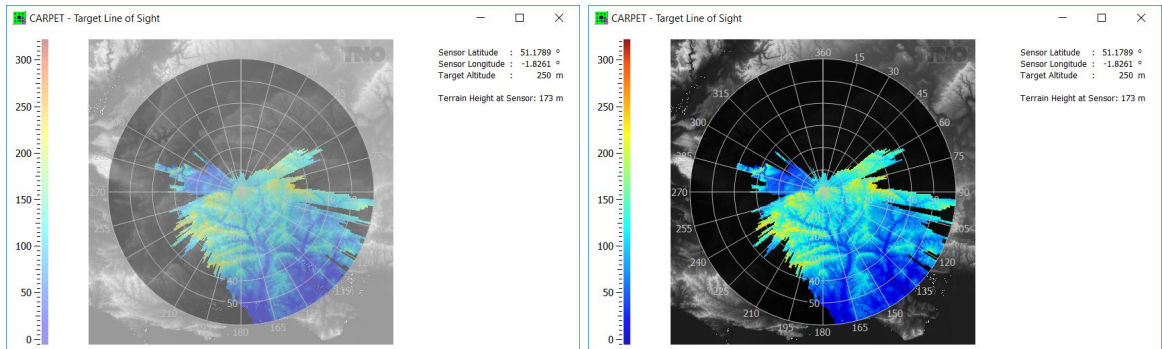


Figure 3.41: Line-of-sight diagrams (see Section 4.4). Left: transparency is 0.4. Right: transparency is 0.9.

### Write Date and Time in Legend

When switched on, a date and time string, formatted `yyyymmdd_hhmmss`, is written in the legend.

### Activate Plot Picker

When switched on, the coordinates of the cursor are displayed in certain diagrams (such as the  $P_d$  versus range diagram), see Figure 3.42.

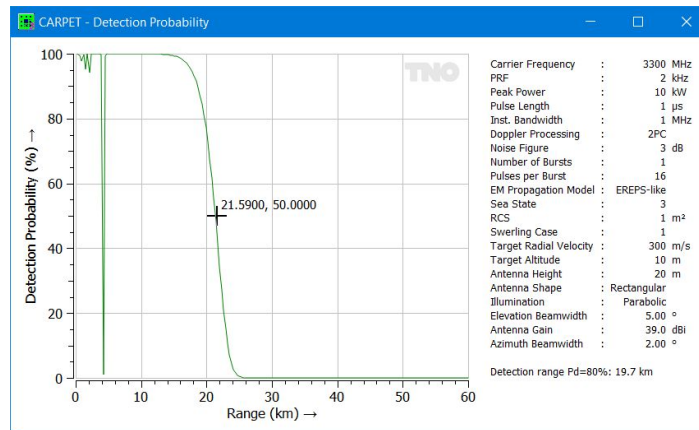


Figure 3.42: Diagram when the plot picker is activated.

### Dark Mode

When switched on, the GUI switches to dark mode, see Figure 3.43.

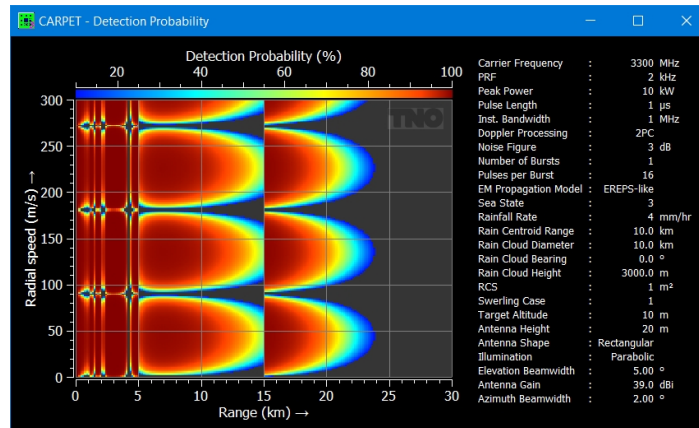


Figure 3.43: Diagram when dark mode is switched on.

### Font Size

The font size in the dialogboxes and in the graphical output can be adjusted. Note: CARPET must be re-started to see the effect.

### 3.18.4 Colours

#### Colour Scheme

Either the Jet, Jet<sup>2</sup>, Jet<sup>3</sup>, Viridis or User Defined colour scheme can be chosen, see Figure 3.44. Viridis is more appropriate for the colourblind; it doesn't have red and green (which colourblind find hard to distinguish). Furthermore the brightness between low and high values is different, see Nathaniel Smith and Stéfan van der Walt, [17]. Also in case a black-and-white copy is made of CARPET's colourful output, Viridis is to be preferred. In coastal regions, Jet<sup>2</sup> and Jet<sup>3</sup> may be preferred over Jet. If User Defined is selected, the table with RGB-values is consulted when painting the diagram.

Default value: Jet. Other values: Jet<sup>2</sup>, Jet<sup>3</sup>, Viridis, User Defined.

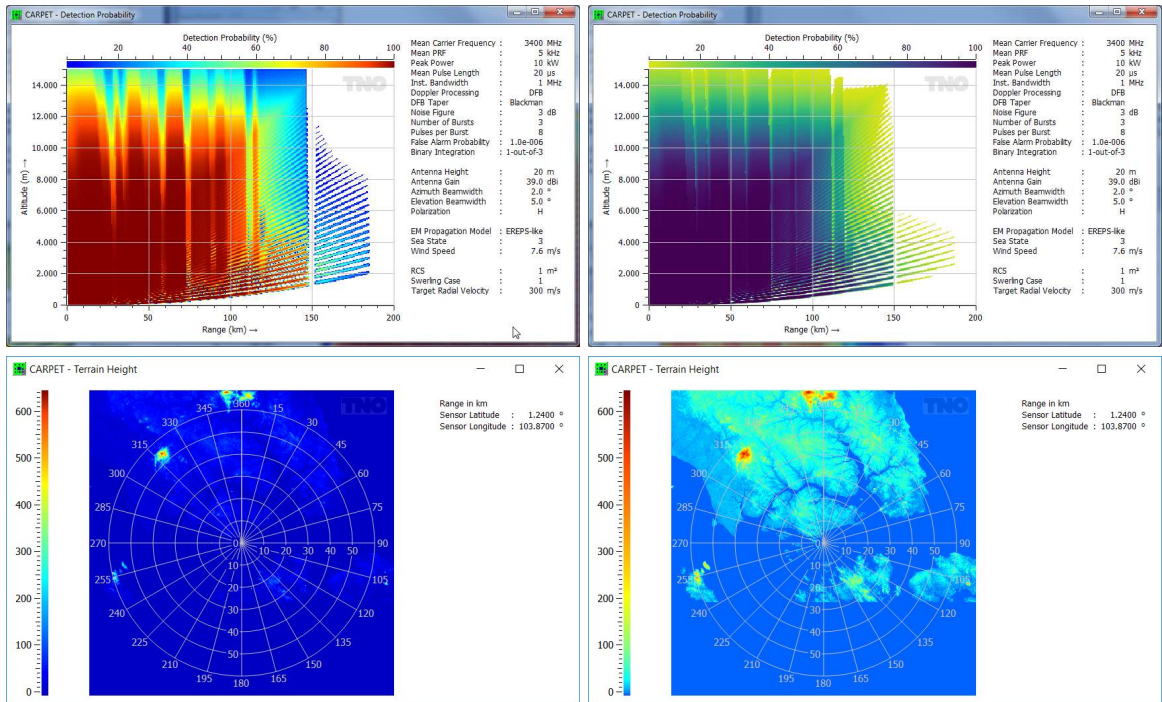


Figure 3.44: Top-left: Jet colour scheme. Top-right: Viridis colour scheme. Bottom: terrain height diagrams, Jet colour scheme (left) and Jet<sup>3</sup> colour scheme (right).

### Fixed Colours

In the on-position colours are not interpolated, an example is given in Figure 3.45. Default value: off. Other values: on.

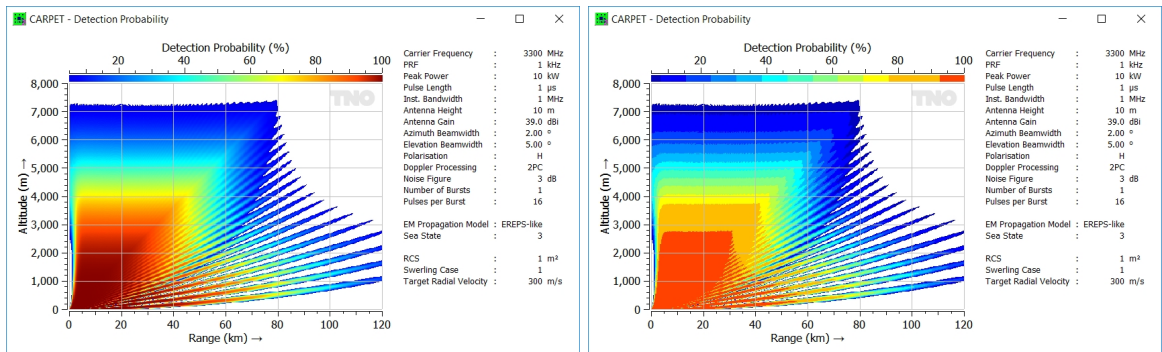


Figure 3.45: Left: fluent colours. Right: fixed colours.

### RGB-table



In case a user defined colour scheme is selected, CARPET consults the colour values in the RGB (Red Green Blue) table. *E.g.*, assume that one wishes, for some reason, to utilise the colours of the Italian flag in a CARPET diagram. The RGB values of the three colours are (0,146,70) (green-ish), (255,255,255) (white) and (206,43,55) (red-ish). The RGB-table filled with these colours and the result is depicted in Figure 3.46.

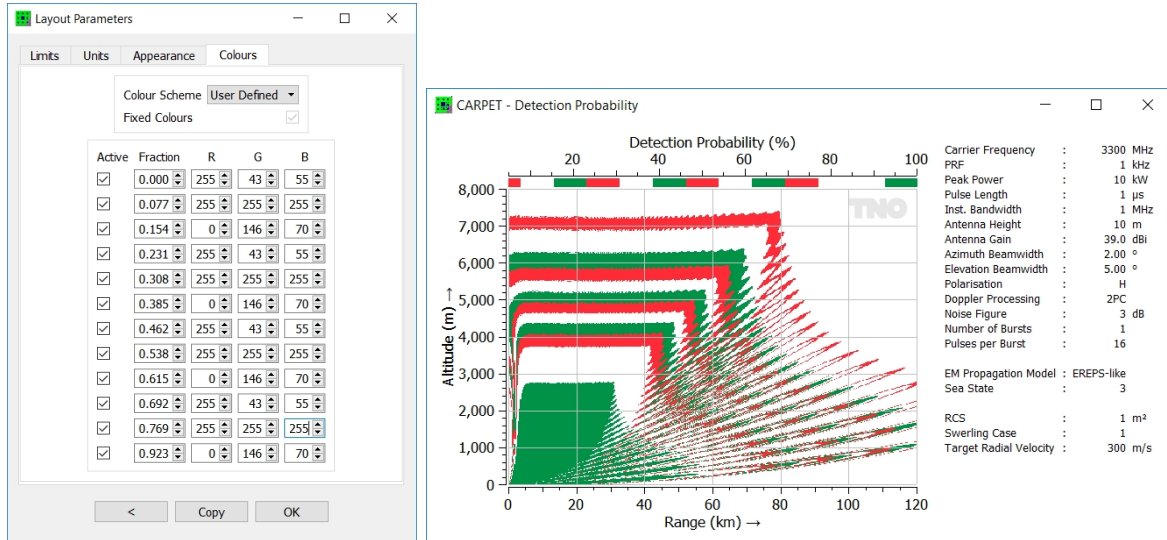


Figure 3.46: CARPET diagram with colours of the Italian flag.

The intervals in which specific colours are applied can be set with the fraction field. To illustrate this, Figure 3.47, shows the settings and emerging diagram if the colour interval is precisely 10%.

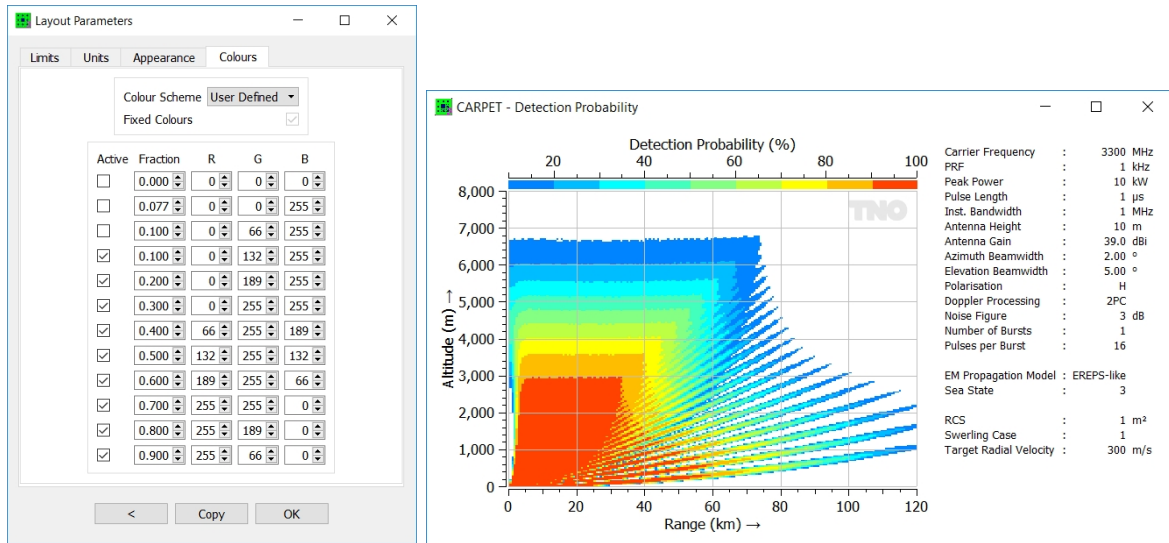


Figure 3.47: CARPET diagram with fixed colours and a 10% stepsize.

## 4 Graphical Output

### 4.1 Introduction

The graphical output of CARPET 3 is discussed in this section. This output is reachable with three pulldown-menus, shown in Figure 4.1. Diagrams under Plot-2 relate to propagation effects. The received powers, SCNR, single dwell detection probability and firm track probability diagrams are available under Plot-1. Note that the ‘performance parameter’ of CARPET 1 and 2 has disappeared, there are now sub-pulldown-menus. Plot-3 contains auxiliary diagrams, such as the antenna pattern.

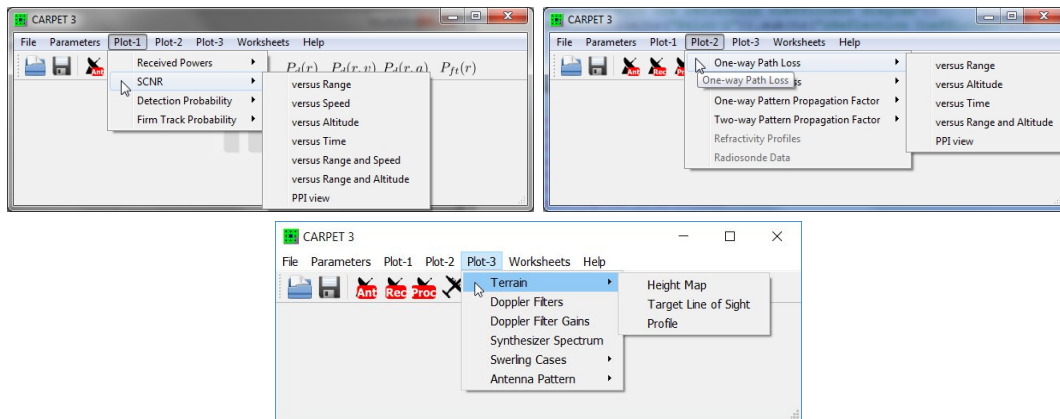


Figure 4.1: The pulldown-menus that reveal the graphical output of CARPET 3.

### 4.2 Plot-1

#### 4.2.1 Received Powers

The received powers from various sources (target, receiver noise, potentially also surface clutter, volume clutter and jamming) are plotted as a function of either ground range, velocity, altitude or time. PPI-view diagrams of the received target power and the received noise plus clutter power can also be made. The pulse compression gain (when pulse compression is applied) and the gain provided by Doppler integration (when applied) are included in the power levels that are shown.

An example of a received powers diagram is given in Figure 4.2. In this particular diagram, the received powers are calculated as a function of target range over ground. A single waveform is active, pulse responses are coherently integrated, and the received powers at the output of the Doppler filter that contains the maximum target response are shown. Received powers in case three waveforms are active, which demands the multi-burst plug-in, are shown in Figure 4.3. Received powers in case of a target made up of three scatterers,

which demands the multi-scatterer plug-in, are shown in Figure 4.4. A medium regime PRF is applied (5 kHz) which causes the gap in the middle of the curves. The uncompressed pulse length is 20  $\mu$ s and only whole received pulses are processed. The first (initial) dead zone is therefore 3 km deep ( $c\tau/2$ ), the second dead zone is twice as deep (see Section 6.9.4).

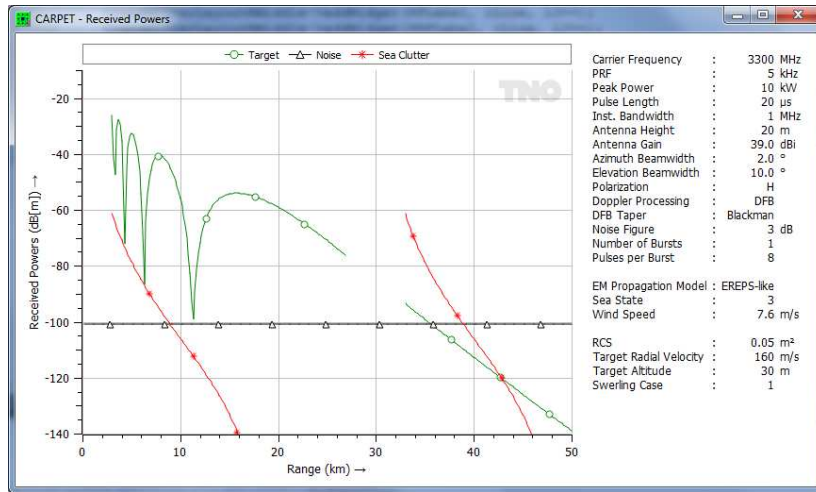


Figure 4.2: Example of a received powers diagram. A single waveform is active, the target ground range is varied.

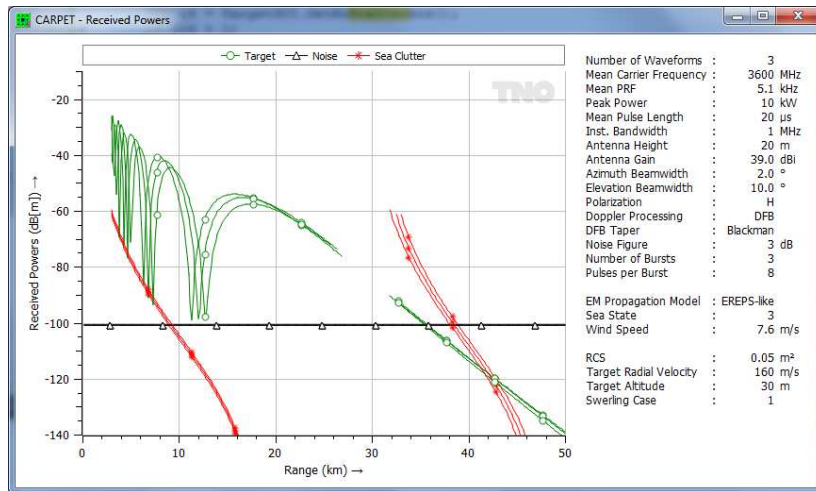


Figure 4.3: Example of a received powers diagram. Three waveforms are active.

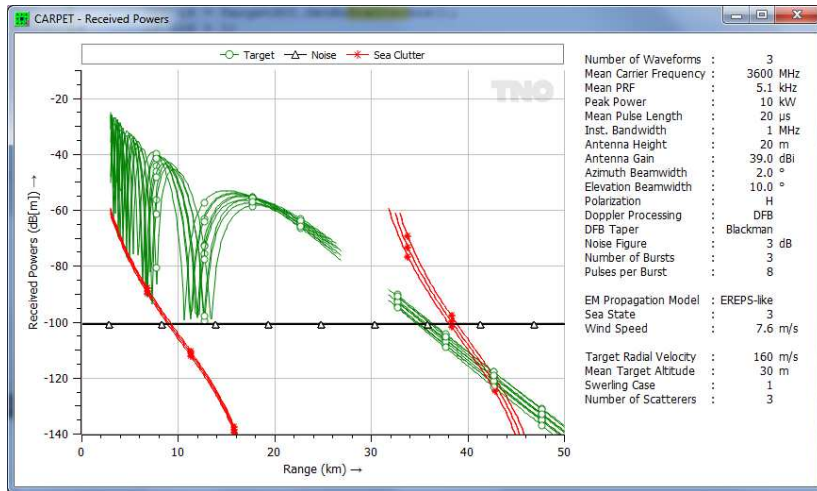


Figure 4.4: Example of a received powers diagram. Three waveforms are active, the target is made up of three scatterers.

The figures 4.5 to 4.7 shows received powers as a function of target velocity, target altitude and time.

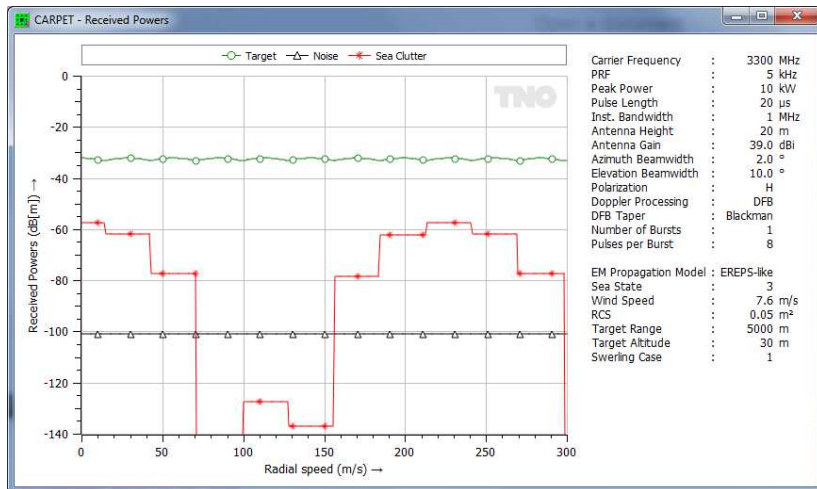


Figure 4.5: Received powers as a function of target velocity. As expected, the sea and rain clutter peaks appear at zero velocity and at target velocities corresponding to multiples of the PRF. The staircase shape of the clutter curves is caused by the fact that different Doppler filter outputs are selected as the target velocity sweeps over the specified interval.

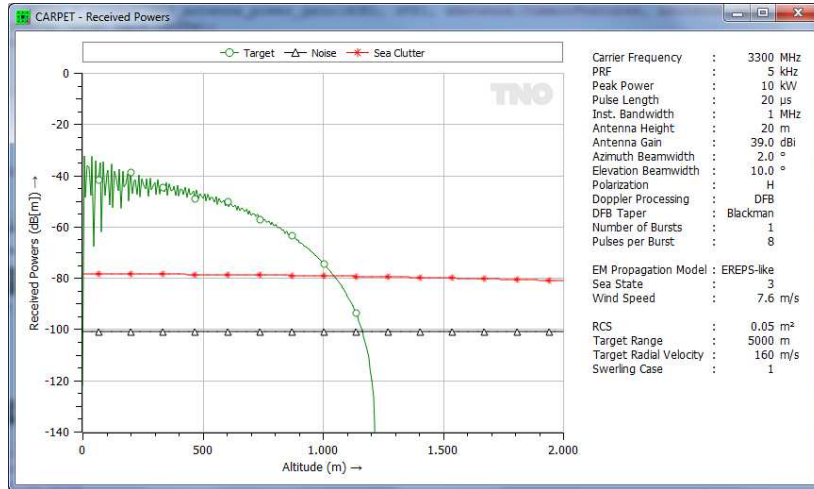


Figure 4.6: Received powers as a function of target altitude.

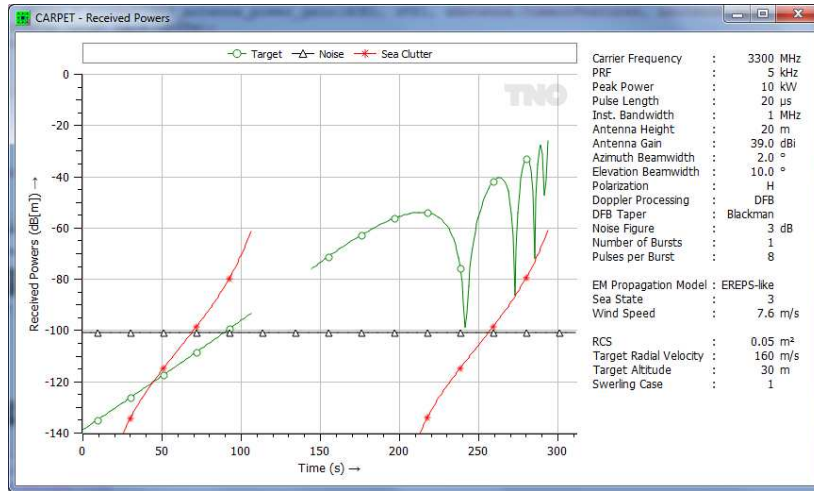


Figure 4.7: Received powers as a function of time.

Figure 4.8 shows a PPI-view diagram of received surface clutter plus jamming powers. The rings arise as a consequence of the high PRF (10 kHz). Two barrage jammers at bearings 35 and 40° illuminate the radar. Figure 4.9 shows a PPI-view diagram of received surface clutter plus volume clutter plus noise powers while the radar is positioned on top of the Matternhorn.

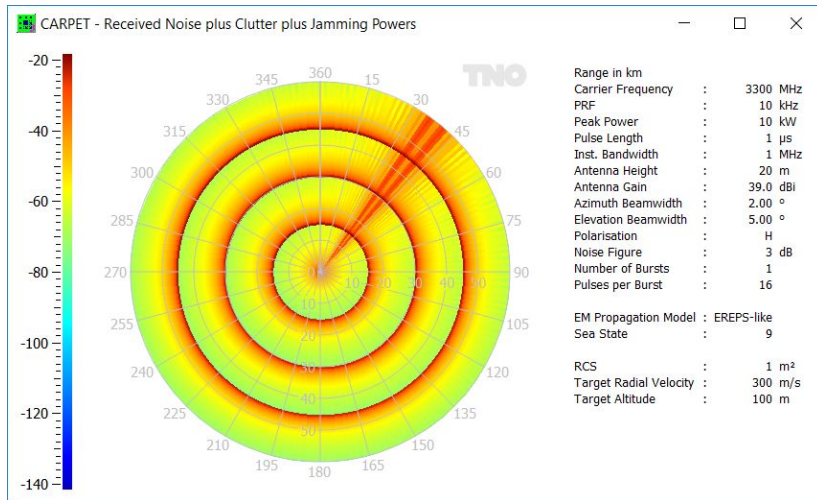


Figure 4.8: Received powers of surface clutter plus jamming plus noise as a function of range and azimuth angle.

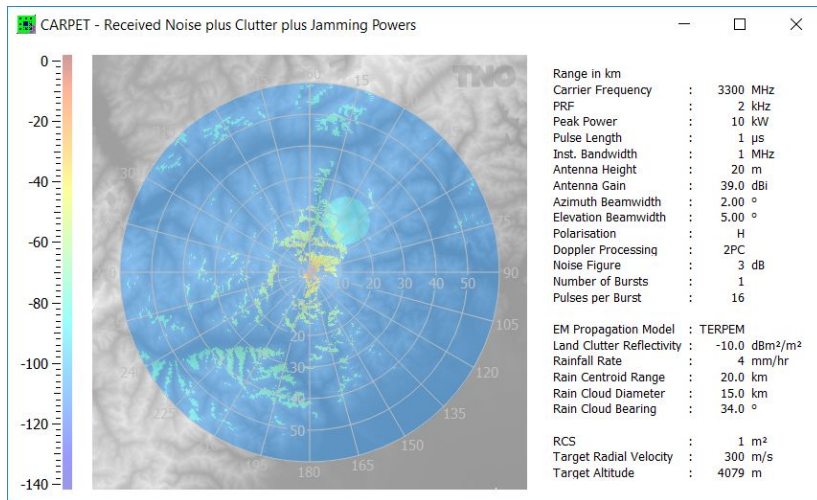


Figure 4.9: Received powers of surface clutter plus noise plus volume clutter as a function of range and azimuth angle.

### 4.2.2 SCNR

The SCNR (Signal to Clutter plus Noise Ratio) is defined as the ratio between the power of the target response to the summed power of receiver noise, surface clutter responses (if present), volume clutter response (if present) and jamming response (if present). The SCNR can be displayed as a function of target ground range, velocity, altitude and as a function of time. Three 2D color diagrams are also available, which show the SCNR as a function

of range and velocity, range and altitude and range and azimuth angle (PPI-view diagram). Examples of these diagrams are given in Figure 4.10. Figure 4.11 shows a PPI-view diagram of the SCNR, range and azimuth angle is varied. In this particular case three jammers are active (at bearings 20, 25 and 30°), while there is also a rain cloud. CARPET 3 determines these three colour-diagrams for the first active waveform (in case multiple waveforms have been specified).

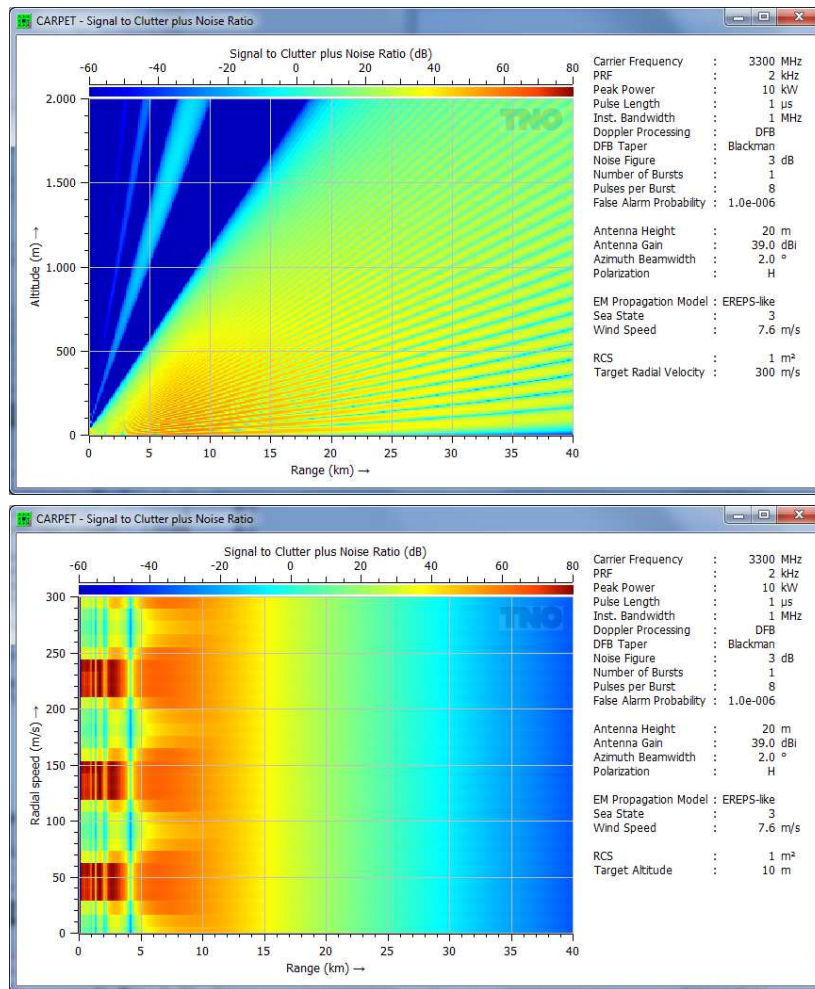


Figure 4.10: Top: SCNR as a function of range and altitude. Bottom: SCNR as a function of range and velocity.



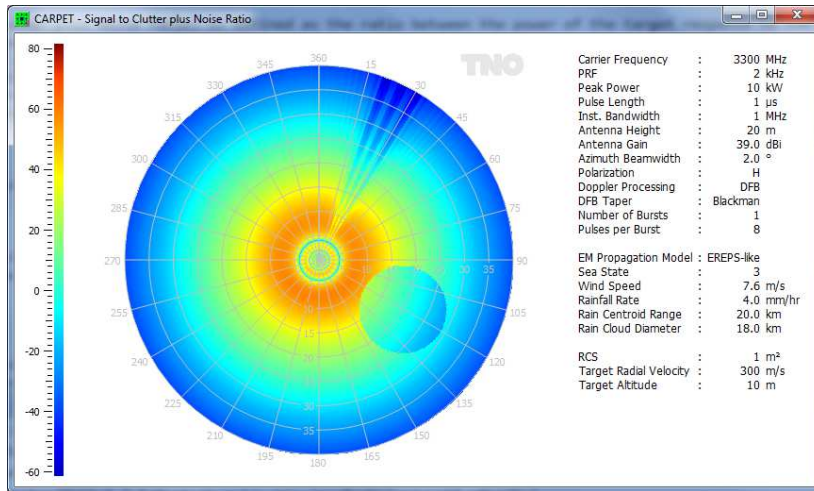


Figure 4.11: PPI-view diagram of the SCNR.

### 4.2.3 Detection Probability

The single dwell detection probability can be shown as a function of range, velocity, altitude, range and velocity, range and altitude and range and azimuth angle (PPI-view diagram). Three colourful examples are presented in Figure 4.12.

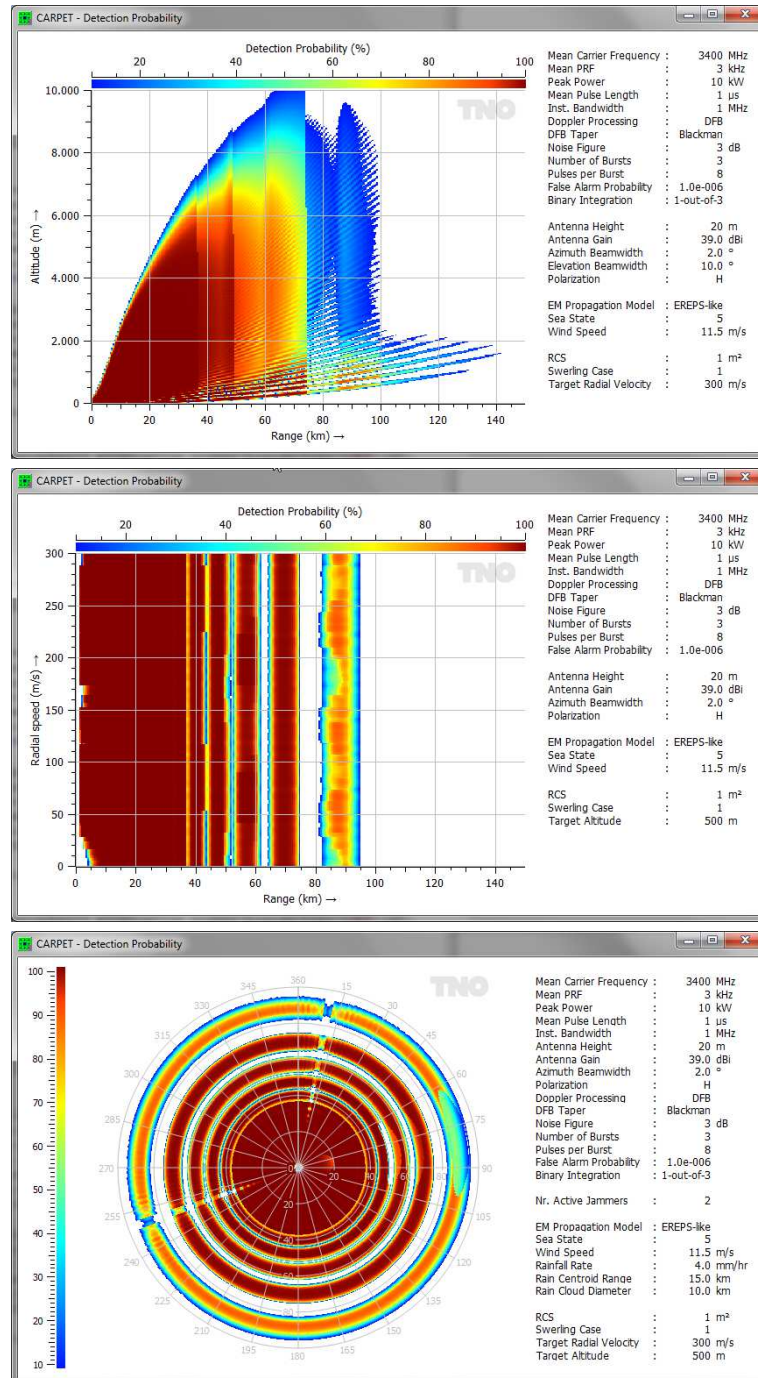


Figure 4.12: Single dwell detection probability versus range and altitude (top), range and speed (middle) and range and bearing (bottom). A waveform consisting of three different bursts is applied.

#### 4.2.4 Firm Track Probability

The firm track probability can be shown as a function of range, time, and range and bearing angle (PPI-view). The first two diagrams show the single-dwell detection probability as well, see Figure 4.13. Since the firm track probability depends on a series of detection probabilities, inbound and outbound motion result in different results, which is shown in Figure 4.13 as well.

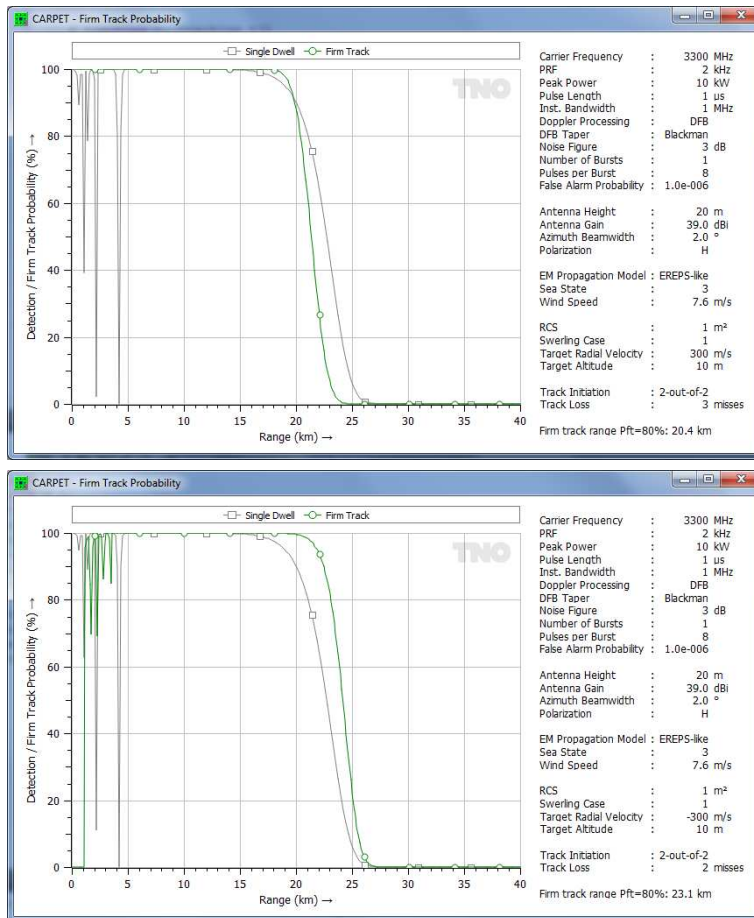


Figure 4.13: Single dwell detection probability (gray curve) and firm track probability (green curve). Top: inbound motion (radial speed 300 m/s). Bottom: outbound motion (radial speed -600 m/s).

## 4.3 Plot-2

### 4.3.1 One-way Path Loss

The one-way path loss can be shown as a function of range, altitude, time, range and altitude and range and azimuth angle (PPI-view diagram). One-way path loss is the quantity that TERPEM primarily determines. The radar equation demands the product of pattern propagation power factors,  $F_{Tx}^2 \cdot F_{Rx}^2$ , which can straightforwardly be derived from the path loss, as described in Section 6.1.8.6. Note that the shape of the elevation antenna pattern, reflection at the earth's surface and absorption by rain as well are included in the path loss (and also in the pattern propagation factor). Two examples of a path loss diagrams are shown in Figure 4.14.

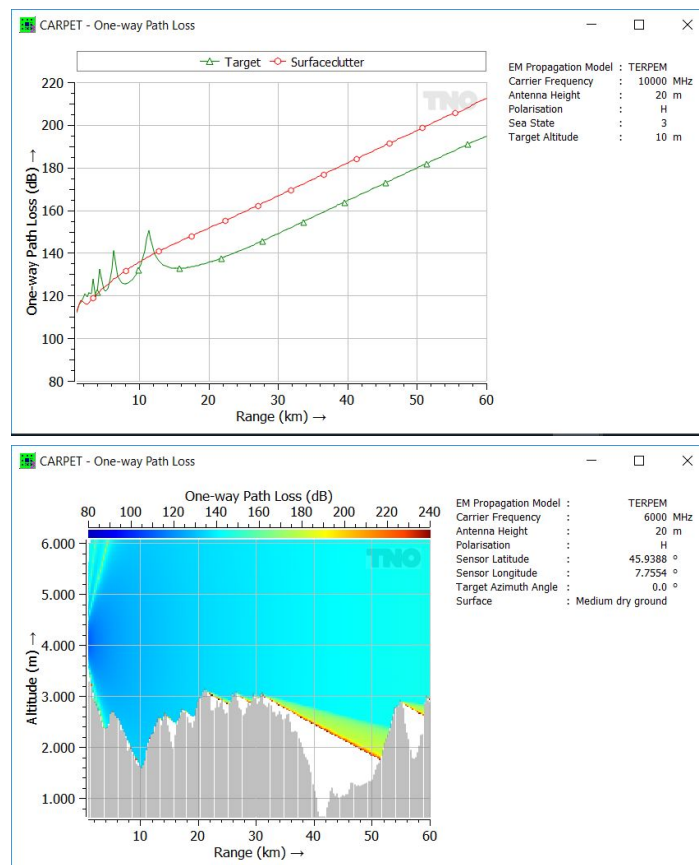


Figure 4.14: Top: One-way path loss versus range, in this case according to the TERPEM propagation model. Bottom: One-way path loss versus range and altitude. The radar is at the top of the Matterhorn, looking North.

### 4.3.2 Two-way Path Loss

The two-way path loss can be shown as a function of range, altitude, time, range and altitude and range and azimuth angle (PPI-view diagram).

### 4.3.3 One-way Pattern Propagation Factor

The one-way pattern propagation power factor ( $F_{Tx}^2$  or  $F_{Rx}^2$ ) can be shown as a function of range, altitude, time, range and altitude and range and azimuth angle (PPI-view diagram). An example is provided in Figure 4.15.

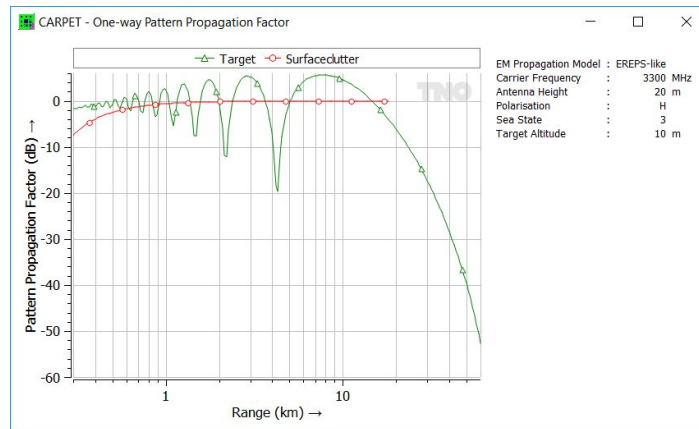


Figure 4.15: Pattern propagation power factor versus range, EREPS-like propagation model.

### 4.3.4 Two-way Pattern Propagation Factor

The two-way pattern propagation factor ( $F_{Tx}^2 \cdot F_{Rx}^2$ ), in dB (so  $10 \cdot \log_{10}(F_{Tx}^2 \cdot F_{Rx}^2)$ ), can be shown as a function of range, altitude, time, range and altitude and range and azimuth angle (PPI-view diagram).

### 4.3.5 Refractivity Profiles

In case the TERPEM plug-in has been purchased, the refractivity N-profile and the refractivity M-profile are depicted, see Figure 4.16. The diagram is not available in case the TERPEM plug-in is not active.

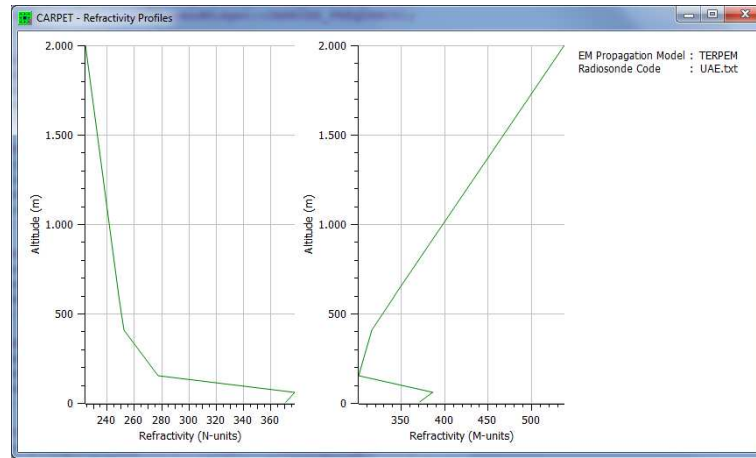


Figure 4.16: Refractivity N-profile (left) and M-profile (right). In this particular case the upper air profile was derived from radiosonde code.

#### 4.3.6 Radiosonde Data

In case the TERPEM plug-in has been purchased, the data that were measured by a weather balloon are shown, as illustrated in Figure 1.3. The diagram is not available in case the TERPEM plug-in is not active.

#### 4.3.7 ERA-15 Data

In case the ITU-R P.835 Annex 3 recipe has been selected to calculate the refractivity profile (which requires the TERPEM license), the meteo-data taken from the ERA-15 database can be shown. Figure 4.17 shows an example.

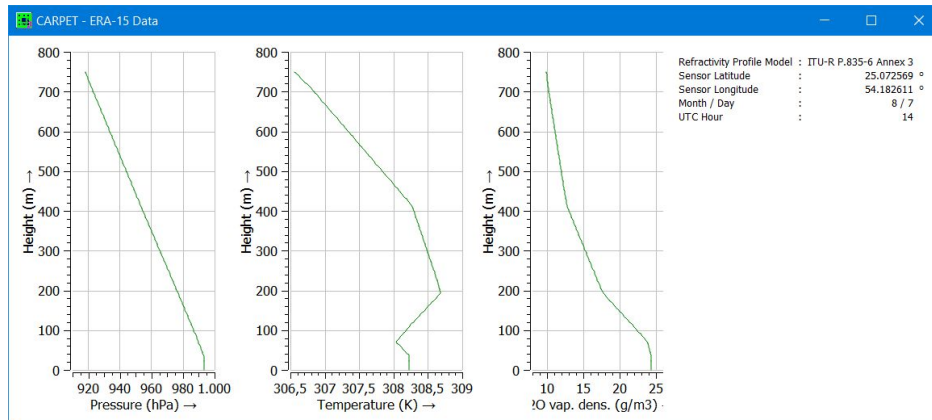


Figure 4.17: From left to right: pressure, temperature and water vapour density profiles, on August 7th, 14 UTC in the Persian Gulf area.

## 4.4 Plot-3

### 4.4.1 Terrain

Six diagrams are available in case:

- The directory that contains the terrain altitude (*i.e.*, SRTM3 or SRTM1) tiles has been specified.
- The sensor location is other than 'At Sea / On Flat Ground'.
- A TERPEM license is available.

#### 4.4.1.1 Height Map - Polar

A terrain height map with the radar location in the centre of the map is shown, as illustrated in Figure 4.18.

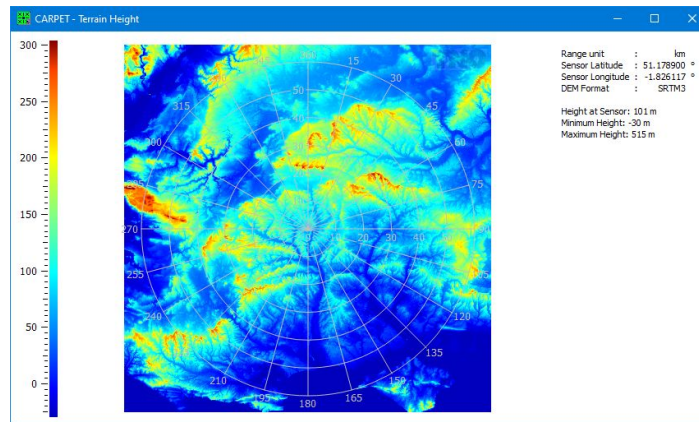


Figure 4.18: Terrain height map. In this case the radar is located close to Stonehenge (near Amesbury, UK).

#### 4.4.1.2 Height Map - Lat/Long

A terrain height map with the radar location in the centre of the map is shown, as illustrated in Figure 4.19.

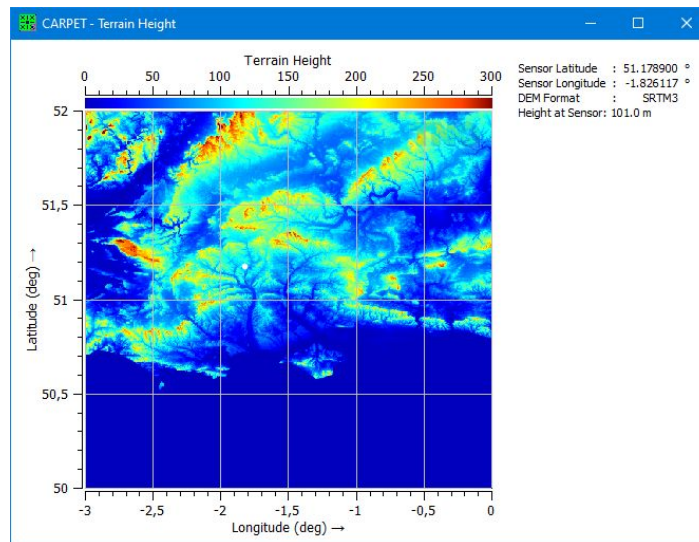


Figure 4.19: Terrain height map. In this case the radar is located close to Stonehenge (near Amesbury, UK).



#### 4.4.1.3 Line of Sight

This diagram shows the terrain that is visible from the position of the antenna, as illustrated in Figure 4.20. Visible terrain is shown in colour, the background is depicted in black and white.

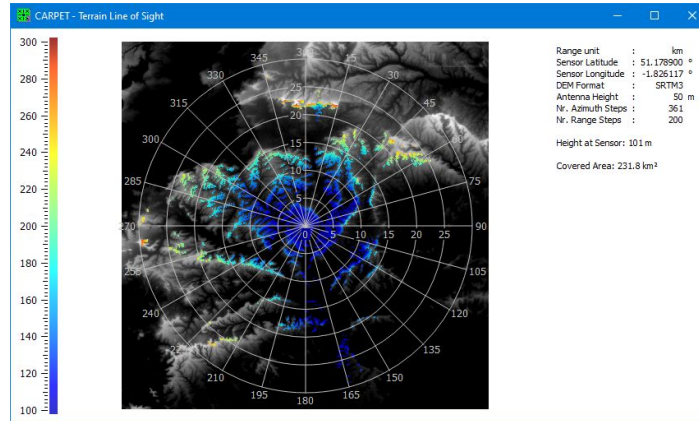


Figure 4.20: Diagram showing line-of-sight to the terrain.

#### 4.4.1.4 Profile Straight

The terrain profile for a given azimuth angle (bearing) is shown, as illustrated in Figure 4.21. A red coloured line means that there is no line-of-sight to the terrain.

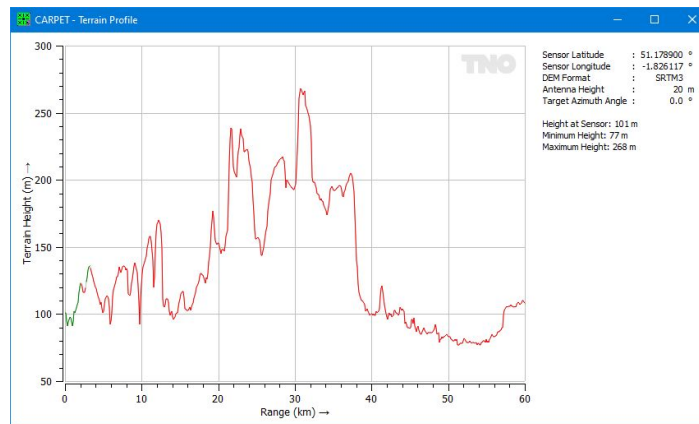


Figure 4.21: Terrain height map. In this case the radar is located close to Stonehenge (near Amesbury, UK).

#### 4.4.1.5 Profile Curved

The terrain profile for a given azimuth angle (bearing) is shown, while taking into account the earth's curvature, as illustrated in Figure 4.22. A red coloured line means that there is no line-of-sight to the terrain.

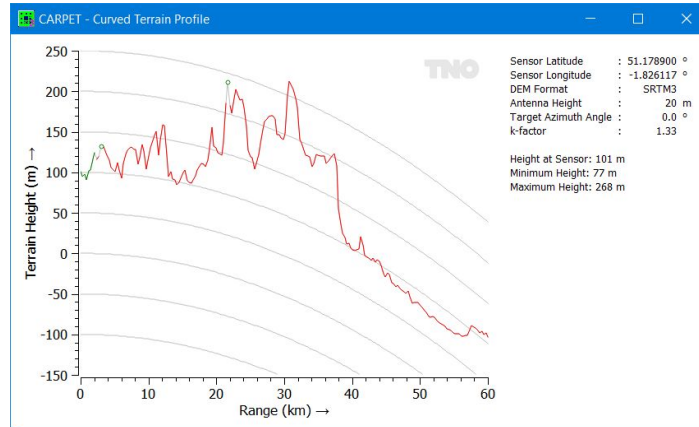


Figure 4.22: Terrain height map. In this case the radar is located close to Stonehenge (near Amesbury, UK).

#### 4.4.1.6 All Profiles

A terrain height map with the radar location in the centre of the map is shown, as illustrated in Figure 4.23.

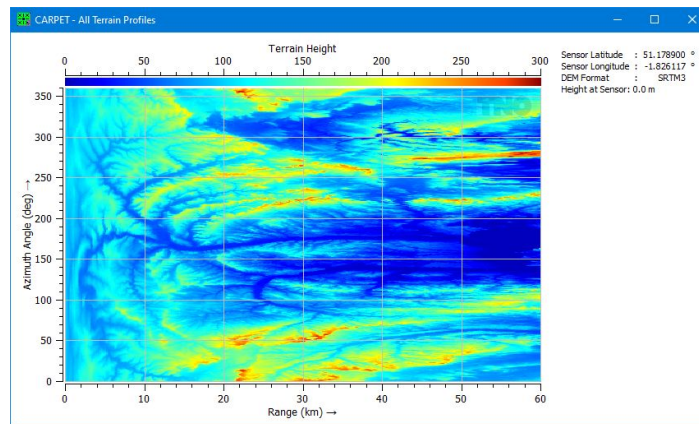


Figure 4.23: Terrain height map. In this case the radar is located close to Stonehenge (near Amesbury, UK).

#### 4.4.2 Target Line of Sight

The diagrams shows where a target at a specific altitude is optically visible. The earth's radius is, however, modified with the co-called k-factor. Figure 4.24 illustrates how line-of-sight is determined, in this case for a target that travels at a constant altitude. The target is visible if the line connecting the target to the radar antenna is not blocked by the terrain profile. Examples of target line of sight diagrams have already been given in Figure 3.41. Examples that shows the blocking of the Monte Rosa massif when a radar sensor is placed on the top of the Matterhorn are shown in Figure 4.25, both for a target at a fixed altitude and for a terrain following target.

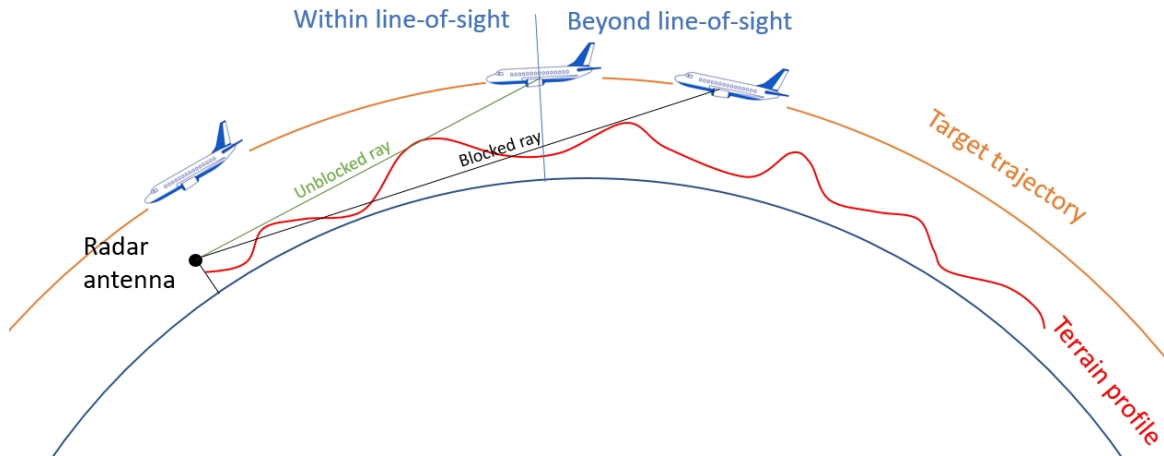


Figure 4.24: Line-of-sight is determined by comparing elevation angles to the target with elevation angles to patches of the terrain profile. In this particular case, the target travels at a constant altitude (not terrain-following).

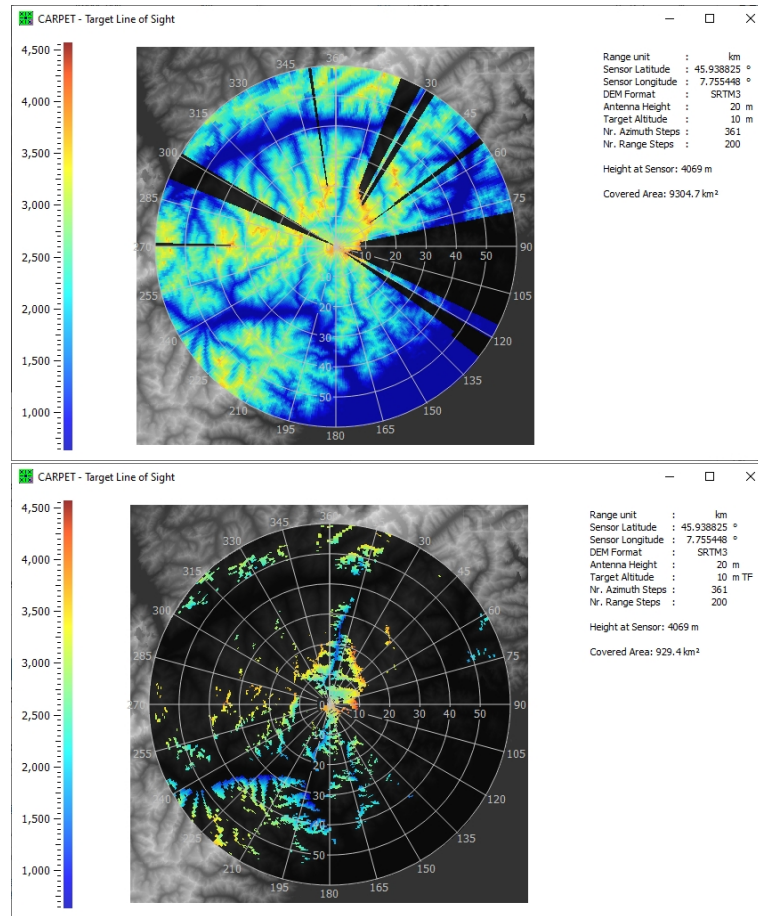


Figure 4.25: Line-of-sight diagrams, the Monte Rosa massif is east of the Matterhorn. Top: the target altitude is 10 m higher than the altitude of the Matterhorn (AMSL). Bottom: the target altitude is 10 m above the local terrain (terrain following).



### 4.4.3 Doppler Filters

This diagram shows response curves of the various Doppler filters. In case of multiple bursts per dwell, the diagram gets fairly crowded, as shown in Figure 4.26. The curves of the filter(s) that match the radial velocity of the target are painted in colors, all other curves are drawn in gray.

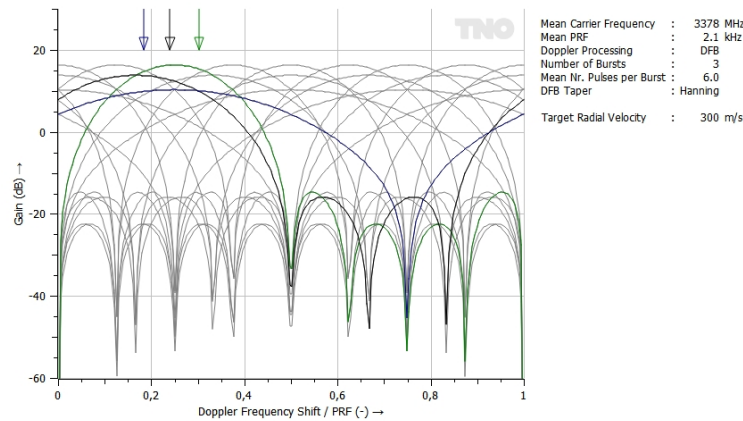


Figure 4.26: Receiver operating curves.

### 4.4.4 Doppler Filter Gains

The diagram reveals the Doppler Filter gain that the target, surface clutter, volume clutter and jamming components of the received signal experience, versus the radial velocity of the target. An example is shown in Figure 4.27.

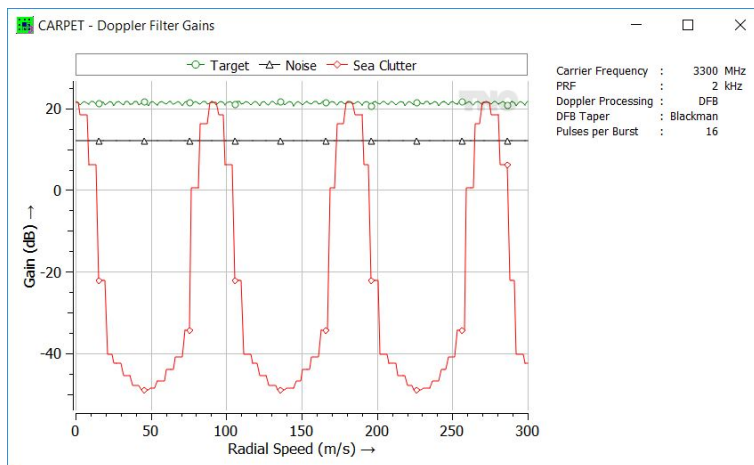


Figure 4.27: Doppler filter gain versus target radial speed.

#### 4.4.5 Synthesizer Spectrum

This diagram shows the phase noise spectrum of the synthesizer used in the radar transmitter. The synthesizer phase noise consists of two components: white noise and coloured noise with a slope of 20 dB/decade. Figure 4.28 gives a typical spectrum.

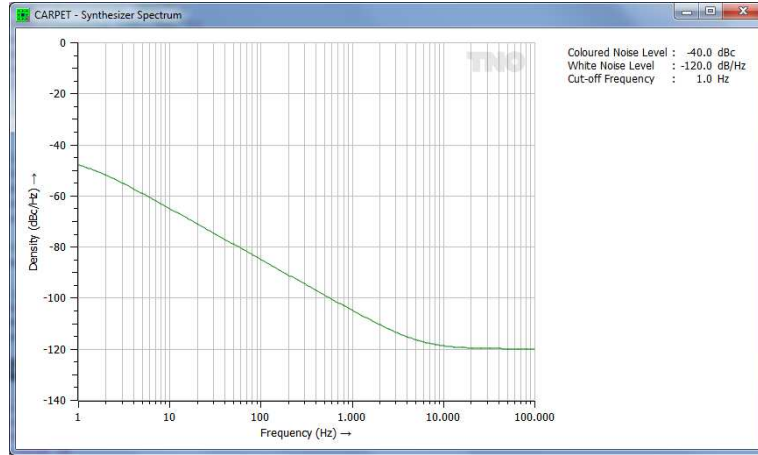


Figure 4.28: Example of synthesizer spectrum.

## 4.4.6 Swerling Cases

### 4.4.6.1 Detection Probability versus SNR

This diagram presents the receiver operating curves for the five Swerling cases (nonfluctuating case = Swerling 0) as a function of the signal-to-noise ratio (SNR), given a specified probability of false alarm and number of non-coherently integrated responses. Figure 4.29 shows the curves for a false-alarm probability of  $10^{-6}$  and 10 responses.

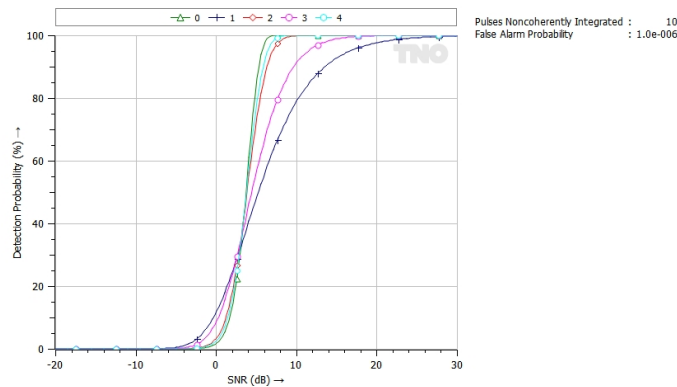


Figure 4.29: Receiver operating curves.

### 4.4.6.2 Fluctuation Loss versus SNR

Fluctuation loss is defined as the increase in the SNR that is required to achieve the same detection and false alarm probability as if the target was nonfluctuating. Figure 4.30 shows an example.

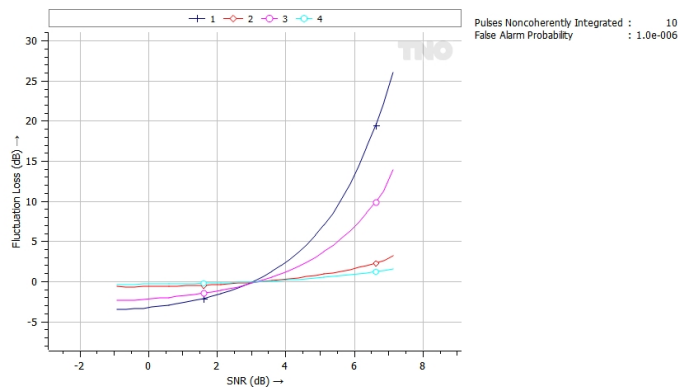


Figure 4.30: Fluctuation loss versus SNR. Above 3 dB SNR a nonfluctuating target is easier to detect, and a Swerling 3 target (purple) is easier to detect than a Swerling 1 target (black).

### 4.4.6.3 Detection Probability versus Fluctuation Loss

The detection probability versus the fluctuation loss is shown for the several Swerling cases, see Figure 4.31.

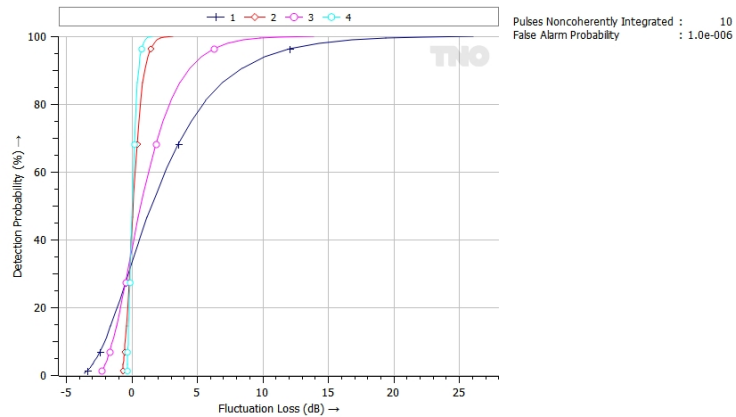


Figure 4.31: Detection probability versus fluctuation loss.

### 4.4.7 Antenna Pattern

The antenna elevation pattern on transmit and/or on receive can be depicted in either polar or cartesian format, as illustrated in Figure 4.32. The elevation angle span can be set in the Layout dialogbox, as discussed in Section 3.18.

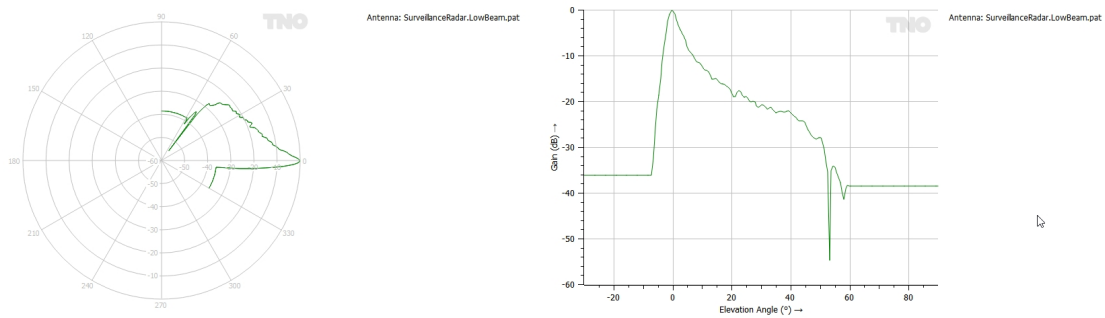


Figure 4.32: Examples of antenna pattern diagrams.



## 4.5 Keyhole Markup Language

Right clicking on a PPI-view diagram enables to save the diagram accompanied by a so-called KML (Keyhole Markup Language) file. By importing the KML file in Google Earth, the diagram will be shown as overlay in Google Earth, see Figure 4.33. Note that detection probability contours can be enabled as well.

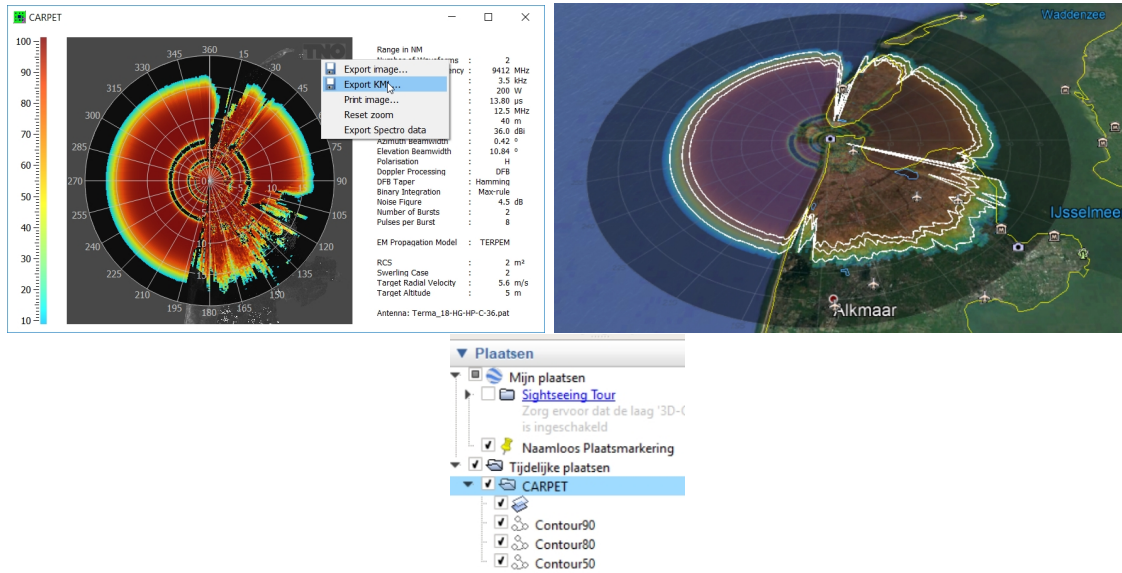


Figure 4.33: Illustration of the KML feature of CARPET 3. At the top-right is the Google Earth picture. The white contour-lines at 90, 80 and 50 % can be switched off (bottom picture).

## 4.6 GeoTIFF

A PPI-view diagram can also be saved in GeoTIFF, which is an open extension of the TIFF; geospatial meta-data have been added to the image. Right-click on the diagram and select 'Export Spectro data'. GeoTIFF can readily be imported in programs such as Quantum GIS (QGIS) and ArcGIS, an example is provided in Figure 4.34. Note: the number of range-points determines the spatial resolution of the GeoTIFF picture.

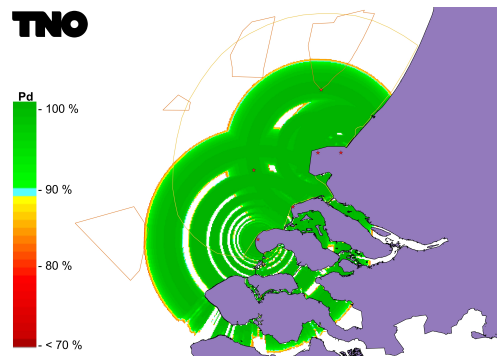


Figure 4.34: Illustration of CARPET's GeoTIFF output, imported in Quantum GIS.

## 5 Worksheets

### 5.1 Introduction

The worksheets listed in the worksheet pulldown menu shown in Figure 5.1 allow a fast and easy access to numerical data found in many radar and propagation handbooks. The worksheets also provide a way to check the results of radar system performance calculations in CARPET. The well-known Blake Chart has also been added to CARPET 3, this particular worksheet was not present in CARPET 1 and 2.

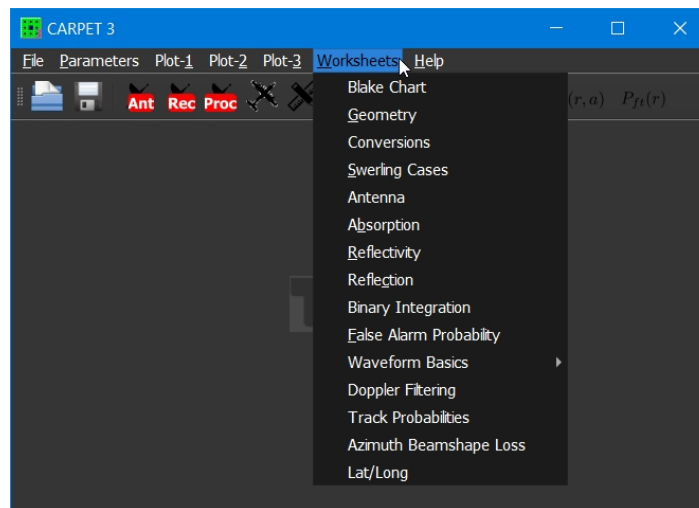


Figure 5.1: The pulldown menu that gives access to the CARPET worksheets.

### 5.2 Blake chart

Radar models such as CARPET are based upon (or inspired by) the Blake chart, a spreadsheet-like form, called worksheet, with which maximum detection range is determined. The worksheet was proposed in 1962 by Lamont Blake, [18] and it is discussed in several well-known textbooks on radar, such as Dave Barton, [19]. The original worksheet is shown in Figure 5.2.

PULSE-RADAR RANGE-CALCULATION WORK SHEET

Based on Eq. (13)

1. Compute the system input noise temperature  $T_s$ , following the outline in section A below.
2. Enter range factors known in other than decibel form in section B below, for reference.
3. Enter logarithmic and decibel values in section C below, positive values in the plus column and negative values in the minus column. For example, if  $V_0$  (dB) as given by Figs. 4 through 9 is negative, then  $-V_0$  (dB) is positive and goes in the plus column. For  $C_B$ , see Figs. 1 through 3. For definitions of the range factors, see Eq. (13).

Radar antenna height: $h =$ ft.		Target elevation angle: $\theta =$ °. (See Fig. 13.)	
<b>A. Computation of <math>T_s</math>:</b> $T_s = T_a + T_r + L_r T_e$			
(a) Compute $T_a$ . For $T_{id} = T_{ra} = 290$ and $T_g = 36$ use Eq. (37a). Read $T'_a$ from Fig. 11. $L_{a(dB)}$ : _____ $L_s$ : _____ $T_a = (0.876 T'_a - 254)/L_s + 290$ $T_a =$ _____ °K			
(b) Compute $T_r$ using Eq. (40). For $T_{rr} = 290$ use Table 1. $L_{r(dB)}$ : _____ $T_r =$ _____ °K			
(c) Compute $T_e$ using Eq. (41) or using Table 1. $F_n$ (dB): _____ $T_e$ : _____ °K $L_r$ : _____ $L_r T_e =$ _____ °K Add. $T_s =$ _____ °K			
<b>B. Range Factors</b>		<b>C. Decibel Values</b>	
$P_t$ (kW)		$10 \log P_t$ (kW)	Plus (+) Minus (-)
$f_{pulse}$		$10 \log f_{pulse}$	
$G_t$		$G_t$ (dB)	
$G_r$		$G_r$ (dB)	
$\sigma$ (sq m)		$10 \log \sigma$	
$f_{MHz}$		$-20 \log f_{MHz}$	
$T_0$ (°K)		$-10 \log T_0$	
$V_0$		$-V_0$ (dB)	
$C_B$		$-C_B$ (dB)	
$L_t$		$-L_t$ (dB)	
$L_p$		$-L_p$ (dB)	
$L_x$		$-L_x$ (dB)	
Range-equation constant ( $40 \log 1.292$ )			4.45
4. Obtain the column totals			
5. Enter the smaller total below the larger			
6. Subtract to obtain the net decibels (dB)			
7. In Table 2 find the range ratio corresponding to this net decibel (dB) value, taking its sign (+) into account. Multiply this ratio by 100. This is $R_0$			
8. Multiply $R_0$ by the pattern-propagation factor (see Eqs. (42) through (65) and Figs. 12 through 19):			
$F =$ _____			
$R_0 \times F = R'$			
9. On the appropriate curve of Figs. 21 and 22 determine the atmospheric-absorption loss factor, $L_{a(dB)}$ , corresponding to $R'$ . This is $L_{a(dB)(1)}$			
10. Find the range factor $\delta_1$ corresponding to $-L_{a(dB)(1)}$ from the formula $\delta = \text{antilog}(-L_{a(dB)}/40)$ or by using Table 2.			
11. Multiply $R'$ by $\delta_1$ . This is a first approximation of the range $R_1$ .			
12. If $R_1$ differs appreciably from $R'$ , on the appropriate curve of Figs. 21 and 22, find the new value of $L_{a(dB)}$ corresponding to $R_1$ . This is $L_{a(dB)(2)}$ .			
13. Find the range-increase factor (Table 2) corresponding to the difference between $L_{a(dB)(1)}$ and $L_{a(dB)(2)}$ . This is $\delta_2$ .			
14. Multiply $R_1$ by $\delta_2$ . This is the radar range in nautical miles, $R$ .			
Note: If the difference between $L_{a(dB)(1)}$ and $L_{a(dB)(2)}$ is less than 0.1 dB, $R_1$ may be taken as the final range value, and steps 12 through 14 may be omitted. If $L_{a(dB)(1)}$ is less than 0.1 dB, $R'$ may be taken as the final range value, and steps 9 through 14 may be omitted. (For radar frequencies up to 10,000 megahertz, correction of the atmospheric attenuation beyond the $L_{a(dB)(2)}$ value would amount to less than 0.1 dB.)			

Figure 5.2: Lamont Blake's worksheet to determine detection range.

The worksheet does not consider clutter so that, unless a suitable clutter loss factor is inserted, the original Blake chart is especially useful for medium to long range radar systems, that apply a low-PRF regime. Coherent integration is also not directly included.

CARPET operates different than a Blake chart; rather than determining maximum detection range, given a required 'visibility factor' ( $V_0$  in the original worksheet, which depends on the target Swerling case, the false alarm probability, and the number of responses that is non-coherently integrated), CARPET firstly calculates an SCNR (Signal-to-Clutter-plus-Noise Ratio), and subsequently a single dwell detection probability (and perhaps a firm track probability in step 3). The Blake chart worksheet of CARPET 3 is shown in Figure 5.3.



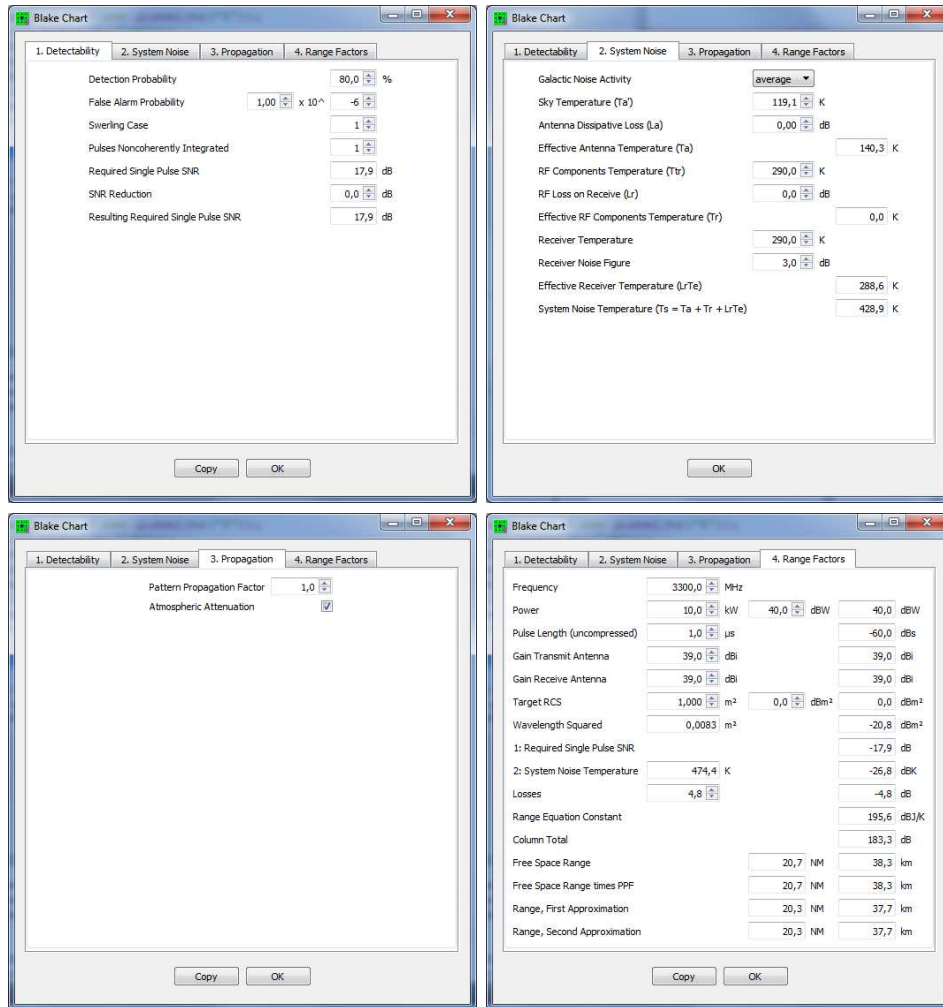


Figure 5.3: The Blake chart of CARPET 3.

The user of CARPET 3 may experience that the detection range according to the Blake chart does not correspond to the detection range that is reported when a detection probability versus range diagram or a vertical coverage diagram is made. There is a series of possible causes:

- As stated, the original Blake chart does not consider coherent integration, also post-detection binary integration is not supported. For this reason, the possibility to adapt the required single pulse SNR (in the first pane) has been added. As will be illustrated below, entering a suitable value is not straightforward.

- The antenna gains may be different. In case a detection probability versus range diagram is made, the antenna gain in the direction of the target is determined, which can differ substantially from the antenna gain that the Blake chart assumes.
- The Blake chart does not consider an instrumented range; the CARPET diagrams do.
- The Blake chart does not really have a ‘multipath model’, only a pattern propagation factor can be specified.

In order to illustrate the case that there doesn’t have to a discrepancy between the two methods to obtain maximum detection range, Figure 5.4 shows the vertical coverage diagram for a rather primitive radar system, in free space propagation conditions. Any form of pulse response integration has been disabled so the radial speed of the target doesn’t matter, all loss factors have been set to 0 dB and there is no pulse compression. Figure 5.5 shows two panes of the Blake chart. Note that the reported maximum detection ranges (29.2 km) match. One may verify that identical noise power levels have been taken, based upon a system noise temperature of 428.9 K.

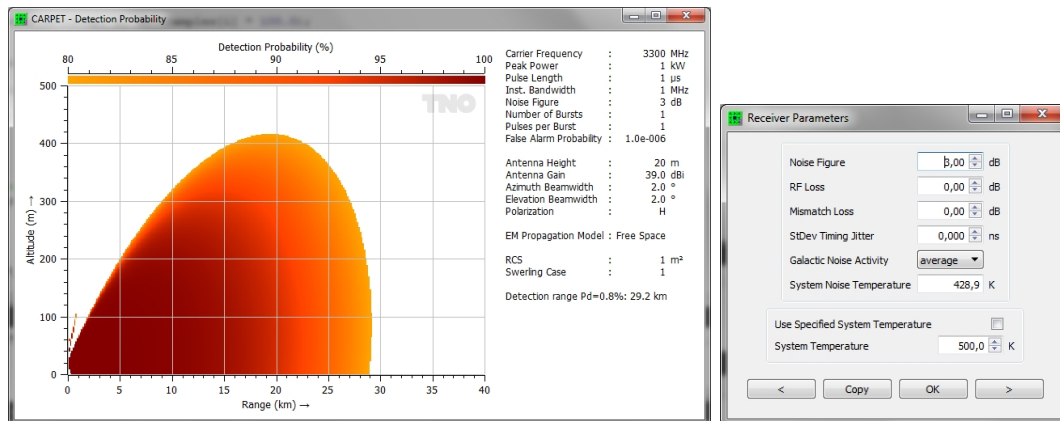


Figure 5.4: Left: Vertical coverage diagram for a simple radar in free space. Right: Receiver settings of the simple radar.

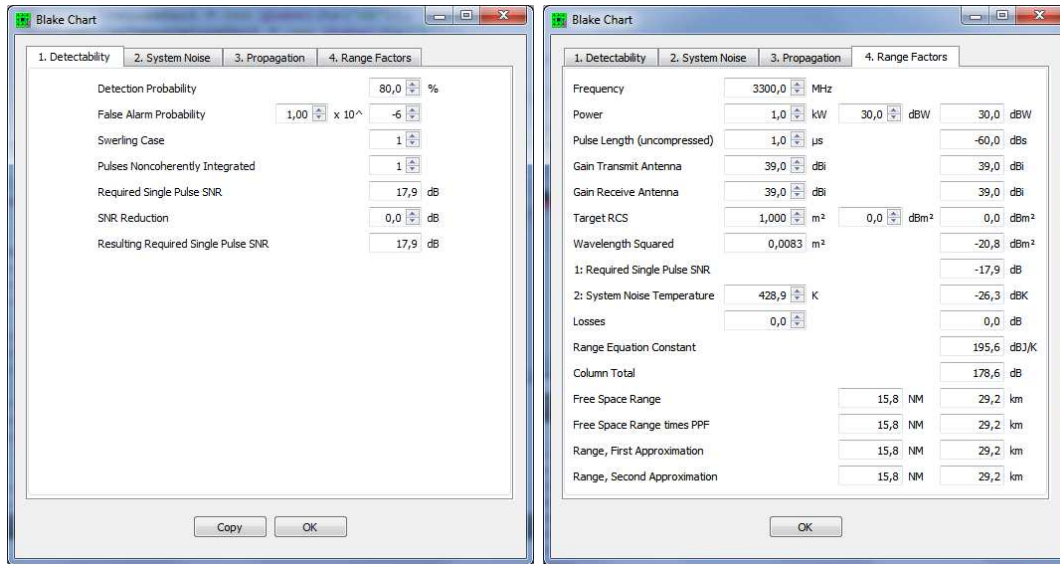


Figure 5.5: A simple radar in free space. The System Noise and Range Factors panes of the Blake chart worksheet.

Now, suppose the loss in the receive RF line is 2 dB. This will change the system noise temperature, it will go up from 428.9 K to 767.4 K so that the receiver noise floor will increase. Consequently, the detection range will go down from 29.2 to 25.3 km. The two methods provide near similar results, as shown in Figure 5.6.

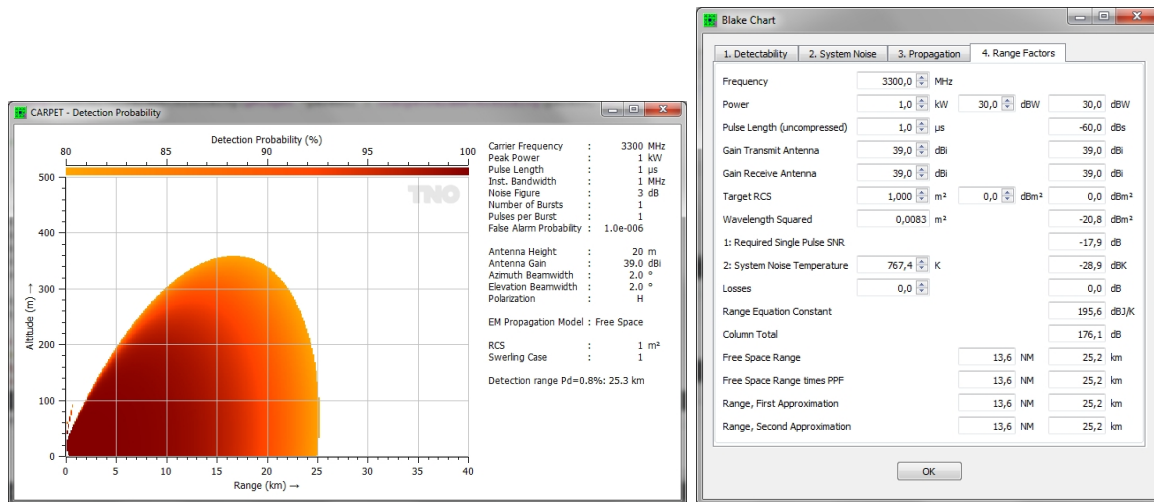


Figure 5.6: Left: Vertical coverage diagram. Right: fourth pane of the Blake chart. A loss in the receive RF line has been introduced.

The effect of pulse compression is shown in Figure 5.7. The uncompressed pulse length has been increased to 10  $\mu\text{s}$ . Again, the two methods provide similar results (44.9 km).

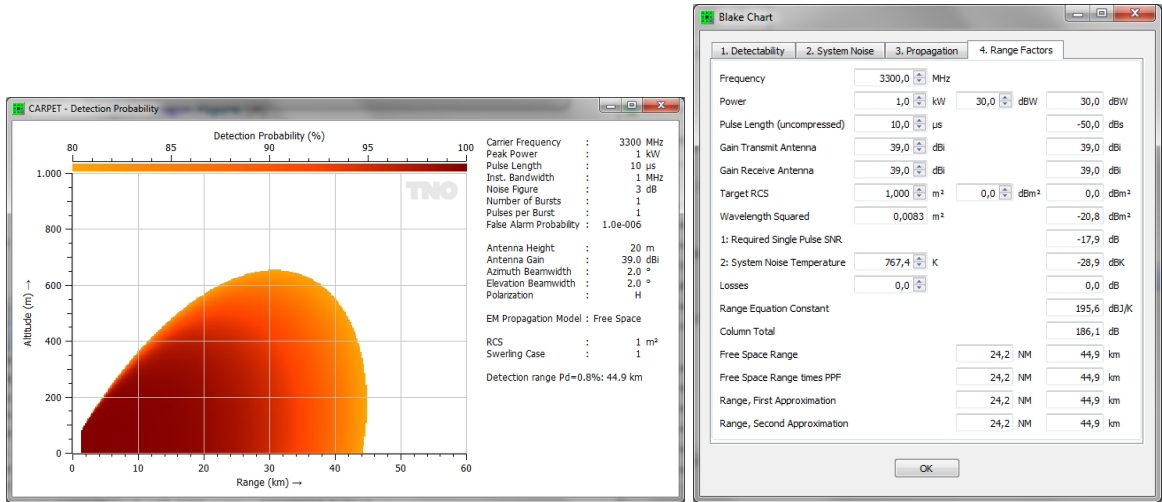


Figure 5.7: Left: Vertical coverage diagram. Right: fourth pane of the Blake chart. Pulse compression is applied.

Finally, coherent integration is introduced, the Doppler filter band is enabled and four pulses are integrated. CARPET reveals an 80% detection range of 54.9 km while Blackman tapering is applied prior to the Doppler integration. In case the required SNR in the Blake chart is diminished with 6 dB ( $10 \cdot \log_{10}(4)$ ), being the optimum Doppler integration gain) it, however, reveals a detection range of 63.4 km.



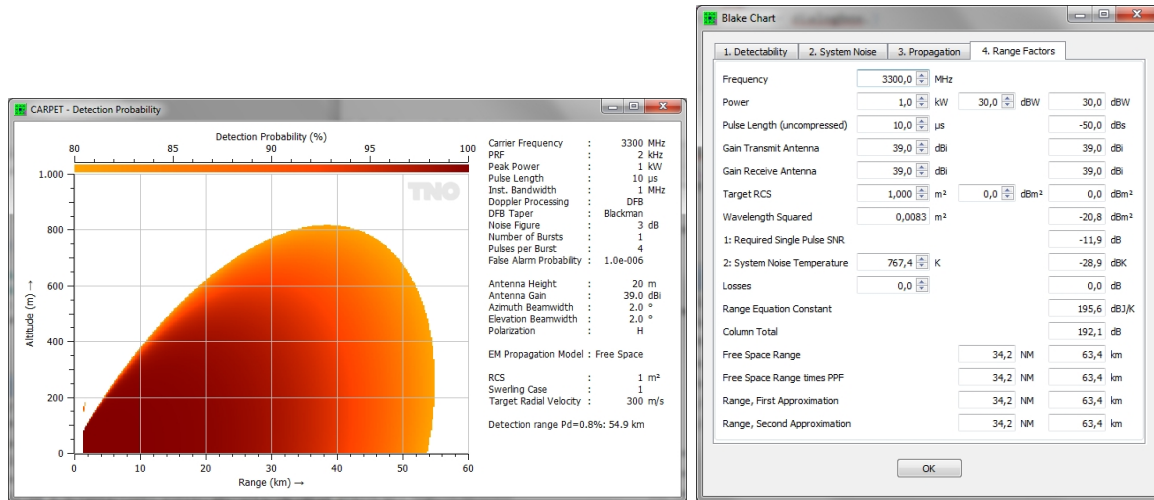


Figure 5.8: Left: Vertical coverage diagram. Right: fourth pane of the Blake chart. Four pulses are integrated coherently. The results do not match.

What causes the substantial difference? It must be artifacts (straddling loss and taper loss) of the Blackman taper, as illustrated in the Doppler Filtering worksheet.

In case a uniform taper is selected, and in case the straddling loss is minimized by 'tuning' the radial velocity of the target, the vertical coverage diagram reports a detection range which is consistent with the Blake chart. Alternatively, one can adapt the of SNR reduction filed in the first pane of the Blake chart.

### 5.3 Geometry

The Geometry worksheet, see Figure 5.9, shows the:

- Target horizon, *i.e.*, the farthest target ground range where the target appears above the horizon, as illustrated in Figure 5.10.
- Radar horizon (farthest ground range where the radar can ‘see’ the earth’s surface).
- Optical horizon (farthest ground range where an optical system can see the earth’s surface).
- Target slant range.
- Target elevation angle.
- The elevation angle of the ray that reflects at the earth’s surface.
- Path length difference, *i.e.*, length indirect path minus length direct path.
- ‘Horizon descent’, which is illustrated in Figure 5.11.

Note that a specific  $k$ -factor can be specified, which affects all quantities that depend on radar wave propagation. The true earth’s radius is, however, used in the calculation of the horizon descent.

Antenna Height	56 ft	20.1 m
Target Altitude	33 ft	10.0 m
Ground Range	5.4 NM	10.0 km
K-factor	1.33	
Beyond the Horizon	<input type="checkbox"/>	
Target Horizon	17.0 NM	31.5 km
Radar Horizon	10.0 NM	18.5 km
Optical Horizon	8.6 NM	16.0 km
Slant Range	5.3996 NM	10.0000 km
Elevation Direct Ray	-0.09 °	
Horizon Elevation	-0.12 °	
Elevation Reflected Ray	-0.20 °	
Path Length Difference	0.03 m	
Horizon Descent	7.8 m	

Figure 5.9: The Geometry worksheet.

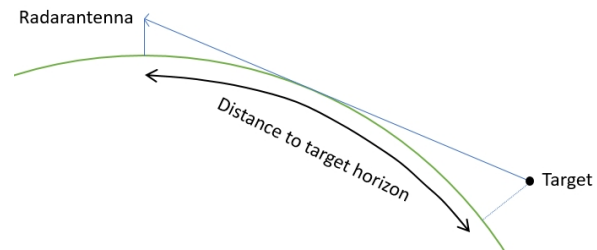


Figure 5.10: Illustration of the quantity 'target horizon'.

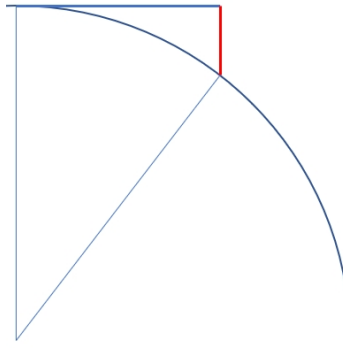


Figure 5.11: The profile of the earth, the red line denotes the horizon descent.

## 5.4 Conversions

The CARPET end-user may find the Conversions worksheet, shown in Figure 5.12 useful. In free space, the relationship between power density  $\Phi$  ( $\text{W}/\text{m}^2$ ) and RMS fieldstrength  $E$  ( $\text{V}/\text{m}$ ) is given by

$$\Phi = \frac{E^2}{Z_0}, \quad (5.1)$$

where  $Z_0 = 377 \Omega$  is the characteristic impedance of free space. A nautical mile is 1852 m, a statute mile is 1609.344 m. A NATO mil is not precisely a mrad (milliradian). There are  $2 \cdot \pi$  radians on a circle ( $360^\circ$ ), so  $2 \cdot \pi \cdot 1000 = 6283.185307179586476925286766559$  milliradians. However, there are 6400 NATO mils on a circle. An atmosphere is an old-fashioned unit of pressure denoting the mean air pressure at sea level. It is approximately equal to 1013.25 hPa, 1.01325 bar en 760 mmHg. A foot is 30.48 cm.

Range	5,4 NM	6,2 statute mile	10,0 km
Angle	0,000 rad	0 mrad	0 NATO Mil
			0,0 °
Altitude	32,8 ft		10,0 m
Pressure	1,00691 atm		1020,25 hPa = mbar
Field Strength & Power Density	19,4 V/m		1,00 W/m2
WGS84 Lat, Long			
	52,077290 °	4,375112 °	
UTM Easting, Northing, Zone			
	594237,3 m	5770526,8 m	31

OK

Figure 5.12: The Conversions worksheet.

## 5.5 Swerling Cases

The signal-to-noise ratio required to provide a specific probability of detection given the Swerling case, the probability of false alarm and the number of non-coherently integrated pulses can be computed in the Swerling Cases worksheet illustrated in Figure 5.13. Conversely, the detection probability corresponding to a specific signal-to-noise ratio can also be calculated. In addition, the threshold level is computed at the specified probability of false alarm and vice versa.

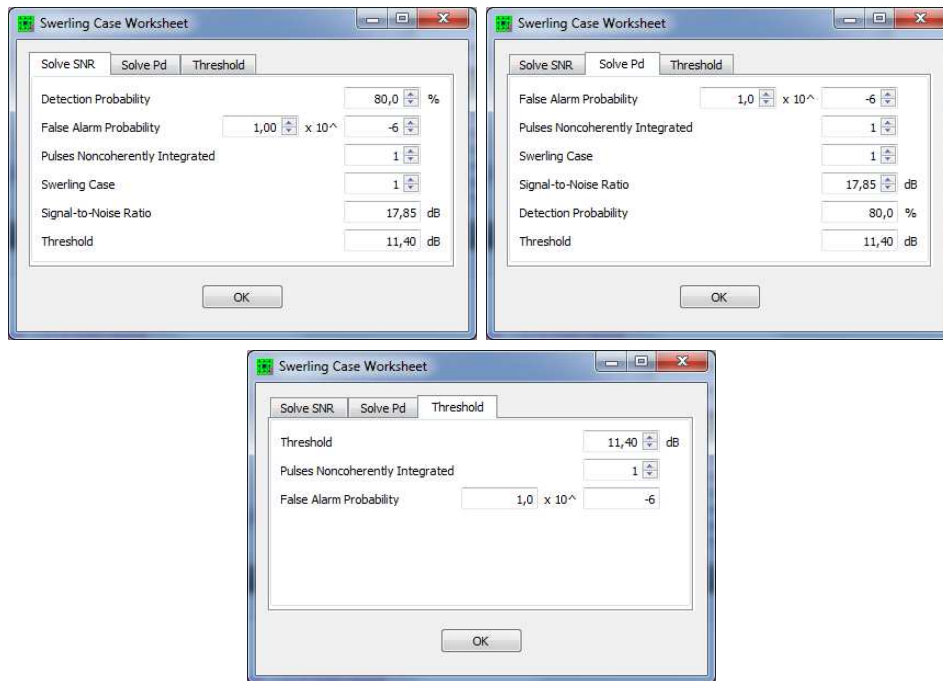
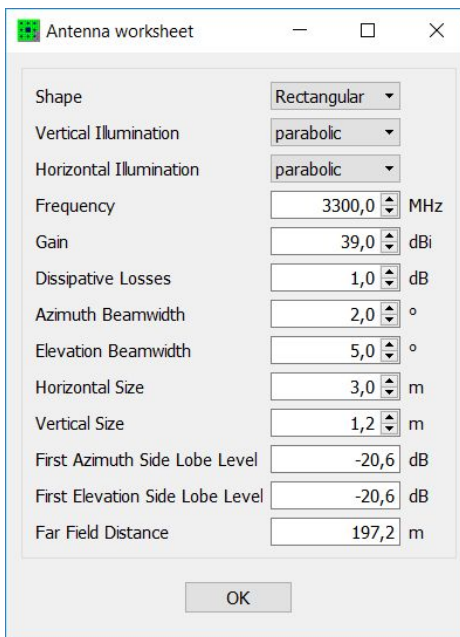


Figure 5.13: The three panes of the Swerling Case worksheet.

The third pane of the worksheet is relevant in order to determine the threshold-to-noise-power-ratio, given the allowed false alarm probability. The inverse procedure may also be relevant, in case the radar OEM provides a threshold-to-noise-power-ratio and the corresponding false alarm probability needs to be determined.

## 5.6 Antenna

The gain and beamwidths of the radar antenna as a function aperture type, illumination, size, and losses can be computed in the Antenna worksheet illustrated in Figure 5.14. Conversely, the size corresponding to the specified gain and beamwidths may also be calculated. The output values are the sidelobe levels in azimuth and elevation corresponding to the illumination function and the far field distance.



Parameter	Value	Unit
Shape	Rectangular	
Vertical Illumination	parabolic	
Horizontal Illumination	parabolic	
Frequency	3300,0	MHz
Gain	39,0	dBi
Dissipative Losses	1,0	dB
Azimuth Beamwidth	2,0	°
Elevation Beamwidth	5,0	°
Horizontal Size	3,0	m
Vertical Size	1,2	m
First Azimuth Side Lobe Level	-20,6	dB
First Elevation Side Lobe Level	-20,6	dB
Far Field Distance	197,2	m

Figure 5.14: The Antenna worksheet.

## 5.7 Absorption

The Absorption worksheet illustrated in Figure 5.15 allows the atmospheric attenuation resulting from oxygen and water vapor absorption (according to the Cooper model, [5]) to be computed. In addition, the attenuation from a rain cloud of uniform density as a function of polarisation and rain rate is calculated.

Radar / Radio	
Frequency	3300 MHz
Polarization	horizontal
Antenna Height	20 m

Target	
Altitude	33 ft / 10.0 m
Range	10.8 NM / 20.0 km
Azimuth Angle	0.0 degrees

Rain Cloud	
Rainfall Rate	4.0 mm/hr
Centroid Range	5.4 NM / 10.0 km
Diameter	5.4 NM / 10.0 km
Azimuth Angle	0.0 degrees

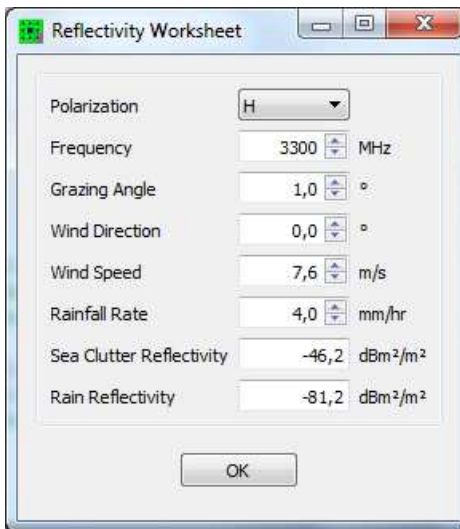
  

One-way Absorption	
O2 and H2O Molecules	0.164 dB
Rain	0.017 dB
Path	20.0 km
Path through Rain	10.0 km

Figure 5.15: The Absorption worksheet of CARPET 3.

## 5.8 Reflectivity

The reflectivity of the sea according to the Georgia Institute of Technology model, see Horst *e.a.*, [11] and the rain and chaff reflectivity are accessible in the worksheet shown in Figure 5.16. The sea reflectivity is a function of polarisation, frequency, grazing angle, sea state, and wind direction. The rain and chaff reflectivity are calculated at the specified rainfall rate and chaff density, respectively.



The image shows a software dialog box titled "Reflectivity Worksheet". It contains several input fields and a dropdown menu, each with a small up/down arrow icon. The fields are: Polarization (dropdown menu set to 'H'), Frequency (3300 MHz), Grazing Angle (1,0 °), Wind Direction (0,0 °), Wind Speed (7,6 m/s), Rainfall Rate (4,0 mm/hr), Sea Clutter Reflectivity (-46,2 dBm<sup>2</sup>/m<sup>2</sup>), and Rain Reflectivity (-81,2 dBm<sup>2</sup>/m<sup>2</sup>). An "OK" button is located at the bottom center of the dialog box.

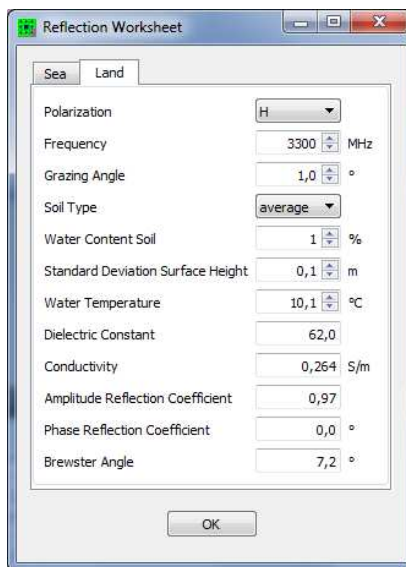
Parameter	Value	Unit
Polarization	H	
Frequency	3300	MHz
Grazing Angle	1,0	°
Wind Direction	0,0	°
Wind Speed	7,6	m/s
Rainfall Rate	4,0	mm/hr
Sea Clutter Reflectivity	-46,2	dBm <sup>2</sup> /m <sup>2</sup>
Rain Reflectivity	-81,2	dBm <sup>2</sup> /m <sup>2</sup>

Figure 5.16: The Reflectivity worksheet.



## 5.9 Reflection

The Reflection worksheet illustrated in Figure 5.17 allows the amplitude and phase of the surface reflection coefficient to be calculated as a function of the environmental parameters. In addition, the Brewster angle is computed, which is defined as the grazing angle at which the amplitude of the smooth plane reflection coefficient for vertical polarisation reaches a minimum. The Environment switch allows the user to select between a land and sea environment. The dielectric constant and conductivity are computed as a function of the environmental parameters, but they may also be changed directly. The standard deviation of the surface height is an input parameter in the land environment, but it is calculated from the sea state in a maritime environment.



Parameter	Value	Unit
Polarization	H	
Frequency	3300	MHz
Grazing Angle	1,0	°
Soil Type	average	
Water Content Soil	1	%
Standard Deviation Surface Height	0,1	m
Water Temperature	10,1	°C
Dielectric Constant	62,0	
Conductivity	0,264	S/m
Amplitude Reflection Coefficient	0,97	
Phase Reflection Coefficient	0,0	°
Brewster Angle	7,2	°

Figure 5.17: The Reflection worksheet.

## 5.10 Binary Integration

The false alarm probability ( $P_{fa}$ ) that is specified in CARPET refers to the ( $P_{fa}$ ) that is used in the SNR to  $P_d$  calculation. In case of detection per Doppler filter and M-out-of-N logic that combines detections of multiple bursts, the ( $P_{fa}$ ) at the end of the signal processing gain differs from the specified  $P_{fa}$ , which can be investigated with the binary integration worksheet, see Figure 5.18. In case of processing with multiple Doppler filters: the  $P_{fa}$  prior to the binary integrator needs to be divided by the number of Doppler filters. The binary Integration worksheet is shown in Figure 5.18.

The figure displays two panes of the Binary Integration worksheet. Both panes have the following common settings:

- Binary Integration: 3 out of 5
- Max. Allowed Gap (0=no gap constraint): 0
- Demand Successiveness:
- Number of Combinations: 16

**Left Pane (Solve Backwards):**

- Detection Probability Post: 80,0 %
- False Alarm Probability Post: 1,00 x 10<sup>-6</sup>
- Detection Probability Prior: 67,2 %
- False Alarm Probability Prior: 4,64 x 10<sup>-3</sup>

**Right Pane (Solve Forwards):**

- Detection Probability Prior: 60,0 %
- False Alarm Probability Prior: 1,00 x 10<sup>-4</sup>
- Detection Probability Post: 68,3 %
- False Alarm Probability Post: 1,00 x 10<sup>-11</sup>

Figure 5.18: The two panes of the Binary Integration worksheet.

### 5.11 False Alarm Probability

This worksheet (see Figure 5.19) relates false alarm probability,  $P_{fa}$ , to false alarm rate, *i.e.*, the number of false alarms per unit of time. A false alarm occurs when the detection threshold (or 'bias level') is overshoot by noise, rather than by a target echo.

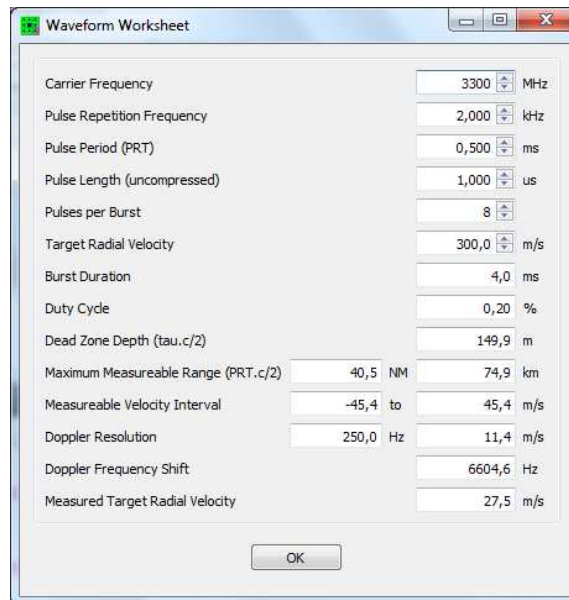
The figure shows two instances of the 'False Alarm Worksheet' dialog box. The left instance is in the 'Solve FAR' tab, and the right instance is in the 'Solve Pfa' tab. Both instances have the same input values for most parameters, but the output values are swapped between the two tabs.

Parameter	Solve FAR (Left)	Solve Pfa (Right)
False Alarm Probability	1,0 x 10 <sup>-6</sup>	16,0 /s
Pulse Repetition Frequency	2,000 kHz	2,000 kHz
Instantaneous Bandwidth	1,0 MHz	1,0 MHz
Instrumented Range	74,9 km	74,9 km
Doppler Filters (1=noncoherent system)	16	16
Number of Range Cells	499	499
False Alarm Rate	16,0 /s	1,0 x 10 <sup>-6</sup>

Figure 5.19: False Alarm Probability worksheet.

### 5.12 Waveform Basics

The Waveform Basics worksheet, shown in Figure 5.20, provides information on the duration of a burst (pulse train), the duty cycle, depth of the dead zone, maximum measurable range, the measurable radial velocity interval, the Doppler resolution (in Hz and in m/s), the Doppler frequency shift (given a specific radial speed), and the measured radial speed of the target. These quantities are discussed in Section 6.9.1.



The screenshot shows a dialog box titled "Waveform Worksheet" with the following parameters and values:

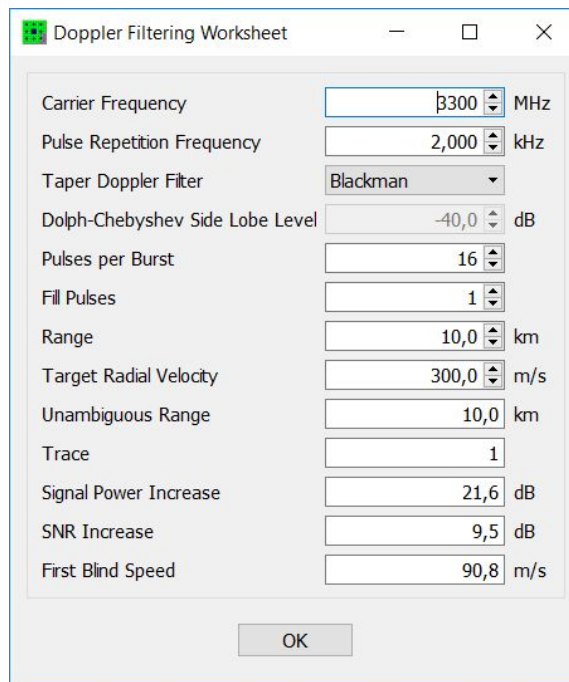
Parameter	Value	Unit
Carrier Frequency	3300	MHz
Pulse Repetition Frequency	2,000	kHz
Pulse Period (PRT)	0,500	ms
Pulse Length (uncompressed)	1,000	us
Pulses per Burst	8	
Target Radial Velocity	300,0	m/s
Burst Duration	4,0	ms
Duty Cycle	0,20	%
Dead Zone Depth ( $\tau \cdot c/2$ )	149,9	m
Maximum Measurable Range (PRT.c/2)	40,5 NM / 74,9 km	
Measurable Velocity Interval	-45,4 to 45,4	m/s
Doppler Resolution	250,0 Hz / 11,4 m/s	
Doppler Frequency Shift	6604,6	Hz
Measured Target Radial Velocity	27,5	m/s

An "OK" button is located at the bottom center of the dialog box.

Figure 5.20: The Waveform Basics worksheet.

### 5.13 Doppler Filtering

The Doppler Filtering worksheet, shown in Figure 5.21, gives information on the gain of the Doppler filtering.



The screenshot shows a dialog box titled "Doppler Filtering Worksheet" with the following parameters:

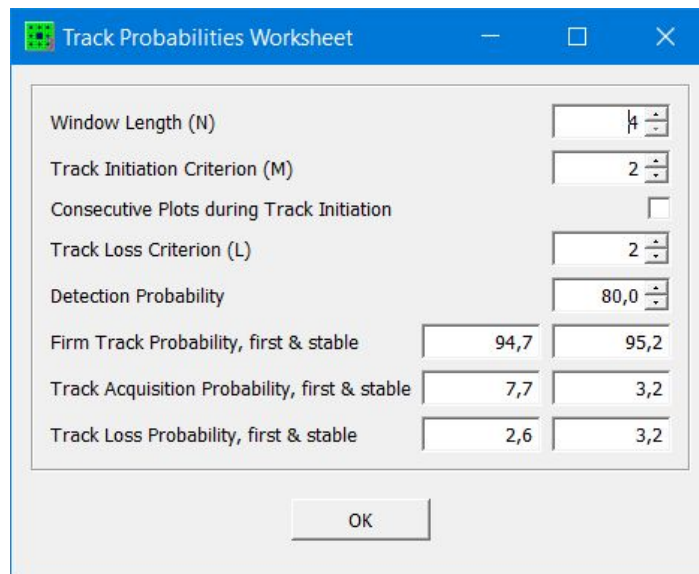
Parameter	Value	Unit
Carrier Frequency	3300	MHz
Pulse Repetition Frequency	2,000	kHz
Taper Doppler Filter	Blackman	
Dolph-Chebyshev Side Lobe Level	-40,0	dB
Pulses per Burst	16	
Fill Pulses	1	
Range	10,0	km
Target Radial Velocity	300,0	m/s
Unambiguous Range	10,0	km
Trace	1	
Signal Power Increase	21,6	dB
SNR Increase	9,5	dB
First Blind Speed	90,8	m/s

An "OK" button is located at the bottom center of the dialog box.

Figure 5.21: The Doppler Filtering worksheet.

### 5.14 Track Probabilities

The Track Probabilities worksheet, shown in Figure 5.22, shows the firm track probability, the track acquisition probability and the track loss probability for a given tracker logic and for a constant detection probability. Note that both first and stable values are calculated. The first values refer to the situation that  $N$  (equal) detection probabilities are offered to the ‘Worsham algorithm’ (the radar has  $M$ -out-of- $N$  track initiation logic). The stable values are obtained when a large number of detection probabilities are offered, so that the emerging probabilities have reached a constant value. For details, we refer to Worsham’s paper, [2].

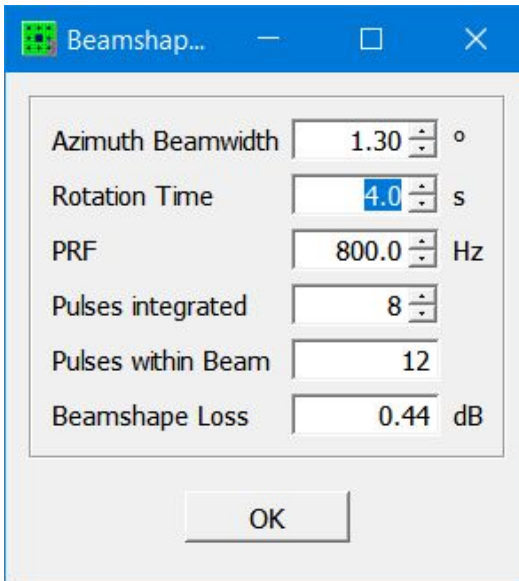


Window Length (N)	4	
Track Initiation Criterion (M)	2	
Consecutive Plots during Track Initiation	<input type="checkbox"/>	
Track Loss Criterion (L)	2	
Detection Probability	80,0	
Firm Track Probability, first & stable	94,7	95,2
Track Acquisition Probability, first & stable	7,7	3,2
Track Loss Probability, first & stable	2,6	3,2

Figure 5.22: The Track Probabilities worksheet.

### 5.15 Azimuth Beamshape Loss

The Azimuth Beamshape Loss worksheet, shown in Figure 5.23, determines the (two-way) azimuth beamshape loss, given a specific PRF, one-way -3 dB azimuth beamwidth, antenna rotation rate and number of pulses that is integrated,  $N$ . This loss accounts for the fact that, in case of a radar with a scanning antenna beam, the target is not observed with maximum antenna gain. It is assumed that the azimuth beam is Gaussian shaped within the -3 dB points (one-way).<sup>5</sup> Furthermore, it is assumed that the target is once illuminated by the very maximum of the beam. Consequently, if no pulses are integrated ( $N = 1$ ) there is no beamshape loss.



The screenshot shows a dialog box titled "Beamshap...". It contains several input fields with numerical values and units, and an "OK" button at the bottom. The fields are:

Parameter	Value	Unit
Azimuth Beamwidth	1.30	°
Rotation Time	4.0	s
PRF	800.0	Hz
Pulses integrated	8	
Pulses within Beam	12	
Beamshape Loss	0.44	dB

Figure 5.23: The Azimuth Beamshape Loss worksheet.

<sup>5</sup>Carl Friedrich Gauß: 1777 – 1855, 'German' mathematician and physicist (Germany did not exist at that time, one might say that Germany exists since the Franco-Prussian war, 1871).

### 5.16 Latitude/Longitude

The Latitude/Longitude worksheet, shown in Figure 5.24 can be used to convert angular latitude-longitude information to UTM (Universal Transverse Mercator) coordinate system and vice versa. There is also a tab referred to as Vincenty, [12], that calculates the arrival point in WGS-84 coordinates, given the sensor's position, an azimuth angle and a range.

Field	Value	Unit
Start Point Latitude	52,110218	°
Start Point Longitude	4,327059	°
Range	43,000	km
Azimuth Angle (Bearing)	43,00	°
Destination Point Latitude	52,392059	°
Destination Point Longitude	4,757839	°
Final Bearing	43,34	°

Figure 5.24: The Latitude/Longitude worksheet.



## 6 CARPET Models

### 6.1 Radio Wave Propagation

#### 6.1.1 Introduction

The performance of surface based radar systems is strongly influenced by meteorological conditions, by physical properties of the earth's surface and, in case of land-based radar, by the terrain profile. CARPET 3 has three models for electro-magnetic (EM) propagation:

- Free Space, which implies that there is no earth, so no multipath, no clutter, no diffraction, no refraction. Absorption within the atmosphere is, however, possible.
- EREPS-like, which was also present in CARPET 1 and 2. EREPS-like is based on SPAWAR's EREPS model (so not the AREPS model), as discussed in [20]. The model can be characterized as being qualitative/semi-empirical, a set of equations have been proposed that fit the observation.
- TERPEM-light, which requires the purchase of the TERPEM-light plug-in. TERPEM (Levy and Craig [21], Levy [22]) determines EM propagation effects, using a suite of quantitative numerical models, taking as input a so-called refractivity profile, earth's surface characteristics, the elevation antenna pattern and, in case of propagation over land, the terrain profile.

The sequel of this section consist of four parts. Information that is not related to the two models is provided in Section 6.1.2. Refractive index, N-profile, M-profile, reference and standard atmosphere and the k-factor are discussed here. Subsequently, the refractivity profile, which is explicitly used by the TERPEM propagation profile is discussed, in Section 6.1.3. Thereafter, the free space model, the EREPS-like model and the TERPEM-light model (which requires a TERPEM license) are discussed (sections 6.1.6, 6.1.7 and 6.1.8). Absorption of EM-energy by rain is discussed in Section 6.1.9.

#### 6.1.2 Refractive index

Within the earth's atmosphere, radiowaves do not propagate along straight lines because the index of refraction,  $n$ , is not constant but generally decreases as the altitude increases. Anomalous propagation occurs as a consequence of variations of the refractive index with altitude. Various manifestations of propagation are depicted in Figure 6.1.

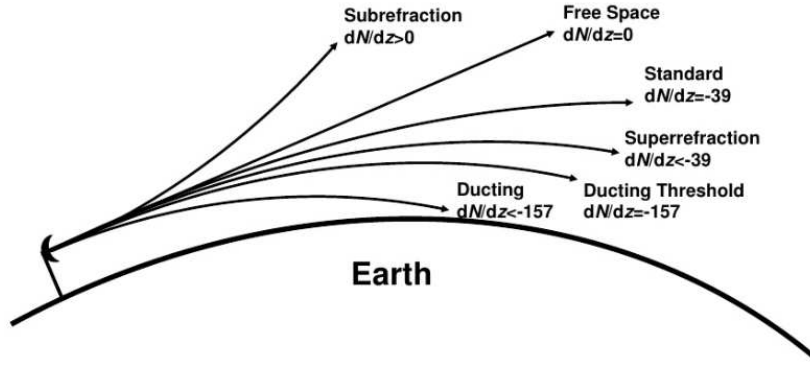


Figure 6.1: Manifestations of anomalous propagation. The accompanying vertical refractivity gradient,  $dN/dz$ , is expressed in  $\text{km}^{-1}$ .

The refractive index of the air is very close to unity. In the troposphere (the lowest part of the earth's atmosphere), it is often more convenient to use a related quantity, the refractivity,  $N$ , defined by

$$N = 10^6 \cdot (n - 1) \quad (6.1)$$

The refractivity can be determined from meteorological parameters using the following empirical expression:

$$N = \frac{77.6}{T} \left( p + \frac{4810}{T} e \right) \quad (6.2)$$

with  $p$  the atmospheric pressure (hPa),  $T$  the temperature (K), and  $e$  the partial pressure of water vapour (hPa).

Tropospheric propagation problems are easier to treat when working in coordinates  $(x, z)$  where  $x$  is the range measured along the earth's surface and  $z$  is the height above the earth's surface. With these 'flat earth' coordinates, the refractive index in the wave equation is replaced with the modified refractive index,  $m$ , defined by

$$m(z) = n(z) + \frac{z}{a} \quad (6.3)$$

where  $a$  is the earth radius. Ducting layers are easily recognised as those where the gradient of  $m$  with respect to height is negative: in these layers the curvature of radio-rays is more than that of the Earth, and hence energy can be trapped for long distances. The corresponding modified refractivity,  $M$ , is defined by

$$M(z) = N(z) + 10^6 \cdot \frac{z}{a} \approx N(z) + 0.157z \Rightarrow N(z) = M(z) - 0.157z, \quad (6.4)$$

( $z$  is expressed in m).

A so-called ‘reference atmosphere’ has been defined by the CCIR (Comité Consultatif International des Radiocommunication). This definition is an attempt to provide a realistic description of the atmosphere under clear, dry conditions. For this reference atmosphere, the refractivity profile is considered to be of exponential form:

$$N = N_0 \exp \left\{ \frac{-z}{z_{ref}} \right\} \quad (6.5)$$

where  $N_0 = 315$  is the refractivity at the surface and  $z_{ref} = 6951$  m is a reference height so that

$$N = 315 \exp \left\{ \frac{-z}{6951} \right\}. \quad (6.6)$$

There is, however, also a ‘standard atmosphere’ which was defined in 1925 by the International Commission for Aeronavigation. Here the refractivity profile is approximated by a linear function, with the refractivity gradient,  $dN/dz$ , being -39 N-units/km (regardless of altitude). For linear profiles of the refractive index, the curved propagation path can be transformed to a straight line by replacing the actual earth radius with an effective earth radius and replacing the actual atmosphere with one that is homogeneous in nature, as depicted in Figure 6.2.

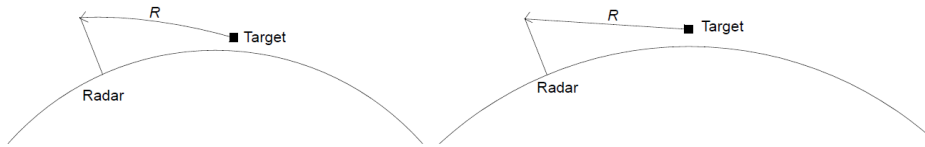


Figure 6.2: Enlarging the earth radius in order to obtain propagation along a straight line.

The effective earth radius factor,  $k$ , is defined as the ratio between the effective earth radius,  $a_e$ , and the actual earth radius (6371 km). The factor  $k$  is related to the refractivity gradient by

$$k = \frac{a_e}{a} = \frac{1}{1 + 10^{-6} a \frac{dN}{dz}}, \quad (6.7)$$

For standard refractivity the value of  $k$  is 1.33 (4/3).

If the refractivity gradient  $dN/dz$  equals -157, a horizontally launched ray will follow the curvature of the earth, which follows from a physical expression that is referred to as Snell’s law (after Willebrord Snel van Royen, a Dutch astronomer and mathematician, 1580-1626), see Figure 6.3.

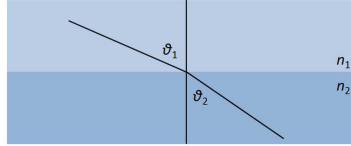


Figure 6.3: Snell's law illustrated; ray-bending due to a medium's density change.

If you travel 1 km over the earth's surface, the top angle of the triangle start-point - earth's centre - end-point changes  $2\pi \cdot 1/40000 = 1.57 \cdot 10^{-4}$  rad.

In case the refractivity gradient is less than  $-157$ , the ray curvature is larger than the earth's curvature; rays will bend towards the earth (curvature = reciprocal of radius). This condition will arise when either temperature is significantly increasing with altitude (called temperature inversion), or when the humidity is rapidly decreasing with altitude, as inspection of equation 6.2 shows. The occurrence of ducting can easily be inferred from especially the M-profile, as illustrated in Figure 6.4.

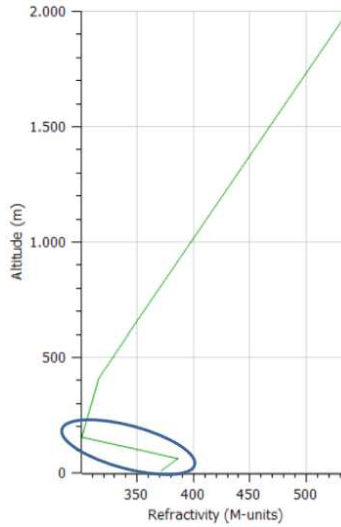


Figure 6.4: Example of an M-profile revealing ducting (negative slope within the blue ellipse).

This particular height behaviour of the refractivity can occur at ground level, which results in a surface-based duct, or at higher elevation, which results in an elevated duct. Evaporation duct is a surface-based duct caused by rapid humidity decrease.

Whether radio or radar waves will travel in a ducting layer depends of the antenna altitude with respect to the altitude and thickness of the layer (the phrase 'thickness' has been described in Section 3.3.1.3). Energy is coupled in if the incidence angle is shallow, *i.e.*, less than  $1^\circ$ . This phenomenon is also visible in Figure 1.4; the vertical coverage above 150 m

is not affected by the presence of the ducting layer, since rays with relatively large elevation angle do not couple in the duct layer.

### 6.1.3 Refractivity Profile

As argued above, the TERPEM propagation model takes the refractivity profile, *i.e.*, refractivity over height, into account. To recapitulate, CARPET 3 offers seven recipes to obtain the refractivity M-profile:

1. A refractivity N-profile can be imported. The M-profile is calculated from the N-profile according to equation 6.4.
2. A refractivity M-profile can be imported.
3. Radiosonde data can be imported. The M-profile is calculated according to the equations 6.2 and 6.4.
4. TERMET data can be imported.
5. The ITU-R P.835 Annex 2, Sections 2 to 4 model is used.
6. The ITU-R P.835 Annex 3 model is used.
7. A synthetic duct model is used.

The recipes 5 and 6 are discussed in ITU Recommendation P.835-6, see [52]. Method 5 is especially relevant for Earth-space propagation; the refractivity profile is covered up to 100 km. Method 6, on the other hand, is relevant for low-elevation propagation over land and over sea. Though the profile is derived from monthly averaged measured profiles, in certain regions, like the Persian Gulf, ducting effects appear to be present in the data, *i.e.*, they do not average out. It is not possible for the CARPET end-user to ‘manipulate’ these refractivity profiles. However, export refractivity profile functionality has been added to CARPET, so that the user can manipulate the profile outside CARPET, if she or he wishes to do so.

### 6.1.4 ITU Recommendation P.835-6 Annex 2, Section 2 to 4

The first method contains a series of equations to calculate the temperature, pressure and water vapour density given the altitude above the Earth’s surface. Besides, there are three latitude intervals:  $|\phi| < 22^\circ$ ,  $22 \leq |\phi| < 45^\circ$ , and  $|\phi| \geq 45^\circ$ ,  $\phi$  being the latitude angle. Also a distinction is made between summer and winter. The recipe to determine the *N*-profile and the *M*-profile from these quantities (temperature, pressure and water vapour density) is given in the manual of CARPET 3. The model was originally developed for integrated effects

along Earth-space paths. The vertical resolution is relatively poor; the model will therefore not show ducting effects or anomalous propagation.

### 6.1.5 ITU Recommendation P.835-6 Annex 3

The method that is discussed in Annex 3 was added to ITU-R P.835-4, in 2005. It is based upon climate data from the ERA-15 data set. The meteorological data was gathered for 15 years, from 1979 to 1993. The data are from  $0^\circ$  to  $360^\circ$  in longitude and from  $+90^\circ$  to  $-90^\circ$  in latitude, with a resolution of  $1.5^\circ$  in both latitude and longitude. The data set contains the mean monthly vertical profiles at 00:00, 06:00, 12:00 and 18:00 UTC (Universal Time Coordinated) of total air pressure, air temperature and water-vapour density at 32 height levels from a reference height located around the local Earth's surface up to about 30 km above the Earth's surface. Although the data represents a monthly average, longer lasting surface features survive in certain regions like the Persian Gulf, where advection ducting is strong and enduring. It is expected, however, that elevated ducts will be less likely to be represented, and that ducting in more temperate climates might be missed in these monthly data.

Given a specific time instance TNO interpolates between the two neighbouring times at which climate data is available. For the interpolation in latitude and longitude four neighbouring profiles are utilised.

This methods demands the ERA-15 database to be present which contains nearly 0.6 Gbyte of data, stored in thirteen files.<sup>6</sup> This dataset is installed together with CARPET 3.03.

### 6.1.6 Free Space

Surface and volume clutter will not be present in case free space propagation is selected. Absorption of EM energy in the atmosphere has been implemented using a model that is applicable for 1 to 10 GHz, see Cooper [5]. The atmospheric loss,  $L_{atm}$  in dB and the absorption rate  $\gamma$  in dB/km because of oxygen and water vapor molecules below the water vapor absorption line at 22 GHz is implemented by a polynomial fit to the attenuation curves as a function of the elevation angle  $\theta$ , the frequency,  $f$ , expressed in GHz, and the slant range  $R$ , expressed in km

$$p = 0.17129 - 0.10848f + 0.0013541f^2 - 0.0013541f^3 + 0.40754 \times 10^4 f^4 + 0.11552 \ln f \quad (6.8)$$

$$q = 0.026681 - 0.5147 \times 10^2 f + 0.17201 \times 10^{-4} f^2 + 0.85994 \times 10^{-3} \ln f \quad (6.9)$$

<sup>6</sup>The files hght.bin, pres\_00.bin, pres\_06.bin, pres\_12.bin, pres\_18.bin, temp\_00.bin, temp\_06.bin, temp\_12.bin, temp\_18.bin, vapd\_00.bin, vapd\_06.bin, vapd\_12.bin and vapd\_18.bin.

$$h = 6586.2 + 10.568f - 12.422f^2 + 0.52631f^3 - 702.06 \ln f \quad (6.10)$$

$$u = e^{\frac{-R(\sin \theta + 2q \cos \theta)}{h}} \quad (6.11)$$

$$L_{atm} = \frac{p(1-u)}{\sin(\theta) + q \cos \theta(1+u)} \quad (6.12)$$

### 6.1.7 EREPS-like

There are three distinct regions that require different methods of obtaining the propagation factor as a function of range as shown in Figure 6.5.

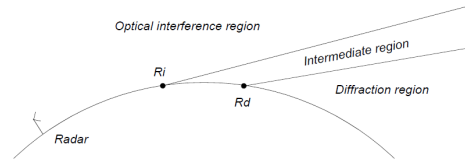


Figure 6.5: The three propagation regions that the EREPS-like model uses.

The first region, called the optical interference region, extends from the transmitter to roughly the radio horizon. In this region, propagation is dominated by two-path coherent interference between direct and surface-reflected waves. The other distinct region is the diffraction region which begins beyond the radio horizon. A third region, called the intermediate region, lies between the optical-interference and the diffraction region. The range limits of the three different propagation regions in the absence of evaporation duct are obtained from the following analysis.

The effective earth radius,  $a_e$  (m), is used in the determination of the three distinct regions of radio wave propagation in the standard atmosphere. To determine the maximum range of the optical-interference region,  $R_i$ , two quantities are compared. One is the range  $R_{1/4\lambda}$ , where the path-length difference between the direct and reflected rays of the earth's surface is equal to one-quarter wavelength. Another criterion for the optical-interference region is the validity of the spherical earth divergence factor that is multiplied by the reflection coefficient of a smooth plane to obtain the spherical earth reflection coefficient. The divergence factor, which is unity at high grazing angles and decreases toward zero as the grazing angle decreases, accounts for the fact that the wave diverges at an increased rate after reflection because reflection occurs at a spherical surface rather than at a plane surface. The range where the spherical earth divergence factor becomes invalid,  $R_s$ , is given by

$$R_s = a_e \left( \sqrt{\psi_s^2 + \frac{2h_a}{a_e}} - \psi_s \right) + a_e \left( \sqrt{\psi_s^2 + \frac{2h_t}{a_e}} - \psi_s \right) \quad (6.13)$$

(see Anderson, [23]), where the limiting grazing angle,  $\psi_i$ , is given by

$$\psi_s = \left( \frac{\lambda}{2\pi a_e} \right)^{1/3} \quad (6.14)$$

The larger of the two ranges,  $R_{1/4\lambda}$  and  $R_s$ , is used as the maximum range of the optical-interference region:

$$R_i = \max(R_{1/4\lambda}, R_s) \quad (6.15)$$

The minimum range at which the diffraction field solutions are applicable and the intermediate region ends,  $R_d$ , is given by [10]

$$R_d = R_{hor} + (a_e^2 \lambda)^{1/3} \quad (6.16)$$

in which  $R_{hor}$  denotes the horizon range which is given by:

$$R_{hor} = \sqrt{2a_e}(\sqrt{h_a} + \sqrt{h_t}) \quad (6.17)$$

where  $h_a$  and  $h_t$  are the heights (altitudes) of the radar antenna and target, respectively.

The propagation factor in the intermediate region is obtained in CARPET by a linear interpolation between the logarithmic value of the propagation factor at the end of the interference region and the logarithmic value at the start of the diffraction region. The propagation factor in the interference and diffraction region is derived in the Sections 8.7.2 and 8.7.3.

### 6.1.7.1 Optical-Interference Region

In the optical-interference region, the propagation factor is dominated by the coherent interaction between the direct and the reflected ray. In case the multipath checkbox is in the on-position, the propagation factor that accounts for this interference is given by

$$F = g(\theta_1) + g(\theta_2)D\rho \exp\left\{-j\frac{2\pi\Delta R}{\lambda}\right\}. \quad (6.18)$$

$g(\theta_1)$  and  $g(\theta_2)$  represent the voltage gains of the radar antenna in the directions of the direct and reflected ray, respectively. The divergence factor is denoted by  $D$  (see equation 110), while  $\rho$  represents the complex reflection coefficient and  $\Delta R$  the difference in path length between the direct and reflected rays. The difference in path length and the elevation angles of the direct and reflected rays are determined from the geometry of the radar-target scenario.

In case multipath is off, the propagation factor is simply  $g(\theta_1)$ .



### 6.1.7.2 Diffraction Region

The electromagnetic field in the diffraction region is in the form of an infinite series of terms called modes [15]. At or near the horizon, many terms must be summed to obtain an accurate solution; the terms of the series decrease very slowly. Well below the horizon, however, the first term represents the field to a good approximation. The first mode can be represented as the product of three factors. The first factor,  $V$ , is called the range-gain function, which accounts for the increase in gain if the range decreases. The other two factors,  $U_1$  and  $U_2$ , are called height-gain functions that account for the dependence of the field on the height of the radar antenna and the target.

Before evaluating the range-gain and the height-gain functions, the range and height are normalized on the natural units of range and height. The natural unit of height is

$$H = \left\{ \frac{\lambda^2 a_e}{2(2\pi n_o)^2} \right\}^{1/3} \quad (6.19)$$

and the natural unit of range is

$$L = \frac{\lambda a_e}{2\pi n_o H} \quad (6.20)$$

where  $n_o$  represents the refractive index at the earth's surface, which is determined from the refractivity at the earth's surface:

$$n_o = 1 + 10^{-6} \frac{77.6}{T_a} \left( p + \frac{4810}{T_a} e \right) \quad (6.21)$$

in which  $T_a$  is the air temperature,  $p$  is the atmospheric pressure, and  $e$  is the water vapor pressure (hPa), given by

$$e = 6.105 h_r \exp \left\{ 25.22 \left( \frac{T_a - 273.2}{T_a} \right) - 5.31 \ln \left( \frac{T_a}{273.2} \right) \right\} \quad (6.22)$$

with  $h_r$  as the relative humidity of the air.

The normalized range is denoted by  $r = R/L$ , and the normalized height by  $z = h/H$ . The range-gain function,  $V(r)$ , and height-gain function,  $U(z)$ , in dB in a standard atmosphere are given by

$$V(r) = 10.99 + 10^{10} \log r - 17.55r \quad (6.23)$$

$$z < 0.6 : \quad U(z) = 20^{10} \log z \quad (6.24)$$

$$0.6 \leq z \leq 1.0 : \quad U(z) = -4.3 + 51.04 \left\{ {}^{10}\log \left( \frac{z}{0.6} \right) \right\}^{1.4} \quad (6.25)$$

$$z > 1.0 : \quad U(z) = 19.85(z^{0.47} - 0.9) \tag{6.26}$$

These expressions are applicable for either horizontal or vertical wave polarisation at frequencies above approximately 100 MHz. The propagation factor in the diffraction region is now given by the product of the range-gain and height-gain functions and an antenna pattern factor that gives a measure of the energy directed toward the diffraction region.

$$F^2 = V(r)U(z_r)U(z_t)g^2(\theta_{opt}) \tag{6.27}$$

where  $g(\theta_{opt})$  represents the antenna voltage gain at an elevation angle corresponding to the lowest possible ray in the optical region.

### 6.1.7.3 Geometry

The calculation of the propagation factor in the interference region requires several geometrical quantities to be determined from the radar-target geometry for a curved earth and a homogeneous atmosphere, as illustrated in Figure 6.6.

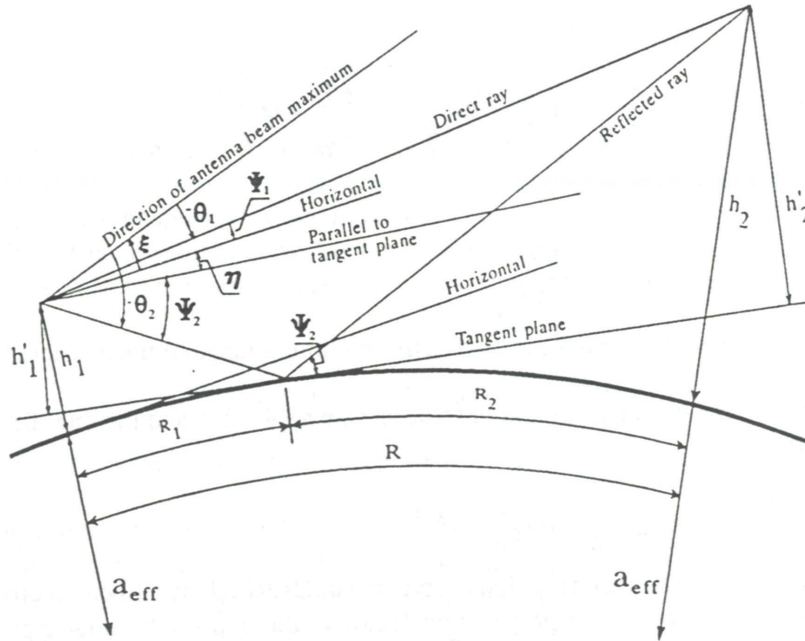


Figure 6.6: Multipath geometry.

The radar antenna at an altitude  $h_1$  and the target at an altitude  $h_2$  are at a ground range  $R$  over a curved earth with an effective radius. The ground range,  $R_1$ , from the radar

to the reflection point is determined by solving the cubic equation

$$2R_1^3 - 3RR_1^2 + \{R^2 - 2a_e(h_1 + h_2)\}R_1 + 2a_e h_2 R = 0 \quad (6.28)$$

see [15]. This equation has the formal solution

$$R_1 = \frac{R}{2} + \operatorname{sgn}(h_1 - h_2)\rho \cos \frac{\theta + \pi}{3} \quad (6.29)$$

$$R_2 = R - R_1 \quad (6.30)$$

where

$$p = \sqrt{\frac{4}{3}} \cdot \sqrt{a_e(h_1 + h_2) + \left(\frac{R}{2}\right)^2} \quad (6.31)$$

$$\theta = a \cos \left( \frac{2a_e |h_1 - h_2| R}{p^3} \right) \quad (6.32)$$

At the reflection point, a tangent plane is defined that becomes the altitude reference for the radar and target. The angles  $\eta_1$  and  $\eta_2$  between the tangent plane at the reflection point and the horizontal planes at the radar and target positions are obtained from

$$\eta_1 = \frac{R_1}{a_e} \quad (6.33)$$

$$\eta_2 = \frac{R_2}{a_e} \quad (6.34)$$

The height of the radar antenna,  $h'_1$ , and the target height,  $h'_2$ , above the tangent plane are given by

$$h'_1 = (h_1 + a_e) \cos \eta_1 - a_e \quad (6.35)$$

$$h'_2 = (h_2 + a_e) \cos \eta_2 - a_e \quad (6.36)$$

which can be approximated by

$$h'_1 = h'_1 - \frac{R_1^2}{2a_e} \quad (6.37)$$

$$h'_2 = h'_2 - \frac{R_2^2}{2a_e} \quad (6.38)$$

The distance between the radar and target positions measured along the tangent plane is expressed by

$$R'_1 = (a_e + h_1) \sin \eta_1 \quad (6.39)$$

$$R'_2 = (a_e + h_2) \sin \eta_2 \quad (6.40)$$

$$R' = R'_1 + R'_2 \quad (6.41)$$

The angle of incidence,  $\psi_2$  (grazing angle), on the tangent plane of the reflected ray becomes

$$\psi_2 = \text{atan} \left( \frac{h'_1}{R'_1} \right) \quad (6.42)$$

The angle of the direct ray with respect to the horizontal plane at the radar antenna position is given by

$$\psi_1 = \text{atan} \left( \frac{h'_2 - h'_1}{R'} \right) \quad (6.43)$$

If the antenna tilt is represented by  $\xi$ , the angles between the direct and reflected rays,  $\theta_1$  and  $\theta_2$ , and the antenna beam maximum are given by

$$\theta_1 = \psi_1 - \xi \quad (6.44)$$

$$\theta_2 = \psi_2 - \eta_1 - \xi \quad (6.45)$$

If mechanical tracking is selected, the antenna tilt is set equal to the elevation angle of the direct ray (i.e., the antenna is tracking the target in elevation):

$$\theta_1 = 0 \quad (6.46)$$

$$\theta_2 = \psi_2 - \eta_1 - \psi_1 \quad (6.47)$$

The slant range between the radar and the target becomes

$$R_1 = \sqrt{(h'_1 - h'_2)^2 + R^2} \quad (6.48)$$

The path difference between the direct and reflected ray is expressed by

$$\Delta R = \sqrt{(h'_1 + h'_2)^2 + R^2} - \sqrt{(h'_1 - h'_2)^2 + R^2} \quad (6.49)$$

The divergence factor,  $D$ , is given by [15]

$$D = \left( 1 + \frac{4R_1R_2}{a_e R \sin(2\psi_2)} \right)^{1/2} \quad (6.50)$$

for  $\psi_2 > 0$ , otherwise  $D = 0$ .

The ‘flat earth geometry’ including multipath in the vertical plane is considered in Appendix A of this document.

#### 6.1.7.4 Reflection Coefficient

The (specular) reflection coefficient of a smooth plane surface for vertical polarisation is given by:

$$\rho_s(V) = \frac{\varepsilon_c \sin \psi - \sqrt{\varepsilon_c - \cos^2 \psi}}{\varepsilon_c \sin \psi + \sqrt{\varepsilon_c - \cos^2 \psi}}, \quad (6.51)$$

For horizontal polarisation:

$$\rho_s(H) = \frac{\sin \psi - \sqrt{\varepsilon_c - \cos^2 \psi}}{\sin \psi + \sqrt{\varepsilon_c - \cos^2 \psi}}, \quad (6.52)$$

where  $\varepsilon_c$  represents the complex dielectric constant of the reflecting surface, see Kerr, [24]. The reflection coefficient in the case of receiving same-sense, circular polarized waves is the vector sum of the vertical and horizontal components [4]:

$$\rho_s(CS) = \frac{\rho_s(H) + \rho_s(V)}{2}, \quad (6.53)$$

while that for an opposite sense circular polarisation is

$$\rho_s(CO) = \frac{\rho_s(H) - \rho_s(V)}{2}. \quad (6.54)$$

In CARPET only the same-sense, circular polarisation is implemented. An example of how the reflection coefficient varies with the grazing angle is given in Figure 6.7. The grazing angle where  $\rho_s(V)$  has a minimum is referred to as Brewster angle.

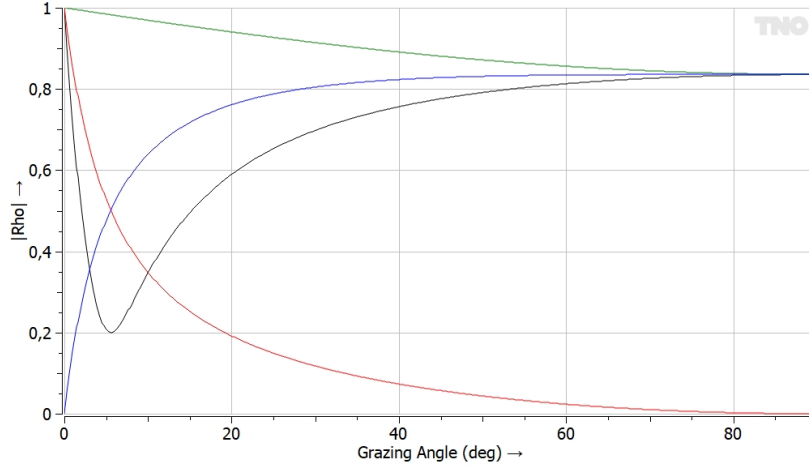


Figure 6.7: Magnitude of the reflection coefficients versus grazing angle, over sea. The radar frequency is 1 GHz, water temperature is 10 °C. Green: horizontal polarisation. Black: vertical polarisation. Blue: circular polarisation, opposite sense. Red: circular polarisation, same sense.

The complex dielectric constant,  $\varepsilon_c$ , is dependent on the electrical properties of the surface that is illuminated. The complex dielectric constant is given by

$$\varepsilon_c = \varepsilon_r - j60\lambda\sigma_g \quad (6.55)$$

where  $\sigma_g$  denotes the conductivity and  $\varepsilon_r$  the dielectric constant of the ground (Kerr, [24]).

In a land-based scenario, the conductivity and the dielectric constant change in the horizontal and vertical direction because of geological stratification. These quantities also exhibit seasonal variations. The dielectric constant and the conductivity can be determined from the following empirical relations [4]:

$$\varepsilon_r = c_s W + 2 \quad (6.56)$$

$$\sigma_g = 7.7 \times 10^5 (0.73W^2 + 1)(1 + 0.03T_w) \quad (6.57)$$

where  $c_s = 0.5$  for sand-like ground, 1.0 for average soil, and 1.5 for clay and electrically similar media;  $T_s$  is the temperature in °C of the water in the soil; and  $W$  is the percentage of weight of water in a given volume to the weight of water that could occupy the same volume.

In a maritime environment, the dielectric constant,  $\varepsilon_r$ , the conductivity,  $\sigma_g$ , and the normalized wavelength,  $\lambda_s$ , depend on the salinity  $s_l$  (per mil) of the water and the temperature,  $T_s$ , of the sea water °C, according to the following empirical relations (see Wu, [25]):

$$\varepsilon_r = 87.8 - \frac{15.3s_l}{58.45} - 0.363T_w \quad (6.58)$$

$$\sigma = \frac{5s_l}{58.45} + \frac{0.12T_w s_l}{58.45} + 0.4T_w \quad (6.59)$$

$$\lambda_s = 0.01(3.38 - 0.11T_w + 0.00147T_w^2 + \frac{0.0173T_w s_l}{58.45} - \frac{0.52s_l}{58.45}) \quad (6.60)$$

From these expressions the real and imaginary part of the complex dielectric constant,  $\varepsilon_c$ , can be derived.

$$\text{Re}\{\varepsilon_c\} = \frac{(\varepsilon_r - 4.8)\{1 + 0.01\pi(\frac{\lambda_s}{\lambda})^{0.98}\}}{1 + 0.02\pi(\frac{\lambda_s}{\lambda})^{0.98} + (\frac{\lambda_s}{\lambda})^{1.96}} + 4.8 \quad (6.61)$$

$$\text{Im}\{\varepsilon_c\} = \frac{-(\varepsilon_r - 4.8)(\frac{\lambda_s}{\lambda})^{0.98}}{1 + 0.02\pi(\frac{\lambda_s}{\lambda})^{0.98} + (\frac{\lambda_s}{\lambda})^{1.96}} - 60\lambda\sigma \quad (6.62)$$

For rough surfaces with a Gaussian collection of sinusoidal surface waves with uniform phase distribution, the reflection coefficient,  $\rho_S$ , is modified according to:

$$\rho = \rho_S \exp \left\{ -2 \left( \frac{2\pi h_{sd} \sin \psi}{\lambda} \right)^2 I_0 \left\{ 2j \left( \frac{2\pi h_{sd} \sin \psi}{\lambda} \right)^2 \right\} \right\} \quad (6.63)$$

where  $\rho_S$  is the specular coefficient,  $I_0(jx)$  is the modified Bessel function, and  $h_{sd}$  is the standard deviation of the surface height distribution (Miller, Brown and Vegh, [9]). In a land-based scenario, the standard deviation is an input parameter, while in a maritime scenario the standard deviation of the wave height is derived from the sea state, according to:

$$h_{sd} = 0.031s_s^2 \quad (6.64)$$

### 6.1.7.5 Troposcatter

At ranges far beyond the horizon, the propagation loss is dominated by the troposcatter. Propagation in the troposcatter region is the result of scattering by small inhomogeneities within the atmosphere's refractive structure as depicted in Figure 6.8.

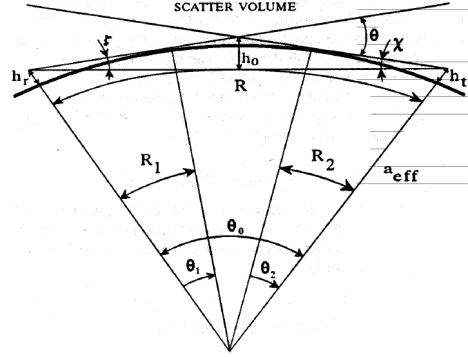


Figure 6.8: Troposcatter geometry.

The propagation factor,  $F^2$ , in dB because of tropospheric scattering is given by the product of the range-gain function  $V(R)$ , the height-gain function  $U(h_a, h_t)$ , and the antenna gain  $g^2(\theta_{opt})$  at the horizon [10]:

$$F^2 = V(R)U_0(h_a, h_t)g^2(\theta_{opt}) \quad (6.65)$$

The range-gain function,  $V(R)$ , in dB is given by

$$V(R) = -107.23 - 89.84x10^{-6} \frac{R - R_{hor}}{k} + 10 \log \lambda + 0.2N_0 \quad (6.66)$$

where  $R$  is the ground range,  $R_{hor}$  is the geometrical horizon range given in equation 73, and  $N_0$  is the surface refractivity. The height-gain function is important for low antenna heights, especially if the frequency is very low. The procedure for obtaining  $U_0$  requires a calculation of the effective scattering height,  $h_0$ , which is equal to

$$h_0 = \frac{sR\theta}{(1+s)^2} \quad (6.67)$$

where  $\theta$  is the scattering angle calculated from

$$\theta = \frac{R}{a_e} - (\theta_1 + \theta_2) \quad (6.68)$$

$$\theta_1 = \sqrt{\frac{2h_a}{a_e}} \quad (6.69)$$

$$\theta_2 = \sqrt{\frac{2h_t}{a_e}} \quad (6.70)$$

and  $s$  is defined by



$$s = \frac{\zeta}{\chi} = \frac{\frac{\theta}{2} + \theta_1 + \frac{h_t - h_a}{R}}{\frac{\theta}{2} + \theta_2 + \frac{h_a - H_t}{R}} \quad (6.71)$$

with  $0.1 \leq s \leq 10.0$ . The height-gain function in dB is given by

$$U_o = U_1 + \Delta U_0 = \frac{U_0(h_a) + U_0(h_t)}{2} + \Delta U_0 \quad (6.72)$$

If  $\Delta U_0$  is greater than  $U_1$  then  $U_0$  is equal to twice the value of  $U_1$ . The frequency gain function,  $U_0(h)$ , in dB is calculated according to

$$U_0(h) = -(16.3 + 13.3\eta_s) \left( 4\eta h \frac{\theta}{\lambda} + 0.40 + 0.16\eta_s \right)^{4/3} \quad (6.73)$$

The factor  $\eta_s$ , which is a function of the effective scattering height,  $h_0$ , is given by

$$\eta_s = 0.5969h_0 \{ + (0.031 - 0.00232N_0 + 5.67 \times 10^{-6}N_0^2) \exp -3.8 \times 10^{-6}h_0^6 \} \quad (6.74)$$

and with  $0.01 \leq \eta_s \leq 5$ .

The term  $\Delta U_0$  is calculated using

$$\Delta U_0 = -6(0.6 - \log \eta_s) \log s \log q, \quad (6.75)$$

where  $q$  is given by

$$q = \frac{h_t}{sh_a}, \quad (6.76)$$

with  $0.1 \leq q \leq 10$ .

The correction term  $\Delta U_0$  is zero for symmetrical paths, i.e.,  $s = 1$  and  $q = 1$ , and for  $\eta_s = 4$ .  $\Delta U_0$  has a maximum value of 3.6 dB for highly asymmetrical paths when  $\eta_s = 1$ .

### 6.1.8 TERPEM-light

TERPEM is based on parabolic equation (PE) techniques, which can model simultaneously refractive and terrain effects. The parabolic approximation is a simplification of the wave equation which is valid for low angles of propagation when the refractive index variations are small compared to the wavelength. The elliptic scalar wave equation:

$$\nabla^2 \psi + k^2 n^2 \psi = 0 \quad (6.77)$$

is approximated by the parabolic equation:

$$\frac{\partial^2 u}{\partial z^2} + 2ik \frac{\partial u}{\partial x} + k^2 (m^2(x, z) - 1) u = 0 \quad (6.78)$$

where  $u$  is obtained from  $\psi$  by factoring out the fast phase variation. A parabolic differential equation is much easier to solve numerically than an elliptic differential equation. An elliptic equation has to be solved simultaneously on the whole two-dimensional domain of integration, which would require impractical amounts of computing power for typical radio-propagation problems. On the other hand, a parabolic equation can be solved by a marching method, where the solution is computed on successive verticals, starting at the aperture field of the antenna. This can be implemented in various ways.

The most efficient method is the split-step algorithm, which was originally pioneered in underwater acoustics. A further approximation is made so that the parabolic equation can be written in terms of Fourier transforms. The resulting error tends to zero with the range step size between two successive verticals. The split-step algorithm alternates between  $z$ -space where the field is expressed as a function of height, and  $p$ -space, where the angular spectrum of the field is expressed as a function of angle with the horizontal.

Memory requirements and execution times of pure (vertical) parabolic equation solutions can become prohibitively large when full coverage diagrams are required. Fortunately in most tropospheric environments, the full power of the PE method is unnecessary for large angles and heights. Severe atmospheric refraction effects are normally limited to a few hundred m above sea level, and even with very strong refractive index gradients, effects on energy propagating at more than a degree or so from the horizontal are relatively easy to model using less sophisticated methods.

The idea of combining the PE with faster techniques in regions of the coverage diagram where the PE is not needed was first used in the Radio Physical Optics model (RPO) developed at NRaD in San Diego. Further developments have extended these hybrid techniques to deal with terrain and speed up calculations involving high antennas. The TERPEM hybrid model restricts the vertical PE to low altitudes and energy propagating at small angles from the horizontal. Ray optics are used for rays that remain in the line-of-sight region and that avoid being trapped in ducts or approaching diffraction shadow zones. The limiting ray beyond which ray optics become invalid is determined by the environment and the frequency. The horizontal parabolic equation method is used to extend the PE solution to higher altitudes. The resulting gain in computing resources is substantial.

The TERPEM hybrid models are very powerful. They include the following capabilities:

- Oversea and overland propagation
- Range-dependent refractivity
- Range-dependent surface impedance

- Fast models for high antennas
- Modelling of rough surface effects
- Modelling of atmospheric absorption
- Algorithms for low frequency operation down to 1 MHz

A number of run-time options are available through the Details pane of the TERPEM propagation dialogbox (see Figure 3.7. In the default ‘Automatic’ mode, the software optimises for speed. When switched off, the choices are made by the user. In particular it is always possible (if memory requirements are not too large) to run the program in pure PE mode to compare the results to the hybrid model.

The TERPEM propagation models are described in Section 6.1.8.1. Sections 6.1.8.4 and 6.1.8.5 describe impedance/roughness and atmospheric absorption modelling. Section 6.1.8.6 is a brief discussion of ‘path loss’, the fundamental quantity calculated by TERPEM, and how it relates to the radar equation.

#### 6.1.8.1 Propagation Models

The TERPEM hybrid model uses the following propagation algorithms:

- Vertical Parabolic Equation method (VPE)
- Horizontal Parabolic Equation Method (HPE)
- Ray Optics (RO)
- Flat Earth (FE)
- High antenna model

##### VPE Model

The basic vertical parabolic equation (VPE) model in TERPEM propagates the field with a sine transform. This is appropriate for modelling a horizontally polarized wave propagating over a perfectly conducting smooth surface. For more complicated situations, TERPEM also includes a more sophisticated algorithm, the Kuttler-Dockery mixed transform, which replaces the field with a function matched to the surface impedance. The VPE uses a wide-angle parabolic equation (WAPE) algorithm.

The way in which TERPEM chooses the VPE height grid is determined by the Output interpolation option in the Details pane of the TERPEM propagation dialogbox.

### HPE Model

The horizontal parabolic equation (HPE) model is a rigorous full-wave solution of the wave equation which calculates the field above a certain height from known values at that height. These are calculated using the VPE. Once the VPE field has been computed, the HPE can compute the field at any larger height by applying Fourier transforms in range. Because the Nyquist criterion for the HPE is based on the square of the propagation angle from the horizontal, the method often require smaller range steps than the VPE.

Height variations of the refractive index above the threshold height can be handled provided there are no strong ducting layers in that region. Range-dependence is not allowed at the heights where HPE is used. Terrain and range-dependent refractivity features below the threshold height can be handled without difficulty.

The way in which TERPEM chooses the HPE height grid is determined by the Fast HPE model option in the Details pane of the TERPEM propagation dialogbox.

### RO Model

Ray optics (RO), or geometrical optics, are based on the principle that radio-rays are the trajectories requiring minimal travel time between two points. This model is fast and accurate for line-of-sight propagation. However it cannot model diffraction in shadow zones due to terrain obstructions (in particular near and beyond the radio-horizon), and is not robust in ducting conditions.

In TERPEM, ray optics are used to model high propagation angles. The ray optics model is an analytical ray-trace model based on approximating the refractive index profile by linear segments. Field-strength is calculated from ray-focusing.

### FE Model

This is a simple two-ray interference model based on geometric optics, assuming the Earth is flat. It is accurate at short ranges, and large propagation angles.

### High Antenna Model

TERPEM includes a novel technique for speeding up calculations with a high antenna. The VPE domain need not include the source, and is determined solely by environmental parameters (terrain and refractivity). When the source is above the VPE domain, energy is fed into the VPE domain by a ray-trace and propagated with the ‘incoming energy’ parabolic equation algorithm. This is particularly efficient when only low altitude coverage of an airborne transmitter is needed. Hybrid models with special matching versions of the ray optics and HPE algorithms are available if the full, high altitude coverage diagram is required.

### Merging the Models

The main task is to define the domains where each model is applied, with the aim of achieving optimal speed while retaining seamless integration of the models and acceptable accuracy.

Execution times essentially depend on the maximum angles of propagation from the horizontal required by the VPE and HPE methods. This in turn is related to the terrain and refractivity environments as well as antenna height and frequency.

- First the refractivity profile is inspected, to obtain a first estimate of the maximum height of the VPE region. This region includes all ducting layers up to a maximum of 500 m above the transmitter, the idea being that layers further above the antenna will not normally be strong enough to have ducting effects. The maximum height of the VPE region is increased if necessary to account for terrain.
- With the novel ‘Incoming energy’ VPE model, there is no need to include the source in the VPE domain. If the antenna is well above duct and terrain features, the high antenna VPE model is used.
- The maximum propagation angle in the VPE region is estimated from ray-trace principles. First the ray limiting the RO region is determined in such a way that rays launched at a larger angle will neither be trapped nor hit terrain. If terrain is present, the angle of the limiting ray is adjusted to account for diffraction effects. Once the limiting ray is determined, the maximum VPE propagation angle is estimated from the refractivity profile in the VPE region. This angle determines the height integration step and the FFT size for the VPE model.
- If irregular terrain is present, an initial search determines whether ground reflections can be modelled by ray optics. This is only possible if terrain close to the antenna is flat, but other checks are needed to ensure that reflected rays do not hit terrain. This affects the size of the RO region, and hence the maximum propagation angle in the VPE region. Terrain constraints can lead to quite a large VPE angle. If this becomes too large, RO reflections are switched off. Generally this seems to provide quite good results, as coherent reflections tend to be destroyed by irregular terrain. However there could definitely be cases where the PE model will see strong terrain reflections which are not modelled in the RO region, producing discontinuities in the coverage diagram.
- The integration range step is now determined. A first estimate is given as a simple function of frequency. If the HPE model is needed, the range step is adjusted to satisfy the Nyquist criterion for HPE. Further checks are now made to see whether the HPE adjustment leads to slower execution times than with the ‘pure VPE’ model. In that case HPE is switched off.

Timings are not very sensitive to the choice of antenna pattern, but they do depend on the dimensions required for the coverage diagram. As a rule they increase linearly with maximum range and logarithmically with maximum height.

### 6.1.8.2 Profile Merging

When evaporation duct and upper air data are both specified, the two refractivity profiles must be merged.

Firstly, the upper air profile is checked for the presence of a surface duct. If one exists, it is assumed that this will dominate the propagation conditions at the surface, and any evaporation duct is ignored. (If a surface duct exists, it is likely that the boundary layer is stable, and the evaporation duct model would be invalid anyway.) If an evaporation duct exists, but has a duct height of less than 0.1 m, it is also ignored.

In cases where an evaporation duct is not required, and the lowest point of the upper air data is above sea level, the vertical profile is extended down to sea level by linearly extrapolating the lowest two points. In cases where an evaporation duct is to be included, the evaporation duct profile replaces the upper air profile at heights below 1.5 times the evaporation duct height. In all cases, the profile is extrapolated upwards from the highest point if necessary by assuming a standard exponential profile.

In the graphic display, all heights are shown with respect to sea level, not station height. When there is no evaporation duct, only the upper air data actually entered is displayed, with no extrapolation to sea level. This is less confusing when editing the upper air data. The lowest point of the ascent shown will therefore be at the station height. If an evaporation duct is also present, the full concatenated ascent is shown. The full extrapolated ascent is always used for the TERPEM calculations.

When terrain is present, the refractivity profiles are still defined relative to sea level. The profiles will be truncated at the ground if necessary.

### 6.1.8.3 Low Frequency Algorithms

From version 6 of the TERPEM software, the lower frequency limit is 1 MHz (compared to a lower limit of 30 MHz in earlier versions) to allow TERPEM to deal with propagation where the ground wave is important. This involved three significant changes.

- New antenna models appropriate to the HF band and accurate source models for antennas on or close to the ground.
- Improved models of surface impedance, including a multilayer ground type, to allow for ground penetration of the lower frequency waves.
- Changes to the algorithm used for combining the different propagation models in the hybrid model.

TERPEM uses a wide-angle algorithm, which can deal accurately with large propagation angles. Selecting Expert mode in the Details pane of the TERPEM propagation dialogbox, a maximum diffraction angle of up to 60° can be specified. In the Automatic mode, model

optimisation automatically ensures that propagation angles up to  $14^\circ$  are taken into account for frequencies below 300 MHz, and that for frequencies below 7.5 MHz all propagation angles are taken into account.

Below 300 MHz, the hybrid model is disabled and a pure VPE model is used. At these frequencies, the large wavelengths mean that the speed-up due to the use of hybrid models becomes far less significant. For example, the wide-angle PE model will be reasonably accurate at all propagation angles if the vertical step size is less than a quarter of the wavelength, and this becomes easily achievable at HF.

Below 300 MHz, the vertical step size is always set to be less than the wavelength, ensuring good representation for angles up to  $14^\circ$  or so. An overall upper limit of 10 m is also set for the vertical step size, automatically ensuring good representation at all angles for frequencies less than 7.5 MHz. If more accurate high angle results are wanted, the diffraction angle can be specified in the Expert mode, or the output grid can be set to force a sufficiently fine vertical resolution.

Optimisation procedures for the maximum integration height have also been adapted for the HF/VHF case.

The HF test cases have been validated against the GRWAVE ground wave propagation program (available from the International Telecommunications Union).

#### 6.1.8.4 Impedance and Roughness Modelling

The discrete mixed Fourier transform (DMFT) is designed to propagate a radiowave from one range to the next while preserving an impedance boundary condition at the air/ground interface. These boundary conditions are of the type:

$$\frac{\partial u}{\partial \vec{n}} = ik\delta u \quad (6.79)$$

where  $\vec{n}$  is the normal to the air/ground interface,

$$k = \frac{2\pi}{\lambda} \quad (6.80)$$

is the wave number and  $\delta$  is the local surface impedance, which depends on frequency, ground electrical properties, and the polarisation and angle of incidence of the incident wave. The angle of incidence is calculated from the TERPEM raytracing algorithm. The effective surface impedance for multiple ground layers is calculated using the formulae in Wait, [26].

It should be noted that the TERPEM parabolic equation model computes the field above the ground only. It cannot model the trapped surface wave, or Elliott mode, which may occur below the surface when a layer of ice is present above sea water.

The Dockery and Kuttler discrete mixed transform PE has been implemented, using a ray-trace to work out incidence angles at the ground. This allows the modelling of a range-

dependent impedance, with great flexibility for the modelling of electrical constants and roughness. Vertical and circular polarisations are correctly taken into account.

Since the DMFT increases computation times in the PE region by a factor of 50% or so, it is best to limit its use as much as possible. At VHF frequencies and above, the surface impedance for most types of smooth ground is very large and it is a good approximation to model the boundary condition as  $u = 0$ . In that case the DMFT can be replaced by a discrete sine transform. However use of the DMFT is essential for rough surface modelling and also when high accuracy is required at vertical polarisation.

For propagation over the rough sea surface, effective reflection coefficients depending on the RMS waveheight can be computed for a given angle of incidence. These can then be used to calibrate the mixed transform at each range. Local angles of incidence are computed with geometrical optics.

The roughness factor which multiplies the smooth case reflection coefficient is given by the Miller-Brown model:

$$\rho = \exp\left(-8\left(\frac{\pi w \sin \psi}{\lambda}\right)^2\right) I_0\left(8\left(\frac{\pi w \sin \psi}{\lambda}\right)^2\right) \quad (6.81)$$

where  $\psi$  is the grazing angle,  $\lambda$  is the wavelength and  $I_0$  is the modified Bessel function of order zero. The RMS waveheight,  $w$ , is computed in terms of the wind speed,  $v_w$  (m/s), using the Phillips model:

$$w = 0.0051 v_w^2 \quad (6.82)$$

For very rough seas, the mixed transform saturates and loses accuracy. It does however provide very good results for moderate to rough seas, and gives a good idea of propagation performance in very rough conditions.

#### 6.1.8.5 Atmospheric Absorption

Atmospheric absorption effects in the oxygen and water-vapour spectral lines become important at large ranges for frequencies above 1 GHz and have to be taken into account even at short ranges for frequencies above 18 GHz.

The full line-by-line calculation of Liebe's MPM is incorporated in TERPEM to compute atmospheric absorption if required. The current version of TERPEM assumes constant atmospheric absorption, *i.e.*, independent of height and range. This is adequate at microwave frequencies and is enough to give an idea of absorption effects for mm-waves. This simple approach has the merit of only requiring three parameters (pressure, temperature and relative humidity) for MPM calculations.

For reference, values of absorption per km,  $\chi$  (dB/km), for typical values of atmospheric parameters ( $P = 1013.25$  mb) are given in Table 6.1.



Table 6.1: Absorption rates,  $\chi$ , for two conditions of temperature,  $T$ , and relative humidity,  $h_r$ .  $f$  is the frequency.

$f$ (GHz)	$\chi$	
	$T = 15^\circ\text{C}, h_r = 75\%$ (dB/km)	$T = 25^\circ\text{C}, h_r = 90\%$ (dB/km)
3	0.01	0.01
10	0.02	0.03
18	0.07	0.15
22	0.23	0.47
35	0.12	0.25

### 6.1.8.6 Path Loss and Pattern Propagation Factor

The basic output of TERPEM is a grid of one-way ‘path loss’ values. Path loss,  $L$ , in dB, is defined as

$$L = 10 \log \left( \frac{P_t^{eirp}}{P_r^{iso}} \right) \quad (6.83)$$

where  $P_t^{eirp}$  is the boresight equivalent isotropic radiated power and  $P_r^{iso}$  is the power that would be received by an isotropic antenna, assuming that there are no system losses. The TERPEM path loss includes beamshape effects. It also includes atmospheric absorption loss when required.

The various forms of the radar equation, which are discussed in the ensuing sections, contain the fourth power of the pattern propagation factor,  $F^4$ , or  $F_{Tx}^2 F_{Rx}^2$  in case of dissimilar transmit and receive antennas. Beamshape effects and all propagation effects including atmospheric absorption are represented by the pattern propagation factor.

Path loss,  $L$ , is related to the pattern propagation (power) factor,  $F^2$ , by:

$$10 \log(F^2) = 20 \log\left(\frac{4\pi r}{\lambda}\right) - L \quad (6.84)$$

$10 \log(F^2)$  is the (logarithmic) quantity referred to as the (one-way) propagation factor in TERPEM, and the equation shows that it is the power received relative to the power received in free space by isotropic antennas.

### 6.1.8.7 Paulus Evaporation Duct Model

CARPET 3 contains the relatively straightforward Paulus evaporation duct model for the low-altitude refractivity profile above sea. Given a specific evaporation duct height,  $\delta$  (m), the M-profile given by:

$$M = M_0 + 0.125 \left\{ z - (\delta + z_0) \ln\left(\frac{z + z_0}{z_0}\right) \right\} \quad (6.85)$$

in which  $z$  (m) is the height,  $M_0$  is the value of  $M$  at the sea surface and  $z_0$  equals  $1.5 \times 10^{-4}$ , see Paulus, [27]. Two examples of the profile are given in Figure 6.9.

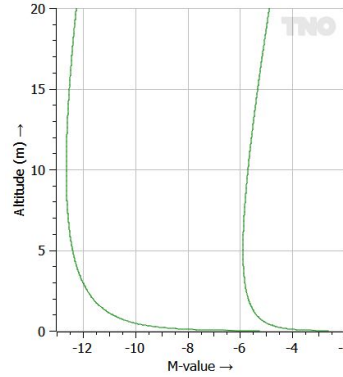


Figure 6.9: Low altitude M-profiles according to the Paulus model. Left: duct height 10 m. Right: duct height 5 m.

#### 6.1.8.8 Surface Clutter Path Loss

In order to determine the power of the surface clutter component, the path loss (or pattern propagation factor) close to the earth's surface must be assessed. Clearly, for a smooth sea and horizontal polarisation the field will be zero at the surface, and how fast it increases above the surface to its 'average' value is wavelength dependent. When there is sea clutter due to waves, the situation is of course much more complicated. Models such as TERPEM and EREPS do not attempt to model the shape of the sea surface, so the 'roughness factor' is just a way of reducing the 'average' reflectivity. How the predicted loss at the lowest grid points relates to the incident field on the wave surface can only be approximate.

Note that the default value of the 'effective clutter height' is at 1 m above the earth's surface (Clutter dialogbox). The user may want to adapt this to the 'average' wave height (mean or RMS or whatever seems appropriate for the specified sea state). At least this encapsulates the notion that the mean backscatter height will on average be higher above nominal sea level for the higher sea states. This gives a physical basis for the choice, even if there is a big uncertainty of the precise scale/offset to apply to wave height.

#### 6.1.9 Rain Attenuation

Besides absorption by the oxygen and water vapor content of the atmosphere, electromagnetic waves are also attenuated by such meteorological phenomena as rain, snow, clouds, and hail. In CARPET, only the attenuation due to a uniform rain cloud is considered. The rain absorption rate (one way),  $\gamma$  (dB/km), is determined by:

$$\gamma = k \cdot r_r^\alpha \quad (6.86)$$

where  $r_r$  is the rainfall rate in mm/hr and  $k$  and  $\alpha$  are two coefficients that are functions of frequency, and also depend to some extent on the distribution of raindrop diameters as well as on polarisation, see for instance Boithias, [28], and Richards, *e.a.*, p.125 to 127, [48].

In Table 6.2 the values of  $k$  and  $\alpha$  are listed for a Laws and Parsons diameter distribution and the Pruppacher and Pitter model for the shape of drops. The table occurs in recommendation 838 of the CCIR, [49]. Figure 6.10 shows  $\gamma$  versus frequency for several rain rates.

Table 6.2: Rain attenuation constants as a function of frequency and polarisation.

$f$ (GHz)	$k_V$	$k_H$	$\alpha_V$	$\alpha_H$
1	0.0000387	0.0000352	0.912	0.880
2	0.000154	0.000138	0.963	0.923
4	0.000650	0.000591	1.121	1.075
6	0.00175	0.00155	1.308	1.265
8	0.00454	0.00395	1.327	1.310
10	0.0101	0.00887	1.276	1.264
12	0.0188	0.0168	1.217	1.200
15	0.0367	0.0335	1.154	1.128
20	0.0751	0.0691	1.099	1.065
25	0.124	0.113	1.061	1.030
30	0.187	0.167	1.021	1.000
35	0.263	0.233	0.979	0.963
40	0.350	0.310	0.939	0.929
45	0.442	0.393	0.903	0.897
50	0.536	0.479	0.873	0.868
60	0.707	0.642	0.826	0.824
70	0.851	0.784	0.793	0.793
80	0.975	0.906	0.769	0.769
90	1.06	0.999	0.753	0.754
100	1.12	1.06	0.743	0.744
120.0	1.18	1.13	0.731	0.732
150.0	1.31	1.27	0.710	0.711
200.0	1.45	1.42	0.689	0.690
300.0	1.36	1.35	0.688	0.689
400.0	1.32	1.31	0.683	0.684

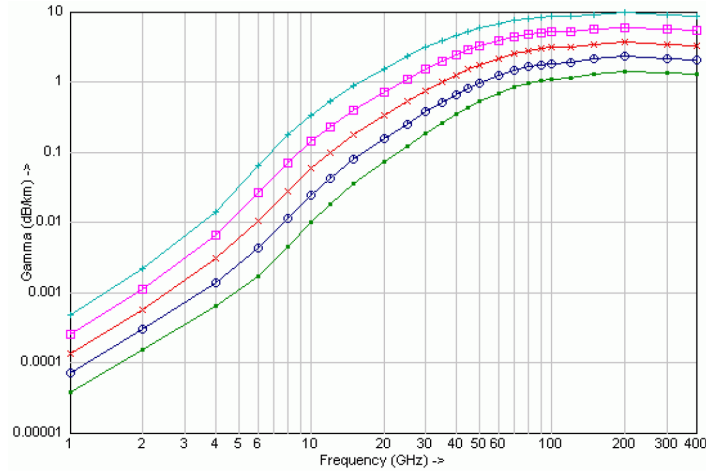


Figure 6.10: Rain attenuation versus frequency. The rain-rates in mm/hr are: green (dot): 1, darkblue (circle): 2, red (x-sign): 4, magenta (square): 8, cyan (+-sign): 16.

As described in a document made by the IEEE 802.16 working group, [29],  $k$  and  $\alpha$  can be derived according to

$$k = \frac{k_H + k_V + (k_H - k_V) \cos^2 \theta \cos(2\tau)}{2} \quad (6.87)$$

$$\alpha = \frac{k_H \alpha_H + k_V \alpha_V + (k_H \alpha_H - k_V \alpha_V) \cos^2 \theta \cos(2\tau)}{2k} \quad (6.88)$$

in which  $\theta$  is the elevation angle of the path and  $\tau$  is the polarisation tilt angle relative to the horizontal. For horizontal polarisation ( $\tau = 0$ ) and elevation angle zero we get  $k = k_H$  and  $\alpha = \alpha_H$ . For vertical polarisation ( $\tau = \pi/2$ ) and elevation angle zero we get  $k = k_V$  and  $\alpha = \alpha_V$ . For circular polarisation ( $\tau = \pi/4$ ) and elevation angle zero we get  $k = (k_H + k_V)/2$  and  $\alpha = (k_H \alpha_H + k_V \alpha_V)/(k_H + k_V)$ .

Figure 6.11 shows the rain attenuation in dB/km versus the rain rate in mm/hr for horizontal polarisation and four different frequencies in the L, S, X, K<sub>u</sub> and K<sub>a</sub> bands.

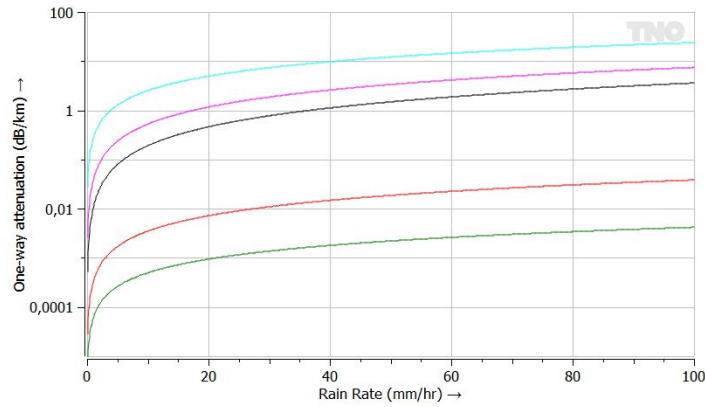


Figure 6.11: Rain attenuation versus rainfall rate. Green: 1.3 GHz. Red: 3 GHz. Black: 10 GHz. Magenta (pink): 15 GHz. Cyan (light blue): 35 GHz.

CARPET 3 also contains the updated version of the CCIR model, as described in ITU Recommendation ITU-R P.838-3, [51]. Expressions to determine  $k$  and  $\alpha$  from 1 to 1000 GHz are given in this publication. The figures 6.12, 6.13 and 6.14 show  $k$ ,  $\alpha$  and the attenuation rate  $\gamma$  versus frequency according to this model.

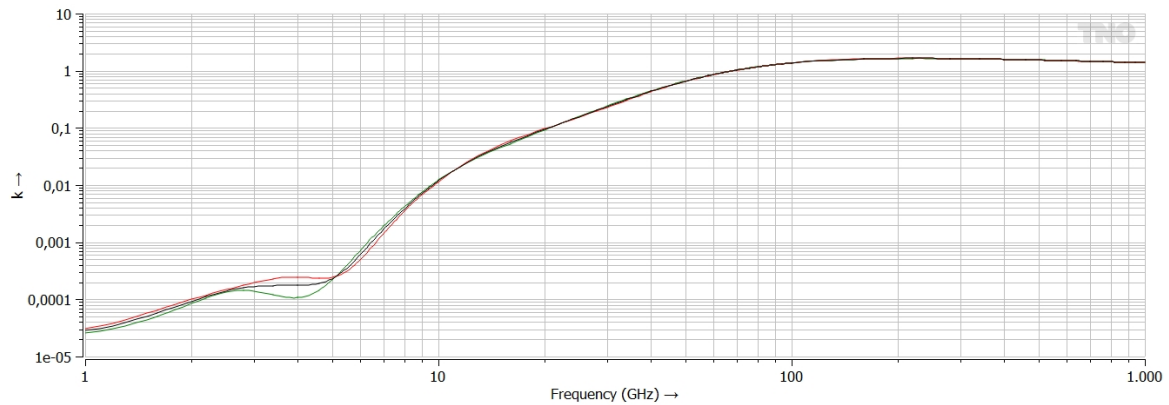


Figure 6.12:  $k_H$  (green),  $k_V$  (red) and  $k_C$  (black) versus frequency.

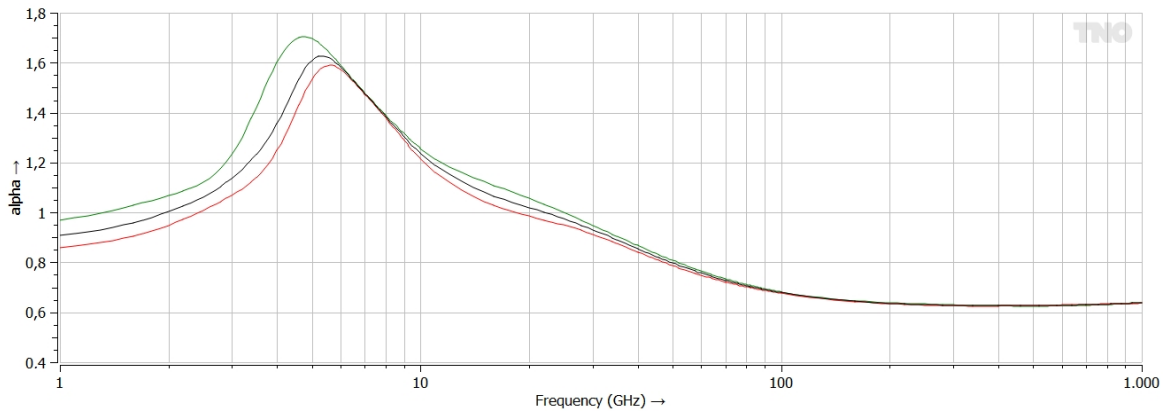


Figure 6.13:  $\alpha_H$  (green),  $\alpha_V$  (red) and  $\alpha_C$  (black) versus frequency.

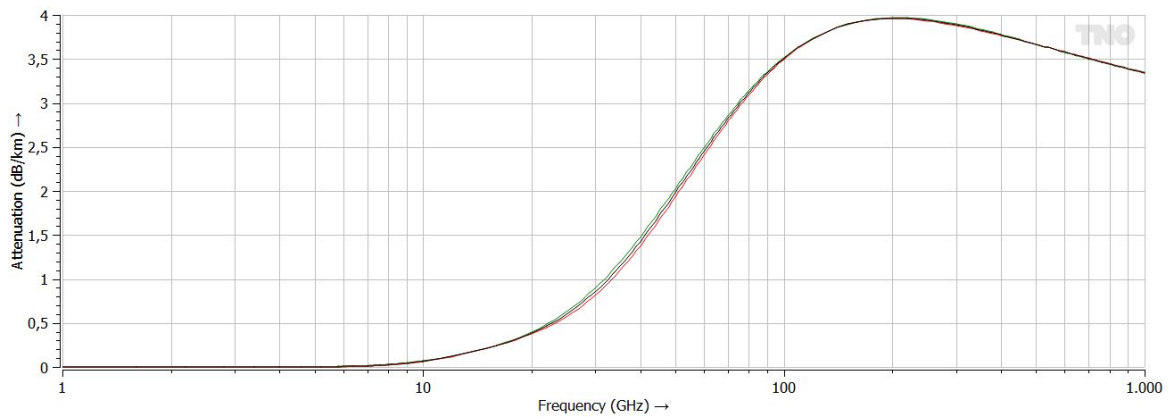


Figure 6.14: Attenuation rate (in dB/km) for horizontal (green), vertical (red) and circular polarisation (black). The ray elevation angle is  $0^\circ$ . The rainfall rate is 4 mm/hr.

## 6.2 System Noise

### 6.2.1 Noise Power

The ability of a radar to detect target echoes depends not only on the power of the target echo (or signal power), but also on returns from surface and volume clutter, and on noise present in the receiver. The sources of noise are both within the radar system and in the radar's environment, *e.g.*, the sun. Dave Barton [30], p.5 presents an illustrative picture of the various noise sources. These sources contribute to the system's noise temperature,  $T_s$  (K), from which the noise power,  $P_n$  (W), is derived according to:

$$P_n = k_B T_s B, \quad (6.89)$$

where  $k_B$  is Boltzmann's constant ( $1.38 \times 10^{-23}$  J/K) and  $B$  is the instantaneous bandwidth of the radar (Hz).  $P_n$  can be determined at different points of the receiver: the output of the antenna, the input of the circulator or the input of the low-noise amplifier (LNA). Whichever reference point is taken is not important, as long as the powers of the other components (signal, surface clutter, volume clutter, jamming) are evaluated at the same point.

The system input noise temperature is generally divided into three major components. Apart from noise generated by the receiver, with effective receiver temperature  $T_e$  (K), there is a temperature term of the antenna,  $T_a$  (K), and a temperature term of RF components that connect the antenna to the receiver,  $T_r$  (K). If the antenna output terminal is taken as reference point, the system noise temperature is given by

$$T_s = T_a + T_r + L_r T_e. \quad (6.90)$$

$L_r$  ( $> 1$ ) is the loss of the receiving RF line. The three components are determined according to:

$$T_a = \frac{0.876(T_{sky} - T_0)}{L_a} + T_0, \quad (6.91)$$

$$T_r = T_{tr}(L_r - 1), \quad (6.92)$$

$$T_e = T_0(F_n - 1), \quad (6.93)$$

in which

- $T_{sky}$  is the apparent sky temperature which is discussed in the subsequent section.
- $L_a$  is the dissipation loss within the antenna.

- $T_0$  is the reference temperature. CARPET assumes 290 K so that equation 6.91 can be written as

$$T_a = \frac{(0.876T_{sky} - 254)}{L_a} + 290. \quad (6.94)$$

- $T_{tr}$  is the physical temperature of the RF components, CARPET assumes this to be equivalent to  $T_0$ .
- $F_n$  is the noise figure of the receiver.

If the galactic noise activity is discarded, CARPET assumes the antenna temperature,  $T_a$ , to be 290 K. With  $T_{tr} = 290$  K equation 6.90 then simplifies to

$$T_s = 290L_rF_n. \quad (6.95)$$

As argued in Section 3.12, CARPET 3 allows the calculated system noise temperature to be ‘overruled’.

### 6.2.2 Doppler Spectrum

The Doppler spectrum of the noise is assumed to be white, which results in an autocorrelation function given by a Dirac impulse:

$$r_n(\tau) = P_n\delta(\tau) \quad (6.96)$$

### 6.2.3 Noise Temperature of the Sky

The noise temperature of the sky, which influences the noise power in the radar receiver in CARPET if the Antenna Noise checkbox is switched on, is determined by galactic and solar noise according to the relation

$$T_{sky} = T_{atm} + \frac{T_{gal} + T_{bb}}{L_\alpha} + T_{a,sun} \quad (6.97)$$

in which  $T_{atm}$  is the atmospheric noise temperature,  $T_{gal}$  is the galactic noise temperature,  $T_{bb}$  is the cosmic black body temperature (2.7 K),  $L_\alpha$  is the atmospheric loss factor (ratio  $\geq 1$ ),  $T_{a,sun}$  is the solar contribution to the antenna temperature (assuming that the sun is in an average level sidelobe of the antenna pattern), see [31].

The tropospheric noise temperature  $T_{atm}$  is computed by numerical integration of the equation

$$T_{atm} = 0.2303 \int_0^\infty \gamma(R)T_t(R) \exp \left\{ -0.2303 \int_0^R \gamma(r)dr \right\} dR \quad (6.98)$$



where  $dR$  is taken along the ray path,  $\gamma$  is the oxygen plus water vapor absorption coefficient, and  $T_t$  is the thermal temperature of the troposphere.

The galactic noise temperature at a frequency  $f$  in MHz is given by

$$T_{gal} = T_{100} \left( \frac{100}{f} \right)^{2.5} \quad (6.99)$$

where the quantity  $T_{100}$  is the galactic noise temperature at a frequency of 100 MHz. In CARPET three values can be specified. The average value is 3050 K, the minimum 500 K and the maximum value is 18,650 K.

The solar contribution to the antenna temperature  $T_{a,sun}$  is obtained from Table 6.3, giving values of the solar temperature  $T_{sun}$  for frequencies in the range 100 MHz to 10 GHz, see also Figure 6.15. At frequencies between the tabulated values,  $T_{sun}$  is found by linear interpolation. Above 10 GHz,  $T_{sun}$  is assumed to have the constant value of 10,000 K.

Table 6.3: Solar temperature versus frequency.

$f$ (MHz)	$T_{sun}$ (K)
100	1,100,000
200	1,300,000
300	1,500,000
400	1,100,000
500	1,000,000
1,000	200,000
3,000	30,000
10,000	11,000

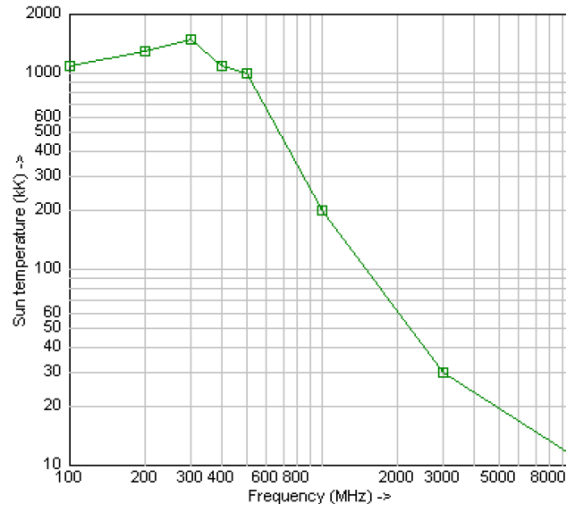


Figure 6.15: Solar temperature versus frequency.

The solar contribution to the antenna noise temperature  $T_{a,sun}$  is related to the solar temperature by the equation

$$T_{a,sun} = \frac{(4.75 \times 10^{-5})T_{sun}}{L_{\alpha}} \quad (6.100)$$

see [31]. The numerical factor takes into account the assumed unity gain average sidelobe level, the ratio of the sun's noise diameter to the total solid angle ( $4\pi$  steradians) viewed by the antenna including its side and back lobes, and the assumption that the sun is on the average ten times noisier than in profiles indicated by the referenced curve, which portrays the 'quiet' sun. In case minimum galactic noise is selected,  $T_{a,sun}$  is decreased by a factor of 10. In case of maximum galactic noise  $T_{a,sun}$  is increased by a factor of 10.

### 6.3 Target

#### 6.3.1 Target Power

For a radar with a pulsed waveform, the average power of the target signal received in the radar after pulse compression,  $P_t$ , is given by

$$P_t = \frac{P_p G_t G_r G_{pc} \lambda^2 \sigma_t F^4}{(4\pi)^3 R_t^4 L}, \quad (6.101)$$

where  $P_p$  (W) is the average power during radar signal transmission<sup>7</sup>,  $G_t$  and  $G_r$  are the power gain factors of the transmit and receive antenna respectively,  $G_{pc}$  is the pulse compression gain,  $\lambda$  (m) is the wavelength,  $\sigma_t$  (m<sup>2</sup>) is the target radar cross section (RCS),  $F$  is the pattern propagation (amplitude) factor that incorporates the effects of the antenna pattern and the radar environment (see Section 6.1),  $R_t$  (m) is the slant range to the target.  $L$  represents a series of losses which can be composed according to:

$$L = L_t L_{bs} L_{CFAR} L_{r,Tx} L_{r,Rx} L_e L_{PC} L_q L_{rs} L_{r,m}, \quad (6.102)$$

in which:

- $L_t$  is transmitter loss,
- $L_{bs}$  is antenna beamshape loss,
- $L_{CFAR}$  is CFAR loss,
- $L_{r,Tx}$  is radome loss on transmit,
- $L_{r,Rx}$  is radome loss on receive,
- $L_e$  is eclipsing loss,
- $L_{PC}$  is pulse compression taper loss,
- $L_q$  is ADC quantisation loss,
- $L_{rs}$  is range straddling loss,
- $L_{r,m}$  is receiver mismatch loss.

Losses within the medium, *i.e.*, the two-way atmospheric loss (oxygen and water vapor absorption) and attenuation by rain are confined in the pattern propagation factor.

Note the following:

<sup>7</sup>We use the formulation of Budge and German, [32].

1. In the case of propagation in free space, the pattern propagation factors only takes the effect of the antenna pattern on the target power into account.
2. The deactivation of the Attenuation checkbox will set the atmospheric losses,  $L_\alpha$ , to 0 dB.
3. In case pulse compression is not applied,  $G_{pc}$  is unity (0 dB). Otherwise, the pulse compression gain is given by the time-bandwidth-product:

$$G_{pc} = \tau B, \quad (6.103)$$

in which  $\tau$  is the (uncompressed) pulsewidth and  $B$  is the instantaneous bandwidth.

4. If circular polarisation is applied, the target power is generally reduced, 5 dB is an appropriate factor, see Nathanson [33]. Since CARPET version 2.13, however, the user can define this reduction.

To understand equation 6.101, R.T. (Bob) Hill, provided the following line of reasoning in his radar course:

- (a) We would expect the received power to be proportional to the power transmitted:

$$P_t \propto P_p \text{ (W)}. \quad (6.104)$$

- (b) To restrict our interest to ‘main beam’ operations we would expect the gain of the directive antenna,  $G_t$ , to come in like so:

$$P_t \propto P_p G_t \text{ (W)}. \quad (6.105)$$

- (c) The spatial power density,  $\Phi$ , at a distance  $R$  is given by:

$$\Phi = \frac{P_p G_t}{4\pi R^2} \text{ (W/m}^2\text{)}. \quad (6.106)$$

- (d) This power density is intercepted by a target of a certain radar cross section,  $\sigma$  ( $\text{m}^2$ ), so that we have ‘Watts’ again:

$$P_t \propto \frac{P_p G_t}{4\pi R^2} \sigma \text{ (W)}. \quad (6.107)$$

- (e) The target puts back ‘Watts’ as though this were a new ‘transmitter’ radiating isotropically, *i.e.*, in all directions. Hence the spatial power density at the radar antenna is given by:

$$\Phi = \frac{P_p G_t}{4\pi R^2} \sigma \frac{1}{4\pi R^2} \text{ (W/m}^2\text{)}. \quad (6.108)$$



- (f) The radar intercepts the incident reflected signal with a receiving aperture of  $A$  square meters; a received signal strength that the antenna provides the receiver to work with:

$$P_t = \frac{P_p G_t}{4\pi R^2} \sigma \frac{1}{4\pi R^2} A \text{ (W)}.^8 \quad (6.109)$$

Antenna gain,  $G$ , is related to aperture area,  $A$ , according to

$$G = \eta \frac{4\pi A}{\lambda^2} \Leftrightarrow A = \frac{G\lambda^2}{4\pi\eta}, \quad (6.110)$$

so that equation 6.109 can be written as:

$$P_t = \frac{P_p G_t G_r \sigma \lambda^2}{(4\pi)^3 R^4 \eta} \text{ (W)}. \quad (6.111)$$

Rather than the antenna efficiency  $\eta$ , a more generic loss factor,  $L$ , may be introduced:

$$P_t = \frac{P_p G_t G_r \sigma \lambda^2}{(4\pi)^3 R^4 L} \text{ (W)}. \quad (6.112)$$

Note that equation 6.101 has two additional factors;  $F^4$  accounts for propagation effects in a non-free-space environment,  $G_{pc}$  accounts for pulse compression gain. Equation 6.112 can obviously also be written as:

$$R = \sqrt[4]{\frac{P_p G_t G_r \sigma \lambda^2}{(4\pi)^3 L P_t}} \text{ (m)}. \quad (6.113)$$

Because the detectability of a target not only depends on properties of the target, but also on receiver noise, on unwanted reflections (clutter) and potentially also on intentional or unintentional jamming, the maximum range at which a radar can observe a target,  $R_{max}$  (m), is given by

$$R_{max} = \sqrt[4]{\frac{P_p G_t G_r \sigma \lambda^2}{(4\pi)^3 L S_{min}}} \text{ (m)}, \quad (6.114)$$

in which  $S_{min}$  is the minimum discernible signal. Equation 6.114 may be referred to as ‘radar equation’, but there are other variants that bear this name as well, as discussed in Section 6.7.

<sup>8</sup>Examples: if the RCS halves, the range scales by a factor  $\sqrt[4]{\frac{1}{2}} \approx 0.84$  to arrive at the same power of the target response. If the RCS reduces with a factor of ten, the range scales by a factor  $\sqrt[4]{\frac{1}{10}} \approx 0.56$  to arrive at the same target power.

### 6.3.2 Doppler Spectrum

The Doppler spectrum of the target is assumed to be a Dirac function at the target Doppler frequency shift,  $\Delta f_t$  (Hz), which is given by

$$\Delta f_t = \frac{2v_t}{\lambda}, \quad (6.115)$$

where  $v_t$  (m/s) represents the radial velocity of the target.

The autocorrelation function  $r_t(\tau)$  corresponding to the target Doppler spectrum is given by

$$r_t(\tau) = P_t \exp\{j2\pi f_t \tau\} \quad (6.116)$$

### 6.3.3 Swerling Cases

Radar cross section (RCS) is a fictitious area (dimension  $\text{m}^2$ ) that represents the reflective properties of a target. A certain value for the RCS is valid for a specific carrier frequency, instantaneous bandwidth, target aspect angle, transmit polarisation and receive polarisation.

Generally, RCS fluctuates over time. Small aspect angle changes can result in significant RCS-changes, as the orientation of dominant scatterers changes, as illustrated in Figure 6.16. RCS fluctuations can also arise as parts of the target (*e.g.*, helicopter blades, jet engine blades) move, or by changes in the carrier frequency. Additional factors cause the received target echo (so not the RCS) to fluctuate, such as turbulence in the atmosphere, changes of the shape of the sea surface.

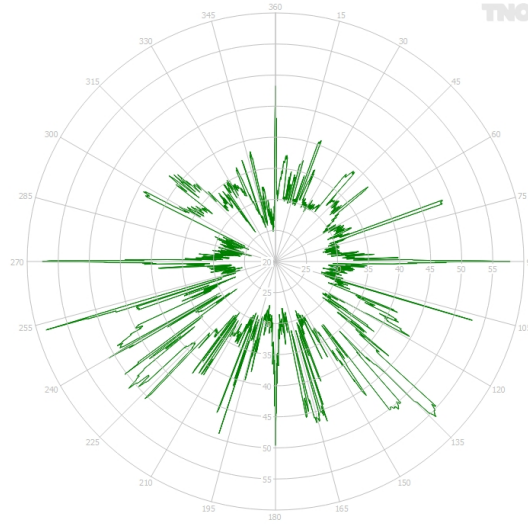


Figure 6.16: Calculated RCS-pattern of a ship of length 30 m for X-band. 0° is bow-on, 90° is starboard-on.

In 1954 Peter Swerling (1929-2000, [34]) published<sup>9</sup> different target fluctuation models, making a distinction between a complex target that consists of multiple similar scatterers, and a target that has a single dominant scatterer. Furthermore, a target echo can vary relatively slowly, *i.e.*, from scan to scan of the radar antenna, or relatively quickly, from pulse to pulse. This results in the four Swerling cases that have been shown in Table 3.2 which is repeated here for convenience.

Table 6.4: The four Swerling cases.

Fluctuation speed	No dominant scatterer	One dominant scatterer
Scan-to-scan	1	3
Pulse-to-pulse	2	4

While there are four Swerling cases (1 up to 4), there are only two PDFs, both belonging to the family of  $\chi^2$  distributions. Swerling has published probability density functions (PDFs) for the signal-to-noise power ratios, in the sequel, we specify PDFs for the RCS, which are equivalent (recall that received power in W is proportional to RCS in  $\text{m}^2$ ).

For the complex targets, Swerling cases 1 and 2, the PDF,  $p(\sigma, \bar{\sigma})$ , is given by

$$p(\sigma, \bar{\sigma}) = \frac{1}{\bar{\sigma}} e^{-\frac{\sigma}{\bar{\sigma}}}, \sigma \geq 0. \quad (6.117)$$

<sup>9</sup>The phrase ‘published’ is used intentionally; Peter Swerling didn’t make a ‘claim to originality’ (sic).

$\bar{\sigma}$  is the average of  $\sigma$ . This is the  $\chi^2$  distribution with two degrees of freedom,  $K$ , also known as the exponential distribution.

The ratio of the standard deviation,  $s$ , to the mean value  $\mu$ , of a  $\chi^2$  distribution is given by

$$\frac{s}{\mu} = \sqrt{\frac{2}{K}}, \quad (6.118)$$

which is unity for the cases 1 and 2.

The PDF as well as the CDF are illustrated in Figure 6.17.

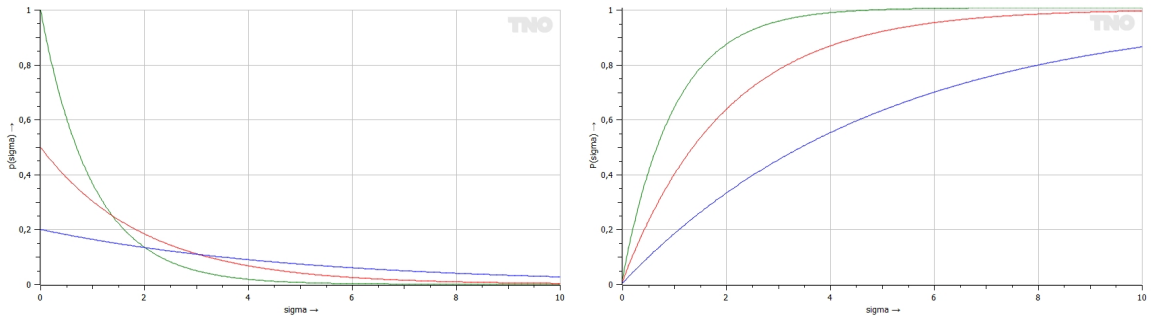


Figure 6.17: PDF (left) and CDF (right) of the Swerling cases 1 and 2 (no dominant scatterer). Green:  $\bar{\sigma} = 1 \text{ m}^2$ , red:  $\bar{\sigma} = 2 \text{ m}^2$ , blue:  $\bar{\sigma} = 5 \text{ m}^2$ . Obviously, the area under the PDF-curves is unity. The probability that the RCS is between  $\sigma$  and  $\sigma + d\sigma$  is equal to the area that is bounded horizontally by  $\sigma$  and  $\sigma + d\sigma$  and at the top by the PDF-curve.

For the single dominant scatterer (cases 3 and 4) the following probability density function was published:

$$p(\sigma, \bar{\sigma}) = \frac{4\sigma}{\bar{\sigma}^2} e^{-\frac{2\sigma}{\bar{\sigma}}}, \sigma \geq 0. \quad (6.119)$$

This is the  $\chi^2$  distribution with four degrees of freedom ( $K = 4$ ).  $s/\mu$  is now  $\sqrt{1/2} \approx 0.71$ . The PDF as well as the CDF are shown in Figure 6.18.



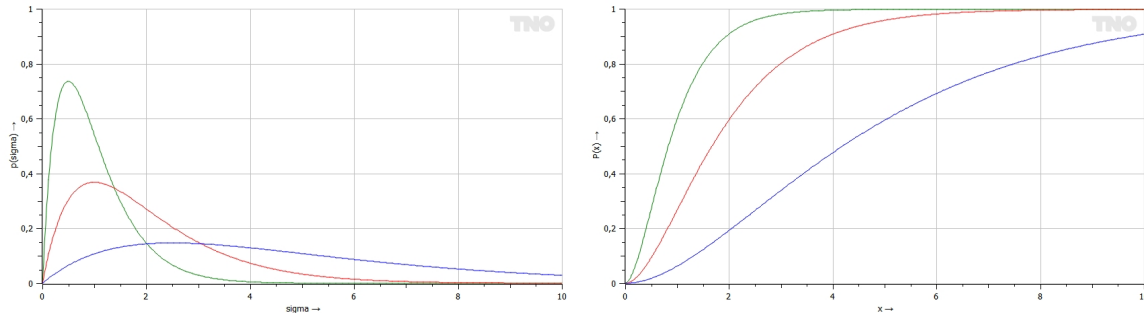


Figure 6.18: PDF (left) and CDF (right) of the Swerling cases 3 and 4 (single dominant scatterer). Green:  $\bar{\sigma} = 1 \text{ m}^2$ , red:  $\bar{\sigma} = 2 \text{ m}^2$ , blue:  $\bar{\sigma} = 5 \text{ m}^2$ .

Note that for the Swerling cases 3 and 4 (one dominant scatterer) an SNR of zero cannot occur.

What Swerling case model is one to apply? Citing Peter Swerling: ‘Thus one would expect objects which are large compared with wavelength (and which are not shaped too much like a sphere) to fluctuate approximately according to the exponential density (6.117). On the other hand, a target which can be represented as one large reflector together with other small reflectors, or as one large reflector subject to fairly small changes in orientation, would be expected to behave more like (6.119). The non-fluctuating model would apply to spherical or nearly spherical objects (*e.g.* balloons, meteors) at fairly large wavelengths.’

It is emphasized, however, that the Swerling case is also a matter of the radar waveform. *E.g.*, in case the RF is staggered pulse-to-pulse so that the target responses of a pulse train decorrelate completely (coherent integration is not applicable) Swerling cases 2 and 4 are more appropriate than the cases 1 and 3. The situation that the target responses from pulse to pulse are not completely correlated (Swerling cases 1 and 3, correlation coefficient  $\rho$  equal to 1) or decorrelated (Swerling cases 2 and 4,  $\rho = 0$ ) is discussed by Irving Kanter, [35].

### 6.3.4 Extended Target

The two mechanisms that are present in CARPET 3 to model extended targets have been introduced in Section 1.2.3. The Figures 6.19 and 6.20 provide results of the two techniques.

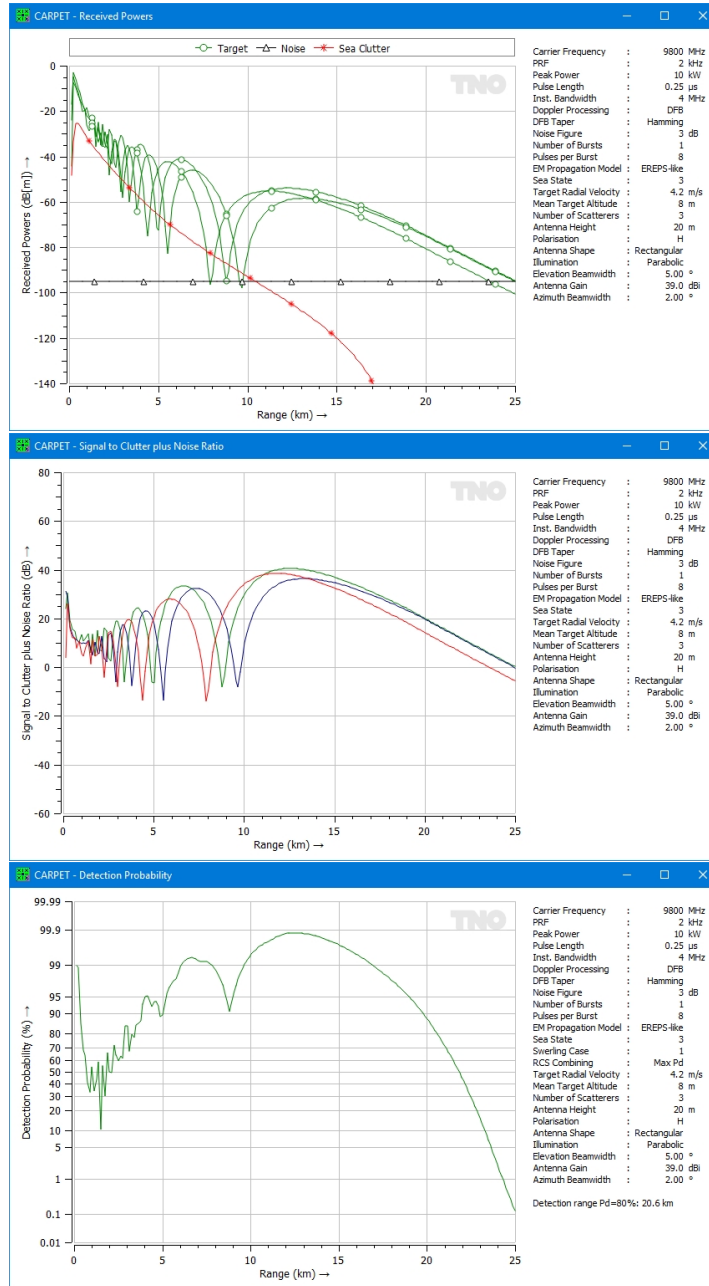


Figure 6.19: Top: Received signals, the target is made up of three scatterers. Middle: SCNRs of the three scatterers. Bottom: detection probability according to the 'Max Pd' method.

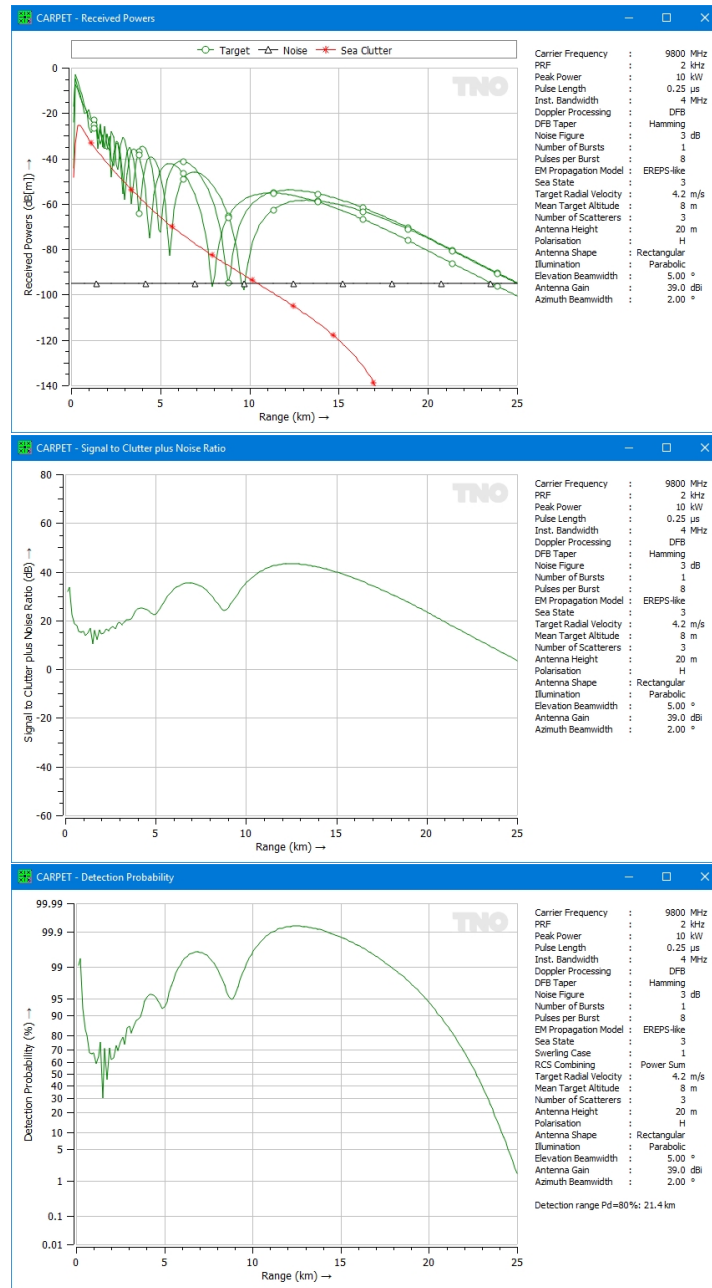


Figure 6.20: Top: Received signals, the target is made up of three scatterers. Middle: SCNR versus range, the three received target powers have been summed. Bottom: detection probability according to the ‘Power Summation’ method.

As one can see the resulting detection ranges according to the two recipes is slightly different: 20.6 km for the maximum detection probability method, 21.4 km for the power summation method. Which recipe is one to choose? Another, more fundamental question is: under what conditions is it actually allowed to add powers? The answer to the last question is: powers of signals can be added if the signals are mutually uncorrelated.<sup>10</sup>

---

<sup>10</sup>The expression for the SCNR, from which the detection probability is derived (given the Swerling case and the number of non-coherently integrated pulses), also assumes that the various signals (target response, surface clutter, volume clutter, noise, jamming) are uncorrelated.

## 6.4 Surface Clutter

### 6.4.1 Surface Clutter Power

Echoes from the surface of the earth may severely limit the detection performance of radar systems. The surface clutter peak power,  $P_{sc}$ , received in the radar from a patch defined by the intersection at the earth's surface of the azimuth beamwidth with a range gate at a range  $R_c$  (m) (see Skillman, [36]) Echoes from the surface of the earth may severely limit the detection performance of radar systems. The surface clutter peak power,  $P_{sc}$ , received in the radar from a patch defined by the intersection at the earth's surface of the azimuth beamwidth with a range gate at a range  $R_c$  (m) (see Skillman, [36])

$$P_{sc} = \frac{P_p G_t G_r G_{pc} g^4(\theta) \lambda^2 \sigma_{sc}}{(4\pi)^3 R_c^4 L}, \quad (6.120)$$

where  $\sigma_{sc}$  represents the surface clutter cross section ( $\text{m}^2$ ),  $g(\theta)$  the voltage gain of the antenna at the elevation angle of the clutter patch.  $L$  is a series of loss factors:

$$L = L_t L_{r,Tx} L_{r,Rx} L_{r,m}, \quad (6.121)$$

see Section 6.3.1 for a clarification of these terms.

The clutter cross section is calculated from the mean clutter reflectivity,  $\sigma^0$ , according to [36]

$$\sigma_{sc} = \sigma^0 A_c, \quad (6.122)$$

in which  $A_c$  ( $\text{m}^2$ ) represents the area of the clutter patch, being the product of its width (*i.e.*, in the cross-range dimension) and its depth (in the range dimension), see Figure 6.21.

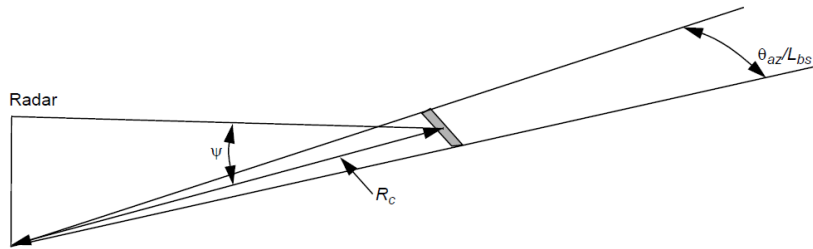


Figure 6.21: The shaded area denotes a clutter patch at ground range  $R_c$ .

If the transmit and receive antenna patterns are identical, the area of the clutter patch is given by:

$$A_c = R_c \frac{\theta_{az}}{L_{bs}} \frac{c\tau_c}{2 \cos \psi} \quad (6.123)$$

$c$  is the velocity of light ( $3 \times 10^8$  m/s),  $\psi$  is the grazing angle, see Figure 6.22,  $\tau_c$  is the duration of the compressed pulse (if pulse compression is applied; otherwise the pulse duration is taken).

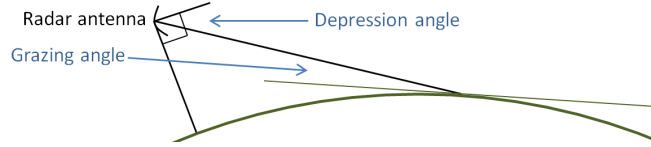


Figure 6.22: Notion of angles.

The grazing angle is calculated from

$$\sin \psi = \frac{h_a}{R_c} - \frac{R_c}{2a_e} \quad (6.124)$$

where  $h_a$  represents the height of the radar antenna and  $a_e$  the effective earth radius (see Section 6.1.2). The clutter range,  $R_c$ , is determined from the slant range between the radar and the target,  $R_t$  and the unambiguous range,  $R_u$ , according to

$$R_c = \text{mod}(R_t, R_u) \quad (6.125)$$

$$R_u = \text{PRI} \frac{c}{2} \quad (6.126)$$

where mod denotes the modulo operation and PRI is the pulse repetition interval (s). Only the contribution of the first-time-around clutter component to the clutter power is taken into account. This can be justified by the fact that the power of multiple-time-around clutter is at least 9 dB weaker than the first-time-around clutter.

In a land-based scenario, CARPET has the disposal of two models for the mean land clutter reflectivity,  $\sigma^0$ :

1. A constant value,  $\gamma$ , before the radar horizon and a zero value beyond.
2. The constant gamma model where  $\sigma^0$  depends on the grazing angle according to:

$$\sigma^0 = \gamma \sin \psi, R_c < R_{\text{horizon}} \quad (6.127)$$

$$\sigma^0 = 0, R_c \geq R_{\text{horizon}} \quad (6.128)$$

where  $\gamma$  is the land clutter reflectivity ( $\text{m}^2/\text{m}^2$ ) and the radar horizon for clutter,  $R_{\text{horizon}}$ , is given by

$$R_{horizon} = \sqrt{2a_e h_a} \quad (6.129)$$

In a maritime scenario, CARPET derives the mean sea clutter reflectivity from the clutter model developed by the Georgia Institute of Technology (GIT), [11]. This clutter model, which is valid for frequencies between 1 and 100 GHz, provides values of the clutter reflectivity under standard propagation conditions (see Section 8.7). The reflectivities in dBm<sup>2</sup>/m<sup>2</sup> are given by:

- 1 to 10 GHz, horizontal polarisation:

$$\sigma^0(H) = 10 \log(3.9 \times 10^{-6} \lambda \psi^{0.4} G_a G_u G_w) \quad (6.130)$$

- 1 to 3 GHz, vertical polarisation:

$$\sigma^0(V) = \sigma^0(H) - 1.73 \ln(h_a + 0.015) + 3.76 \ln \lambda + 2.46 \ln(\psi + 0.0001) + 22.2 \quad (6.131)$$

- 3 to 10 GHz, vertical polarisation:

$$\sigma^0(V) = \sigma^0(H) - 1.05 \ln(h_a + 0.015) + 1.09 \ln \lambda + 1.27 \ln(\psi + 0.0001) + 9.7 \quad (6.132)$$

- 1 to 10 GHz, circular polarisation:

$$\sigma^0(C) = \max\{\sigma^0(H), \sigma^0(V)\} - 6 \quad (6.133)$$

The interference term,  $G_a$ , the upwind/downwind factor,  $G_u$ , the wind speed factor,  $G_w$ , and the adjustment factor,  $q$ , are given by

$$G_a = \frac{a^4}{1 + a^4} \quad (6.134)$$

$$G_u = \exp\{0.2 \cos \phi (1 - 2.8\psi)(\lambda + 0.015)^{-0.4}\} \quad (6.135)$$

$$G_w = \left( \frac{1.94 v_w}{1 + \frac{v_w}{15.4}} \right)^q \quad (6.136)$$

$$q = \frac{1.1}{(\lambda + 0.015)^{0.4}} \quad (6.137)$$

where  $\phi$  represents the azimuth look direction relative to the wind direction,  $v_w$  is the wind speed (m/s) and  $a$  is the roughness factor.

In the frequency range from 10 to 100 GHz, the reflectivities are given by:

$$\sigma^0(H) = 10 \log(5.78 \times 10^{-6} \lambda \psi^{0.547} G_a G_u G_w) \quad (6.138)$$

$$\sigma^0(V) = \sigma^0(H) - 1.38 \ln h_a + 3.43 \ln \lambda + 1.31 \ln \psi + 18.55 \quad (6.139)$$

$$\sigma^0(C) = \max\{\sigma^0(H), \sigma^0(V)\} - 6 \quad (6.140)$$

and the adjustment factors by

$$G_a = \frac{a^4}{1 + a^4} \quad (6.141)$$

$$G_u = \exp\{0.25 \cos \phi (1 - 2.8\psi) \lambda^{-0.33}\} \quad (6.142)$$

$$G_w = \left( \frac{1.94 v_w}{1 + \frac{v_w}{15.4}} \right)^q \quad (6.143)$$

$$q = 1.93 \lambda^{-0.04} \quad (6.144)$$

The roughness factor,  $a$ , is given by

$$a = \frac{(14.4\lambda + 5.5)\psi h_a}{\lambda} \quad (6.145)$$

The average wave height,  $h_w$  (m), is derived from the wind velocity,  $v_w$  (m/s), according to:

$$h_w = 4.52 \times 10^{-3} v_w^{2.5}, \quad (6.146)$$

#### 6.4.2 Surface Clutter Doppler Spectrum

The Doppler spectrum of surface clutter has a Gaussian shape with a specific standard deviation,  $\sigma_{sc}$  (Hz), and a specific mean Doppler frequency,  $f_{sc}$  (Hz):

$$S_{sc}(f) = P_{sc} \exp\left\{-\frac{(f - f_{sc})^2}{2\sigma_{sc}^2}\right\}. \quad (6.147)$$

The mean Doppler frequency shift,  $\Delta f_{sc}$  (Hz), for land clutter is zero. The mean Doppler frequency shift for sea clutter depends on the wind speed vector and the antenna's azimuth look-direction:



$$\Delta f_{sc} = k_f \frac{2v_{w,r}}{\lambda} = k \frac{2v_w \cos \Delta\phi}{\lambda}, \quad (6.148)$$

with

$$\Delta\phi = \phi_w - \phi_a - \pi. \quad (6.149)$$

$v_{w,r}$  is the radial component of the wind speed vector,  $\phi_w$  is the wind direction,  $\phi_a$  is the antenna's azimuth look direction. The value of  $k_f$  is 0.1. The standard deviation,  $\sigma_{sc}$ , of the Gaussian shaped spectrum is determined from

$$\sigma_{sc} = k_\sigma \frac{2v_{w,r}}{\lambda} \quad (6.150)$$

where  $k_\sigma = 0.01$  for land clutter and 0.125 for sea clutter [2].

Figure 6.23 shows  $f_{sc}$  and  $\sigma_{sc}$  versus the wind speed for X-band (10 GHz) and S-band (3 GHz) and for  $\Delta\phi = 0^\circ$  ('up-wind').

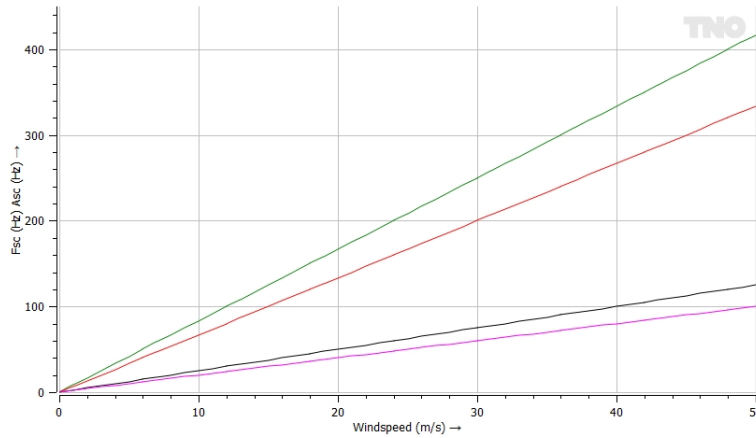


Figure 6.23: Green:  $\sigma_{sc}$  X-band. Red:  $f_{sc}$  X-band. Black:  $\sigma_{sc}$  S-band. Pink:  $f_{sc}$  S-band.

Surface clutter Doppler spectra at 10 and 20 m/s for X-band and S-band are shown in Figure 6.24.

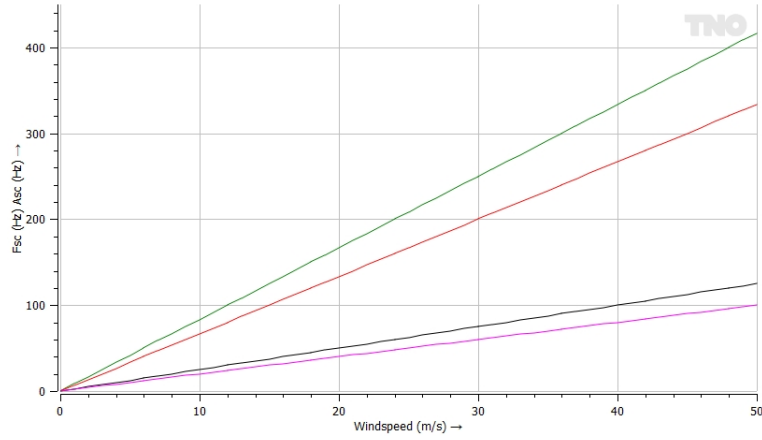


Figure 6.24: Green:  $\sigma_{sc}$  at X-band. Red:  $f_{sc}$  at X-band. Black:  $\sigma_{sc}$  at S-band. Pink:  $f_{sc}$  at S-band.

The corresponding autocorrelation function  $r_{sc}(\tau)$  of the surface clutter is given by

$$r_{sc}(\tau) = P_{sc} \exp\{-2(\pi\sigma_{sc}\tau)^2\} \exp\{j2\pi f_{sc}\tau\} \quad (6.151)$$

## 6.5 Volume Clutter

### 6.5.1 Volume Clutter Power

Rain clutter or chaff is assumed to fill a column of the atmosphere. The rain clutter or chaff starts and ends at user-definable ranges. The power of the volume clutter backscatter,  $P_{vc}$ , received in the radar is determined by

$$P_{vc} = \frac{P_p G_t G_r G_{pc} G_{pol} \lambda^2 \sigma_{vc}}{(4\pi)^3 R_c^4 L}, \quad (6.152)$$

with

$$L = L_t L_{r,Tx} L_{r,Rx} L_{r,m}, \quad (6.153)$$

Only first-time-around volume clutter is taken into account in CARPET. If the polarisation of the antenna is same-sense circular, the power of rain clutter is reduced by a factor of 20 dB, *i.e.*,  $G_{pol} = 0.01$ , otherwise  $G_{pol} = 1$ . The cross section of the volume clutter,  $\sigma_{vc}$ , is calculated from

$$\sigma_{vc} = \eta V_c \quad (6.154)$$

in which  $\eta$  represents the volume clutter reflectivity and  $V_c$  the volume of the clutter cell ( $\text{m}^3$ ):

$$V_c = R_c \frac{\theta_{az}}{L_{bs}} \Delta h \frac{c\tau_c}{2} \quad (6.155)$$

$\Delta h$  is the height of the volume cell, given by

$$\Delta h = R_c \frac{\theta_{el}}{L_{bs}} \quad (6.156)$$

where  $h_{max}$  is the maximum height of the rain or chaff cloud, and  $\theta_{el}$  is the 3-dB beamwidth in elevation.

Following Barton, [19], p.105, the reflectivity of rain clutter,  $\sigma_d$  in  $\text{m}^2/\text{m}^3$ , at a rainfall rate of  $r_r$  mm/hr, and a radar wavelength,  $\lambda$ , is given by

$$\sigma_d = \frac{\pi^5 |K|^2 200 r_r^{1.6}}{\lambda^4} \cdot 1 \times 10^{-18} \quad (6.157)$$

with  $|K|^2 = 0.93$  this results in <sup>11</sup>

<sup>11</sup>Rather than reflectivity factor  $Z = 200 r_r^{1.6}$ , the CCIR (forerunner of the ITU-R) has proposed  $Z = 400 r_r^{1.4}$ , see Boithias, [28], p.143.

$$\sigma_d = \frac{5.69 \times 10^{-14} r_r^{1.6}}{\lambda^4} \quad (6.158)$$

Rain reflectivity versus rainfall rate at different wavelengths is shown in Figure 6.25.

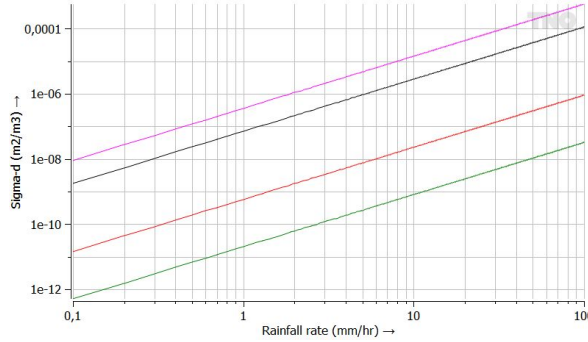


Figure 6.25: Rain clutter reflectivity versus rainfall rate for L-band (1.3 GHz, green), S-band (3 GHz, red), X-band (10 GHz, black) and Ku-band (15 GHz, magenta).

The reflectivity of chaff is given by

$$\sigma_d = 22 \times 10^{-9} \lambda W, \quad (6.159)$$

where  $W$  is the chaff density in  $\text{g}/\text{km}^3$  (see Skolnik, [37]).

### 6.5.2 Volume Clutter Spectrum

The spectrum of the volumetric clutter, rain and chaff, has a Gaussian shape with a standard deviation,  $\sigma_{vc}$  (Hz), and a mean Doppler frequency,  $f_{vc}$  (Hz):

$$S_{vc}(f) = P_{vc} \exp\left\{-\frac{(f - f_{vc})^2}{2\sigma_{vc}^2}\right\}. \quad (6.160)$$

The mean Doppler frequency shift is given by equation 6.148, however, with  $k = 1$ . The standard deviation of the Gaussian shaped spectrum Doppler spectrum,  $\sigma_{vc}$  (Hz), is given by:

$$\sigma_{vc} = \frac{2\sigma_w}{\lambda}. \quad (6.161)$$

The standard deviation of the wind velocity,  $\sigma_w$  (Hz), is determined by a wind shear and a turbulence component, see Nathanson, [33], p.206, equation (6-8). CARPET 3 therefore neglects the beam broadening effect and the spread in fall velocities.

$$\sigma_w = \sqrt{\sigma_{shear}^2 + \sigma_{turb}^2} \quad (6.162)$$

The standard deviation of the wind shear is given by

$$\sigma_{shear} = 0.42k_{shear}\Delta h \quad (6.163)$$

where  $k_{shear}$  is the shear component with a value of  $4 \times 10^{-3} s^{-1}$  and  $\Delta h$  is the height of the column of precipitation within the two-way 3-dB beamwidth in elevation, see equation (50).  $\sigma_{turb}$  is given by a value of 1 m/s.

Figure 6.26 shows  $f_{vc}$  and  $\sigma_{vc}$  versus the wind speed for X-band (10 GHz) and S-band (3 GHz), for  $\phi_w = 0^\circ$  and for rain cloud heights 100 m (left) and 1000 m (right).

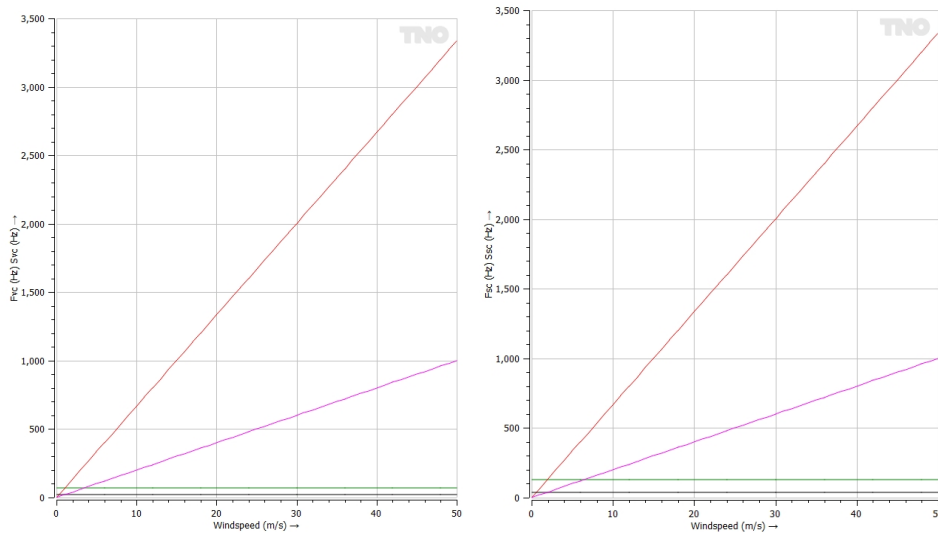


Figure 6.26: Left:  $\Delta h = 100$  m. Right:  $\Delta h = 1000$  m. Green:  $\sigma_{vc}$  at X-band. Red:  $f_{vc}$  at X-band. Black:  $\sigma_{vc}$  at S-band. Pink:  $f_{vc}$  at S-band.

The corresponding autocorrelation function  $r_{vc}(\tau)$  of the volume clutter is expressed by

$$r_{vc}(\tau) = P_{vc} \exp\{-2(\pi\sigma_{vc}\tau)^2\} \exp\{j2\pi f_{vc}\tau\} \quad (6.164)$$

## 6.6 Jamming

### 6.6.1 Jamming Power

The objective of electronic counter measures (ECM) is to deny the use of the electromagnetic spectrum to the opponent. This can be accomplished by emitting noise-like waveforms that reduce the sensitivity of the radar system (noise jamming), or by emitting replicas of the radar waveform (deception jamming). In CARPET, the effect of noise jamming entering the radar receiver through the azimuth sidelobes of the antenna has been modelled. Two noise-jamming modes are available. In the wide band ‘barrage’ jamming mode the whole frequency agility band of the radar is covered. In the narrow band ‘responsive’ jamming mode, the radar frequency is measured and the jamming signal is concentrated in a narrow band around the radar frequency, which results in a higher jammer spectral density (W/Hz). In the responsive mode, the delay between the emission of a new frequency at the radar and the reception of jamming at that frequency is also taken into account.

The power of the jamming signal received in the radar,  $P_j$  (W), is given by

$$P_j = \frac{P_{p,j} G_j G_r F^2 \lambda^2}{(4\pi)^2 R_j^2 L_j} \cdot \frac{B}{B_j}, \quad (6.165)$$

where  $P_{p,j}$  is the power of the jammer,  $G_j$  is the gain of the jammer antenna,  $G_r$  is the gain of the radar receive antenna,  $F^2$  is the one-way pattern propagation power factor,  $R_j$  is the slant range of the jammer (which depends on the height and downrange of the jammer and the height of the receive antenna),  $B$  is the instantaneous bandwidth of the radar,  $B_j$  is the instantaneous bandwidth of the jamming signal,  $L_j$  is a loss term which is given by

$$L_j = \frac{L_{bs}}{2} L_{r,Rx} L_{r,m}. \quad (6.166)$$

see Section 6.3.1 for a clarification of these terms.

The jamming-to-signal-ratio ( $J/S$ ) prior to pulse compression is given by

$$J/S = \frac{P_j}{P_s} = \frac{P_{p,j} G_j F_j^2 4\pi R_t^4 L_t}{P_p G_t R_j^2 L_j \sigma_t F_t^4} \cdot \frac{B}{B_j}. \quad (6.167)$$

In the case of self-screening jamming, *i.e.*, the jammer is mounted on the target, this simplifies to

$$J/S = \frac{P_{p,j} G_j 4\pi R_t^2 L_t}{P_p G_t L_j \sigma_t F_{Tx}^2} \cdot \frac{B}{B_j}. \quad (6.168)$$

So, the jamming-to-signal-ratio diminishes with the square of the range as the target approaches. The furthest range where the target can be detected is called ‘burn through range’.

Clearly, noise jamming does not benefit from the gains that pulse compression and Doppler filtering provide.

### 6.6.2 Jamming Doppler Spectrum

Both barrage and responsive jamming signals are assumed to have a white Doppler spectrum which gives the following autocorrelation function:

$$r_j(\tau) = P_j \delta(\tau) \tag{6.169}$$

## 6.7 Radar Equation

Discarding clutter, a different form of the radar equation is obtained by specifying the signal-to-noise-ratio,  $SNR$ , as a power ratio:

$$SNR = \frac{P_t}{P_n} = \frac{P_p G_t \sigma A}{(4\pi)^2 R^4 L k T_s B}, \quad (6.170)$$

which we have obtained by dividing equation 6.109 by equation 6.89. With equation 6.110 ( $G = \eta 4\pi A / \lambda^2$ ) equation 6.170 can be written as

$$SNR = \frac{P_p G_t G_r \sigma \lambda^2}{(4\pi)^3 R^4 L k T_s B}. \quad (6.171)$$

Budge and German, [32], also discuss a radar range equation that is a ratio of energies,  $E_t$  and  $E_n$ :

$$SNR = \frac{E_t}{E_n} = \frac{P_p G_t G_r \sigma \lambda^2 \tau}{(4\pi)^3 R^4 L k T_s}, \quad (6.172)$$

in which  $\tau$  (s) is uncompressed pulse duration. Note that this equation lacks the noise bandwidth,  $B$  (Hz). This version shows more clearly that the duration of the pulse matters.

Modern radar systems integrate multiple pulse responses prior to detection. In case pulse responses are integrated coherently the  $SNR$  increases with the number of pulse responses,  $N$ , that is summed. Thus:

$$SNR' = \frac{P_p G_t G_r \sigma \lambda^2 \tau N}{(4\pi)^3 R^4 L k T_s}. \quad (6.173)$$

Since the coherent processing interval,  $T_{cpi}$  is given by

$$T_{cpi} = \frac{N}{PRF}, \quad (6.174)$$

and since

$$P_p = \frac{P_{avg}}{\eta} = \frac{P_{avg}}{\tau PRF} = \frac{P_{avg} T_{cpi}}{\tau N}, \quad (6.175)$$

with  $\eta$  the duty cycle, we get

$$SNR' = \frac{P_{avg} T_{cpi} G_t G_r \sigma \lambda^2}{(4\pi)^3 R^4 L k T_s}. \quad (6.176)$$



## 6.8 Antenna Pattern

The antenna pattern is an important factor in determining the power levels of the target, surface clutter and standoff jamming signal received by the radar. As discussed in Section 2.10.2, CARPET 3 can load Tx and Rx elevation patterns. The corresponding files are in two column format: an elevation angle in degrees in the first column, and an antenna gain term (in dB) in the second column. Antenna gain (in dBi) can also be specified in the Antenna dialogue box. The resulting gain is a combination of the value specified in the file and the value specified in the dialogbox.

There are also several ‘internal’ elevation patterns available within CARPET which are discussed in this Section. As discussed in Section 3.11, the user can specify an aperture shape and an illumination function. Expressions for the so-called ‘voltage gain’ are summarised in Table 6.5. In this table,  $J_1$ ,  $J_2$  and  $J_3$  are Bessel functions of the first kind of order 1, 2 and 3 respectively, and  $u$  is given by

$$u = \frac{D\pi \sin \theta}{\lambda}, \quad (6.177)$$

with  $D$  (m) either the diameter or the vertical size of the aperture and  $\theta$  (rad) the elevation angle.

Table 6.5: Overview of antenna illumination functions.

Illumination	Circular aperture	Square aperture
Uniform	$\frac{2J_1(u)}{u}$	$\frac{\sin u}{u}$
Parabolic	$\frac{8J_2(u)}{u^2}$	$\frac{3 \sin u}{u^3} - \frac{3 \cos u}{u^2}$
Parabolic <sup>2</sup>	$\frac{48J_3(u)}{u^3}$	$\frac{45 \sin u}{u^5} - \frac{45 \cos u}{u^4} - \frac{15 \sin u}{u^3}$

The vertical beamwidth,  $\theta_{el}$  (rad), of a circular or rectangular aperture is given by

$$\theta_{el} = \frac{\kappa\lambda}{D} \quad (6.178)$$

where  $\kappa$  is the beamwidth factor. The power gain,  $\Gamma$ , of a circular or rectangular aperture with aperture area  $A$  is computed from

$$\Gamma = \frac{\varepsilon 4\pi A}{\lambda^2 L}, \quad (6.179)$$

where  $\varepsilon$  is the efficiency of the aperture illumination and  $L$  represents the losses due to dissipation in the antenna feed, mismatch, and spillover. The efficiency, the beamwidth factor and the first sidelobe level for the different apertures and illumination functions are listed in Table 6.6. Note that applying a ‘heavier’ taper results in a reduced sidelobe level and a broader main lobe.

Table 6.6: Characteristics of built-in elevation patterns.

Aperture	Illumination	Efficiency	Beamwidth Factor	Sidelobe Level dB
Circular	Uniform	1.00	1.02	-17.6
	Parabolic	0.64	1.27	-24.5
	Parabolic <sup>2</sup>	0.55	1.47	-30.6
Rectangular	Uniform	1.00	0.88	-13.2
	Parabolic	0.83	1.15	-20.6
	Parabolic <sup>2</sup>	0.68	1.36	-28.6

There is also an cosec<sup>2</sup> elevation pattern and an inverse (upside-down) cosec<sup>2</sup> pattern. The cosec<sup>2</sup>-pattern given by:

$$\theta < 0 : g(\theta) = \max\left(1 + \frac{\theta}{\theta_{el}}, 0.03\right), \quad (6.180)$$

$$0 \leq \theta \leq \theta_{el} : g(\theta) = 1, \quad (6.181)$$

$$\theta > \theta_{el} : g(\theta) = \frac{\sin \theta_{el}}{\sin \theta}. \quad (6.182)$$

A tilt angle,  $\theta_t$ , can be specified that results in a shift of the antenna pattern in the elevation plane (*i.e.*, the antenna pattern becoming  $g(\theta - \theta_t)$ ). If a mechanically tracking antenna is selected, the specified tilt angle is not used; the antenna tilt equals the target elevation angle. If electronic tracking is selected in CARPET, the gain and the beamwidth of the transmit and receive antenna are adjusted for the off-broadside elevation angle, according to

$$g(\Delta\theta) = G \cos(\Delta\theta), \quad (6.183)$$

$$\theta_{el}(\Delta\theta) = \frac{\theta_{el}}{\cos(\Delta\theta)}, \quad (6.184)$$

where  $G(\Delta\theta)$  is the gain of the transmit or receive antenna at an off-broadside angle  $D_q$ , and  $\theta(D_q)$  is the corresponding elevation beamwidth.

In the azimuth plane, CARPET 3 assumes a sync-pattern until the specified azimuth sidelobe level,  $G_{az}$ , is met, which is then maintained.

## 6.9 Radar Signal Processing

### 6.9.1 Basics

Target range is determined by multiplying the half of the round-trip transit time by the speed of light,  $c$  (m/s, from Latin *celeritas*), which is constant, regardless of the relative motion of the target and the sensor, as Albert Einstein postulated in 1905 [38].<sup>12</sup> When the available time interval is bounded since a specific pulse repetition frequency ( $PRF$ ) is applied, the farthest range that can be determined unambiguously,  $R_u$  (m), is given by:

$$R_u = \frac{c}{2 \cdot PRF}. \quad (6.185)$$

The velocity of light in vacuum is close to  $3 \times 10^8$  m/s. A diagram showing  $R_u$  over the  $PRF$  is shown in Figure 6.27.

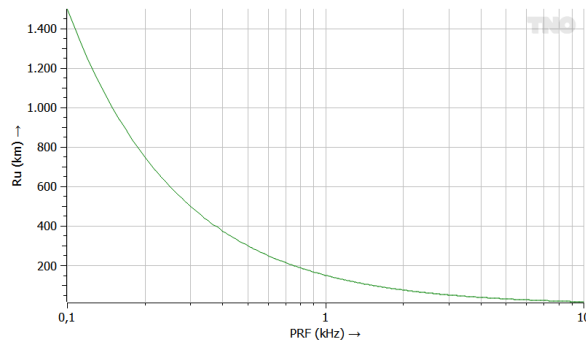


Figure 6.27: Unambiguous range (in km) versus the  $PRF$  (in kHz).

If the target range is slightly larger than the unambiguous range, its echo arrives after the time instance at which the subsequent pulse is transmitted. When detected, such a ‘second trace target’ will be displayed at close range on an A-scope or a PPI.

Unless the radar is capable to operate with partially eclipsed pulse responses, the depth of the initial dead zone,  $R_b$  (m), is given by:

$$R_b = \frac{c \cdot \tau}{2}, \quad (6.186)$$

with  $\tau$  (s) the (uncompressed) pulse length.

The Doppler shifted frequency,  $f_r$  (Hz), of a wave that is emitted by a source with radial velocity with respect to the observer  $v_r$  (m/s) is given by:

<sup>12</sup>Before Einstein, few others considered the speed of light to be finite (against Aristotle), one of the few being Danish astronomer Ole Rømer, who derived an estimation of the speed of light from eclipses of Jupiter’s moon Io in 1676. His estimate was 26% off.

$$f_r = \frac{f}{\gamma(1 - \frac{v_r}{c_m})}. \quad (6.187)$$

with

$$\gamma = \frac{1}{\sqrt{1 - \frac{v_r^2}{c^2}}}. \quad (6.188)$$

$f$  (Hz) is the radar frequency in the inertial system of the radar,  $c_m = c/n$  (m/s) is the speed of light in a medium,  $n$  ( $\geq 1$ ) is the refractive index,  $\gamma$  is referred to as Lorentz factor.<sup>13</sup> Note that the equation that Christian Doppler postulated in [39] did not have the Lorentz factor.

In case of vacuum  $n$  equals 1, in case of air  $n \approx 1$ . Equation 6.187 then becomes

$$f_r = f \frac{\sqrt{c^2 - v_r^2}}{c - v_r}. \quad (6.189)$$

For two-way propagation and a mono-static radar we get:

$$f_r = f \frac{c + v_r}{c - v_r}. \quad (6.190)$$

The Doppler frequency shift,  $\Delta f_D$  (Hz), is therefore given by:

$$\Delta f_D = f_r - f = \frac{2v_r f}{c - v_r}. \quad (6.191)$$

When  $v_r \ll c$ , equation 6.191 can be written as:

$$\Delta f_D = \frac{2v_r f}{c} = \frac{2v_r}{\lambda}, \quad (6.192)$$

with  $\lambda$  (m) the wavelength of the carrier.

If the radial displacement of a target during the time interval between two observations,  $T_r$  (s), is half the wavelength, the received phase will rotate  $2\pi$  rad:  $\pi$  from antenna to target plus  $\pi$  from target to antenna. The corresponding radial velocity,  $v_b$  (m/s), is given by:

$$v_b = \frac{\lambda}{2T_r} = \frac{\lambda \cdot PRF}{2}. \quad (6.193)$$

This specific radial velocity is referred to as first blind speed, since no distinction can be made between this specific velocity and velocity 0. A target response with a Doppler frequency shift that is equal to a multiple of the PRF might therefore be difficult to detect in case

<sup>13</sup>Hendrik Antoon Lorentz (1853–1928), friend to Albert Einstein (1879–1955), is not only famous for his contributions to special relativity, but also for the ‘Afsluitdijk’ (enclosure dike).



low-Doppler clutter is also received. To remedy this, multiple bursts with different PRFs and/or RFs must be transmitted per dwell. Alternatively, a pulse-to-pulse staggered PRF pulse canceler can be applied.<sup>14</sup>

By combining 6.185 and 6.193 we get a ‘PRF-less’ equation:

$$v_b = \frac{c\lambda}{4R_u}, \quad (6.194)$$

which is illustrated for various frequencies in Figure 6.28.

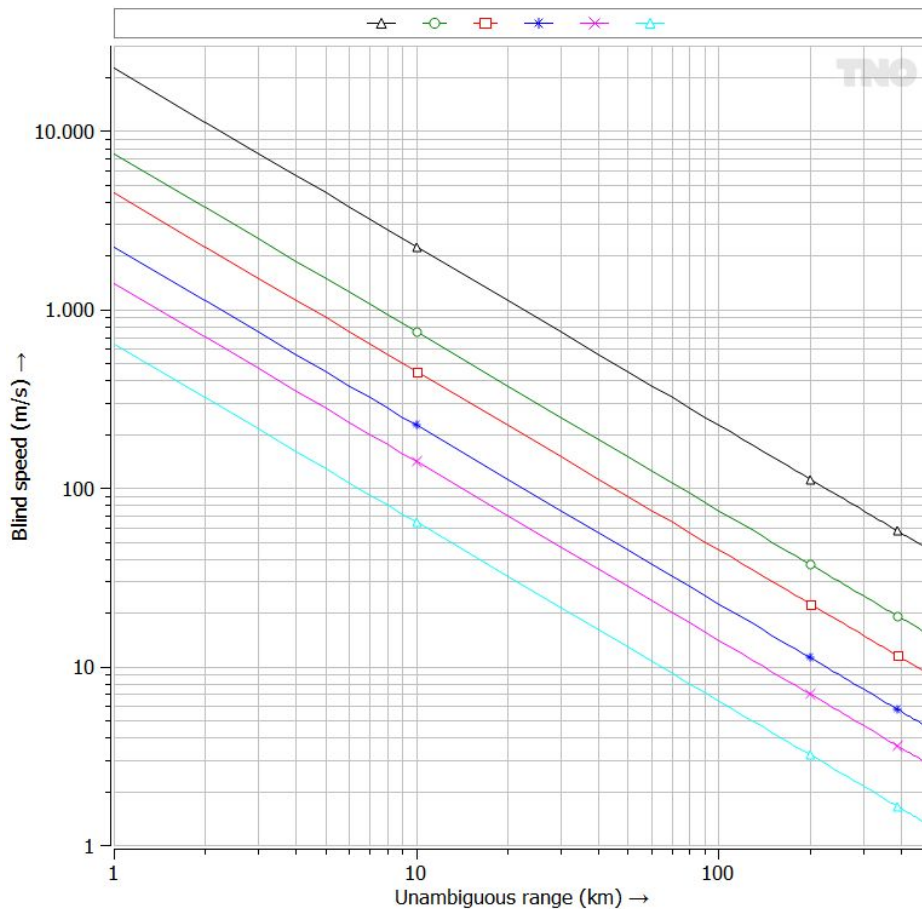


Figure 6.28: Blind speed versus unambiguous range. Black-triangle: 1 GHz. Green-circle: 3 GHz. Red-square: 5 GHz. Blue-star: 10 GHz. Pink-cross: 16 GHz. Lightblue-triangle: 35 GHz.

The phase change,  $\Delta\phi$  (rad), during the PRT (pulse repetition time) is given by:

<sup>14</sup>This option, however, does not support the extraction of radial speed.

$$\Delta\phi = -\frac{4T_r v_r \pi}{4}. \quad (6.195)$$

A pulse-Doppler radar derives radial velocity from the pulse-to-pulse phase change of the received pulse. The Doppler resolution is inversely proportional to the time during which measurements are taken: the longer the integration time, the better the Doppler resolution.<sup>15</sup> ('good Doppler resolution requires a long integration time'). In case  $N$  pulse responses are integrated, the Doppler resolution,  $\delta f_D$  (Hz), is given by:

$$\delta f_D = \frac{1}{NT_r} = \frac{PRF}{N}. \quad (6.196)$$

Expressed in m/s, the radial velocity resolution,  $\delta v_r$ , is given by:

$$\delta v_r = \frac{\lambda \cdot PRF}{2N}, \quad (6.197)$$

since  $\delta v_r = \lambda \delta f_D / 2$ . In case radial velocities are represented in a radial velocity interval around 0, the size of the interval is given by:

$$-\frac{\lambda \cdot PRF}{4} < v_r < \frac{\lambda \cdot PRF}{4}. \quad (6.198)$$

This interval is referred to as the unambiguous velocity interval, see Figure 6.29. The principle of radial velocity estimation with a pulse Doppler radar is illustrated in Figure 6.30.

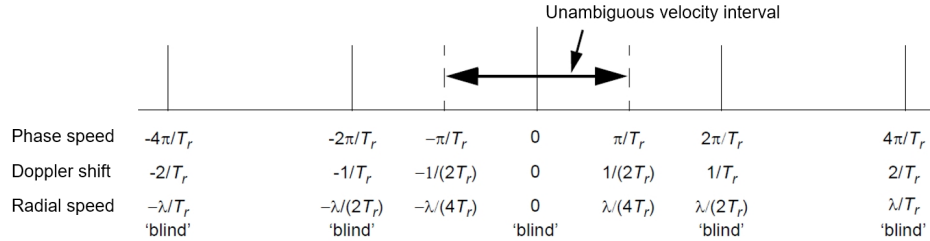


Figure 6.29: Illustration of the unambiguous velocity interval.

<sup>15</sup>The available integration time can, however, be limited as the signal response de-correlates as a consequence of aspect angle change.

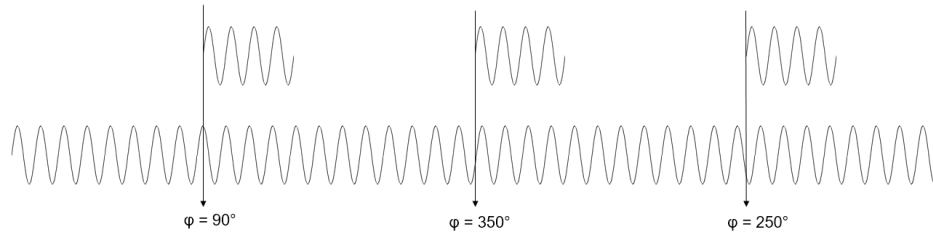


Figure 6.30: Pulse-Doppler radar derives radial speed from the pulse to pulse phase change, which is  $100^\circ$  in this example. The received signal is shown at the top. At the bottom is the signal of the coherent oscillator.

Radar systems that operate in a low-PRF regime can straightforwardly determine target range. Radars operating in the high-PRF regime can straightforwardly determine target radial velocity, since the unambiguous velocity interval (equation 6.198) widens. Such radars take range ambiguity for granted, which implies that other means are required to determine range. As already stated, such radars often apply different PRFs, that are varied (staggered) from burst-to-burst. A burst (or pulse train) refers to a series of transmissions with constant RF, so that responses within a burst can be integrated. The ‘unfolded’ range is determined from the first trace range estimates provided by the processing of each burst, *e.g.*, by utilizing the Chinese remainder theorem. Radars operating in the medium-PRF regime need to apply unfold-algorithms to determine both range and radial velocity.

So-called fill pulses can be applied in medium and high-PRF radars to ensure efficient pulse integration (*e.g.* Doppler filtering). To provide an example: with a PRF of 2 kHz, range can be determined up to 75 km (equation 6.185). The radar is to provide detection capability up to 200 km so that a substantial part of third-trace targets (range between 150 and 225 km) must be detected. Given the dynamics of the targets that one is interested in, one wishes to integrate coherently 32 pulse responses; targets are therefore not supposed to de-correlate within 4 ms. If 34 pulses are transmitted rather than 32, and if responses of the last 32 pulses are integrated, even third trace targets will benefit from the full integration gain, which is 15.3 dB (proportional to the number of pulses) in the case of coherent integration.  $34 - 32 = 2$  is the number of fill pulses. If one would not apply fill pulses, third trace targets will receive 0.3 dB less integration gain.

A potential drawback of medium or high-PRF radars is that a distant target may have to compete with short range clutter. Let us illustrate all these aspects with CARPET images. Figure 6.31 shows detection probability over range and radial speed. Eight responses are coherently integrated in a Doppler filter bank. Note that there are poor- $P_d$ -regions at short ranges, which is caused by the reception of surface clutter. The effect of increasing the PRF to 10 kHz is shown in Figure 6.32. We now see a dead zone at 15 km, which follows from equation 6.185. Furthermore there is only a single poor- $P_d$ -region in the diagram. But what is the reason of the strange green island in the south-east quadrant of the diagram? To understand this, we take a view at the Doppler filter responses, shown in Figure 6.33. Note

that when applying a Blackman taper prior to the Doppler Fourier transformation, 5 of the 8 Doppler filters are sensitive to signals with low Doppler frequency shifts. Low velocity second trace targets therefore have to compete with surface clutter. If we take a Hanning taper, less Doppler filters will be polluted, as shown in Figure 6.34. The effect of increasing the number of pulses to 32 is shown in Figure 6.35.

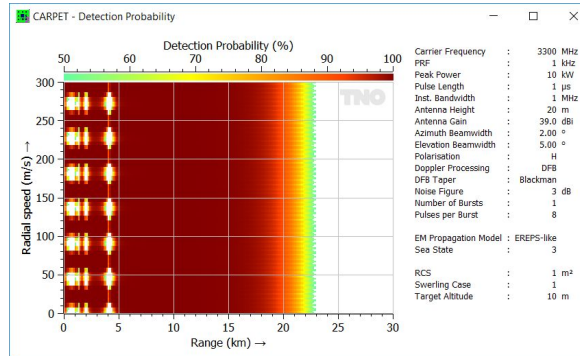


Figure 6.31: Detection probability versus range and radial speed. The PRF is 1 kHz, 8 pulses are integrated after Blackman tapering.

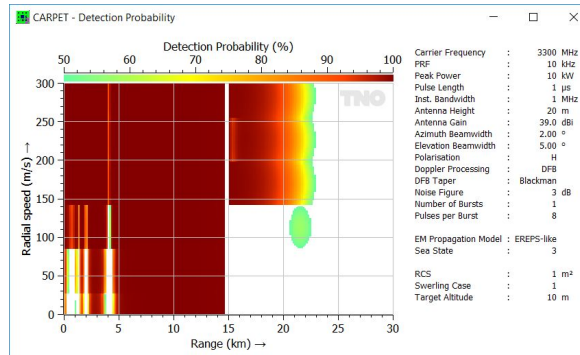


Figure 6.32: Detection probability versus range and radial speed. The PRF is 10 kHz, 8 pulses are integrated after Blackman tapering.



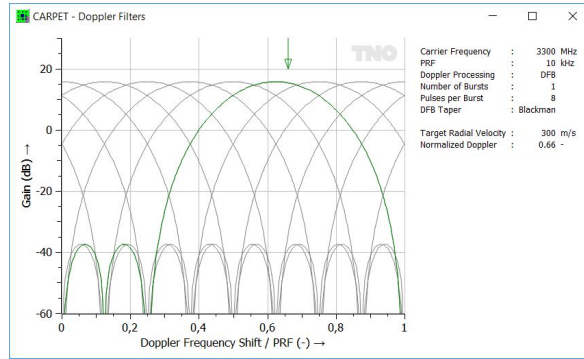


Figure 6.33: Doppler filter characteristics. Integration of 8 pulses after Blackman tapering.

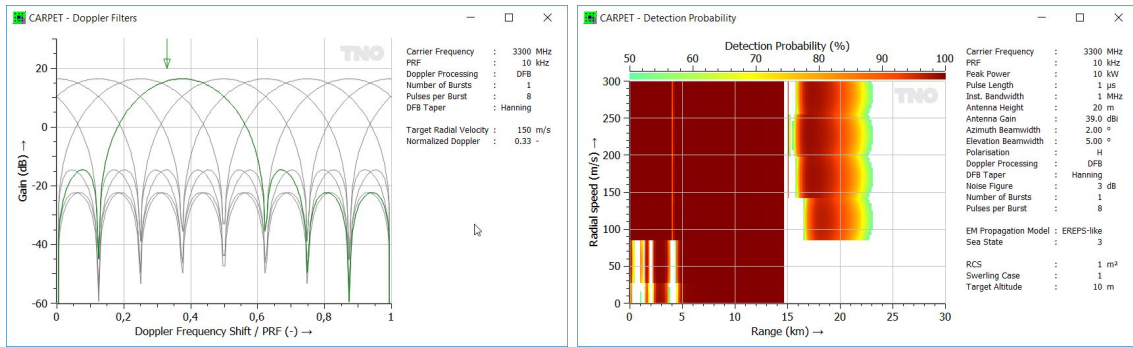


Figure 6.34: Left: Doppler filter characteristics. Integration of 8 pulses after Hanning tapering. Right: Detection probability versus range and radial speed. The PRF is 1 kHz, 8 pulses are integrated, Hanning tapering.

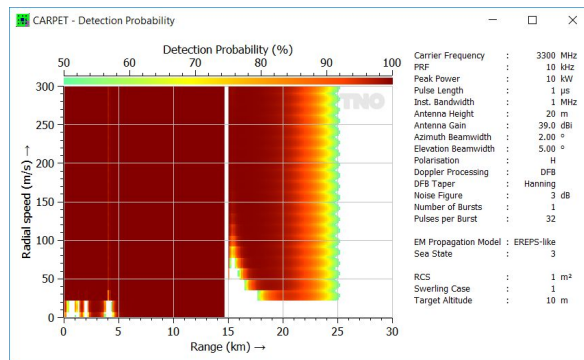


Figure 6.35: Right: Detection probability versus range and radial speed. The PRF is 10 kHz, 32 pulses are integrated, Hanning tapering.

For the sake of being complete we report that sonar systems as well as continuous wave

(CW) radars, such as police speed guns and target illumination radars measure the detuning of the transmitted wave directly. This is achieved by mixing the received signal with the transmitted signal.

### 6.9.2 Hilbert Filtering

As argued above, phase information is essential if the radar's signal processor is to exploit the different radial velocity between a target and between clutter. Phase information is also important for coherent integration, discussed in Section 6.9.5, which improves the SNR prior to detection. On the other hand, amplitude information is exploited during detection; the 'strength' of echoes is compared with a detection threshold. The frequency of the signal received by a radar is generally first down-converted to a more convenient lower frequency. The received signal,  $s(t)$ , can be expressed as

$$s(t) = a(t) \cos\{\omega_0 t + \phi(t)\}, \quad (6.199)$$

$t$  is time (s),  $a(t)$  is the envelope,  $\omega_0 = 2\pi/f_0$  is angular velocity (rad/s),  $f_0$  is the down-converted frequency,  $\phi(t)$  is phase. Equation 6.199 can be written as

$$s(t) = a(t) \{\cos(\omega_0 t) \cos \phi(t) - \sin(\omega_0 t) \sin \phi(t)\} = I(t) \cos \phi(t) - Q(t) \sin \phi(t), \quad (6.200)$$

with

$$I(t) = a(t) \cos(\omega_0 t), \quad (6.201)$$

$$Q(t) = a(t) \sin(\omega_0 t). \quad (6.202)$$

$I(t)$  and  $Q(t)$  are referred to as in-phase and quadrature-phase components of the received signal,  $s(t)$ . The envelope and the phase can be derived from  $I(t)$  and  $Q(t)$  according to:

$$a(t) = \sqrt{I(t)^2 + Q(t)^2}, \quad (6.203)$$

$$\phi(t) = \arctan\left\{\frac{Q(t)}{I(t)}\right\}. \quad (6.204)$$

A processing scheme that provides access to the I and Q-signals is shown in Figure 6.36.

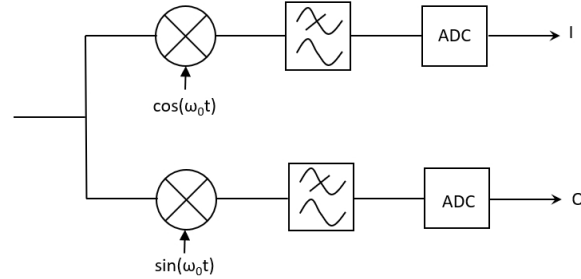


Figure 6.36: Sampling scheme to obtain I and Q-signals.

Other schemes are, however, also possible such as the scheme that has been described by V. Considine [40], which requires only one analog-to-digital converter (ADC) and which samples at four times the (down-converted) carrier frequency. The scheme is referred to as ‘Hilbert filter’, named after David Hilbert (1862 - 1943) who laid the mathematical foundation of an all-pass operator that establishes a  $\pm 90^\circ$  phase shift.

### 6.9.3 Pulse Compression

Modern ‘solid-state’ radar systems commonly apply pulse compression to combine desired range resolution with desired detection range. Energy is the product of power and time ( $J = Ws$ ), so, rather than transmitting short high power pulses, long modulated (or ‘coded’) pulses are transmitted. A relatively deep dead-zone is a disadvantage of pulse compression. Many modern radar systems therefore combine long and short pulses. The short pulses take care of detection at short ranges.

The pulse compression ratio,  $PCR$ , is given by the ratio of the uncompressed pulse duration (or ‘length’),  $\tau_u$  (s), and the compressed pulse duration, *i.e.*, after processing,  $\tau_c$  (s):

$$PCR = \frac{\tau_u}{\tau_c}, \quad (6.205)$$

see for instance Walden and Pollard, [41]. The compressed pulse length is inversely proportional to the instantaneous bandwidth,  $B$  (Hz), so that

$$PCR = B\tau_u. \quad (6.206)$$

The PCR is often referred to as pulse compression gain,  $G_{pc}$ .

If a pulse compression checkbox is not switched on, a  $B\tau_u$ -product greater than unity implies a poorly matched receiver. In this case, only the noise power will increase with bandwidth ( $kTB$ ), so that the detection capability will degrade, regardless of the presence of clutter.

The losses of the pulse compressor can be specified in the Processing dialogbox. The effects of pulse compression time-sidelobes are not considered in CARPET 3. The Doppler dependency of the pulse compression gain (the ambiguity function) has also not been modelled.

#### 6.9.4 Eclipsing

If the radar receiver is protected while a pulse is being transmitted, *e.g.* with a T/R switch, a so-called ‘dead zone’ is being introduced. The depth of the dead zone,  $\Delta R$  (m), is given by

$$\Delta R = \frac{c \cdot \tau}{2} \quad (6.207)$$

$c$  (m/s) is the speed of light,  $\tau$  (s) is the duration of the (uncompressed) pulse. For pulse compression radars, this dead zone depth might be considerable, for instance 15 km if  $\tau$  is 100  $\mu$ s. Such radars therefore generally transmit short pulses as well, in order to obtain short range coverage.

If the range to the target is  $c \cdot \tau/2$  or larger, the radar will receive the entire echo. If the range is less than  $c \cdot \tau/2$ , the radar will receive a part (the tail) of the pulse. Modern radar systems might be able to process partially eclipsed pulses which diminishes the depth of the dead zone.

CARPET version 3 contains a more elaborate modeling of the eclipsing effect than CARPET versions 1 and 2. The received target and clutter powers are adapted in case the target and clutter responses are partially eclipsed. Eclipsing occurs when an arrived echo is not fully processed because the radar receiver is disconnected from the antenna during part of the pulse arrival time span. Full eclipsing means that the entire echo goes lost. Partial eclipsing means that a fragment of the echo goes lost. The eclipsing factor,  $E$ ,  $0 \leq E \leq 1$ , is the ratio between the duration of the eclipsed pulse,  $\tau_e$  (s), and the duration of the whole (uncompressed) pulse,  $\tau$  (s):

$$E = \frac{\tau_e}{\tau}. \quad (6.208)$$

Full eclipsing therefore corresponds with  $E = 1$ . Figure 6.37 shows the amplitude of the waveform and the eclipsing factor over time.

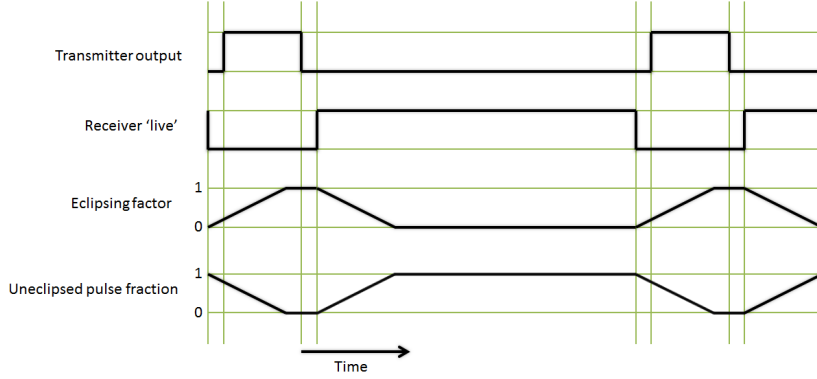


Figure 6.37: Transmit period and eclipsing factor over time.

Proper modeling of eclipsing is especially important in radars that apply pulse compression and that have a relatively high duty factor, such as modern solid-state radars. To determine the duration of the eclipsed pulse, the ‘first trace’ or ‘folded back’ target slant range,  $R_u$  (m), is first determined. Subsequently, there are three possibilities:

$$\frac{c\tau}{2} \leq R_u \leq \frac{c(PRT - \tau)}{2} \Rightarrow E = 0, \quad (6.209)$$

$$0 < R_u < \frac{c\tau}{2} \Rightarrow E = 1 - \frac{2R_u}{c\tau}, \quad (6.210)$$

and

$$\frac{c(PRT - \tau)}{2} < R_u < \frac{cPRT}{2} \Rightarrow E = \frac{1}{\tau} \left\{ R_u - \frac{c(PRT - \tau)}{2} \right\}. \quad (6.211)$$

In [42], Eugene R. Billam discusses how partial eclipsing affects the range (or time) sidelobe level of the compressed pulse, the clutter-to-noise-ratio (CNR), the clutter-to-signal-ratio (CSR), the signal-to-noise-ratio (SNR), the width of the compressed pulse and the peak power of the compressed pulse. As expected, partial eclipsing causes a reduction of the amplitude of the compressed pulse, a broadening of the peak of the compressed pulse and an increase of the range (or time) side lobe level. For the received clutter power, the widening of the compressed pulse partly compensates the reduction of pulse compression gain.

CARPET version 3 models the effect of partial eclipsing by multiplying the received target power,  $P_t$  (W), by the square of the uneclipsed pulse fraction,  $1 - E$ , according to

$$P_{t,e} = P_t(1 - E)^2. \quad (6.212)$$

Volume and surface clutter responses are modified differently in order to take the compensation effect into account:

$$P_{sc,e} = P_{sc}(1 - E) \quad (6.213)$$

with  $P_{sc}$  and  $P_{sc,e}$  the received surface clutter power prior and post the eclipsing.

Since March 2019, CARPET 3 provides the ability to specify a time gate for each waveform. This is especially relevant for radars that apply multiple waveforms, the multi-burst plug-in must be active.

### 6.9.5 Doppler Processing

Doppler processing is employed in radar systems to discriminate between stationary and moving targets. Besides, coherent integration, *i.e.*, the summation of complex-valued (in-phase/quadrature-phase, amplitude/phase) pulse responses, provides optimum integration gain, provided the target does not de-correlate within the integration time. The integration time that is applied is referred to as CPI: Coherent Processing Interval. The principle of improving the SNR by integrating radar echoes is illustrated in Figure 6.38. The left column shows I and Q samples (green and red line), which amplitudes follow a Gauß-distribution. A Swerling 0 (constant) target response has however been added to sample 42. The middle column shows the power ( $i^2 + q^2$ ) of the I and Q samples. The rightmost column shows the integrated power, *e.g.*, the rightmost diagram on the fourth row is the averaged power of the first four rows.

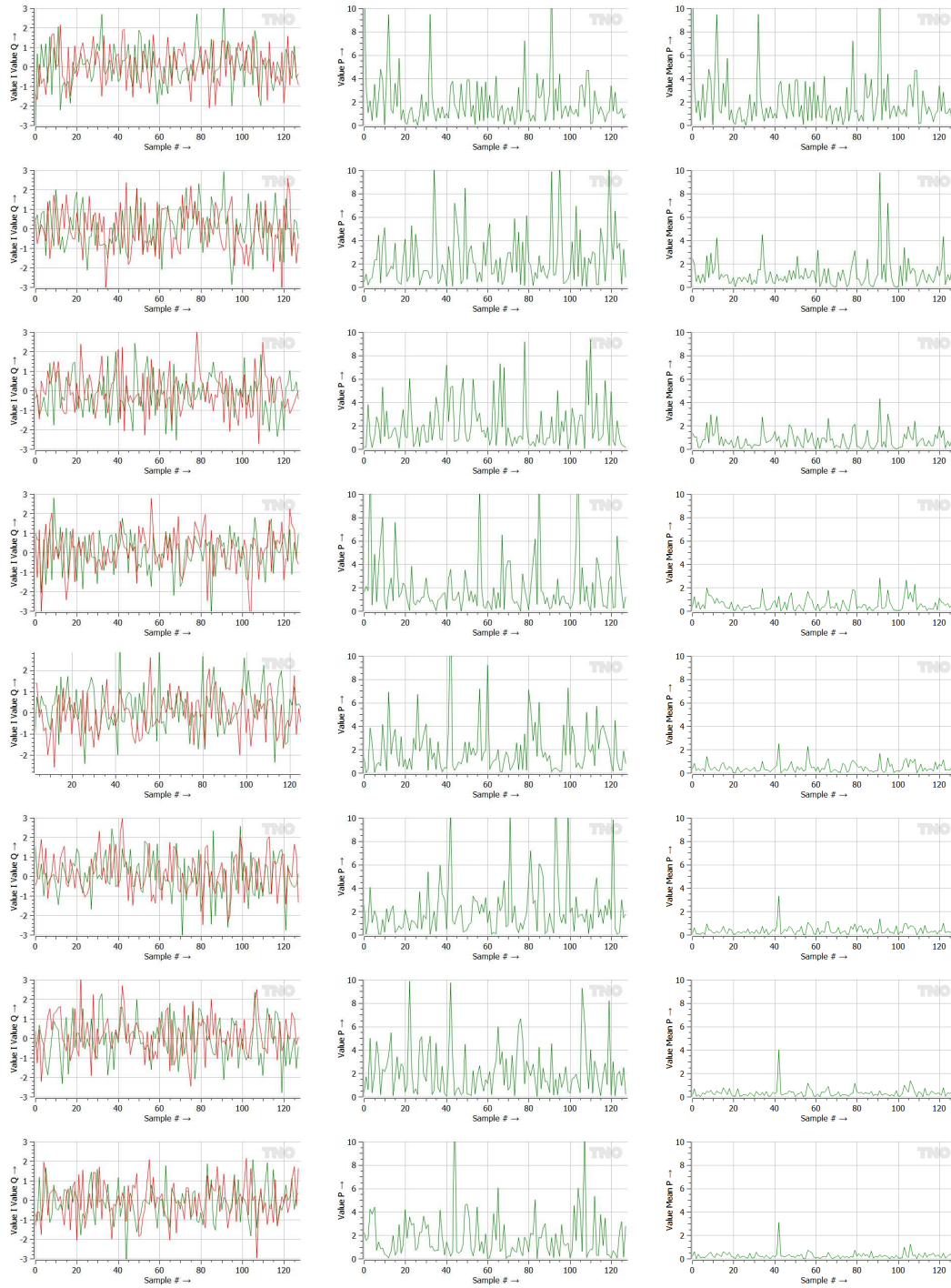


Figure 6.38: Illustration of the effect of coherent pulse response integration.

It appears that doubling the number of pulses reduces the average power of the sequence with 3 dB, a factor of 2 therefore. In other words: in the case of coherent integration, the increase of the SNR goes with the number of responses that is integrated.

Two types of Doppler processors are available in CARPET: a pulse canceler, and a Doppler filter bank (DFB). Of these, a Doppler filter bank allows for the extraction of radial velocity.

A pulse canceler circuit subtracts returns of successive pulses. There are four different pulse cancelers available in CARPET 3: a two-pulse canceler that subtracts the echoes of two successive pulses, a three-pulse canceler which is a cascade of two two-pulse cancelers, a four pulse canceler and a five pulse canceler. Schemes of the two and three pulse cancelers circuits are presented in Figure 6.39. The delay equals the pulse repetition interval (PRI).

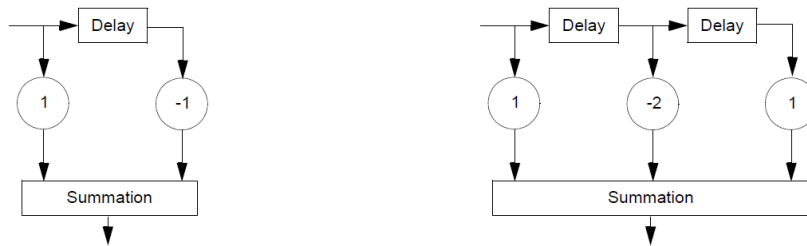


Figure 6.39: Left: two pulse canceler. Right: three pulse canceler.

The filter coefficients are given by:

$$\text{Two-pulse canceler: } w(1) = 1, \quad w(2) = -1 \quad (6.214)$$

$$\text{Three-pulse canceler: } w(1) = 1, \quad w(2) = -2, \quad w(3) = 1 \quad (6.215)$$

$$\text{Four-pulse canceler: } w(1) = 1, \quad w(2) = -3, \quad w(3) = 3, \quad w(4) = -1 \quad (6.216)$$

$$\text{Five-pulse canceler: } w(1) = 1, \quad w(2) = -4, \quad w(3) = 6, \quad w(4) = -4, \quad w(5) = 1 \quad (6.217)$$

The  $n + 1$  weights,  $w_i$ , for a transversal (non-recursive) filter with  $n$  delay lines are the binomial coefficients with alternating sign:

$$w_i = (-1)^{i-1} \frac{n!}{(n-i+1)!(i-1)!}, \quad i = 1 \dots n+1. \quad (6.218)$$

A pulse canceler rejects echoes of stationary (non-moving) objects. These pulse cancelers also reject echoes with a Doppler frequency shift equal to a multiple of the PRF, see the



discussion in Section 6.9.1, resulting in so-called ‘blind speeds’. To remedy this, staggered PRF pulse cancelers are employed, these are currently not supported in CARPET 3.

A Doppler filter bank (DFB) provides a number of band-pass filters that cover the Doppler domain. For each filter, the returns of a series of successive pulses are multiplied with complex weight factors, so the phase angles of the returns are manipulated as well. CARPET 3 assumes Doppler filters that are equally spaced in the Doppler domain. The number of Doppler filters,  $N_d$ , must be equal or larger than the number of pulses within a burst,  $N_p$ , minus the number of fill-pulses,  $N_f$ :

$$N_d = N_p - N_{p,f}. \quad (6.219)$$

In the case of medium and high PRF radars that must be able to detect second or more time around echoes, fill pulses may be transmitted in order to ensure that such multiple time around target responses will benefit from the full integration gain that the DFB offers.

The coefficient  $w_d(n)$  of Doppler filter  $n$  with center frequency  $f_d$  is computed according to

$$w_d(n) = t(n)e^{j2\pi(n-1)f_dPRI}, n = 1 \dots N. \quad (6.220)$$

Taper coefficients,  $t(n)$ , are used to reduce spillover, resulting from the sidelobes from other filters. Apart from uniform weighting, four different tapers are available in CARPET 3: Hanning, Hamming, Blackman and Dolph-Chebyshev. The latter window function demands specification of the side lobe level. For details, we refer to Frederic Harris [43].

CARPET also supports a pulse canceler and a DFB cascaded, such as the architecture shown in Figure 6.40.

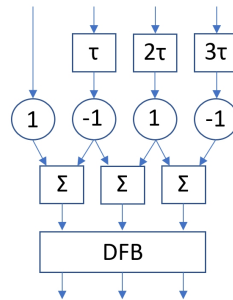


Figure 6.40: A cascade of a two-pulse canceler and a three-point Doppler filter bank.  $\tau$  means a delay over the PRI. The DFB contains complex weights and summatoms.

Pulse cancelers and the filters that make up a Doppler filter band are FIR (finite impulse response) filters. The impulse response of a FIR filter goes to zero in a restricted (finite) time interval. The relationship between the filter output,  $y$ , and a series of input samples  $x(n), n = 1 \dots N_d$  is given by the convolution equation:

$$y = \sum_{n=1}^{N_d} w(n) \cdot x(n). \quad (6.221)$$

with  $w(n)$  the (potentially complex valued) Doppler filter weights (see for instance Richard G. Lyons, [44], p.158).

Given a certain radial velocity of the target, CARPET first determines the set of Doppler filter weights that provide the highest Doppler filter gain for the target responses. (In the case of a pulse canceler this step is obsolete since there is only a single Doppler filter.) Subsequently, gain factors for the noise and clutter signal components are derived, given this specific set of weights.

The Doppler filter gain factors do not only depend on the values of the weights. The ‘Doppler spectral content’ of the signal is also important. To illustrate this, Figure 6.41 shows Doppler filter gains for the target, sea clutter and noise signal components versus the radial speed of the target, made with CARPET. A low PRF (700 Hz) S-band surveillance radar is assumed and eight pulses are integrated in a Doppler filter bank. As expected, the sea clutter is ‘Doppler spectrally’ more narrow in the case of the uniform taper, while the leakage into adjacent Doppler filters is more dominant compared to the case that Dolph-Chebyshev tapering is applied. Note also that the velocity response of the sea clutter filter gain is asymmetric. This is caused by the fact that the sea waves move inbound, the course of the sea wave front is identical to the course of the target. Doppler filter gains in case the waves move perpendicular to the radar azimuth look direction are shown in Figure 6.42.

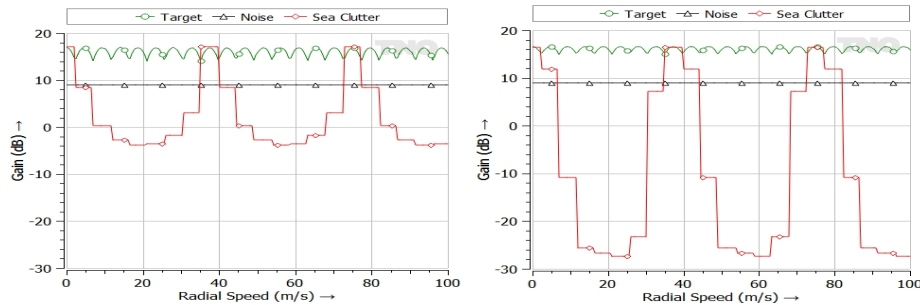


Figure 6.41: Doppler Filter gains versus target radial speed. Left: uniform pre-Doppler-FFT filter. Right: -40 dB Dolph-Chebyshev pre-Doppler FFT taper. The sea waves are moving inbound.

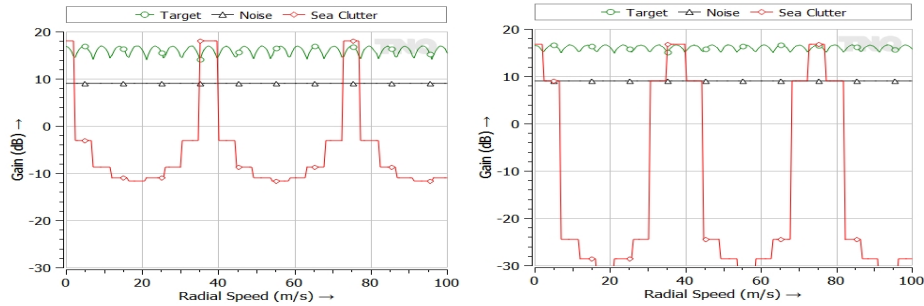


Figure 6.42: Doppler Filter gains versus target radial speed. Left: uniform pre-Doppler-FFT filter. Right: -40 dB Dolph-Chebyshev pre-Doppler FFT taper. The course of the sea waves is  $90^\circ$ .

What happens if we double the number of pulses that is integrated in the Doppler filter bank while keeping the PRF at a fixed value? The unambiguous velocity interval will not change (equation 6.198). The observation time, however, doubles, so the Doppler resolution improves by a factor of two.

The signal power,  $P$ , at the output of a Doppler filter is given by:

$$\begin{aligned}
 P &= \left\{ \sum_{k=1}^{N_d} w(k)x(k) \right\} \cdot \left\{ \sum_{n=1}^{N_d} w(n)x(n) \right\}^c \\
 &= \sum_{n=1}^{N_d} |w(n)|^2 r(0) + \sum_{k=1}^{N_d-1} \sum_{n=1}^{N_d-k} 2\text{Re}\{w^c(n)w(n+k)r(kPRI)\},
 \end{aligned} \tag{6.222}$$

where  $^c$  represents the complex conjugate operation,  $w(n)$ ,  $n = 1 \dots N_d$  are the Doppler filter weights,  $x(n)$  are the signal samples,  $r(t)$  is the autocorrelation function of the signal samples. Expressions of the autocorrelation functions of the various signal components have been given above, as indicated in Table 6.7.

Table 6.7: Features of the various signal components.

Signal component	Equation	Doppler spectrum shape
Noise	6.96	White
Target	6.116	Single tone
Surface clutter	6.151	Gaussian
Volume clutter	6.164	Gaussian
Jamming	6.169	White

For thermal noise and jamming the expression for the output power,  $P_n$  or  $P_j$ , reduces to

$$P = \sum_{n=1}^{N_d} |w(n)|^2 r(0), \tag{6.223}$$

since the autocorrelation function in these cases is zero except for  $\tau = k \cdot PRI = 0$ .

If a target is multiple times around, it may be necessary to set to zero the first  $N_t$  filter coefficients, depending on the number of fill pulses. This number is given by:

$$N_t = \text{int} \left( \frac{2R_t}{cPRI} \right) - N_{p,f}. \quad (6.224)$$

For responsive jamming, the first  $N_j$  filter coefficients are set to zero for the calculation of the responsive jamming power:

$$N_j = \text{int} \left( \frac{2R_j}{cPRI} \right) - N_{p,f}. \quad (6.225)$$

### 6.9.6 Antenna Rotation

Rotation of the radar antenna during the coherent dwell time results in a spread of the clutter spectrum in the radar receiver because of amplitude modulation of the clutter signal by the two-way antenna pattern. If the radar mode is surveillance, the variance of the clutter spectrum is adjusted according to:

$$\alpha_{rot} = \alpha_c^2 + \alpha_{rot}^2 \quad (6.226)$$

where  $\alpha_c^2$  is the original variance of the surface or volume clutter and  $\alpha_{rot}^2$  is the variance resulting from the antenna rotation, which is calculated from

$$\alpha_{rot} = \frac{2\pi}{5.35\theta_2 T_{frame}} \cdot \frac{T_{int}}{T_{dwell}} \quad (6.227)$$

Here,  $\theta_2 = \theta_{az}/\sqrt{2}$  is the two-way, half-power azimuth beamwidth and  $T_{frame}$  is the time needed to complete one antenna revolution. The coherent integration time,  $T_{int}$ , is given by

$$T_{int} = (N_p - N_{p,f})PRI \quad (6.228)$$

if a Doppler filter bank (possibly in combination with a pulse canceler) is used for clutter suppression, or

$$T_{int} = kPRI \quad (6.229)$$

with  $k = 2$  for a two-pulse canceler and  $k = 3$  for a three-pulse canceler. The dwell time,  $T_{dwell}$ , which may consist of multiple coherent integration intervals, is computed from

$$T_{dwell} = \frac{T_{frame}\theta_{az}}{2\pi} \quad (6.230)$$

### 6.9.7 Phase and Amplitude Noise

It is argued in Section 6.9.1 how, in a pulse-Doppler radar, the radial velocity of a target can be derived from the pulse-to-pulse phase-change of the received target echo.<sup>16</sup> In this Section we discuss the consequence of phase and amplitude noise, *i.e.*, fluctuations of the phase and amplitude of the transmitted RF signal. This noise is multiplicative, its manifestation depends on the strength of the target echo; no target implies no amplitude and phase noise is present in the received signal:

$$s_m = s\xi + n. \quad (6.231)$$

$s_m$  is the measured signal,  $s$  is the target echo in the absence of phase and amplitude noise,  $n$  is additive noise,  $\xi$  represents the phase and amplitude noise.

One consequence is that the accuracy of the radial velocity estimate degrades. Generally more serious, however, is the phenomenon that the shape of the Doppler spectra of clutter and target responses changes.

Any Doppler filter will pick up clutter when present. When the mainlobe of the Doppler filter is ‘Doppler spectrally’ sufficiently distant from the Doppler frequency shift where the clutter has its peak, the clutter will mostly be picked up by sidelobes of the Doppler filter. An ‘off peak’ increase of the clutter level due to phase and/or amplitude noise causes an increase of the collected clutter signal. This desensitises the radar, since the detection threshold that is put-up by the CFAR detection process is linked to the background (clutter and noise). A remedy is to have Doppler filters with lower sidelobe levels, which, unfortunately, implies a higher taper loss.

An other effect is that the target response is Doppler spectrally not a mere ‘spike’, *i.e.*, Dirac pulse. Due to phase and amplitude noise, residual target signals can be picked up by non-target Doppler filters which may even result in false detections, or ‘ghosts’.

CARPET models the influence of phase and amplitude to the received clutter signal. The received clutter signal is decorrelated, which results in an increase of the clutter residue at the output of the Doppler processor. If the clutter residue at Doppler shifts corresponding to moving targets is larger than the thermal noise contribution, a degradation in the detection of moving targets occurs. The effect of phase noise on the radar performance is taken into account in CARPET if the Phase Noise checkbox is switched on. Amplitude noise is not modelled in the current version of CARPET.

The phase spectrum of the reference oscillator consists of a white-noise contribution and a colored-noise contribution with a Lorentzian spectrum:

$$S_{\Phi}(f) = \frac{P_{cn}}{\pi f_{co}} \frac{f_{co}^2}{f_{co}^2 + f^2} + Q_{wn} \quad (6.232)$$

<sup>16</sup>Not all pulse-Doppler radar systems provide radial velocity estimates. Especially when the PRF is relatively low, radial velocity estimation can be problematic because of ambiguities.

The phase spectrum is defined by the colored-noise power,  $P_{cn}$ , with respect to the carrier, the cut-off frequency,  $f_{co}$ , and the white-noise power density,  $Q_{wn}$ . The corresponding autocorrelation function of the phase noise is

$$r_\phi(\tau) = P_{cn} \exp\{-2\pi f_{co}|\tau|\} + Q_{wn}B\delta(\tau) \quad (6.233)$$

The autocorrelation function of the phase noise of the clutter at a distance  $R_c$  minus the phase noise from the oscillator,  $\Delta\phi(t) = \phi(t - 2R_c/c) - \phi(t)$ , becomes

$$r_{\Delta\phi}(\tau) = 2r_\phi(\tau) - \left\{r_\phi\left(\tau - \frac{2R_c}{c}\right) + r_\phi\left(\tau + \frac{2R_c}{c}\right)\right\}. \quad (6.234)$$

The autocorrelation function of the decorrelated clutter signal is given by

$$r(\tau) = r_c(\tau) \exp\{r_{\Delta\phi}(\tau) - r_{\Delta\phi}(0)\} \quad (6.235)$$

here  $r_c(\tau)$  is the autocorrelation function of the original surface or volume clutter signal.

### 6.9.8 Timing Jitter

The timing uncertainty or jitter in clock signals affects the clutter cancellation in pulse Doppler radars because of the decorrelation of the clutter signal. If the Timing Jitter toggle is switched on in CARPET, the increase in clutter residue at the output of a Doppler filter is calculated for independent Gaussian distributed transmitter and receiver timing jitter with zero mean and a rectangular compressed pulse of length  $1/B$ . In this case, the increase in residue may be approximated by

$$\Delta P = 3B^2(\delta_{tx}^2 + \delta_{rx}^2) \sum_{n=1}^{N_d} \frac{|w(n)|^2}{4} \quad (6.236)$$

where  $\delta_{tx}$  and  $\delta_{rx}$  are the RMS timing jitters of the transmitter and receiver, respectively,  $w(n)$ ,  $n = 1 \dots N_d$  are the coefficients of the Doppler filter and  $B$  is the instantaneous bandwidth (Sabatini, [45]).

### 6.9.9 Detection

Targets are detected by applying a threshold to the received radar signal and declaring the presence of a target when the threshold is exceeded, as depicted in Figure 6.43. Because of the stochastic nature of the received signal, incorrect decisions may be made *i.e.*, the target is not detected because the threshold is not exceeded, a miss, or a noise fluctuation exceeds the threshold in the absence of a target, which results in a false alarm. The four possibilities are indicated in Table 6.8. The failure to detect the target (a miss) is also called a type II

error, error of the second kind, or false negative. Publishing a detection while a target is not present (a false alarm), is called a type I error, error of the first kind, or false positive.

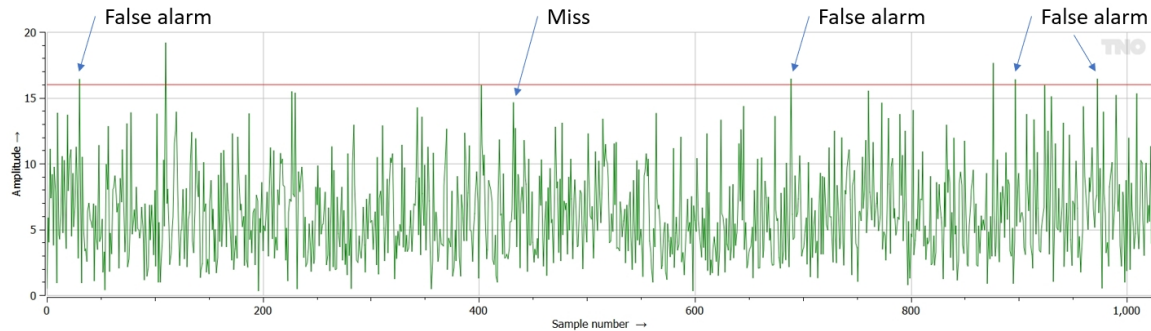


Figure 6.43: Time series illustrating a miss, several false alarms and two ‘hits’.

Table 6.8: The four detection cases.

Truth	Decision	
	Don't declare	Do declare
No target	$\mathbb{I} \Rightarrow$	$\mathbb{I} \Rightarrow$ False alarm
Target	$\mathbb{I} \Rightarrow$ Miss	$\mathbb{I} \Rightarrow$ Detection

The detection process sets up a decision rule to classify the received data. There are two hypotheses:

- $H_0$ , null hypothesis: the measured response is not caused by the reflection against a target of interest.
- $H_1$ , alternative hypothesis: the measured response is caused by the reflection against a target of interest.

In radar systems a detection threshold is set up so that the detection probability is as large as possible while the false alarm probability is at a fixed value, a strategy that is referred to as CFAR: constant false alarm rate. A comparison with a detection threshold is the decision rule; when the signal strength is larger than the threshold a target is declared. The mathematics to derive at the proper value of the detection threshold has been described by Jerzy Neyman and Egon S. Pearson in 1933, [15].

As described by Daniel P. Meyer and Herbert A. Mayer, [16], p.19, there are at least two different definitions of false alarm time,  $t_{fa}$  (s).

- Marcum's definition: the time during which the probability that noise will not exceed the threshold is  $\frac{1}{2}$ .

- Kaplan and McFall definition: the average time interval between false alarm detections.

Within CARPET, the second definition is applied. The number of false alarms per unit of time (*e.g.*, 1 false alarm in two minutes, so 8.33 mHz) is called FAR ( $\text{s}^{-1}$ ), false alarm rate:

$$FAR = \frac{1}{t_{fa}} \quad (6.237)$$

The false alarm probability,  $P_{fa}$ , is defined as 1 over the false alarm number,  $N_{fa}$ :

$$P_{fa} = \frac{1}{N_{fa}}. \quad (6.238)$$

There are two ways to define false alarm number. Marcum's definition,  $N_{fa,M}$ , is:

$$N_{fa,M} = PRF \cdot N_{rq} \cdot t_{fa}, \quad (6.239)$$

in which  $N_{rq}$  is the number of range bins. The definition referred to as Fehlner's false alarm number<sup>17</sup>,  $N_{fa,F}$ , is given by

$$N_{fa,F} = \frac{N_M}{N_p}, \quad (6.240)$$

in which  $N_p$  is the number of pulses that is integrated.

CARPET's  $P_{fa}$  is applicable for the point in the signal processing chain where detection is done. CARPET therefore complies with Marcum's false alarm number, however, per Doppler filter. To relate the FAR after Doppler filtering to CARPET's false alarm probability requires knowledge on the number of resolution cells and on the number of Doppler filters. The number of independent range bins,  $N_{rq}$ , is given by:

$$N_{rq} = \frac{R_i}{\tau_c} = \frac{R_i}{c/(2B)} \quad (6.241)$$

with  $R_i$  (m) the radar's instrumented range,  $\tau_c$  (s) the compressed pulse length,  $c$  (m/s) the speed of light and  $B$  (Hz) the instantaneous bandwidth of the radar pulse.

CARPET 3 contains a worksheet with which the user can investigate the relationship between the FAR after Doppler filtering and the false alarm probability (for a single receive beam radar) as discussed in Section 5.11. This worksheet assumes that a false alarm in one of the Doppler filters 'propagates to the end', *i.e.*, it will appear as a false target report (or 'plot').

The probability that the threshold is exceeded in the absence of a target, depends on the noise statistics, the threshold level (obviously) and on the number of non-coherently integrated responses.

<sup>17</sup>Meyer and Mayer point out that Marcum has put forward this definition as well.



In CARPET, the noise within the I (in-phase) and Q (quadrature phase) channel is assumed to be Gaussian distributed, as illustrated in Figure 6.44.

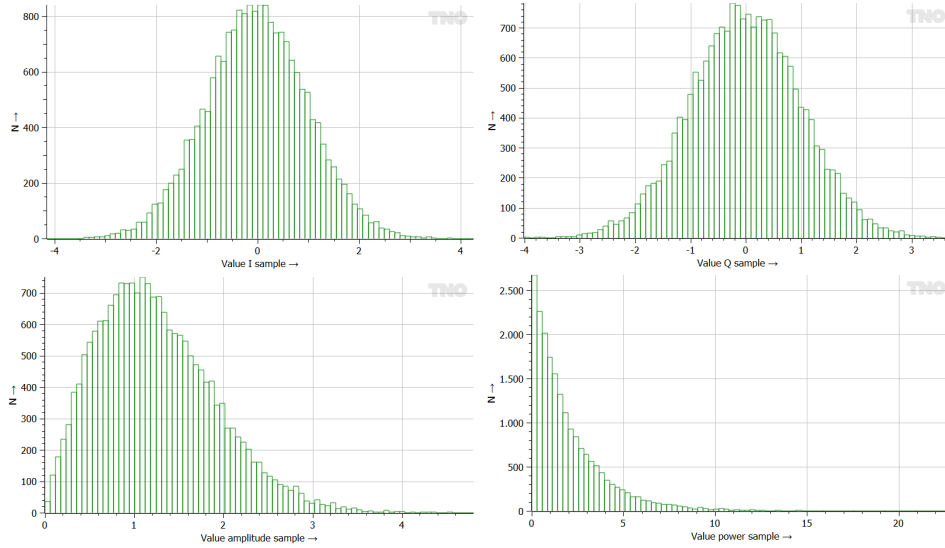


Figure 6.44: The pair of Gaussian distributed in-phase (I) and quadrature-phase (Q) samples lead to Rayleigh distributed amplitude values ( $\sqrt{I^2 + Q^2}$ ) and exponentially distributed power values ( $I^2 + Q^2$ ). The samples were generated using the ‘basic form’ of the Box-Muller transform, [46].

Note that the amplitude follows a Rayleigh distribution.<sup>18</sup> The probability density function (PDF),  $f(a; \sigma)$ , of the amplitude,  $a$ , is given by:

$$f(a; \sigma) = \frac{a}{\sigma^2} e^{-\frac{a^2}{2\sigma^2}}, \quad a \geq 0. \quad (6.242)$$

with  $\sigma^2$  the variance of the noise in the I and Q channel, see for instance Harry Urkowitz, p.322, [47]. The probability density function of the phase,  $f(\phi)$ , is given by:

$$f(\phi) = \frac{1}{2\pi}, \quad 0 < \phi \leq 2\pi. \quad (6.243)$$

The cumulative distribution function (CDF),  $F(a; \sigma)$ , of the amplitude is given by:

$$F(a; \sigma) = 1 - e^{-\frac{a^2}{2\sigma^2}}, \quad a \geq 0. \quad (6.244)$$

PDFs and CDFs of the amplitude are illustrated in Figure 6.45.

<sup>18</sup>Named after John William Strutt, the third Baron of Rayleigh (which is in Essex, England).

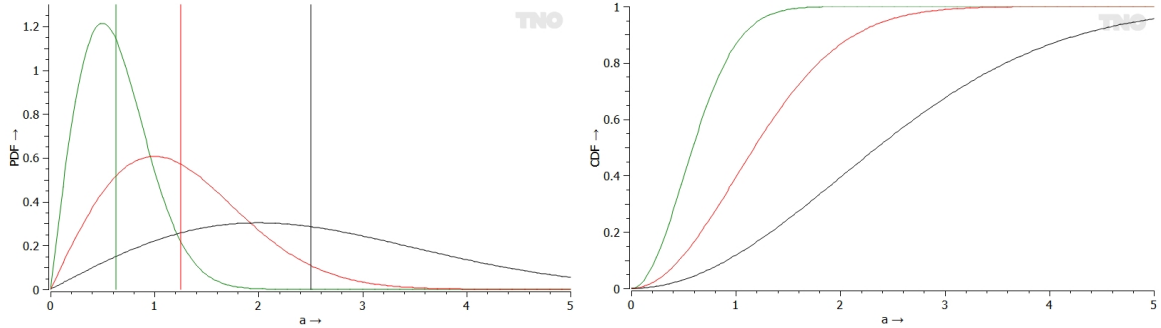


Figure 6.45: Left: Rayleigh PDFs for  $\sigma = 0.5$  (green),  $\sigma = 1.0$  (red) and  $\sigma = 2.0$  (black). The vertical lines represent the expected values. Right: CDFs.

Suppose a detection threshold, is placed ‘somewhere’ along the amplitude (or voltage) axis at value  $Y_b$ , as depicted in Figure 6.46.

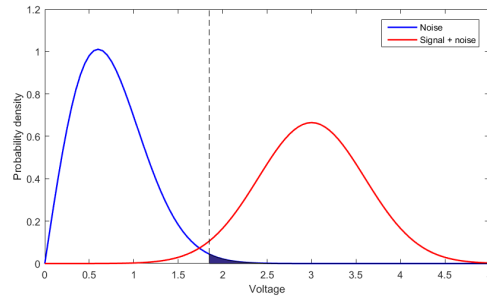


Figure 6.46: PDFs of noise and target versus amplitude. The interrupted line is the detection threshold.

The false alarm probability,  $P_{fa}$ , is the area under the PDF-curve of the noise at the right of the threshold.

In case of a number,  $N_b$ , of non-coherently integrated samples,  $P_{fa}$ , can be calculated according to

$$P_{fa} = 1 - \Gamma(N_b, Y_b), \tag{6.245}$$

where  $\Gamma$  denotes the incomplete gamma function given by:

$$N > 0 : \quad \Gamma(N, Y) = \int_0^Y \frac{\exp\{-u\}u^{N-1}}{\Gamma(N)} dh \tag{6.246}$$

$$N = 0 : \quad \Gamma(N, Y) = 1 \tag{6.247}$$



The single-scan detection probability,  $p_d$ , of a target depends on the fluctuation characteristics of the target signal (Swerling case), the threshold level ( $Y_b$ ) and the number of non-coherently integrated samples ( $N_b$ ). Given a specified false alarm probability  $P_{fa}$ , the threshold level can be determined, and, subsequently, the detection probabilities for the non-fluctuating (Swerling 0) target and the four fluctuating targets (Swerling 1, 2, 3, 4) that are usually considered. For the third time, we repeat a table for convenience reasons.

Table 6.9: The four Swerling cases.

Fluctuation speed	No dominant scatterer	One dominant scatterer
Scan-to-scan	1	3
Pulse-to-pulse	2	4

In the expressions for the detection probabilities, the auxiliary variables  $a$ ,  $b$ ,  $c$ , and  $d$  are introduced:

$$a = \frac{1}{1+x} \quad (6.248)$$

$$b = \frac{1}{1+N_b x} \quad (6.249)$$

$$c = \frac{1}{1+\frac{x}{2}} \quad (6.250)$$

$$d = \frac{1}{1+\frac{N_b x}{2}} \quad (6.251)$$

where  $x$  represents the average SNR (signal-to-noise-ratio, where clutter and jamming are considered as ‘noise’), given by the ratio of the target power and the noise + clutter + jamming power:

$$x = \frac{P_t}{P_n + P_{cs} + P_{vc} + P_j} \quad (6.252)$$

The SNR can be determined at different points in the radar’s receive path, for instance at the output of the antenna, or at the input of the receiver. Considerations about the so-called ‘reference point’ are given in Appendix B.

The expressions for the detection probability,  $P_d$ , for the different Swerling models are as follows:

Swerling case 0: Nonfluctuating target model.

$$Y_b \geq N_b(x+1) : P_d = e^{-N_b x} \sum_{k=0}^{\infty} \frac{(N_b x)^k}{k!} \{1 - \Gamma(N_b + k, Y_b)\} \quad (6.253)$$

$$Y_b < N_b(x+1) : P_d = 1 - e^{-N_b x} \sum_{k=0}^{\infty} \frac{(N_b x)^k}{k!} \Gamma(N_b + k, Y_b) \quad (6.254)$$

Swerling case 1: Rayleigh distributed signal (exponentially distributed power) with scan-to-scan fluctuation.

$$P_d = 1 - \Gamma(N_b - 1, Y_b) + \frac{e^{-bY_b}}{(N_b, xb)^{N_b-1}} \Gamma(N_b - N_b xb Y_b) \quad (6.255)$$

Swerling case 2: Rayleigh distributed signal (exponentially distributed power) with pulse-to-pulse fluctuation.

$$P_d = 1 - \Gamma(N_b, aY_b) \quad (6.256)$$

Swerling case 3: Four-degrees-of-freedom chi-square distributed signal with scan-to-scan fluctuation.

$$P_d = 1 - \Gamma(N_b - 1, Y_b) + \frac{c(N_b - 1)e^{-Y_b} Y_b^{N_b} - 1}{(N_b - 1)!} + \frac{e^{-cY_b}}{(1-c)^{N_b-2}} \left( 1 - \frac{(N_b - 2)c}{1-c} + cY_b \right) \Gamma\{N_b - 1, Y_b(1-c)\} \quad (6.257)$$

Swerling case 4: Four-degrees-of-freedom chi-square distributed signal with pulse-to-pulse fluctuation.

$$Y_b \geq N_b(2-d) : P_d = d^{N_b} \sum_{k=0}^{N_b} \frac{N_b!}{k!(N_b-k)!} \cdot \frac{(1-d)^{N_b-k}}{d^{N_b-k}} \{1 - \Gamma(2N_b + k, dY_b)\} \quad (6.258)$$

$$Y_b < N_b(2-d) : P_d = 1 - d^{N_b} \sum_{k=0}^{N_b} \frac{N_b!}{k!(N_b-k)!} \cdot \frac{(1-d)^{N_b-k}}{d^{N_b-k}} \Gamma(2N_b + k, dY_b) \quad (6.259)$$

In case of a single pulse these equations simplify drastically:

Swerling cases 1 and 2:

$$P_d = e^{\frac{\ln P_{fa}}{1+x}} \Leftrightarrow x = \frac{\ln P_{fa}}{\ln P_d} - 1 \quad (6.260)$$

Swerling cases 3 and 4:

$$P_d = \left(1 - \frac{2 \ln P_{fa}}{1+x}\right) e^{\frac{2 \ln P_{fa}}{1+x}} \quad (6.261)$$

The CARPET user can verify the relationships between  $P_d$ ,  $P_{fa}$ , SNR, detection threshold and the number of pulse responses that are non-coherently integrated with the Swerling Case worksheet, shown in Figure 5.5, while CARPET's Swerling-case diagrams are also illustrative, *e.g.*, the diagram shown in Figure 6.47.

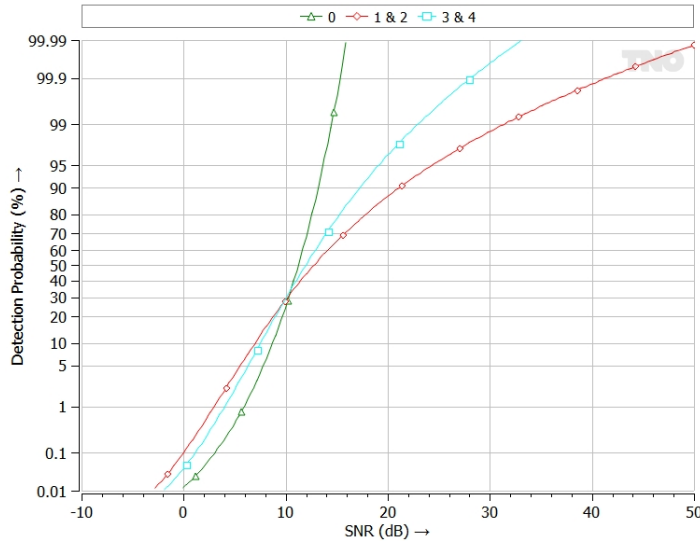


Figure 6.47: Single-pulse probability of detection versus signal-to-noise-ratio.  $P_{fa} = 1 \times 10^{-6}$ .

The figure shows that in the case of a sufficiently high SNR, a non-fluctuating target is more easily detected than a Swerling 3 or 4 target (one dominant scatterer), than a Swerling 1 or 2 target (no dominant scatterer). This makes sense; if the SNR is high enough to detect a non-fluctuating target, fluctuations will do the process no good. If, on the other hand, the SNR is that low so that a non-fluctuating target is difficult to detect, fluctuations will do the process good.

### 6.9.10 Post-detection Binary Integration

Contrast to CARPET 1 and 2, CARPET 3 with multi-burst plug-in supports  $M$ -out-of- $N$  post-detection binary integration. This logic is widely applied in modern multi-waveform radars since it effectively reduces the false alarm rate.  $N$  refers to the number of available waveforms (or 'bursts') during a dwell. The radar's signal processor will report a detection if at least  $M$  ( $\leq N$ ) 'pre-detections' have occurred.

In case of equal pre-detection probabilities from burst to burst,  $p_{pd}$ , the detection probability at the output of the binary integrator,  $p_d$ , is given by:

$$p_d = \sum_{m=M}^N \binom{N}{m} p_{pd}^m (1 - p_{pd})^{N-m} \quad (6.262)$$

with

$$\binom{a}{b} = \frac{a!}{b!(a-b)!} \quad (6.263)$$

In case of  $N$ -out-of- $N$ ,  $\binom{N}{N}$  is 1 while the summation cancels, so that the resulting detection probability is given by:

$$p_d = p_{pd}^N \Leftrightarrow p_{pd} = \sqrt[N]{p_d}. \quad (6.264)$$

In case of ‘at least 1-out-of- $N$ ’, the resulting probability is given by:

$$p_d = 1 - (1 - p_{pd})^N \Leftrightarrow p_{pd} = 1 - \sqrt[N]{1 - p_d}. \quad (6.265)$$

The left-hand side of equation 6.264 follows from

$$\begin{aligned} \sum_{m=1}^N \binom{N}{m} p_{pd}^m (1 - p_{pd})^{N-m} &= \sum_{m=0}^N \binom{N}{m} p_{pd}^m (1 - p_{pd})^{N-m} - (1 - p_{pd})^N = \\ &= \{p_{pd} + (1 - p_{pd})\}^N - (1 - p_{pd})^N = 1 - (1 - p_{pd})^N \end{aligned} \quad (6.266)$$

where the good-old binomial formula has been applied ( $(x + y)^n = \sum_{k=0}^n \binom{n}{k} x^k y^{n-k}$ ).

CARPET obviously supports dissimilar pre-detection probabilities (from burst to burst). *E.g.*, the left-hand side of equation 6.265 becomes

$$p_d = 1 - \prod_{n=1}^N (1 - p_{pd,n}), \quad (6.267)$$

where  $p_{pd,n}$  is the pre-detection probability that is obtained with burst  $n$ . Furthermore:

- The  $M$ -out-of- $N$  logic can abandon combinatorics in case a series of subsequent misses are experienced, the length of the series can be specified as well ( $G$ ). *E.g.*, assume  $M = 3$ ,  $N = 6$  and  $G = 2$ , implying that series with a gap larger than 2 misses are rejected. Thus, the series 110001 and 100011 are discarded (1 represents a hit, 0 represents a miss).

- The  $M$ -out-of- $N$  logic can only allow combinatorics with successive hits. *E.g.*, assume  $M = 3$ ,  $N = 6$  and successive hits are demanded. Thus, the series 111000, 011100, 001110, 000111, 111100, 011110, 001111, 111110, 011111 and 111111 will result in a target-report (or ‘plot’).

The CARPET user can verify how  $M$ -out-of- $N$  circuitry affects the detection and the false alarm probability in the Binary Integration worksheet, as discussed in Section 5.10.

As stated before: it is important to realize that the false alarm probability that is specified in the Detection pane of the Processing dialogbox refers to the false alarm probability at the detector, so the false alarm probability that is used in the calculation of the detection probability, given the SNR, the number of pulses that is non-coherently integrated and the Swerling case. In case the false alarm probability ‘at the output of the radar’ (or the expected number of false plots per unit of time) is specified, the CARPET-user has to derive the false alarm probability at the detector. The Solve Backwards pane of the Binary Integration worksheet can be utilized for this purpose. In case the radar contains a Doppler filter bank and detection logic in each Doppler filter, as illustrated in Figure 6.48, it is advised to also consider the number of Doppler filters: divide the false alarm probability prior to the  $M$ -out-of- $N$  integrator by the number of Doppler filters. This is a somewhat ‘cautious’ approach since it assumes that a false alarm in a single Doppler filter propagates to the end of the processing chain.

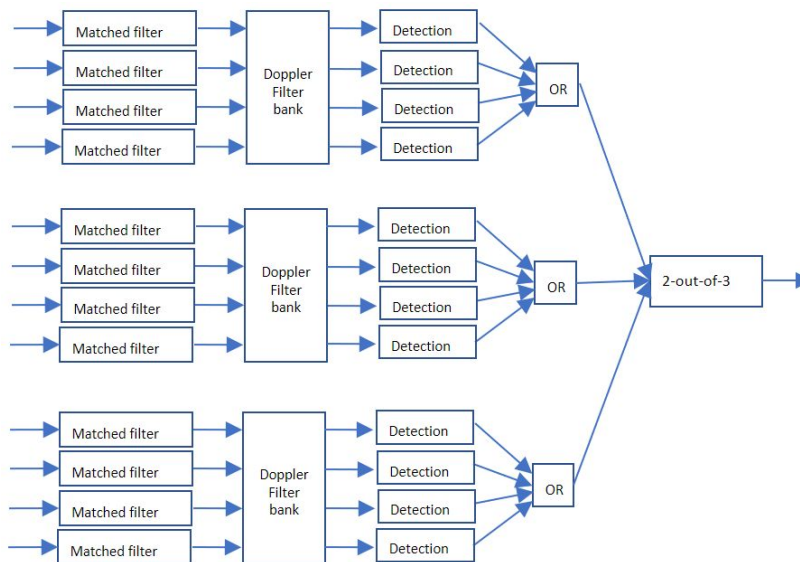


Figure 6.48: A fairly common processing scheme of a modern coherent radar system. Detection is applied per Doppler interval. In this (fictitious) case a dwell consists of three bursts and four pulses are processed per burst. The  $M$ -out-of- $N$  logic in this case is 2-out-of-3.

CARPET 3 also has the straightforward ‘max-rule’ integrator which combines detection probabilities according to:

$$p_{post} = \max(p_{prior,n}), n = 1 \dots N \quad (6.268)$$

The number of transmit and receive channels can be specified since January 2021, provided the multi-burst license is active. In case of multiple channels, *i.e.*,  $N_c > 1$ , and if multiple waveforms are defined,  $M_c$ -out-of- $N_c$  integration is applied prior to integrating the individual waveforms. In case of a single waveform, only  $M_c$ -out-of- $N_c$  integration is applied.

### 6.9.11 Multi-scatterer Target

In case the multi-scatterer target license is available, CARPET determines the single dwell detection probability for each scatterer. Subsequently the maximum of these detection probabilities is taken. One may argue that this is a somewhat ‘conservative’ approach, *i.e.*, on the safe side. Note that the Swerling case can differ from scatterer to scatterer. Results of the multi-scatterer model have been shown in Figure 1.8.



## 6.10 Tracking

In many modern radar systems, multi-scan correlation or tracking is an inherent part of the signal processing chain. In case of a tracker, such radars issue reports (also called ‘plots’ or ‘contacts’) that associate with local tracks to a display process or to a (plot-level) sensor fusion process. Alternatively, track messages or both plot and track messages are published. It can be argued that single scan detection range is hardly a relevant feature for such systems. TNO has therefore added firm track probability ( $P_{ft}$ ) diagrams to CARPET 3. Results of this capability have already been presented in Section 1.3.3. A track-initiation criterion in the style  $M$ -out-of- $N$  has to be specified and a track loss criterion, being a number of subsequent misses that result in a lost (or dropped) track.

With respect to the working principle of the firm track probability calculation, we refer to the paper of Richard Worsham, [2]. Note that the Worsham’s definitions of the probability of acquiring a track ( $P_{acq}$ ), of losing (or dropping) a track ( $P_{loss}$ ), and of being in track ( $P_{ft}$ ) are connected. These definitions reflect the fact that track acquisition can only occur when there is no track, and track loss can only occur when there is a track. Hence,  $P_{acq}$  must be low when  $P_{ft}$  is high, and  $P_{loss}$  must be low when  $P_{ft}$  is low (if there is no track, the probability to lose it is low). The diagram in Dick Worsham’s paper that is duplicated in Section 7.5 is illustrative.

It must be realized that the shape of the  $P_{ft}$  curve depends on the radial velocity of the target and also on the ‘revisit rate’,  $T_{frame}$  (s). It is advised that the maximum target ground range is set sufficiently distant, so that the detection probability at the most distant point is 0%.

### 6.11 Sensitivity Time Control

Generally, variable gain amplifiers or diode attenuators are applied to implement STC. Moreover, STC can be invoked at RF, at IF or at both frequencies. Furthermore, the response over time can be either continuous or stepped. STC not only affects the received power of ‘outside sources’ (target, jamming, clutter), the effective receiver noise figure of the entire receiver chain will vary over time as well, according to the chain rule, see for instance Pettit and McWhorter [53], Skolnik [54] Section 9.2, p.344 and Skolnik [55] Section 11.2, p.729.

The scheme of an architecture where STC is applied both at RF and at IF is shown in Figure 6.49.

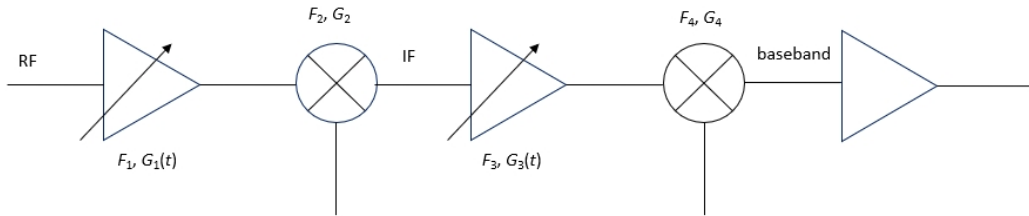


Figure 6.49: STC both at RF and at IF.

The expressions for the overall gain,  $G(t)$ , and noise figure,  $F(t)$ , are given by:

$$G(t) = G_1(t)G_2G_3(t)G_4, \quad (6.269)$$

$$F(t) = F_1 + \frac{F_2 - 1}{G_1(t)} + \frac{F_3 - 1}{G_1(t)G_2} + \frac{F_4 - 1}{G_1(t)G_2G_3(t)}. \quad (6.270)$$

The scheme of an architecture where STC is applied at RF only is shown in Figure 6.50.

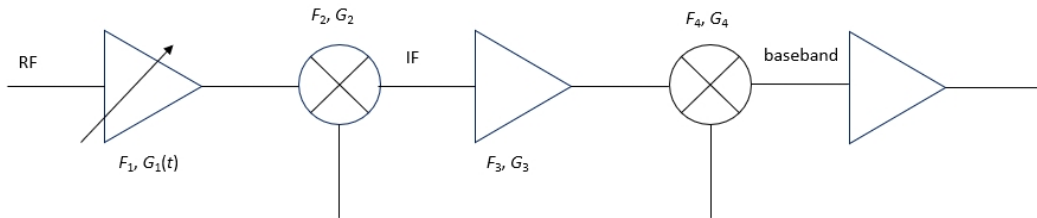


Figure 6.50: STC at RF only.

The expressions for the overall gain and noise figure are given by:

$$G(t) = G_1(t)G_2G_3G_4, \quad (6.271)$$

$$F(t) = F_1 + \frac{F_2 - 1}{G_1(t)} + \frac{F_3 - 1}{G_1(t)G_2} + \frac{F_4 - 1}{G_1(t)G_2G_3}. \quad (6.272)$$

The scheme of an architecture where STC is applied at IF is shown in Figure 6.51.

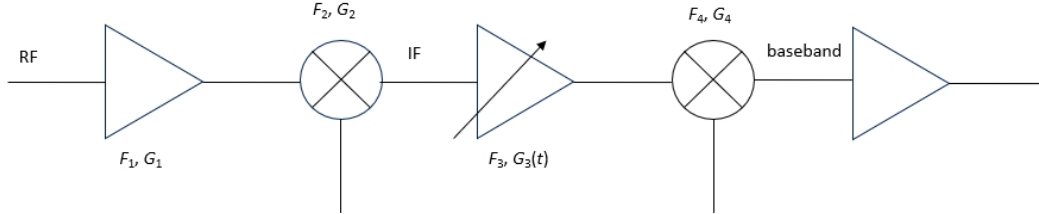


Figure 6.51: STC at IF only.

The expressions for the overall gain and noise figure are given by:

$$G(t) = G_1G_2G_3(t)G_4, \quad (6.273)$$

$$F(t) = F_1 + \frac{F_2 - 1}{G_1} + \frac{F_3 - 1}{G_1G_2} + \frac{F_4 - 1}{G_1G_2G_3(t)}. \quad (6.274)$$

The scheme of an architecture where STC is applied at IF while there is no RF amplifier is shown in Figure 6.52.

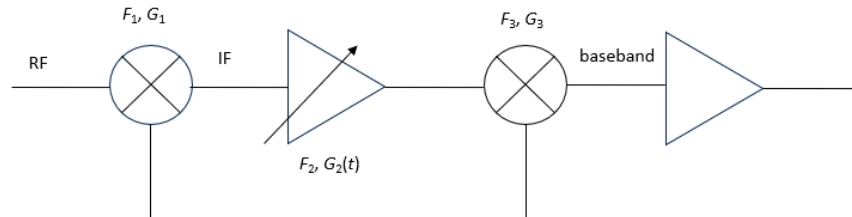


Figure 6.52: STC at IF, no amplification at RF.

The expressions for the overall gain and noise figure are given by:

$$G(t) = G_1G_2(t)G_3, \quad (6.275)$$

$$F(t) = F_1 + \frac{F_2 - 1}{G_1} + \frac{F_3 - 1}{G_1G_2(t)}. \quad (6.276)$$

Let us illustrate this. Suppose the radar applies swept-gain STC at IF.  $G_1 = 35$  dB,  $F_1 = 3$  dB,  $G_2 = -2$  dB ('conversion loss'),  $F_2 = 2$  dB,  $G_3$  follows a 1 over  $R^3$  response with

maximum gain of 0 dB at 50 km ( $PRF = 3$  kHz),  $F_3 = 5$  dB,  $G_4 = -2$  dB,  $F_4 = 2$  dB. The STC response is shown in Figure 6.53. Received powers versus range is shown in Figure 6.54. The propagation model is EREPS-like.

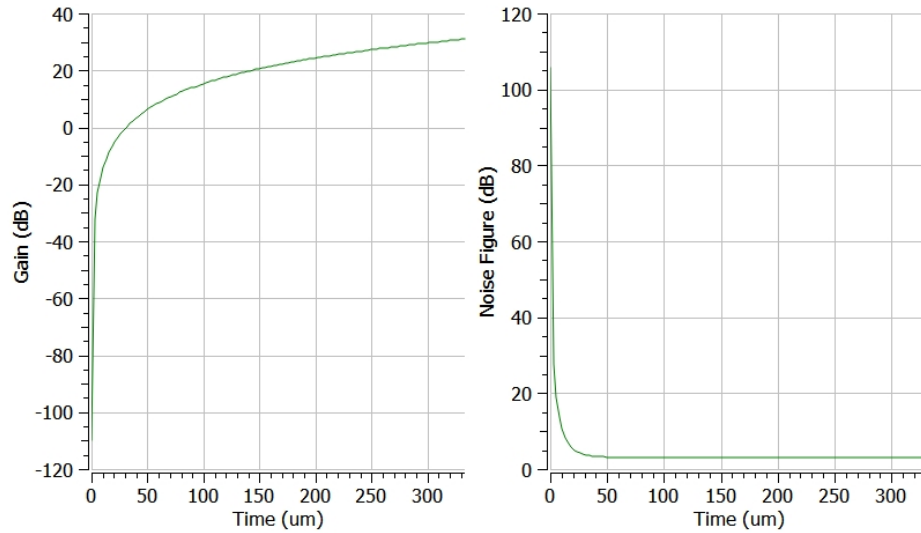


Figure 6.53: Swept gain STC characteristics.

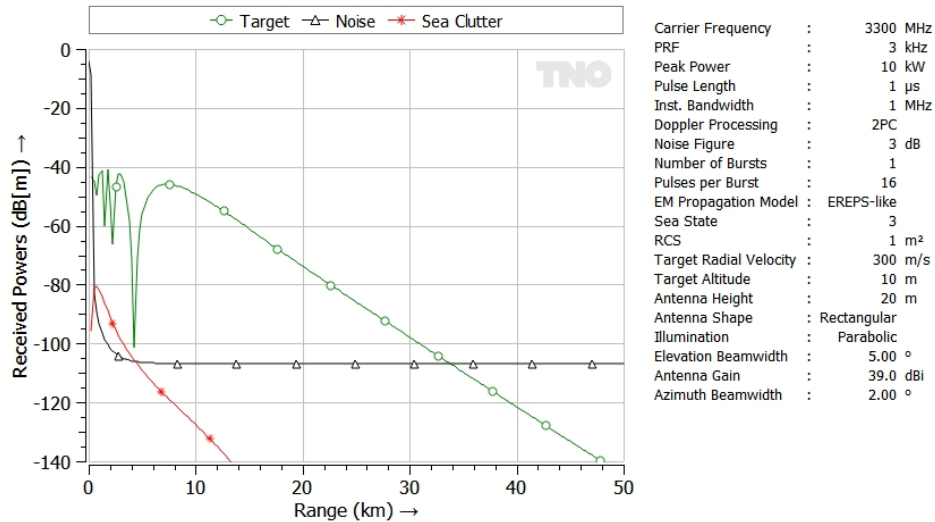


Figure 6.54: Swept gain STC characteristics.

Thus, in order to utilise the STC functionality of CARPET 3, the user has to sort out

gain factors and noise figures for a number of time instances, and put this information in an ASCII file (the STC-file).

The application of STC can affect radar coverage, especially for low RCS targets at short distances. Clearly, the use of STC is troublesome for (medium and high PRF) radars that operate ambiguously in range.

## 7 Python Plug-in

### 7.1 Introduction

The Python plug-in enables loading, saving, editing and execution of Python programs. A brief description of the plug-in is given in this Section. The parameters that can be modified are summarised in Section 7.2. The CARPET functions that are currently supported are considered in Section 7.3. A list of diagrams that can be made is given in Section 7.4. Seven example Python programs are given in Section 7.5.

### 7.2 Parameters

The input parameters of CARPET are organized in so-called C++ data structures. CARPET users can access and the member variables of these structures. The tables 7.1 to 7.14 describe these member variables.

Table 7.1: Elements of CARPET's model structure.

Parameter	Type	Unit
carpet.Model_PropagationModel	int	0=free space 1=EREPS like 2=TERPEM light
carpet.Model_AverageVrad	bool	

Table 7.2: Elements of CARPET's propagation structure.

Parameter	Type	Unit
carpet.Propagation_Troposcatter	bool	
carpet.Propagation_Attenuation	bool	
carpet.Propagation_TSurface	float	K
carpet.Propagation_WindDirection	float	rad
carpet.Propagation_Vwind	float	m/s
carpet.Propagation_K_Earth	float	
carpet.Propagation_Refractivity	float	
carpet.Propagation_EarthsSurface	int	0=sea water 1=fresh water 2=wet ground 3=medium dry ground 4=very dry ground 5=user defined
carpet.Propagation_StdSurfaceHeight	float	m
carpet.Propagation_bGridSetCleverly	bool	
carpet.Propagation_dGridHeightIncrement	float	
carpet.Propagation_dGridRangeIncrement	float	
carpet.Propagation_Conductivity	float	S/m
carpet.Propagation_TERPEM_MPMHumidity	float	
carpet.Propagation_TERPEM_MPMPressure	float	atmosphere
carpet.Propagation_TERPEM_MPMTemperature	float	K
carpet.Propagation_Permittivity	float	F/m
carpet.Propagation_HeightReflectionPoint	float	m



Table 7.3: Elements of CARPET's refractivity profile structure.

Parameter	Type	Unit
carpet.RefractivityProfile_TERPEM_MeasurementHeight	float	
carpet.RefractivityProfile_TERPEM_EvapDuct	int	0=none 1=Paulus
carpet.RefractivityProfile_TERPEM_UpperAir	int	0=k-factor 1=synthetic duct
carpet.RefractivityProfile_TERPEM_UA_SyntheticDuct_ED_Include	bool	
carpet.RefractivityProfile_TERPEM_UA_SyntheticDuct_ED_Alt	float	m
carpet.RefractivityProfile_TERPEM_UA_SyntheticDuct_ED_Strength	float	N-units
carpet.RefractivityProfile_TERPEM_UA_SyntheticDuct_ED_Thickness	float	m
carpet.RefractivityProfile_TERPEM_UA_SyntheticDuct_SBD_Include	bool	
carpet.RefractivityProfile_TERPEM_UA_SyntheticDuct_SBD_Strength	float	N-units
carpet.RefractivityProfile_TERPEM_UA_SyntheticDuct_SBD_Thickness	float	m
carpet.RefractivityProfile_TERPEM_MProfileFileName	string	
carpet.RefractivityProfile_TERPEM_NProfileFileName	string	
carpet.RefractivityProfile_TERPEM_RadiosondeFileName	string	
carpet.RefractivityProfile_TERPEM_TERMETFFileName	string	
carpet.RefractivityProfile_RadiosondeLaunchHeight	float	m

Table 7.4: Elements of CARPET's clutter structure.

Parameter	Type	Unit
carpet.Clutter_VolumeClutter	int	0=none 1=rain 2=chaff
carpet.Clutter_Gamma	float	
carpet.Clutter_RainfallRate	float	m/s
carpet.Clutter_ChaffDensity	float	g/km <sup>3</sup>
carpet.Clutter_Range	float	m
carpet.Clutter_Diameter	float	m
carpet.Clutter_Azimuth	float	rad
carpet.Clutter_SurfaceClutter	bool	

Table 7.5: Elements of CARPET's jamming structure.

Parameter	Type	Unit
carpet.Jamming_JammingType0	int	0=none 1=barrage 2=responsive
carpet.Jamming_Power0	float	W
carpet.Jamming_Gain0	float	
carpet.Jamming_BwBarrage0	float	Hz
carpet.Jamming_BwResponsive0	float	Hz
carpet.Jamming_GroundRange0	float	m
carpet.Jamming_Altitude0	float	m
carpet.Jamming_Azimuth0	float	rad
carpet.Jamming_FreeSpace0	bool	
carpet.Jamming_JammingType1	int	0=none 1=barrage 2=responsive
carpet.Jamming_Power1	float	W
carpet.Jamming_Gain1	float	
carpet.Jamming_BwBarrage1	float	Hz
carpet.Jamming_BwResponsive1	float	Hz
carpet.Jamming_GroundRange1	float	m
carpet.Jamming_Altitude1	float	m
carpet.Jamming_Azimuth1	float	rad
carpet.Jamming_FreeSpace1	bool	
carpet.Jamming_JammingType2	int	0=none 1=barrage 2=responsive
carpet.Jamming_Power2	float	W
carpet.Jamming_Gain2	float	
carpet.Jamming_BwBarrage2	float	Hz
carpet.Jamming_BwResponsive2	float	Hz
carpet.Jamming_GroundRange2	float	m
carpet.Jamming_Altitude2	float	m
carpet.Jamming_Azimuth2	float	rad
carpet.Jamming_FreeSpace2	bool	
carpet.Jamming_JammingType3	int	0=none 1=barrage 2=responsive
carpet.Jamming_Power3	float	W
carpet.Jamming_Gain3	float	
carpet.Jamming_BwBarrage3	float	Hz
carpet.Jamming_BwResponsive3	float	Hz
carpet.Jamming_GroundRange3	float	m
carpet.Jamming_Altitude3	float	m
carpet.Jamming_Azimuth3	float	rad
carpet.Jamming_FreeSpace3	bool	



Table 7.6: Elements of CARPET's transmitter structure.

Parameter	Type	Unit
carpet.Transmitter_Jitter	bool	
carpet.Transmitter_PeakPower	float	W
carpet.Transmitter_RFLoss	float	
carpet.Transmitter_D_WhitePhaseNoise	float	
carpet.Transmitter_P_ColouredPhaseNoise	float	
carpet.Transmitter_CutOffFrequency	float	Hz
carpet.Transmitter_TimingJitter	float	s
carpet.Transmitter_InstantBandwidth1	float	Hz
carpet.Transmitter_InstantBandwidth2	float	Hz
carpet.Transmitter_InstantBandwidth3	float	Hz
carpet.Transmitter_InstantBandwidth4	float	Hz
carpet.Transmitter_InstantBandwidth5	float	Hz
carpet.Transmitter_InstantBandwidth6	float	Hz
carpet.Transmitter_InstantBandwidth7	float	Hz
carpet.Transmitter_InstantBandwidth8	float	Hz
carpet.Transmitter_InstantBandwidth9	float	Hz
carpet.Transmitter_InstantBandwidth10	float	Hz
carpet.Transmitter_NrBursts1	int	
carpet.Transmitter_NrBursts2	int	
carpet.Transmitter_NrBursts3	int	
carpet.Transmitter_NrBursts4	int	
carpet.Transmitter_NrBursts5	int	
carpet.Transmitter_NrBursts6	int	
carpet.Transmitter_NrBursts7	int	
carpet.Transmitter_NrBursts8	int	
carpet.Transmitter_NrBursts9	int	
carpet.Transmitter_NrBursts10	int	
carpet.Transmitter_PulsesPerBurst1	int	
carpet.Transmitter_PulsesPerBurst2	int	
carpet.Transmitter_PulsesPerBurst3	int	
carpet.Transmitter_PulsesPerBurst4	int	
carpet.Transmitter_PulsesPerBurst5	int	
carpet.Transmitter_PulsesPerBurst6	int	
carpet.Transmitter_PulsesPerBurst7	int	
carpet.Transmitter_PulsesPerBurst8	int	
carpet.Transmitter_PulsesPerBurst9	int	
carpet.Transmitter_PulsesPerBurst10	int	
carpet.Transmitter_NrFillPulses1	int	
carpet.Transmitter_NrFillPulses2	int	
carpet.Transmitter_NrFillPulses3	int	
carpet.Transmitter_NrFillPulses4	int	
carpet.Transmitter_NrFillPulses5	int	
carpet.Transmitter_NrFillPulses6	int	
carpet.Transmitter_NrFillPulses7	int	
carpet.Transmitter_NrFillPulses8	int	
carpet.Transmitter_NrFillPulses9	int	
carpet.Transmitter_NrFillPulses10	int	

Table 7.7: Elements of CARPET's transmitter structure, continued.

Parameter	Type	Unit
carpet.Transmitter_RF1	float	Hz
carpet.Transmitter_RF2	float	Hz
carpet.Transmitter_RF3	float	Hz
carpet.Transmitter_RF4	float	Hz
carpet.Transmitter_RF5	float	Hz
carpet.Transmitter_RF6	float	Hz
carpet.Transmitter_RF7	float	Hz
carpet.Transmitter_RF8	float	Hz
carpet.Transmitter_RF9	float	Hz
carpet.Transmitter_RF10	float	Hz
carpet.Transmitter_PRF1	float	Hz
carpet.Transmitter_PRF2	float	Hz
carpet.Transmitter_PRF3	float	Hz
carpet.Transmitter_PRF4	float	Hz
carpet.Transmitter_PRF5	float	Hz
carpet.Transmitter_PRF6	float	Hz
carpet.Transmitter_PRF7	float	Hz
carpet.Transmitter_PRF8	float	Hz
carpet.Transmitter_PRF9	float	Hz
carpet.Transmitter_PRF10	float	Hz
carpet.Transmitter_Tau1	float	s
carpet.Transmitter_Tau2	float	s
carpet.Transmitter_Tau3	float	s
carpet.Transmitter_Tau4	float	s
carpet.Transmitter_Tau5	float	s
carpet.Transmitter_Tau6	float	s
carpet.Transmitter_Tau7	float	s
carpet.Transmitter_Tau8	float	s
carpet.Transmitter_Tau9	float	s
carpet.Transmitter_Tau10	float	s
carpet.Transmitter_PC1	bool	
carpet.Transmitter_PC2	bool	
carpet.Transmitter_PC3	bool	
carpet.Transmitter_PC4	bool	
carpet.Transmitter_PC5	bool	
carpet.Transmitter_PC6	bool	
carpet.Transmitter_PC7	bool	
carpet.Transmitter_PC8	bool	
carpet.Transmitter_PC9	bool	
carpet.Transmitter_PC10	bool	
carpet.Transmitter_BlankingActive0	bool	
carpet.Transmitter_BlankingAzStart0	float	rad
carpet.Transmitter_BlankingAzStop0	float	rad
carpet.Transmitter_PowerReduction0	float	
carpet.Transmitter_BlankingActive1	bool	
carpet.Transmitter_BlankingAzStart1	float	rad
carpet.Transmitter_BlankingAzStop1	float	rad
carpet.Transmitter_PowerReduction1	float	
carpet.Transmitter_BlankingActive2	bool	
carpet.Transmitter_BlankingAzStart2	float	rad
carpet.Transmitter_BlankingAzStop2	float	rad
carpet.Transmitter_PowerReduction2	float	

Table 7.8: Elements of CARPET's antenna structure.

Parameter	Type	Unit
carpet.Antenna_Mode	int	0=surveillance 1=tracking
carpet.Antenna_Polarisation	int	0=horizontal 1=vertical 2=circular
carpet.Antenna_DissipativeLoss	float	
carpet.Antenna_FrameTime	float	s
carpet.Antenna_BeamshapeLoss	float	
carpet.Antenna_MinSideLobe	float	
carpet.Antenna_TxShape	int	0=rectangular 1=circular
carpet.Antenna_TxIllVer	int	0=uniform 1=parabolic 2=parabolic <sup>2</sup> 3=Gauß 4=cosec <sup>2</sup> 5=inverse cosec <sup>2</sup>
carpet.Antenna_TxGain	float	
carpet.Antenna_TxAltitude	float	m
carpet.Antenna_TxAzBeamwidth	float	rad
carpet.Antenna_TxEIBeamwidth	float	rad
carpet.Antenna_TxElevation	float	rad
carpet.Antenna_TxFileName	string	
carpet.Antenna_RxShape	int	0=rectangular 1=circular
carpet.Antenna_RxIllVer	int	0=uniform 1=parabolic 2=parabolic <sup>2</sup> 3=Gauß 4=cosec <sup>2</sup> 5=inverse cosec <sup>2</sup>
carpet.Antenna_RxGain	float	
carpet.Antenna_RxAltitude	float	m
carpet.Antenna_RxAzBeamwidth	float	rad
carpet.Antenna_RxEIBeamwidth	float	rad
carpet.Antenna_RxElevation	float	rad
carpet.Antenna_RxFileName	string	
carpet.Antenna_NrApertures	int	0=single 1=dual
carpet.Antenna_TxRadomeLoss	float	
carpet.Antenna_RxRadomeLoss	float	

Table 7.9: Elements of CARPET's receiver structure.

Parameter	Type	Unit
carpet.Receiver_NoiseFigure	float	
carpet.Receiver_TimingJitter	float	s
carpet.Receiver_RFLoss	float	
carpet.Receiver_MismatchLoss	float	
carpet.Receiver_EclipsingLoss	float	
carpet.Receiver_UseSpecifiedNoisePower	bool	
carpet.Receiver_NoiseTemperature	float	K
carpet.Receiver_GalacticActivity	int	0=none 1=minimum 1=average 2=maximum

Table 7.10: Elements of CARPET's processing structure.

Parameter	Type	Unit
carpet.Processing_Pfa	float	
carpet.Processing_DFB	bool	
carpet.Processing_MTI	int	0=no pulse canceler 1=two pulse canceler 2=three pulse canceler
carpet.Processing_Integrator	int	0=m-out-of-n 1=max-rule
carpet.Processing_M	int	
carpet.Processing_Gap	int	
carpet.Processing_CFARLoss	float	
carpet.Processing_RangeStraddlingLoss	float	
carpet.Processing_PulseCompressionTaperLoss	float	
carpet.Processing_MinRequiredPulseFraction	float	
carpet.Processing_InstrumentedRange	float	m
carpet.Processing_TaperDF	int	0=uniform 1=Hanning 2=Hamming 3=Blackman 4=Dolph Chebyshev

Table 7.11: Elements of CARPET's tracking structure.

Parameter	Type	Unit
carpet.Tracking_InitiationM	int	
carpet.Tracking_InitiationN	int	
carpet.Tracking_Misses	int	

Table 7.12: Elements of CARPET's target structure.

Parameter	Type	Unit
carpet.Target_GroundRange	float	m
carpet.Target_RadialVelocity	float	m/s
carpet.Target_Altitude	float	m
carpet.Target_CPRCSReduction	float	
carpet.Target_Active1	bool	
carpet.Target_Active2	bool	
carpet.Target_Active3	bool	
carpet.Target_Active4	bool	
carpet.Target_Active5	bool	
carpet.Target_Active6	bool	
carpet.Target_Active7	bool	
carpet.Target_Active8	bool	
carpet.Target_Swerling1	int	
carpet.Target_Swerling2	int	
carpet.Target_Swerling3	int	
carpet.Target_Swerling4	int	
carpet.Target_Swerling5	int	
carpet.Target_Swerling6	int	
carpet.Target_Swerling7	int	
carpet.Target_Swerling8	int	
carpet.Target_RCS1	float	m <sup>2</sup>
carpet.Target_RCS2	float	m <sup>2</sup>
carpet.Target_RCS3	float	m <sup>2</sup>
carpet.Target_RCS4	float	m <sup>2</sup>
carpet.Target_RCS5	float	m <sup>2</sup>
carpet.Target_RCS6	float	m <sup>2</sup>
carpet.Target_RCS7	float	m <sup>2</sup>
carpet.Target_RCS8	float	m <sup>2</sup>
carpet.Target_AltOffset1	float	m
carpet.Target_AltOffset2	float	m
carpet.Target_AltOffset3	float	m
carpet.Target_AltOffset4	float	m
carpet.Target_AltOffset5	float	m
carpet.Target_AltOffset6	float	m
carpet.Target_AltOffset7	float	m
carpet.Target_AltOffset8	float	m
carpet.Target_Azimuth	float	rad

Table 7.13: Elements of CARPET's siting structure.

Parameter	Type	Unit
carpet.Siting_Latitude	float	rad
carpet.Siting_Longitude	float	rad
carpet.Siting_MinAltitude	int	m
carpet.Siting_Location	int	0=at sea or on flat ground 1=at TNO The Hague 2=on the Matterhorn 3=at Stonehenge 4=somewhere

Table 7.14: Elements of CARPET's layout structure.

Parameter	Type	Unit
carpet.Layout_Rmin	float	m
carpet.Layout_Rmax	float	m
carpet.Layout_Vmin	float	m/s
carpet.Layout_Vmax	float	m/s
carpet.Layout_Altmin	float	m
carpet.Layout_Altmax	float	m
carpet.Layout_Elmin	float	rad
carpet.Layout_Elmax	float	rad
carpet.Layout_RangeUnit	int	0=km 1=NM
carpet.Layout_VelocityUnit	int	0=m/s 1=knots
carpet.Layout_AltitudeUnit	int	0=m 1=ft 2=kft
carpet.Layout_Pd	float	
carpet.Layout_NrSteps	int	
carpet.Layout_GraphicsBoxSize	int	0=small 1=medium 2=large
carpet.Layout_LogRangeAxis	bool	
carpet.Layout_DrawGrid	bool	
carpet.Layout_Contour	bool	
carpet.Layout_NrAzPoints	int	
carpet.Layout_AlphaChannel	float	
carpet.Layout_Polar	bool	
carpet.Layout_PathLossMin	float	dB
carpet.Layout_PathLossMax	float	dB
carpet.Layout_PPFMin	float	dB
carpet.Layout_PPFMax	float	dB
carpet.Layout_DrawAltitudeVertically	bool	
carpet.Layout_GainMin	float	dB
carpet.Layout_GainMax	float	dB
carpet.Layout_ColorMap	int	0=Jet 1=Jet <sup>2</sup> 2=Jet <sup>3</sup> 3=Viridis
carpet.Layout_ReceivedPowersMin	float	dBm
carpet.Layout_ReceivedPowersMax	float	dBm
carpet.Layout_ElErrorMin	float	rad
carpet.Layout_ElErrorMax	float	rad
carpet.Layout_Meyer	bool	
carpet.Layout_PowerRatioUnit	int	0=dBm 1=dBW
carpet.Layout_ContourValue	float	

### 7.3 Functions

The following functions are available ('float' = floating point (rational) number, 'int' = integer number):

- `carpet.GetPd()`: float return argument  
Calculates the detection probability given the current CARPET settings.
- `carpet.GetDetectionRange()`: float return argument  
Calculates the (most distant) detection range (in m) given the current CARPET settings. The detection probability that is specified in the Layout structure serves as threshold.
- `carpet.GetSCNR()`: float return argument  
Calculates the SCNR of the first active waveform, given the current CARPET settings.
- `carpet.GetTerrainProfile()`: 'tuple' return argument  
Returns the terrain profile, given a specific sensor position and antenna azimuth direction.
- `carpet.LoadConfig(fileName: string)`: no return argument  
Loads a CARPET settings file.
- `carpet.SaveConfig(fileName: string)`: no return argument  
Saves a CARPET settings file.
- `carpet.ImportMProfile(fileName: string)`: no return argument  
Imports a refractivity M-profile.
- `carpet.ImportTxAntennaPattern(fileName: string)`: no return argument  
Imports a Tx antenna pattern.
- `carpet.ExportTxAntennaPattern(fileName: string)`: no return argument  
Exports a Tx antenna pattern.
- `carpet.GetFirmTrackProbabilities(Pd: float array)`: float array return argument  
Calculates the firm track probabilities, given a sequence of single-dwell detection probabilities.
- `carpet.GetTrackLossProbabilities(Pd: float array)`: float array return argument  
Calculates track loss probabilities, given a sequence of single-dwell detection probabilities.

- `carpet.GetTrackAcquisitionProbabilities(Pd: float array): float array` return argument  
Calculates track acquisition probabilities, given a sequence of single-dwell detection probabilities.
- `carpet.GetPdSwerling(SC: int, N: int, Pfa: float, SNR: float): float` return argument  
Calculates the detection probability given the Swerling Case, the number of pulses that is non-coherently integrated, the false alarm probability and the signal-to-noise-ratio.
- `carpet.GetTxAntennaGain(Angle: float): float` return argument  
Returns the antenna gain, given the elevation angle.
- `carpet.GetPPF(RF: float, Range: float, Height: float): float` return argument  
Returns the one-way pattern propagation factor, given the carrier frequency, range and height of the target.
- `carpet.GetPathLoss(RF: float, Range: float, Height: float): float` return argument  
Returns the one-way path loss, given the carrier frequency, range and height of the target.

In case additional functionality is demanded, please contact TNO.

## 7.4 Diagrams

CARPET diagrams can be launched and manipulated using the built-in `CarpetCode` object. Deleting the plot object will close the plot. The `CarpetCode` object has the following functions:

- `carpet.CarpetCode(plotID: string)`  
Constructor for a carpet plot object which requires a plot ID as input (for available ID's see below).
- `carpet.CarpetCode.wait()`  
Wait until the plot has been fully calculated and plotted.
- `carpet.CarpetCode.saveImage(fileName: string)`  
Save the plot as an image to the provided filename.
- `carpet.CarpetCode.data: dict`  
Retrieve the underlying data from the plot. The result is a dictionary with the name of the data as key and a tuple containing lists with  $x$ ,  $y$ , and, if applicable,  $z$  data.
- `carpet.CarpetCode.saveData(dataName: string, fileName: string)`  
Saves underlying data from a plot to either a txt-file or a GeoTIFF-file. Use "Spectro" as `dataName` in the case of a PPI-view diagram of the detection probability. Filename extension "txt" will result in a txt-file, extension "tif" will result in a GeoTIFF file.





The diagrams that are available are summarised in Table 7.15.

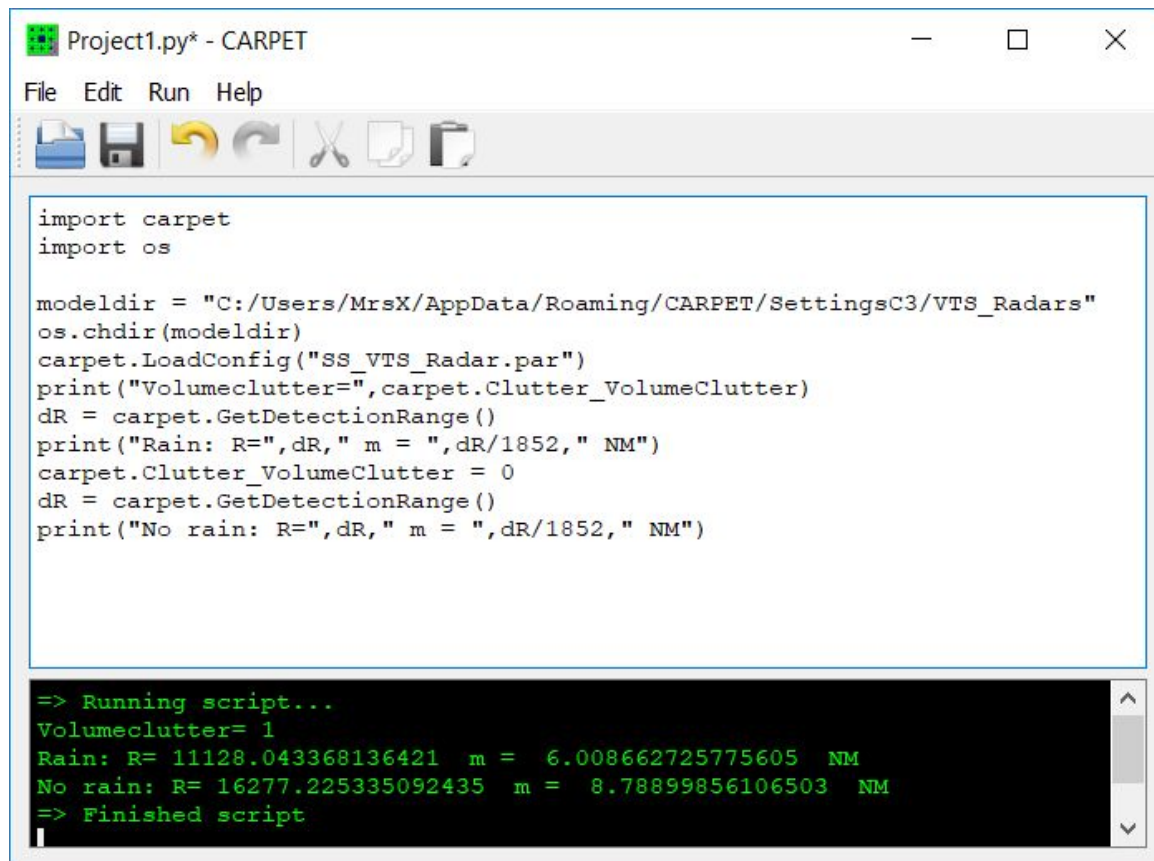
Table 7.15: Overview of antenna illumination functions.

ID	Type
rp_r	Received powers versus target ground range
rp_v	Received powers versus target radial speed
rp_a	Received powers versus target altitude
rp_t	Received powers versus time
rp_ppi_t	Received target power, PPI style
rp_ppi_nc	Received noise + clutter + jamming powers, PPI style
sir_r	Signal to clutter plus noise ratio versus target ground range
sir_v	Signal to clutter plus noise ratio versus target radial speed
sir_a	Signal to clutter plus noise ratio versus target altitude
sir_t	Signal to clutter plus noise ratio versus time
sir_rv	Signal to clutter plus noise ratio versus range and speed
sir_ra	Signal to clutter plus noise ratio versus range and altitude
scnr_ppi	Signal to clutter plus noise ratio, PPI view
pd_r	Detection probability versus target ground range
pd_v	Detection probability versus target radial speed
pd_a	Detection probability versus target altitude
pd_t	Detection probability versus time
pd_rv	Detection probability versus range and radial speed
pd_ra	Detection probability versus range and altitude
pd_ppi	The horizontal coverage diagram (in 'PPI view')
ftp_r	Firm track probability versus target ground range
ftp_t	Firm track probability versus time
ftp_t	Firm track probability versus time
pft_ppi	The horizontal firm track probability diagram (in 'PPI view')
1wpl_r	One-way path loss versus range diagram
1wpl_a	One-way path loss versus altitude diagram
1wpl_ra	One-way path loss versus range and altitude diagram
1wpl_ppi	One-way path loss versus range and azimuth diagram
2wpl_r	Two-way path loss versus range diagram
2wpl_a	Two-way path loss versus altitude diagram
2wpl_ra	Two-way path loss versus range and altitude diagram
2wpl_ppi	Two-way path loss, PPI view
1wppf_r	One-way pattern propagation factor versus range diagram
1wppf_a	One-way pattern propagation factor versus altitude diagram
1wppf_ra	One-way pattern propagation factor versus range and altitude diagram
1wppf_ppi	One-way pattern propagation factor versus range and azimuth diagram
2wppf_r	Two-way pattern propagation factor versus range diagram
2wppf_a	Two-way pattern propagation factor versus altitude diagram
2wppf_ra	Two-way pattern propagation factor versus range and altitude diagram
2wppf_ppi	Two-way pattern propagation factor versus, PPI view
refractivity_profile	Refractivity profile diagrams
radiosonde_code	Imported radiosonde data
terrain_height	Height map of the terrain that surrounds the radar
line_of_sight	Line of sight to the target
terrain_profile	Terrain profile
doppler_filter	Doppler filter diagram
doppler_filter_gains	Doppler filter gains diagram
synthesizer_spectrum	Synthesizer spectrum diagram
swerling_cases	Swerling cases diagram
fluctuation_loss	Fluctuation loss diagram
pd_versus_lf	Detection probability versus fluctuation loss
ant_tx	Elevation antenna pattern on transmit
ant_rx	Elevation antenna pattern on receive
ant_tsr	Elevation antenna pattern(s)

## 7.5 Examples

### 7.5.1 Example 1

A relatively straightforward example of a Python program is given in Figure 7.1. A CARPET settings file is loaded, the detection range in the presence of rain is calculated and printed. Subsequently, rain is switched off and the detection range is printed again.



```
Project1.py* - CARPET
File Edit Run Help
import carpet
import os

modeldir = "C:/Users/MrsX/AppData/Roaming/CARPET/SettingsC3/VTS_Radars"
os.chdir(modeldir)
carpet.LoadConfig("SS_VTS_Radar.par")
print("Volumeclutter=",carpet.Clutter_VolumeClutter)
dR = carpet.GetDetectionRange()
print("Rain: R=",dR," m = ",dR/1852," NM")
carpet.Clutter_VolumeClutter = 0
dR = carpet.GetDetectionRange()
print("No rain: R=",dR," m = ",dR/1852," NM")

=> Running script...
Volumeclutter= 1
Rain: R= 11128.043368136421 m = 6.008662725775605 NM
No rain: R= 16277.225335092435 m = 8.78899856106503 NM
=> Finished script
```

Figure 7.1: Example of a relatively simple Python program.

### 7.5.2 Example 2

A more advanced example is provided in Figure 7.2. This program makes diagrams for a series of rainfall rates and writes results in JSON (JavaScript Object Notation) format.

```

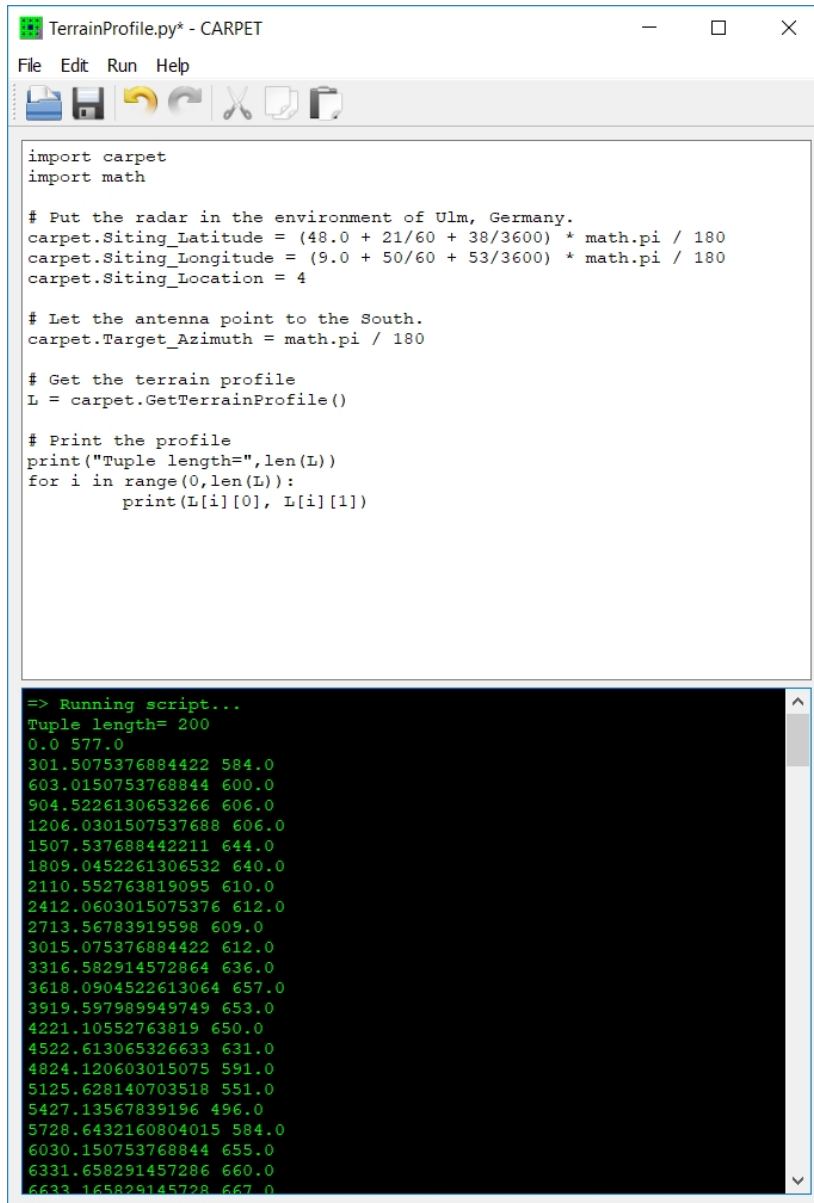
1  """
2  The following script illustrates the use of CARPET's batch mode. In this
3  example, the probability of detection is calculated for the specific radar
4  system defined in the standard CARPET par-file, for a large number of rainfall
5  scenarios.
6  """
7
8  import carpet
9  import os
10 import json
11
12 modeldir = "C:/Users/MrsX/Documents/CARPET/models/CARPET"
13 workdir = "C:/Users/MrsX/Documents/CARPET/work/CARPET"
14 os.chdir(modeldir)
15
16 # define the rainfall parameters of interest.
17 rainfallDistance = [5.0, 7.0, 10.0] # [km]
18 rainfallDiameter = [2.0, 5.0, 10.0] # [km]
19 rainfallRate = [1.0, 2.0, 4.0, 7.0, 10.0] # [mm/hr]
20
21 # initialize a data structure to capture the data
22 carpet_rainfall_data = []
23
24 # load general CARPET parameter file for radar
25 os.chdir(modeldir)
26 carpet.LoadConfig('radar.par')
27
28 # activate rain clutter calculation
29 carpet.Clutter_VolumeClutter = 1
30
31 # loop over rainfall ranges of interest
32 for distance in rainfallDistance:
33     # set rainfall distance, convert to m
34     carpet.Clutter_Range = distance * 1e3 # [m]
35
36     # loop over rainfall diameters of interest
37     for diameter in rainfallDiameter:
38         # set rainfall diameter, convert to m
39         carpet.Clutter_Diameter = diameter * 1e3 # [m]
40
41         # loop over rainfall rates of interest
42         for rate in rainfallRate:
43             # Set rainfall rate
44             carpet.Clutter_RainfallRate = rate * 1e-3 / 3600 # [m/s]
45
46             # save parameter definitions
47             carpetFileName = 'carpet_rainfall_example-distance()-diam()-rate()'.format(
48                 distance, diameter, rate)
49             os.chdir(modeldir)
50             carpet.SaveConfig(carpetFileName + '.par')
51
52             # start calculations
53             os.chdir(workdir)
54             # plot probability of detection versus range
55             plt = carpet.CarpetPlot('pd_r')
56             plt.wait()
57             # save the plot
58             plt.saveImage(carpetFileName + '-Pd.png')
59             # extract the data
60             data = plt.data()
61             carpet_rainfall_data.append(
62                 { 'Distance': distance, 'Diameter': diameter, 'Rate': rate,
63                   'Range': data['Detection Probability'][0],
64                   'Pd': data['Detection Probability'][1] }
65             )
66
67 # save data in convenient format for further analysis
68 with open('carpet_rainfall_example.json', 'w') as f:
69     json.dump(carpet_rainfall_data, f)
70

```

Figure 7.2: Example of a more advanced Python program.

### 7.5.3 Example 3

A program that delivers the terrain profile is given in Figure 7.3.



```
import carpet
import math

# Put the radar in the environment of Ulm, Germany.
carpet.Siting_Latitude = (48.0 + 21/60 + 38/3600) * math.pi / 180
carpet.Siting_Longitude = (9.0 + 50/60 + 53/3600) * math.pi / 180
carpet.Siting_Location = 4

# Let the antenna point to the South.
carpet.Target_Azimuth = math.pi / 180

# Get the terrain profile
L = carpet.GetTerrainProfile()

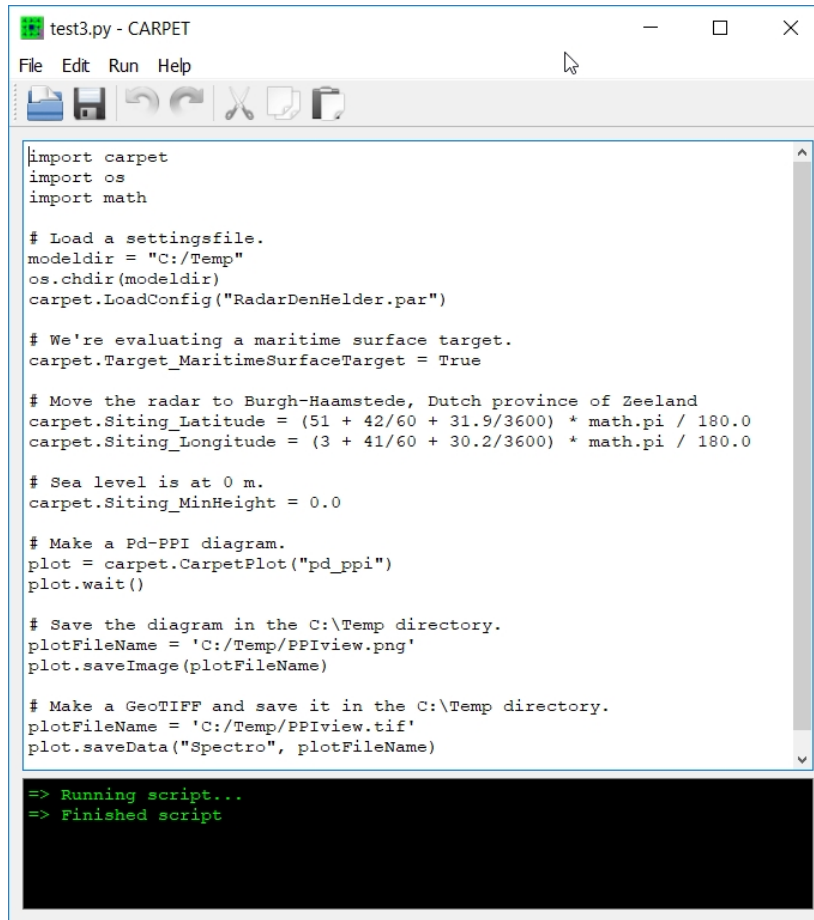
# Print the profile
print("Tuple length=", len(L))
for i in range(0, len(L)):
    print(L[i][0], L[i][1])

=> Running script...
Tuple length= 200
0.0 577.0
301.5075376884422 584.0
603.0150753768844 600.0
904.5226130653266 606.0
1206.0301507537688 606.0
1507.537688442211 644.0
1809.0452261306532 640.0
2110.552763819095 610.0
2412.0603015075376 612.0
2713.56783919598 609.0
3015.075376884422 612.0
3316.582914572864 636.0
3618.0904522613064 657.0
3919.597989949749 653.0
4221.10552763819 650.0
4522.613065326633 631.0
4824.120603015075 591.0
5125.628140703518 551.0
5427.13567839196 496.0
5728.6432160804015 584.0
6030.150753768844 655.0
6331.658291457286 660.0
6633.165829145728 667.0
```

Figure 7.3: The radar antenna is placed West of Ulm, Germany, the terrain profile in the South direction is queried.

#### 7.5.4 Example 4

Figure 7.4 presents a program in which a PPI-view diagram of the detection probability is made. Subsequently, the diagram is saved in both PNG-format and GeoTIFF.



```
test3.py - CARPET
File Edit Run Help
import carpet
import os
import math

# Load a settingsfile.
modeldir = "C:/Temp"
os.chdir(modeldir)
carpet.LoadConfig("Radardenhelder.par")

# We're evaluating a maritime surface target.
carpet.Target_MaritimeSurfaceTarget = True

# Move the radar to Burgh-Haamstede, Dutch province of Zeeland
carpet.Siting_Latitude = (51 + 42/60 + 31.9/3600) * math.pi / 180.0
carpet.Siting_Longitude = (3 + 41/60 + 30.2/3600) * math.pi / 180.0

# Sea level is at 0 m.
carpet.Siting_MinHeight = 0.0

# Make a Pd-PPI diagram.
plot = carpet.CarpetPlot("pd_ppi")
plot.wait()

# Save the diagram in the C:\Temp directory.
plotFileName = 'C:/Temp/PPiView.png'
plot.saveImage(plotFileName)

# Make a GeoTIFF and save it in the C:\Temp directory.
plotFileName = 'C:/Temp/PPiView.tif'
plot.saveData("Spectro", plotFileName)

=> Running script...
=> Finished script
```

Figure 7.4: Python program in which a PPI-view diagram is saved in both PNG format and GeoTIFF.

### 7.5.5 Example 5

The listing of a program that illustrates the use of the functions `GetFirmTrackProbabilities`, `GetTrackAcquisitionProbabilities` and `GetTrackLossProbabilities` is given below. The program replicates the diagram in Dick Worsham's paper, [2], see Figure 7.5.

```
1 import carpet
2 import os
3 import math
4 import sys
5
6 # Investigate 3-out-of-8 and L=6, similar to the plot in the IEEE paper of Dick Worsham.
7 carpet.Tracking_Misses = 6
8 carpet.Tracking_InitiationM = 3
9 carpet.Tracking_InitiationN = 8
10
11 # Open a file for output, write some strings to the file.
12 f = open("C:/Temp/test.txt","w")
13 f.write("x-label:Observation number\n")
14 f.write("y-label:Pd / Pft / Pacq / Ploss (%) \n")
15
16 # Construct Pds, three sines.
17 dPd = [];
18 for i in range (0,3,1):
19     dPd.append(0.0);
20     dPd.append(0.005);
21     dPd.append(0.01);
22     dPd.append(0.025);
23     dPd.append(0.04);
24     dPd.append(0.07);
25     dPd.append(0.12);
26     dPd.append(0.2);
27     dPd.append(0.4);
28     dPd.append(0.6);
29     dPd.append(0.8);
30     dPd.append(0.88);
31     dPd.append(0.93);
32     dPd.append(0.96);
33     dPd.append(0.975);
34     dPd.append(0.99);
35     dPd.append(0.995);
36     dPd.append(1.0);
37     dPd.append(0.995);
38     dPd.append(0.99);
39     dPd.append(0.975);
40     dPd.append(0.96);
41     dPd.append(0.93);
42     dPd.append(0.88);
43     dPd.append(0.8);
```

```
44         dPd.append(0.6);
45         dPd.append(0.4);
46         dPd.append(0.25);
47         dPd.append(0.12);
48         dPd.append(0.07);
49         dPd.append(0.04);
50         dPd.append(0.02);
51         dPd.append(0.01);
52         dPd.append(0.005);
53 dPd.append(0.0);
54
55 # Write the Pds to file.
56 for i in range(len(dPd)):
57     print(i, dPd[i])
58     f.write("%d " % i)
59     f.write("%f\n" % (dPd[i]*100))
60 f.write("\n")
61
62 # Calculate firm track probability.
63 v = carpet.GetFirmTrackProbabilities(dPd)
64
65 # Write the Pfts to file.
66 for i in range(len(v)):
67     print(i, v[i])
68     f.write("%d " % i)
69     f.write("%f\n" % (v[i]*100))
70 f.write("\n")
71
72 # Calculate track acquisition probability.
73 v = carpet.GetTrackAcquisitionProbabilities(dPd)
74
75 # Write the Pacqs to file.
76 for i in range(len(v)):
77     print(i, v[i])
78     f.write("%d " % i)
79     f.write("%f\n" % (v[i]*100))
80 f.write("\n")
81
82 # Calculate track loss probability.
83 v = carpet.GetTrackLossProbabilities(dPd)
84
85 # Write the Ploss to file.
86 for i in range(len(v)):
87     print(i, v[i])
88     f.write("%d " % i)
89     f.write("%f\n" % (v[i]*100))
90 f.write("\n")
91
92 f.close()
```





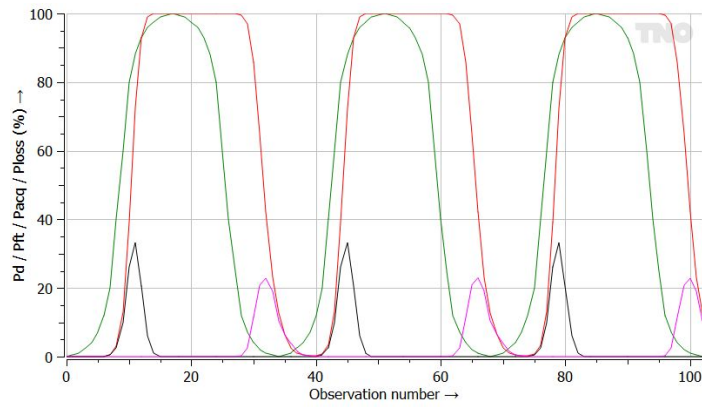
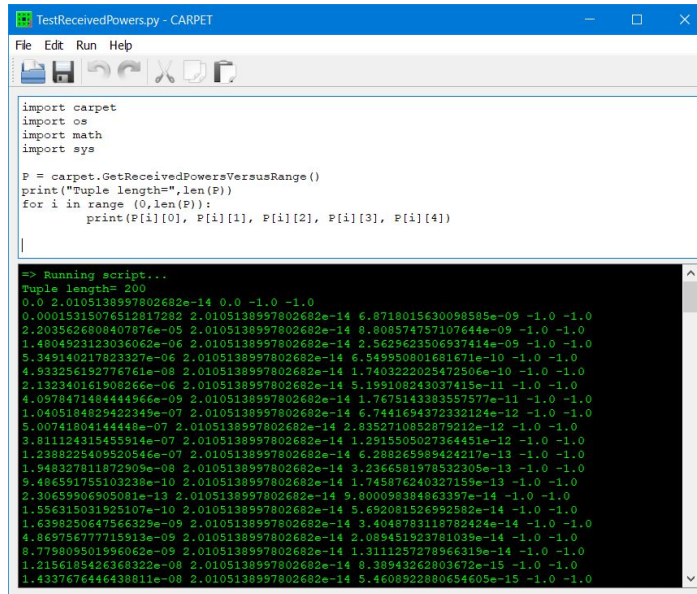


Figure 7.5: Dick Worsham's figure, reconstructed with CARPET's Python plug-in. Green: single dwell detection probability. Red: firm track probability. Black: track acquisition probability. Pink: track loss probability. Track initiation is according to 3-out-of-8. Track loss (or 'track drop') after six misses.

### 7.5.6 Example 6

Figure 7.6 presents a program in which received powers versus range are queried. The tuple that is returned contains five columns. The received target power is in the first column, the received noise power is in the second column, the received surface clutter power is in the third column, the received volume clutter power is in the fourth column, the received jamming power is in the last (fifth) column.



```

TestReceivedPowers.py - CARPET
File Edit Run Help

import carpet
import os
import math
import sys

P = carpet.GetReceivedPowersVersusRange()
print("Tuple length=",len(P))
for i in range(0,len(P)):
    print(P[i][0], P[i][1], P[i][2], P[i][3], P[i][4])

|

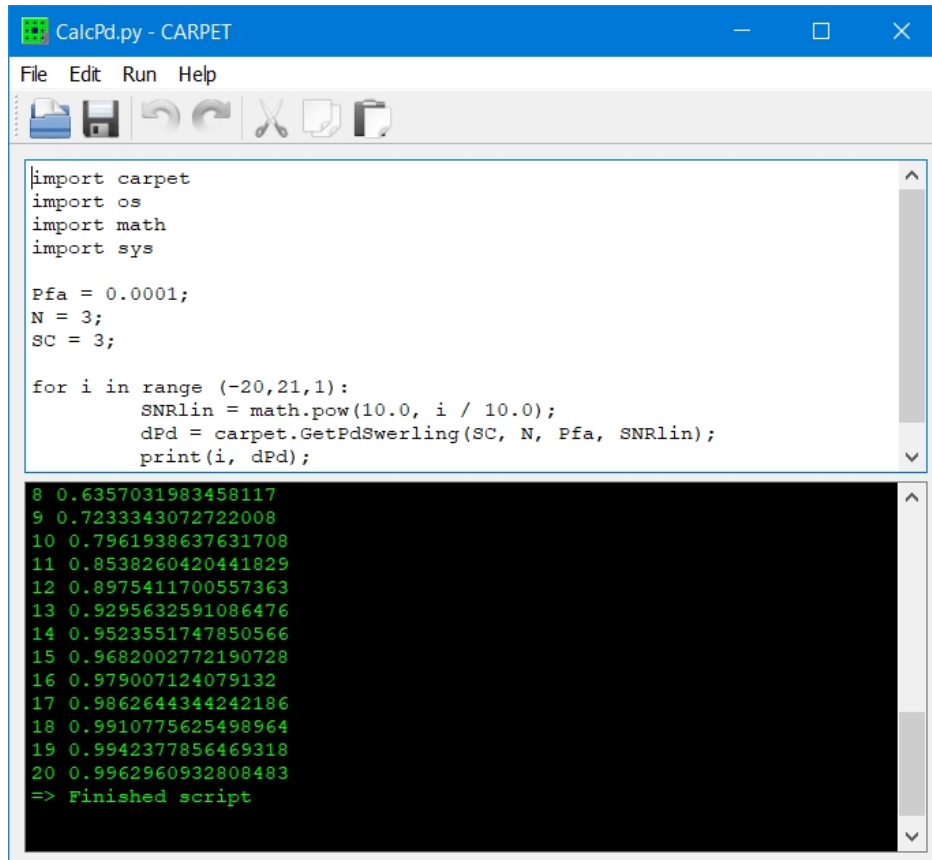
=> Running script...
Tuple length= 200
0.0 2.0105138997802682e-14 0.0 -1.0 -1.0
0.00015315076512817282 2.0105138997802682e-14 6.8718015630098589e-09 -1.0 -1.0
2.2035626809407876e-05 2.0105138997802682e-14 8.808574757107644e-09 -1.0 -1.0
1.480492312303606e-06 2.0105138997802682e-14 2.5629523506937414e-09 -1.0 -1.0
5.349140217823327e-06 2.0105138997802682e-14 6.549950801681671e-10 -1.0 -1.0
4.93256192776761e-08 2.0105138997802682e-14 1.7403222025472506e-10 -1.0 -1.0
2.132340161908266e-06 2.0105138997802682e-14 5.199108243037415e-11 -1.0 -1.0
4.0978471484444966e-09 2.0105138997802682e-14 1.7675143383557577e-11 -1.0 -1.0
1.0405184829422349e-07 2.0105138997802682e-14 6.7441694372332124e-12 -1.0 -1.0
5.00741804144448e-07 2.0105138997802682e-14 2.8352710852879212e-12 -1.0 -1.0
3.01112431545914e-07 2.0105138997802682e-14 1.2915505027384451e-12 -1.0 -1.0
1.2388225409520546e-07 2.0105138997802682e-14 6.288265989424217e-13 -1.0 -1.0
1.948327811872909e-08 2.0105138997802682e-14 3.2366581978532305e-13 -1.0 -1.0
9.486591755103298e-10 2.0105138997802682e-14 1.745876240327159e-13 -1.0 -1.0
2.30659906905081e-13 2.0105138997802682e-14 9.800098384863397e-14 -1.0 -1.0
1.556315031925107e-10 2.0105138997802682e-14 5.692081526992582e-14 -1.0 -1.0
1.6398250647566329e-09 2.0105138997802682e-14 3.4048783118782424e-14 -1.0 -1.0
4.869786977718913e-09 2.0105138997802682e-14 2.089451323781039e-14 -1.0 -1.0
8.77809901996062e-09 2.0105138997802682e-14 1.3111257278966319e-14 -1.0 -1.0
1.2156185426368322e-08 2.0105138997802682e-14 8.38943262803672e-15 -1.0 -1.0
1.4337676446438811e-08 2.0105138997802682e-14 5.4608922880654605e-15 -1.0 -1.0

```

Figure 7.6: Python program that queries received powers versus range.

### 7.5.7 Example 7

Figure 7.7 presents a program that asks for the detection probability, given the Swerling case, number of pulses non-coherently integrated, false alarm probability and signal-to-noise-ratio.



```
CalcPd.py - CARPET
File Edit Run Help
import carpet
import os
import math
import sys

Pfa = 0.0001;
N = 3;
SC = 3;

for i in range (-20,21,1):
    SNRlin = math.pow(10.0, i / 10.0);
    dPd = carpet.GetPdSwerling(SC, N, Pfa, SNRlin);
    print(i, dPd);

8 0.6357031983458117
9 0.7233343072722008
10 0.7961938637631708
11 0.8538260420441829
12 0.8975411700557363
13 0.9295632591086476
14 0.9523551747850566
15 0.9682002772190728
16 0.979007124079132
17 0.9862644344242186
18 0.9910775625498964
19 0.9942377856469318
20 0.9962960932808483
=> Finished script
```

Figure 7.7: Python program that queries the detection probability.

## 7.5.8 Example 8

Figure 7.8 presents a program that loads a transmit antenna pattern and subsequently queries the antenna gain for different distances from the antenna.

```

import carpet
import os
import math
import sys

# Load an antenna pattern.
carpet.Antenna_TxFileName = 'C:/Temp/TxPattern.txt';
carpet.ImportTxAntennaPattern(carpet.Antenna_TxFileName);

# Set the vertical tilt angle, the height and the boresight gain of the aperture.
carpet.Antenna_TxElevation = 25.0 * math.pi / 180.0;
carpet.Antenna_TxHeight = 24.0;
carpet.Antenna_TxGain = math.pow(10.0, 30.0 / 10.0);

# Vary the range from 300 to 1500 m with steps of 10 m.
for i in range (300, 1501, 10):

# Calculate depression angle.
    ang = -1.0 * math.atan(carpet.Antenna_TxHeight / i);

# Query the antenna gain at the depression angle.
    G = carpet.GetTxAntennaGain(ang);

# Print distance (in m), depression angle (in degrees) and gain (in dBi).
    print('i=', i, ' ang=', ang*180.0/math.pi, ' Gain=',10.0*math.log10(G));

i= 1410  ang= -0.9751531430925626  Gain= 29.963444213033053
i= 1420  ang= -0.9682871795413128  Gain= 29.96282291982368
i= 1430  ang= -0.9615172162199928  Gain= 29.962210270049727
i= 1440  ang= -0.9548412538721887  Gain= 29.961606084601158
i= 1450  ang= -0.9482573483678572  Gain= 29.961010189282277
i= 1460  ang= -0.9417636088164733  Gain= 29.960422414644363
i= 1470  ang= -0.9353581957571454  Gain= 29.959842595825048
i= 1480  ang= -0.9290393194220559  Gain= 29.959270572394246
i= 1490  ang= -0.9228052380697901  Gain= 29.958706188206175
i= 1500  ang= -0.9166542563852879  Gain= 29.958149291257303
=> Finished script

```

Figure 7.8: Python program that queries the antenna gain at different distances from the antenna.

### 7.5.9 Example 9

The python plug-in can also be used to model 3D surveillance radars, *i.e.*, radars that not only determine slant range and azimuth angle, but also elevation angle. Both the stacked beams on receive architecture and the steered beams architecture can be simulated. A python example program goes as follows:

```

1 import carpet
2 import os
3 import math
4
5 # Select free space propagation.
6 carpet.Model_PropagationModel = 0
7
8 # Adapt maximum altitude.
9 carpet.Layout_Altmax = 10000.0
10
11 # Adapt the antenna tilt and also the beamwidth.
12 carpet.Antenna_TxElevation = 1.0 * math.pi / 180.0
13 carpet.Antenna_TxEIBeamwidth = 2.0 * math.pi / 180.0
14
15 # We want to see Pd's higher than 50%.
16 carpet.Layout_Pd = 0.5
17
18 # Safety first, needed when re-executing this script.
19 carpet.Sensorfusion_SubSystem = 0
20
21 # Make a vertical coverage diagram of the single beam radar.
22 plot = carpet.CarpetPlot("pd_ra")
23 plot.wait()
24
25 # Save the diagram in the C:\Temp directory.
26 plotFileName = 'C:/Temp/one_beam_radar.png'
27 plot.saveImage(plotFileName)
28
29 #####
30
31 # Create a 2nd (sub)radar, print the number of (sub)radars.
32 i = carpet.CreateRadar()
33 print("Number of (sub)radars: ",i)
34
35 # Select the 2nd (sub)radar (we start counting from zero) and adapt
36 # its antenna tilt (to 4 degrees elevation angle).
37 carpet.Sensorfusion_SubSystem = 1
38 carpet.Antenna_TxElevation = 4.0 * math.pi / 180.0
39
40 # Make a vertical coverage diagram of (sub)radar number 1, i.e., the 2nd one.
41 plot = carpet.CarpetPlot("pd_ra")
42 plot.wait()

```

```

43
44 # Now combine the two (sub)radars and re-make a vertical coverage diagram.
45 carpet.Sensorfusion_Combine = True
46 plot = carpet.CarpetPlot("pd_ra")
47 plot.wait()
48
49 # Save the diagram in the C:\Temp directory.
50 plotFileName = 'C:/Temp/two_beams_radar.png'
51 plot.saveImage(plotFileName)
52
53 #####
54
55 # Create a 3rd (sub)radar, print the number of (sub)radars.
56 i = carpet.CreateRadar()
57 print("Number of (sub)radars: ",i)
58
59 # Select the 3rd (sub)radar (we start counting from zero) and adapt its
60 # antenna tilt.
61 carpet.Sensorfusion_SubSystem = 2
62 carpet.Antenna_TxElevation = 7.0 * math.pi / 180.0
63
64 # Re-make a vertical coverage diagram, the three radars are combined.
65 plot = carpet.CarpetPlot("pd_ra")
66 plot.wait()
67
68 # Save the diagram in the C:\Temp directory.
69 plotFileName = 'C:/Temp/three_beams_radar.png'
70 plot.saveImage(plotFileName)
71
72 #####
73
74 # Create a 4th (sub)radar, print the number of (sub)radars.
75 i = carpet.CreateRadar()
76 print("Number of (sub)radars: ",i)
77
78 # Select the 4th (sub)radar, we start counting from zero!
79 carpet.Sensorfusion_SubSystem = 3
80
81 # Adapt the antenna tilt of the fourth (sub)radar.
82 carpet.Antenna_TxElevation = 10.0 * math.pi / 180.0
83
84 # Make a vertical vertical coverage diagram of the four (sub)radars combined.
85 plot = carpet.CarpetPlot("pd_ra")
86 plot.wait()
87
88 # Save the diagram in the C:\Temp directory.
89 plotFileName = 'C:/Temp/four_beams_radar.png'
90 plot.saveImage(plotFileName)
91

```



```

92 #####
93
94 # Create a 5th (sub)radar, print the number of (sub)radars.
95 i = carpet.CreateRadar()
96 print("Number of (sub)radars: ",i)
97
98 # Select the 5th subradar, we start counting from zero!
99 carpet.Sensorfusion_SubSystem = 4
100
101 # Adapt the antenna tilt of the 5th (sub)radar.
102 carpet.Antenna_TxElevation = 13.0 * math.pi / 180.0
103
104 # Make a vertical vertical coverage diagram of the five (sub)radars combined.
105 plot = carpet.CarpetPlot("pd_ra")
106 plot.wait()
107
108 # Save the diagram in the C:\Temp directory.
109 plotFileName = 'C:/Temp/five_beams_radar.png'
110 plot.saveImage(plotFileName)
111
112 # Select a more realistic propagation model (EREPS-like).
113 carpet.Model_PropagationModel = 1
114
115 # Make a vertical vertical coverage diagram of the five (sub)radars combined.
116 plot = carpet.CarpetPlot("pd_ra")
117 plot.wait()
118
119 # Save the diagram in the C:\Temp directory.
120 plotFileName = 'C:/Temp/five_beams_radar_EREPS.png'
121 plot.saveImage(plotFileName)
122
123 # Remove all (sub)radars, in order to enable re-executing.
124 carpet.RemoveRadars()

```

Note that in this listing multiple (sub)radars are created by calling `CreateRadar()` multiple times. A specific (sub)radar is selected by the statement `Sensorfusion_SubSystem = n`. This means that specifying parameters (such as `Antenna_TxElevation`) applies to the  $n + 1$ -th (sub)radar. `Sensorfusion_Combine = True` means the detection probability values obtained with each (sub)radar are combined. CARPET 3 contains two mechanisms to do so:

- $M$ -out-of- $N$ , with  $N$  the number of (sub)radars. Set `Sensorfusion_MSI` to zero. The value of  $M$  can be specified by setting `Sensorfusion_M` to a specific value.
- The maximum detection probability is taken. Set `Sensorfusion_MSI` to unity.

The diagrams that the Python program produces are shown in Figure 7.9.

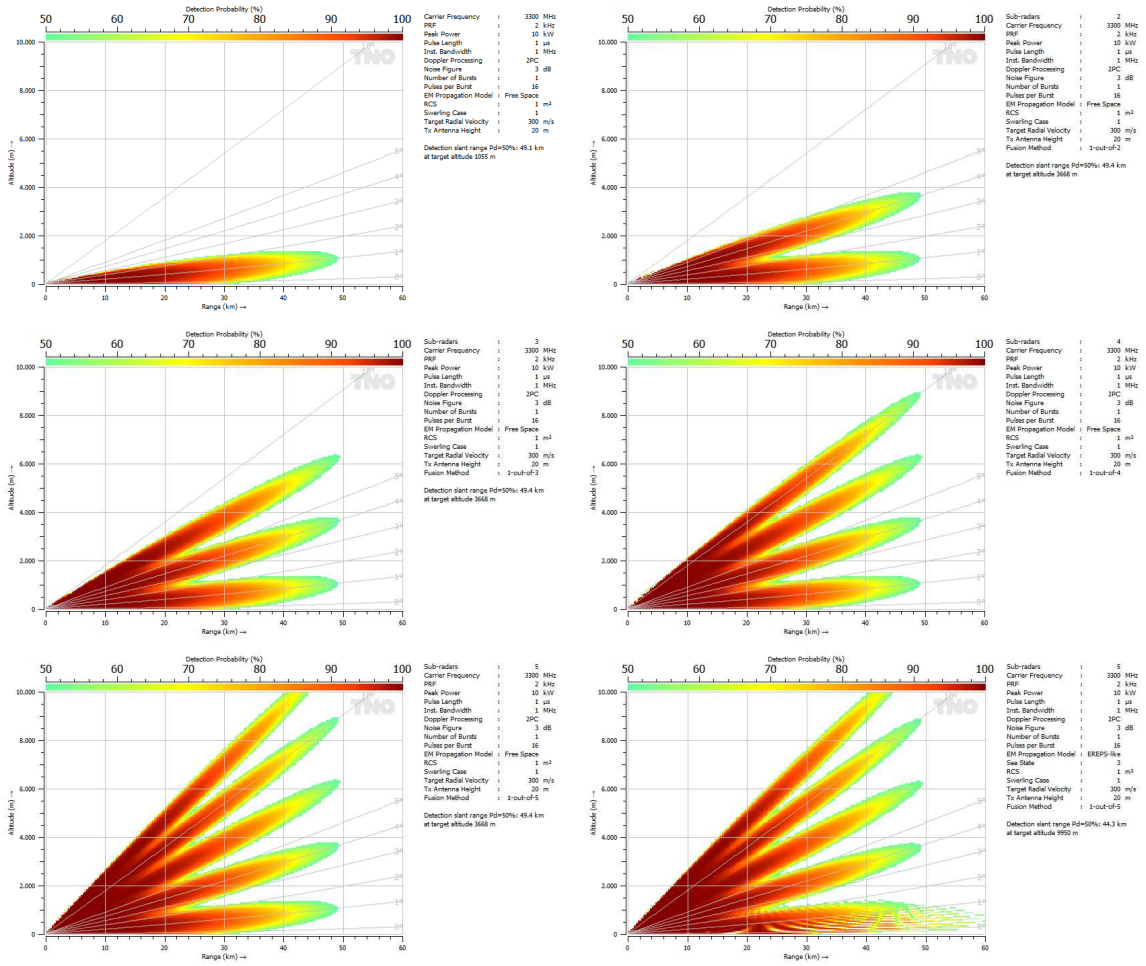


Figure 7.9: Graphical output of a Python program that simulates a stacked beams on receive radar.





## 8 Abbreviations

ADC	Analog to Digital Convertor
AESA	Active Electronically Scanned Array
AREPS	Advanced Refractive Effects Prediction System
ASCII	American Standard Code for Information Interchange
CARPET	Computer Aided Radar Performance Evaluation Tool
CCIR	Comité Consultatif International pour la Radio
CDF	Cumulative Density Function
CFAR	Constant False Alarm Rate
CI/CD	Continuous Integration / Continuous Delivery and/or Deployment
CUT	Cell Under Test
DFMT	Discrete Mixed Fourier Transform
DLL	Dynamic Link Library
DTED	Digital Terrain Elevation Data
ECMWF	European Centre for Medium-Range Weather Forecasts
EIRP	Effective Isotropically Radiated Power
EM	Electro Magnetic
EPM	Electronic Protection Measure
ERA	ECMWF Re-Analysis
EREPS	Engineer's Refractive Effects Prediction System
FAR	False Alarm Rate
FE	Flat Earth
FFT	Fast Fourier Transform
FIR	Finite Impulse Response
FMCW	Frequency Modulated Continuous Wave
GIS	Geographic Information System
HF	High Frequency
HPE	Horizontal Parabolic Equation
http	HyperText Transfer Protocol
https	HyperText Transfer Protocol Secure
IALA	International Association of Lighthouse Authorities
IGRA	Integrated Global Radiosonde Archive
IMO	International Maritime Organisation
ITU-R	International Telecommunication Union - Radiocommunications sector
JSON	JavaScript Object Notation
KML	Keyhole Markup Language
LNA	Low Noise Amplifier
MPM	Millimetre-wave Propagation Model
NM	Nautical Mile

NATO	North Atlantic Treaty Organization
NSIS	Nullsoft Scriptable Install System
OEM	Original Equipment Manufacturer
PDF	Probability Density Function
PE	Parabolic Equation
PNG	Portable Network Graphics
PRF	Pulse Repetition Frequency
PRT	Pulse Repetition Time
PSR	Primary Surveillance Radar
RAM	Random Access Memory
RF	Radar Frequency
RGB	Red Green Blue
RMS	Root Mean Square
RO	Ray Optics
RPM	Rounds Per Minute
SRTM	Shuttle Radar Topography Mission
SRTM1	1 arc second (30 m) SRTM
SRTM3	3 arc second (90 m) SRTM
STC	Sensitivity Time Control
TIFF	Tagged Image File Format
TNO	Netherlands Organisation for Applied Scientific Research
URL	Uniform Resource Locator
UTC	Universal Time Coordinated
UTM	Universal Transverse Mercator
VHF	Very High Frequency
VPE	Vertical Parabolic Equation
VTS	Vessel Traffic Services
WAPE	Wide Angle Parabolic Equation
WMO	World Meteorological Organization

## References

- [1] Albert G. Huizing, Arne Theil, *CARPET: Computer-Aided Radar Performance Evaluation Tool, Radar Performance Analysis, Software and User's Manual, Version 1.0*, Artech House Publishers, 1993, ISBN 0-89006-636-1
- [2] Richard Worsham, *The probabilities of track initiation and loss using a sliding window for track acquisition*, IEEE Radar Conference 2010
- [3] [https://www.metoffice.gov.uk/media/pdf/e/a/No.\\_13\\_-\\_Upper\\_Air\\_Measurements.pdf](https://www.metoffice.gov.uk/media/pdf/e/a/No._13_-_Upper_Air_Measurements.pdf)
- [4] <http://signalscience.co.uk/TERMET.htm>
- [5] D. Cooper, *Atmospheric Absorption Losses for Microwave Radars*, The Marconi Review, Vol.XLV, Nr. 224, 1st quarter 1982
- [6] H.J. Liebe, G.A. Hufford, M.G. Cotton, *Atmospheric Propagation Effects through Natural and Man-Made Obscurants for Visible to MM-Wave Radiation*, AGARD, November 1993
- [7] *Manual on Marine Meteorological Services Volume I - Global Aspects*, WMO publication 558, 2012 edition, [https://library.wmo.int/pmb\\_ged/wmo\\_558\\_en-v1.pdf](https://library.wmo.int/pmb_ged/wmo_558_en-v1.pdf)
- [8] Hendrik Wallbrink, Frits Koek, *Historical wind speed equivalents of the Beaufort scale, 1850 - 1950*, KNMI-memorandum HISKLIM-13, De Bilt, 2009
- [9] A.R. Miller, R.M. Brown, E. Vegh, *New derivation for the rough surface reflection coefficient and for the distribution of the sea-wave elevations*, Proceedings of the IEE, Vol.131, Nr.2, pt. H, pp. 114-116, Apr. 1984.
- [10] ITU Report 229-6, *Electrical Characteristics of the Surface of the Earth*, 1990
- [11] M.M. Horst, F.B. Dyer, M.T. Tuley, *Radar Sea Clutter Model*, IEE International Conference on Antennas and Propagation, 1978, pp.6-10.
- [12] Thaddeus Vincenty, *Direct and inverse solutions of geodesics on the ellipsoid with application of nested equations*, Survey Review XXII, 176, April 1975
- [13] M.R. Battaglia, *Modelling the Radar Evaporative Duct*, RANRL Technical Note No. 3/85, 1985

- [14] Alexander M.J. van Eijk, Gerard J. Kunz, *The introduction of horizontal inhomogeneity of meteorological conditions in the EO STAR propagation model*, Proceedings of SPIE, Vol.6303, 63030G, 2006
- [15] Jerzy Neyman, Egon S. Pearson, *On the Problem of the most Efficient Tests of Statistical Hypotheses*, Philosophical Transactions of the Royal Society of London. Series A, Containing Papers of a Mathematical or Physical Character, Vol. 231 (1933), pp. 289-337
- [16] Daniel P. Meyer, Herbert A. Mayer, *Radar Target Detection, Handbook of Theory and Practice*, Academic Press, 1973
- [17] Nathaniel Smith, Stéfan van der Walt, *A Better Default Colormap for Matplotlib*, SciPy conference 2015, Austin, Texas, U.S.A.
- [18] Lamont V. Blake, *A Guide to Basic Pulse-Radar Maximum Range Calculation*, NRL Report 6930, December 23, 1969
- [19] David K. Barton, *Modern Radar System Analysis*, Artech House Publishers, 1988
- [20] W.L. Patterson, C.P. Hattan, G.E. Lindem, P.A. Paulus, H.V. Hitney, K.D. Anderson, A.E. Barrios, *Engineer's Refractive Effects Prediction System (EREPS), Version 3.0*, Naval Command, Control and Ocean Surveillance Center, Technical Document 2648, May 1994
- [21] Mireille F. Levy, Kenneth H. Craig *TERPEM propagation package for operational forecasting with EEMS*, Proceedings of the 1996 Battlespace Atmospheric Conference, Technical Document 2938, NCCOSC, RDT&E Division, San Diego, pp. 497-505, 1996
- [22] Mireille Levy, *Parabolic equation methods for electromagnetic propagation*, IEE Electro Magnetic Waves Series 45, ISBN 0 85296 764 0, 2000
- [23] K.D. Anderson, A.E. Barrios, C.P. Hattan, H.V. Hitney, G.E. Lindern, W.L. Patterson and R.A. Paulus, *EREPS: Engineer's Refractive Effects Prediction System Software and User's Manual*, Artech House Publishers, 1990
- [24] D.E. Kerr, *Propagation of Short Radio Waves*, McGraw-Hill 1951
- [25] S.T. Wu and A.K. Fung, *A Theory of Microwave Apparent Temperature of the Ocean*, University of Kansas, November 1973, NASA CR-2329
- [26] James R. Wait, *Electromagnetic Waves in Stratified Media*, Pergamon, 1st January 1970
- [27] Richard A. Paulus, *Evaporation Duct Effects on Sea Clutter*, IEEE Transaction on Antennas and Propagation, Vol. 38, No. 11, November 1990



- [28] L. Boithias, *Radio Wave Propagation*, North Oxford Academic Publishers 1987
- [29] Wei Zhang, Nader Moayeri, *Power Law Parameters of Rain Specific Attenuation*, IEEE 802.16cc-99/24, 1 November 1999
- [30] David K. Barton, *Radar System Analysis and Modelling*, Artech House Publishers, 2005, ISBN 1-58053-681-6
- [31] John F. Fielding and Gary D. Reynolds, *User's Manual RG CALC*, Artech House Publishers, 1987
- [32] Mervin C. Budge Jr., Shawn R. German, *Basic Radar Analysis*, Artech House Publishers, 2nd edition, 2020
- [33] Fred E. Nathanson, *Radar Design Principles*, McGraw-Hill Inc. 1969
- [34] Peter Swerling, *Probability of Detection for Fluctuating Targets*, RM-1217, March 17, 1954
- [35] Irving Kanter, *Exact Detection Probability for Partially Correlated Rayleigh Targets*, IEEE Transactions on Aerospace and Electronic Systems, Vol. AES-22, No. 2, March 1986
- [36] W. William, A. Skillman, *User's Manual SIG CLUT*, Artech House Publishers, 1987
- [37] Merrill I. Skolnik, *Radar Handbook*, McGraw-Hill Inc. 1970
- [38] Albert Einstein, *Ist die Trägheit eines Körpers von seinem Energiegehalt abhängig?*, Annalen der Physik, 18:639-641, September 27<sup>th</sup> 1905
- [39] Christian Doppler, *Über das farbige Licht der Doppelsterne und einiger anderer Gestirne des Himmels*, Abhandlungen der Königl. Böh. Ges. d. Wiss. (V. Folge, Bd. 2, S. 465-482), 1842
- [40] V. Considine, *Digital Complex Sampling*, IET Electronics Letters, Volume 19, Issue 16, 4 August 1983
- [41] Marcus C. Walden, Roger D. Pollard *On the Processing Gain and Pulse Compression Ratio of Frequency Hopping Spread Spectrum Waveforms*, IEEE, 1993
- [42] Eugene R. Billam, *Eclipsing effects with high-duty-factor waveforms in long-range radar*, IEE Proceedings, Vol.132, Pt. F, Nr.7, December 1985
- [43] Frederic J. Harris, *On the Use of Windows for Harmonic Analysis with the Discrete Fourier Transform*, Proceedings of the IEEE, Vol.66, Nr.1, January 1978

- 
- [44] Richard G. Lyons, *Understanding Digital Signal Processing*, Prentice Hall, 2nd edition, ISBN 0-13-108989-7
- [45] Sergio Sabatini, *Reference Oscillator Stability Effect on Clutter Cancellation in a Radar System*, Rivista Technica SELENIA, Vol.9, Nr.1
- [46] George E.P. Box, Mervin E. Muller, *A Note on the Generation of Random Normal Deviates*, The Annals of Mathematical Statistics (1958), Vol. 29, No. 2 pp. 610–611
- [47] Harry Urkowitz, *Signal Theory and Random Processes*, Artech House Publishers, 1983, ISBN 0-890006-121-1
- [48] Mark A. Richards, James A. Scheer, William A. Holm (Editors), *Principles of Modern Radar - Basic Principles*, Scitech Publishing, Inc., ISBN 978-1-891121-52-4
- [49] CCIR Recommendation 838, Specific Attenuation Model for Rain for Use in Prediction Methods, 1992
- [50] Recommendation ITU-R P.676-11, Attenuation by Atmospheric Gases, 2016
- [51] Recommendation ITU-R P.838-3, Specific Attenuation Model for Rain for Use in Prediction Methods, 2005
- [52] Recommendation ITU-R P.835-6 (12/2017) Reference standard atmospheres
- [53] J.M. Pettit, M.M. McWorther, *Electronic Amplifier Circuits*, McGraw-Hill Electrical and Electronic Engineering Series, 1961
- [54] Merrill I. Skolnik, *Introduction to Radar Systems*, McGraw-Hill, 2nd edition, 1980, ISBN 0-07-057909-1
- [55] Merrill I. Skolnik, *Introduction to Radar Systems*, McGraw-Hill, 3rd edition, 2001, ISBN 0-07-290980-3

## A Multipath in the Vertical Plane

The ‘flat earth geometry’ is shown in Figure A.1.  $h_a$  (m) is the height of the antenna,  $h_t$  (m) is the altitude of the target,  $d$  (m) is the ground range of the target.

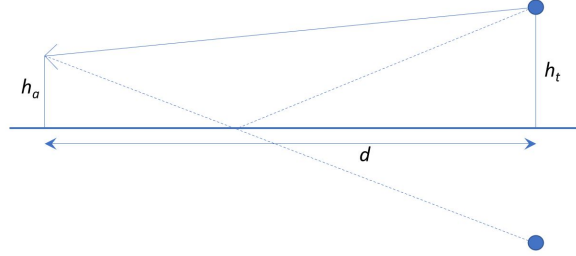


Figure A.1: Flat earth geometry.

The slant range to the target,  $l_d$  (m), is given by:

$$l_d = \sqrt{(h_t - h_a)^2 + d^2}. \quad (\text{A.1})$$

The slant range to the image of the target,  $l_i$  (m), is given by:

$$l_i = l_d + \Delta l = \sqrt{(h_t + h_a)^2 + d^2}, \quad (\text{A.2})$$

with  $\Delta l$  (m) the path length difference. Thus,

$$l_i^2 - l_d^2 = (l_d + \Delta l)^2 - l_d^2 = (h_t + h_a)^2 + d^2 - \{(h_t - h_a)^2 + d^2\}, \quad (\text{A.3})$$

so that

$$2l_d\Delta l + \Delta l^2 = 4h_th_a. \quad (\text{A.4})$$

Because  $\Delta l \ll l_d$  the second term on the left side can be neglected, so that we get

$$\Delta l \approx \frac{2h_th_a}{l_d}. \quad (\text{A.5})$$

The phase difference,  $\Delta\phi$  (rad), between the signal that travels along the indirect path and the signal that travels along the direct path is given by

$$\Delta\phi = \frac{2\pi\Delta l}{\lambda} + \phi_r = \frac{4\pi h_th_a}{\lambda l_d} + \phi_r. \quad (\text{A.6})$$

with  $\lambda$  (m) the radar wavelength and  $\phi_r$  the phase-jump upon reflection at the earth’s surface.

Figure A.2 shows how the phase difference changes for a target at 25 m altitude and an antenna height also at 25 m, for 1 GHz (L-band) and for 3 GHz (S-band). The phase-jump upon reflection is fixed at  $180^\circ$ . The phase change speed is proportional to the radar frequency, which makes low frequency radar less attractive when having to observe targets that travel at a low altitude. Additionally, the reflection coefficient is generally larger ( $\rho$  closer to unity) when the radar frequency is lower.

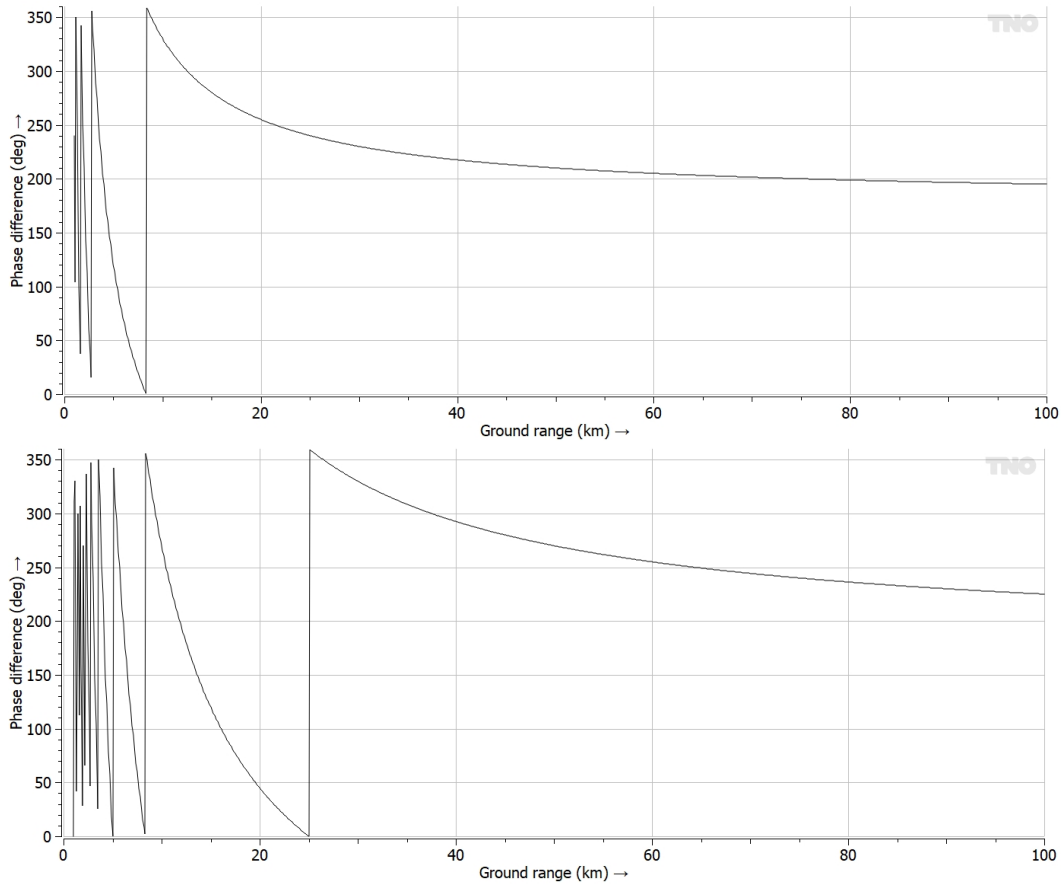


Figure A.2: Phase difference  $\Delta\phi$  versus target ground range, Top: L-band. Bottom: S-band.